12-2022

First Development and Demonstration of Fiber Optic Bolometer

Seungsup Lee
slee148@vols.utk.edu

To the Graduate Council:

I am submitting herewith a dissertation written by Seungsup Lee entitled "First Development and Demonstration of Fiber Optic Bolometer." I have examined the final electronic copy of this dissertation for form and content and recommend that it be accepted in partial fulfillment of the requirements for the degree of Doctor of Philosophy, with a major in Nuclear Engineering.

David C. Donovan, Major Professor

We have read this dissertation and recommend its acceptance:

David Donovan, Jamie Coble, Matthew Reinke, Morgan Shafer

Accepted for the Council:

Dixie L. Thompson

Vice Provost and Dean of the Graduate School

(Original signatures are on file with official student records.)

First Development and Demonstration of Fiber Optic Bolometer

A Dissertation Presented for the
Doctor of Philosophy
Degree
The University of Tennessee, Knoxville

Seungsup Lee
December 2022

ACKNOWLEDGEMENTS

ABSTRACT

The fiber optic bolometer (FOB) was demonstrated observing a fusion plasma for the first time, and 2D FOB was developed and demonstrated to have high spatial resolution. The FOB is a novel type of a bolometer that is theoretically immune to electromagnetic interferences (EMI). A bolometer is a sensor that measures the power of the incoming electromagnetic radiation. The most common bolometer used in fusion research is a resistive bolometer that utilize resistors in an electrical circuit. Due to high EMI in fusion environment, noise level can be a serious problem in determining accurate plasma radiation for a resistive bolometer. The demonstration at DIII-D tokamak utilized a single-channel system having a measurement FOB and a reference FOB, which was blocked of incoming radiation. The demonstration showed negligible increase in noise in fusion environment and acceptable absolute-value comparisons with the resistive bolometers. Plasma radiations contain information relating to plasma phenomena, and the structures are unique depending on plasma conditions. 2D FOB array was designed to investigate plasma radiations near the divertor more rigorously with higher resolutions for DIII-D. The design parameters were optimized using the machine learning technique called Bayesian global optimization, which was efficient for the multivariate non-linear problem. A physics-based regularization was developed using a magnetic reconstruction profile for the DIII-D implementation with an iterative inversion method. Neural network inversion methods were developed to not depend on an arbitrary regularization strength and to do between-plasma-shot inversions, but the methods could not overcome the problem of biasing on input data A new processing method of raw spectra data that used Fourier transform was developed for real time analysis. The design from the optimization was validated with several analysis methods to characterize the performance. The forward-modelled radiated power divided into different sections compared to the values from the original synthetic radiation profiles. The central location and shape of various radiation profiles were analyzed and compared to the original values using a computer vision library. The comparison results demonstrated that the optimized 2D FOB array system displayed good performance and will be able to answer important questions relating plasma radiation structures.

Table of Contents

LIST OF TABLES

LIST OF FIGURES

Chapter One
Introduction

Heat Exhaust and Plasma Radiation

In magnetic confinement fusion, plasma is confined by magnetic fields away from machine walls to protect materials from high temperature plasmas [1]. However, the confinement is not perfect and that plasma escapes from the confinement region, where it is referred to as the plasma core (Figure 1). The core consists of magnetic fields with closed configurations. The outside of the core is called the scrape-off layer, and it has magnetic fields ending at specific locations that the plasma is diverted to where it is separately designed to handle hot plasma [2]. It is essential to direct plasma to specifically designed locations because fusion plasma reach over one hundred million degrees Celsius, which will be detrimental to regular materials [3]. In addition, the atoms that originated from the walls will enter plasma, where they will be impurities that contaminate the plasma core. This will be harmful to fusion processes by diluting fuels and cooling the core. By directing the escaped plasmas to a specific location, divertor, the above problems are mitigated to a manageable level that will improve performances of fusion devices. For instance, the divertor is further away from the core with methods to trap or pump out the particles that will contaminate the plasma. The process is called heat and particle exhaust in fusion devices.

However, as the fusion devices reach higher plasma temperature and density to achieve better fusion performances, the particle and heat exhaust are exceeding the design and material limitations [4]. Especially, the heat flux to the target of the divertor is exceeding the material limitations that no material can withstand the heat flux [5]. Also, it is expected to have the peak heat flux to reach higher values rather than spreading out on the divertor for more advanced future machines (Figure 2) [6]. This will be a serious problem as the materials will melt. This will damage the machine and produce more impurities that will contaminate the core to reduce the rate of fusion reactions. This will lower the performance of fusion machines.

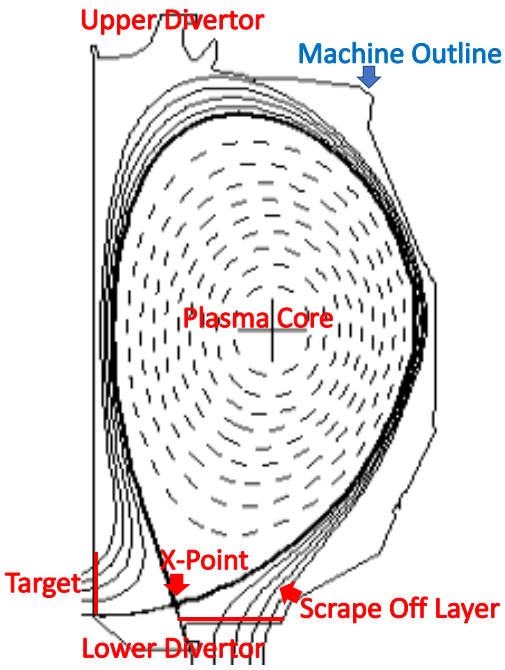

Figure 1 Radial cross section of DIII-D tokamak with a divertor magnetic configuration [72] (black lines inside the machine outline) showing important nomenclatures.

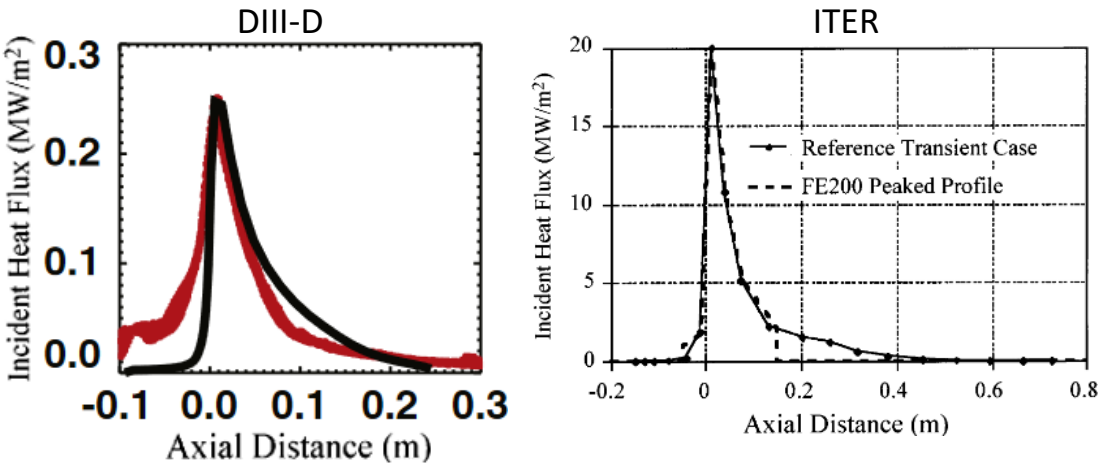

Figure 2 Left: DIII-D heat flux measured by infrared camera (red) and simulation (black) [28]. Right: ITER reference heat flux profile [6]. ITER is the bigger and more advance tokamak that is under construction. ITER is expected to have ~8 times higher peak heat-flux.

The most common method to mitigate heat flux to a divertor is to use controlled impurities injection [7]. The impurities could be from the materials of the divertor or walls, which are usually carbon, or artificially injected near the divertor, which are usually noble gases with high atomic numbers like argon or neon. The impurities increase plasma radiation due to increased neutral charge-exchange, elastic ion collisions, and plasma recombination [8]. The impurities have higher atomic numbers that result in higher possible electric field of nuclei when electrons are stripped in the plasma compared to fuel atoms, which are isotopes of hydrogen. The plasma radiation will isotopically spread heat exhaust near the divertor to the walls due to isotropic creation of photons [9] from the above processes. As a result, heat flux to the divertor will be reduced mitigating the whole problem.

One of the most important diagnostics characterizing plasma radiation is bolometry in fusion devices. In this dissertation, the first demonstration of a novel type of bolometers, which is called a fiber optic bolometer (FOB), will be presented. Before this dissertation, the FOB was in the technology readiness level of 3 or early 4 (Table 1). The FOB was being tested for proving the advantage at the bench. Previous benchtop results showed the negligible susceptibility to strong magnetic fields and the stability after high temperature baking (>350°). However, the FOB was never tested in vacuum and never calibrated to an incoming radiation. Also, the FOB operating/analyzing principles were still in development. When the author started the project, the scanning laser system, which will be discussed in the chapter three, was the system being pursued for the development. The I-MON system (discussed in the chapter three) was the system used for the demonstrations because of the results from the experiments done by the author (discussed in the chapter four).

The biggest challenges of the FOB project emerged from the fact that a lot of work were the first attempt. Some of the experimental results were completely unexpected. For instance, the significant increase in the responsivity and the time constant of the FOB was not expected (discussed in the chapter four), and the measurement range of the scanning laser system became too narrow due to the increase.

Table 1 European Union Technology Readiness Level [96]

Technology Readiness Level	**Description**
1	Basic principles observed
2	Technology concept formulated
3	Experimental proof of concept
4	Technology validated in lab
5	Technology validated in relevant environment
6	Technology demonstrated in relevant environment
7	System prototype demonstration in operational environment
8	System complete and qualified
9	Actual system proven in operational environment

Also, some problems required completely new solutions. For example, the FOB required a new method of calibration.

The demonstration of the FOB has taken place in a fusion environment (DIII-D experiment). The challenges of the demonstration were in the analysis. The installed location of the FOB complicated important analysis due to additional measurements, and the comparison between the FOB and the resistive bolometers were difficult due to the location and the differences in dimension. Nevertheless, the demonstration of a proof-of-concept for the FOB was successful with good results showing that the FOB only has negligible susceptibility to electromagnetic interference and is comparable to a resistive bolometer.

The next question that has arisen and that will be addressed in this work was, "how can a 2D FOB array be successfully designed and deployed to obtain a higher spatial and/or temporal resolution necessary to properly assess the radiative emission processes occurring in a fusion reactor?" The higher spatial (or temporal) resolution will be achieved with increased sightlines and immunity to electromagnetic interferences of the FOB, which has been proved in the proof-of-concept testing. The development and the demonstration of the 2D imaging array had their own challenges even with referencing the development and the demonstration of different types of bolometers. The optimization of 2D FOB array design required a combination of forward modeling and machine learning due to the design parameters. To the best of the author's knowledge, advanced demonstrations of the performance of the 2D FOB design were the first attempt. The demonstration showed that the optimized 2D FOB array has high spatial resolution with quantitative values (limits and error values). The author believes the work done for this dissertation pushed the technology readiness level of the FOB to 6 or early 7.

The 2D imaging array could be used to measure plasma radiation structures that are related to several open physics questions. The questions are,

- "Is the radial spread of plasma radiation near the divertor due to and can be controlled by plasma turbulence?"

- "Is similar total radiated power from different magnetic divertor configurations due to the increased flux expansion compensating the increased connection length?"
- "Are substructures of plasma radiation (and their evolutions in time) controllable and are they able to be used for the heat flux problem?"

Answering these questions will help understand and control the heat flux problem better. The information on plasma radiation structures will be obtained from data measured by the array and using tomographic reconstruction.

In the next chapter, physics reviews on the questions above are presented with reasoning why answering the questions will be important and a better bolometer system, FOB, will be beneficial. In Chapter 3, background information for this proposal is provided that includes bolometers, DIII-D tokamak, etc. Chapter 4 includes the research done with the single-channel FOB system including benchtop testing, plasma testing, and code development for FOB. Chapter 5 presents the research done for the development and demonstration for 2D FOB array. In Chapter 6, the conclusion for this research is presented. The Chapter 7 includes future work.

Chapter Two

Plasma Radiation Structure and Open Questions

Plasma Radiation Structure and Plasma Turbulence

Plasma radiation structures will be unique depending on conditions like plasma parameters, gas-puffing rate, etc. [10]. This means that plasma radiation structures could provide information about a state of plasma operations. The information will be measured by bolometers and will be contained in the tomographic reconstructed results. Plasma radiation structures near the X-point (magnetic null point where magnetic fields are aligned like an X, Figure 1) or divertor are localized and contain important information about heat exhaust. The information could be related to a spatial structure of the plasma radiation, which relates to the spatial resolution of bolometers, or a transformation of the structure, which relates to the time resolution of bolometers.

When observing the plasma radiation structure near the divertor, the author has noticed a discrepancy between the plasma simulations and the tomographic reconstructions from the resistive bolometers (Figure 3). The plasma simulation used is called SOLPS (Scrape Off Layer Plasma Simulation, [11]) that did not include charged particle drifts. The simulation predicts the plasma radiation structure to be narrower and more localized radiation along magnetic fields. Whereas the tomographic reconstruction shows a broader and less localized along the magnetic fields. Also, the plasma radiation structure on the left side (inner leg) is not present in the tomographic reconstruction.

There are many possible reasons for the discrepancy. The first culprit could be the charged particle drifts that are not included in the simulation. However, ExB drift directions (Figure 4) cannot result in the structural differences. The drift would make the plasma radiation structure narrower for the right side (outer leg) and the inner leg structure more pronounced. Another reason could be due to the tomographic reconstruction errors from a lack of sightlines, ill-posedness, or regularizations. This will be discussed more in the later part of this section with more evidence, but the conclusion is that one cannot be certain with the current resistive bolometers at DIII-D.

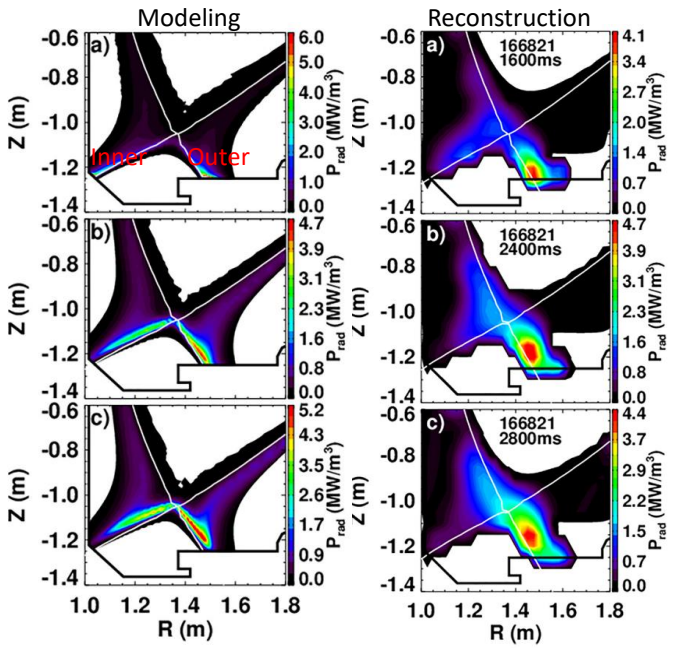

Figure 3 Left: the plasma radiation structure of a SOLPS simulation. Right: the tomographic reconstruction from the resistive bolometers [12].

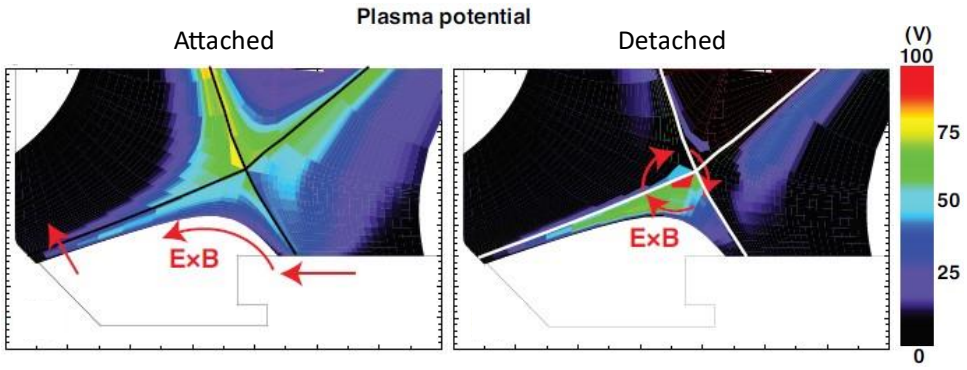

Figure 4 Directions of ExB drift flow for attached and detached cases of DIII-D [13]

Assuming the discrepancy is not due to the problems with the tomographic reconstruction, the discrepancy could be due to physical processes in detached plasma. The first physical process is the plasma recombination. The plasma recombination is reported to enhanced cross-field transports [14], which will result in broader plasma radiation structures. NAGDIS-II linear plasma device experimented with detached He plasma. He gasses remove molecular processes and reduce charge-exchange momentum losses to look at mostly plasma recombination. The result showed local spreading of the radial distribution of electron density that shows the enhanced cross-field transport.

Also, a plasma simulation coupled the collisionality of plasma to the perpendicular diffusivity of the simulation that showed better agreement with experiments for detached plasma [15]. The perpendicular diffusivity is the parameter that dictates cross-field transports in the simulation. Attached plasma is low density plasma with electron temperature profiles consistent with electron thermal conductions, and detached plasma consists of high-density regions with electron temperature lower than 10eV that is consistent with parallel convections [8]. As the plasma becomes more convection dominated (detached), the plasma increases in volume with electron temperature lower than 10 eV. In this region, neutral charge-exchange, elastic ion collisions (collisonality), and plasma recombination are increased. Thus, the enhanced cross-field transports due to the plasma recombination and the collisonality could be the reason for the wider plasma radiation structure in detached plasma.

The discrepancies are not present only in the detached plasma but in attached plasma as well (Figure 5, a). It needs to be noted that the tomographic reconstruction will not be reliable due to the plasma radiation structure so close to the wall. Another report showed similar discrepancies without the tomographic reconstructions in attached and detached plasma [13]. The plasma radiation structures from resistive bolometers showed wider features compared to simulations for both attached and detached plasma (Figure 5 and Figure 6). The simulations were done with UEDGE (plasma edge) code that included electric and magnetic cross-field drifts and currents. This shows that the discrepancies are not due to charged particle drifts. Also, the results shows that the discrepancies are present in both attached and detached plasma. Finally, the results show that the

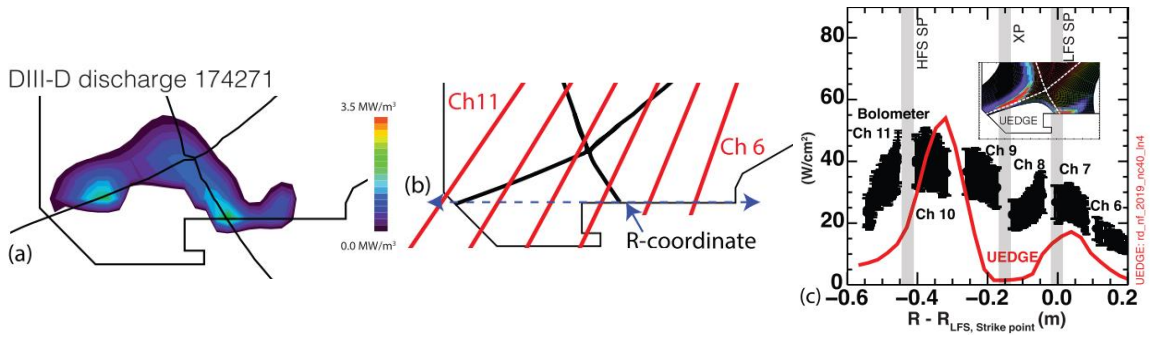

Figure 5 Attached plasma, a) tomographic reconstruction, b) resistive bolometer sightlines, c) black – resistive bolometer measurements, red – UDEDGE simulation, showing clear discrepancies between the two. [13]

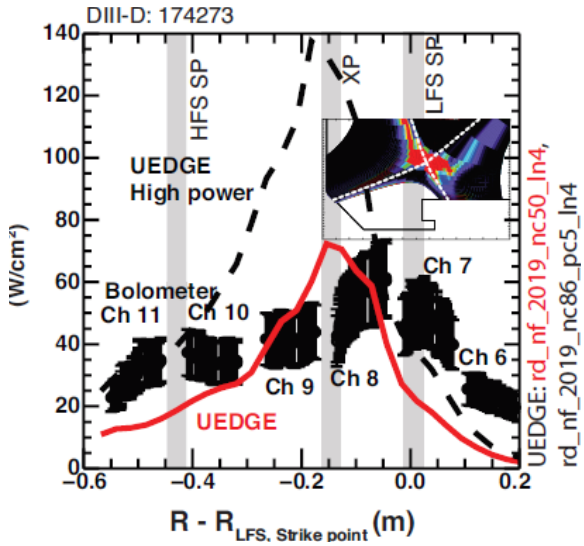

Figure 6 Detached plasma. Black circles with error bars: bolometer measurements, red line: UEDGE simulation. Bolometer measurements show broader plasma radiation structures than simulated results. [13]

discrepancies are not entirely due to the problems of tomographic reconstructions. However, the viewing cones of the resistive bolometers widen as they are farther away from the sensors due to the pinhole design and the finite area of the sensors. Thus, the discrepancies still could be an error from the resistive bolometers. A bolometer system with a higher spatial resolution will prove if the discrepancies are true plasma radiation structures.

Turbulence is a state of plasma where nonlinear interactions occur to generate chaotic structure and dynamics [17]. Turbulence could generate global structures [18], such as transport barriers, enhanced transport, and quenching transport [19]. A simulation of plasma turbulences combined with edge plasma transports showed broadened heat and particle flux profiles (Figure 7) [16]. The 3D turbulence code called Bout 3D was used for simulating the plasma turbulences. UEDGE is used for the edge plasma transport. The explanation of the widened profiles is that the plasma turbulence creates a "blob" of plasma that is convectively transported in a radial direction. The radial transport result in a strong outward convection into the scrape off layer that both profiles are broadened. Experiments regarding broadening of the particle flux profile has been performed at DIII-D [20]. Plasma turbulences (intermittent plasma objects) transported a significant number of particles in perpendicular direction (enhanced transport) in the scrape off layer and edge of the DIII-D tokamak. For broadening of the heat flux profile, experiments have been performed at ASDEX upgrade tokamak [21]. Plasma turbulences (filaments) enhanced energy transport in the scrape off layer for both attached and detached plasma.

The simulations and experiments showed that the plasma turbulence increased outward convections of plasma that resulted in broadened profiles. This should be shown as the broadened plasma radiation structure. Also, plasma turbulence is present for both attached and detached plasma. In addition, from the earlier arguments, other possible processes are excluded as a culprit for the discrepancies. Thus, the author hypothesizes the physical reason for the discrepancies is plasma turbulences. Adjusting parameters that relate to the plasma turbulence like magnetic curvature [16] and the density of scrape off layer [21] will change the broadening of the plasma radiation structures. In addition, the plasma turbulence could be used as a "knob" for controlling the heat flux at the divertor

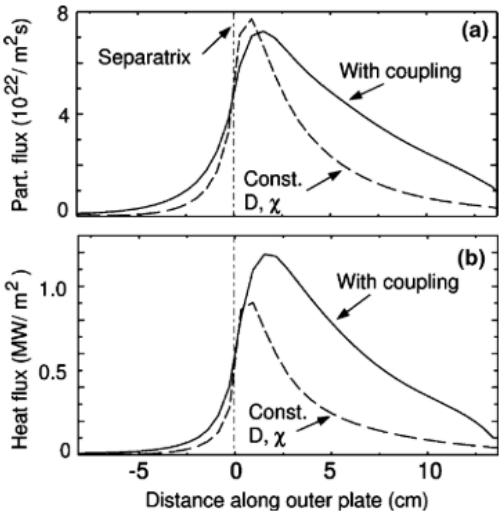

Figure 7 Particle and heat flux profiles of simulations with (solid line) and without (dotted line) including plasma turbulences. [16]

for the heat flux problem. The measurements will require a bolometer system with a higher spatial resolution to prove the hypothesis. The 2D FOB system with high spatial resolution will be required due to low resolution of the tomographic inversion of the DIII-D resistive bolometers (Figure 10). Also, a quantitative analysis of the radial spread will be required for the tomographic inversion results.

Divertor Magnetic Configuration and Plasma Radiation Structure

A snowflake (SF) divertor magnetic configuration [23] is a potential solution for the exhaust problem by partitioning heat and particle fluxes. The SF divertor experiments were conducted in DIII-D with various divertor magnetic configurations (Figure 8) [22]. The SF configuration results in an increased connection length (a length of a field line connecting upstream midplane or X-point and the target (strike point)) and the increased poloidal flux expansion (lower magnetic flux gradient) (Figure 9). The connection length and the flux expansion have significant impacts to the plasma radiation.

The increased connection length result in increased plasma volume at the divertor. This will increase the volume of the plasma radiation near the divertor, increasing the radiated power of the plasma. The increased flux expansion results in an increased plasma-wetted area causing the particle and heat fluxes to be more spread out. However, the plasma density could be lowered due to the flux expansion assuming the identical perpendicular transport compared to the standard divertor magnetic configuration and the conservation of plasma at the flux surfaces. Basically, the volume of the plasma is increasing, but the number of plasma species are conserved such that the density will be a lower value. As a result, the plasma radiation structure changed with different divertor magnetic configurations (Figure 10), but the analysis was only visual. An interesting result from the experiments is that the total radiated power of plasma at near the divertor only differed 10 - 15%. It was noted that the differences were insignificant, and that it was unclear as to why the difference in the magnetic divertor configurations did not result in larger differences in the total radiated power.

Since the plasma emission is heavily related to the plasma density [8], it can be hypothesized that the increase in plasma radiation from the increased connection length is

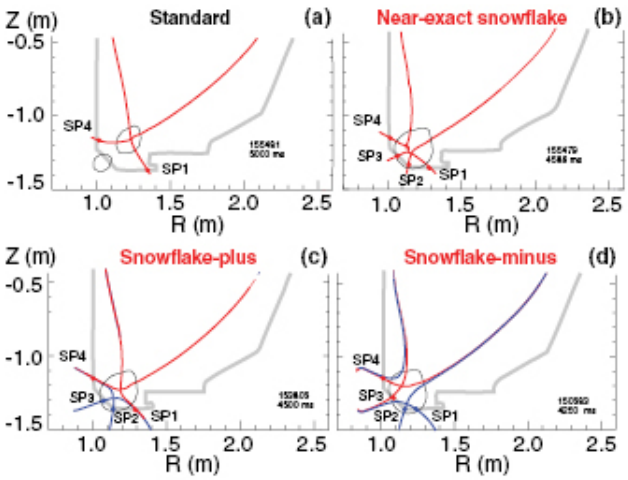

Figure 8 Various magnetic equilibria of the standard (a), near-exact SF (b), SF-plus (c), and SF-minus (d) divertor configurations [22].

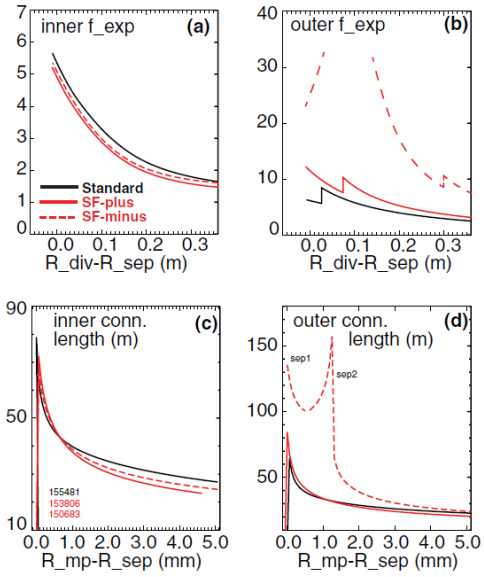

Figure 9 Flux expansion (a, b) for inner and outer legs. Connection lengths (c, d) for inner and outer legs [22]

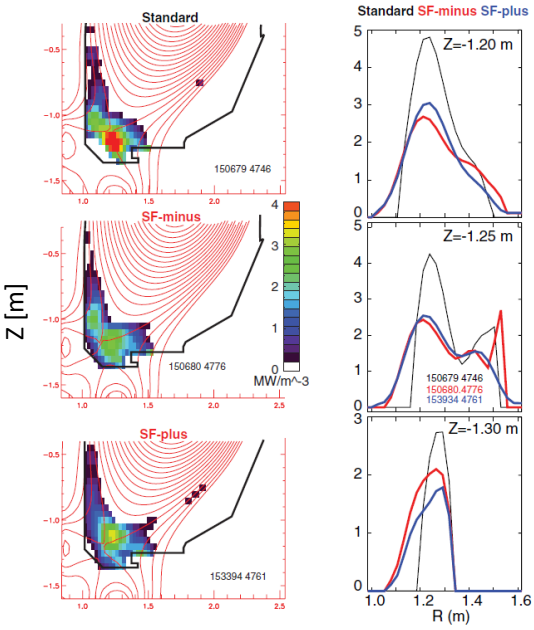

Figure 10 Left: radiated power density from tomographic bolometer inversions. Right: radial profiles of radiated power density from different Z. [22]

offset by the decrease in plasma radiation from the decrease in plasma density due to the increased flux expansion. However, a bolometer system with a higher spatial resolution will be required to look at the problem. With a higher spatial resolution, dividing the plasma radiation structures into substructures will be possible. The hypothesis will be proved by calculating the volume and the radiated power of the substructures. Also, the detailed structures (dimensions, shapes, etc.) will provide more information on the effects of the different magnetic-divertor configurations. The 2D FOB system with high spatial resolution could reveal bigger differences in the total radiated power at the divertor for different magnetic divertor configurations. Also, a structural analysis with associated radiated power using the system could prove the increased radiator volume with a reduced emissivity, thus a similar total radiated power.

Evolution of Plasma Radiation Structure

As mentioned in the introduction, plasma radiation from impurities near the divertor is essential in overcoming the problem of the heat exhaust. The plasma radiation does not appear out of nowhere as the impurities are injected. The plasma radiation evolves as the impurities are injected as shown in the Figure 3 from a) to c). Research into the evolution of the 2D deuterium and impurity radiation profiles during transitions from attached to detached divertor operation were performed at DIII-D [24].

For the experiment (a constant power injection and a constant plasma current), deuterium gas was injected with a constant rate for the transition between ELMing (edge localized mode: a disruptive instability [25]) H-mode to partially detached divertor (PDD) operation in DIII-D. CIII emission measured for the experiment is a proxy for the impurity radiation, which is the bulk of the plasma radiated power. The result (Figure 11) shows that the plasma radiation structure (substructure shapes and locations) evolves with time during an important transition of the status of the plasma even with constant operating parameters. If most of the plasma radiation evolves into the core, it could excessively cool the plasma through radiative losses, which is undesirable. Also, if most of the plasma radiation is located inside the core, it could result in MARFE (multifaceted asymmetric radiation from the edge) that could collapse the plasma discharge [26].

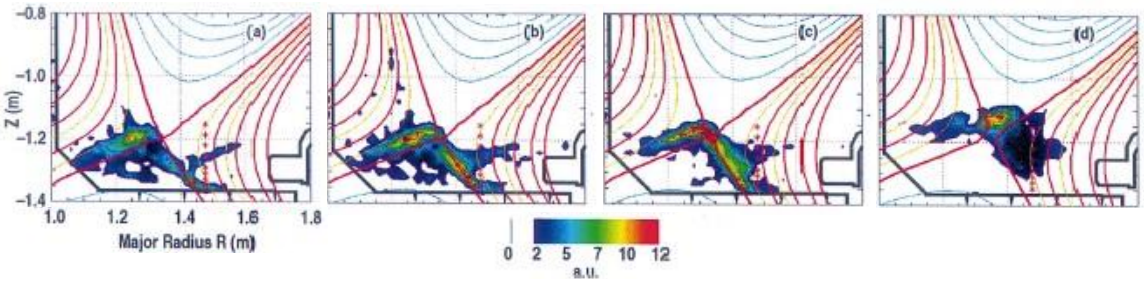

Figure 11 Profiles of CIII emission. (a) 1889 ms, during the ELMing H-mode phase. (b) 2040 ms, deuterium injection starts at 1900 ms, (c) 2107 ms, during the transition and (d) 4085 ms, the PDD phase. [24]

An interesting study at ASDEX Upgrade tokamak showed that a certain height of the plasma radiation above the X-point resulted in an ELM-suppressed regime with minimal reduction of confinement (Figure 12) [27]. The location of the plasma radiation is only possible during a full detachment with a dissipated power fraction of around 95 %, in which case the heat flux to the divertor is greatly reduced. The experiment required the installation of dedicated photodiodes to accurately measure and control the plasma radiation location. The fact that the suppression requires a certain location and the state of plasma changed with moving plasma radiation shows that the plasma radiation structure contains important information relating to the plasma conditions. A center location analysis of radiators using the 2D FOB system with high spatial resolution will be able to reproduce the ability of the dedicated photodiodes. In addition, the location along R-direction, which could have important implications in operating/plasma conditions, will be determined for the 2D FOB system, which was not possible with the ASDEX Upgrade system.

A bolometer system with a higher spatial resolution that will be able to resolve the plasma radiation structures (substructure shapes, locations, and associated radiated power) will reveal more details that could help better understand and control the heat flux problem. Although the author could not find any experiments relating the substructures to the heat flux problem (possibly due to the limited spatial resolution of bolometers), the shapes should also be an important factor. In addition, a bolometer system with a higher temporal resolution can also be beneficial for looking into the change of plasma radiation structure that evolves in time. The bolometers are usually averaged over a certain time-period to reduce noise, which could blur an important change of the structure happening at a fast timescale. In addition, the substructures will evolve at a certain speed that depends on the various operation parameters. Relating the speed to the parameters could help better understand and control the heat flux problem as well.

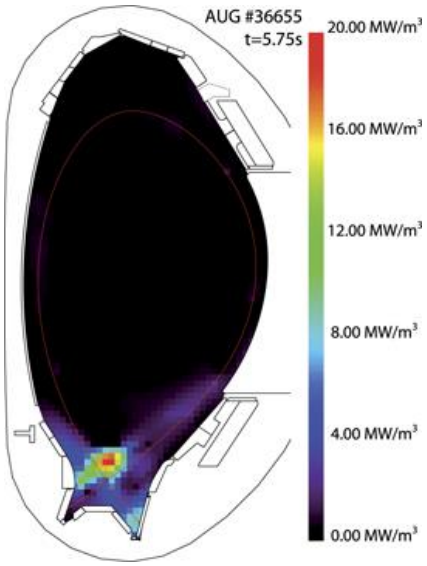

Figure 12 Tomographic reconstruction of the radiated power for ASDEX upgrade where the plasma radiation is above the X-point [27].

Chapter Three
Background

Bolometers

A Bolometer measures electromagnetic radiation that is incident on and absorbed by the bolometer. Most commonly, the absorbed radiation is heating the bolometer, and the temperature of the bolometer is being measured to obtain the information of the incident electromagnetic radiation [29]. There are various ways to measure the temperature/temperature change of a bolometer. In addition, there is a method of using a photodiode to measure the electromagnetic radiation rather than heating up a bolometer [30].

A plasma emits electromagnetic radiation with an energy range up to an energy roughly equivalent to the temperature of the plasma that is typically a few to several tens of keV [30]. There is a variety of processes that emit electromagnetic radiation from electrons and ions of the plasma, and atoms that are not fully ionized. Also, magnetically confined fusion plasmas are generally optically thin in the spectrum from the visible to soft X-ray range [31]. Thus, from the conservation of energy, an essential part of the power balance is plasma radiation in magnetic confinement fusion experiments [4]. In addition, the plasma radiation provides important information for the power exhaust problems and divertor detachment (discontinuity in energy, momentum, and particle flux parallel to the magnetic field lines from the midplane scrape-off-layer (SOL) to the divertor due significant losses [8]). The plasma radiation can be used to understand plasma instabilities and transport effects as well.

The resistive bolometer is a most common type of a bolometer used in a fusion environment. The resistive bolometer consists of a metallic absorber like a gold or platinum foil, an insulator below the absorber, and a resistor (detector) below the insulator (Figure 13), measuring the temperature change of the absorber due to the incoming plasma radiation using the resistor. The design of the resistive bolometer operates with an AC-excited bridge circuit, a Wheatstone bridge (Figure 14) [33]. One channel of a resistive bolometer consists of a measurement and a reference absorber

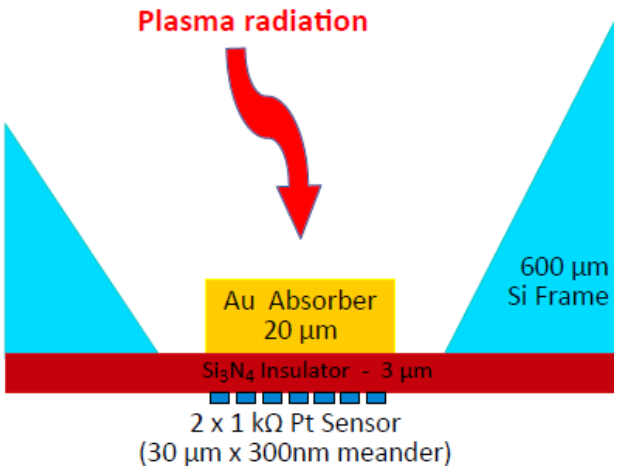

Figure 13 A schematic of a resistive bolometer. The plasma radiation is absorbed by the gold absorber. There is the insulator between the resistor (sensor) and the absorber [4].

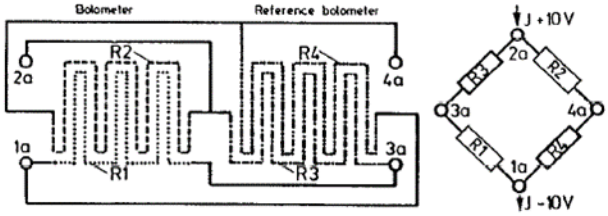

Figure 14 Arrangement of the Wheatstone bridge circuit in a resistive bolometer [33].

where the reference absorber is blocked of incoming plasma radiation. An environment temperature that would affect the measurement and the reference absorbers are compensated in the Wheatstone bridge, so that the plasma radiation signal is not contaminated.

Another bolometer, measuring the temperature of an absorber due to the incoming plasma radiation, is the infrared (IR) imaging video bolometer. A thin metallic foil is heated by plasma radiation and the temperature distribution on the foil is measured by an IR camera to determine the incoming plasma radiation [4]. The infrared imaging video bolometer requires more complex calibration, 2D calibration, due to using one thin metallic foil that diffuses heat. The infrared imaging video bolometer can have high number of pixels depending on the IR camera. The time-resolution is typically 10 ms, but it is limited due to noise and the complex calibration.

AXUV photodiodes are used as a bolometer in fusion environments. AXUV photodiodes measure plasma radiation from a photo current generated in a p-n-junction [30]. Due to the nature of photodiodes, the AXUV photodiodes are not sensitive to energetic neutral particles or pressure changes [32] unlike the temperature measuring bolometers [4]. Also, the AXUV bolometers result in low noise with the time-resolution that can reach up to 2 MHz, which is not possible for other types of bolometers. However, the photodiodes react differently to different wavelength photons, which is not the case for other types of bolometers. The sensitivity or the response is constant only for photon energies above 200 eV. It is difficult (maybe not possible) to correctly measure total radiated power of plasma and radiation from scrape off layers and near divertor due to the sensitivity changing with the photon energy below 200 eV.

Fiber Optic Bolometer

A fiber optic bolometer (FOB) is a novel type of bolometer that utilizes a fiberoptic temperature sensor based on a Fabry-Pérot design [34]. The FOB is operated by a resonant interaction region that is embedded, attached, or encoded to a fiber-optic cable [35]. The FOB response due to local environmental changes is encoded in the transmitted light carried by the fiber-optic cable. The main advantage of FOBs is that it is

theoretically immune to electromagnetic interferences. There are two types of FOBs system that were developed for magnetic confinement fusion. The first system is the scanning laser system. The second system is a spectrometer (I-MON 512 USB) system.

The scanning laser system requires a high-finesse (narrow band-pass) Fabry-Perot interferometer (FPI) that features narrower spectral features in its reflection spectrum compared to a low-finesse (broad band-pass) FPI [36] This resulted in a lower noise in temperature sensing compared to a low-finesse FPI. The construction of the FOB is presented in Figure 15. The interrogator components of the scanning laser system consist of a scanning laser setup (a laser, a current controller, a temperature controller, and a waveform generator), fiber circuit components (a coupler, attenuators, and circulators), and photodetectors (Figure 16). The one interrogator system measures two FOBs (a reference and a measurement).

The laser is scanned in a certain range of wavelengths by controlling the current controller. As the current is changing (200 mA in range), the wavelength of the laser is scanned (280 pm in range) [36]. The range depends on the lasers. The reflection notch of the high-finesse FPI needs to be inside the wavelength range. The notch position changes as the temperature of the FOB changes due to incoming radiation or ambient temperatures. The temperature sensitivity of the FOB is 84.5 pm/°C, which is used to relate wavelength changes of the notch to temperature changes. The temperature change is related to incoming radiation with a calibration process.

The I-MON spectrometer system does not require a high-finesse FPI. The low-finesse FPI used for the I-MON system is less complicated (Figure 17) than the high-finesse FPI [37]. The noise equivalent power density measured by the FOB was reduced compared to the previous design [34] utilizing a bigger gold plate in front of the silicon pillar. The I-MON system consists of a Superluminescent Light-Emitting Diode (SLED) light source, a I-MON spectrometer, a coarse wavelength division multiplexer (CWDM), a polarization scrambler, and attenuators (Figure 18). The polarization scrambler rapidly varies the polarization of light running through the fiberoptic circuit such that the average polarization over time is effectively randomized. This is required to cancel out errors caused by polarization effects due to vibrations and magnetic fields on fiberoptic cables

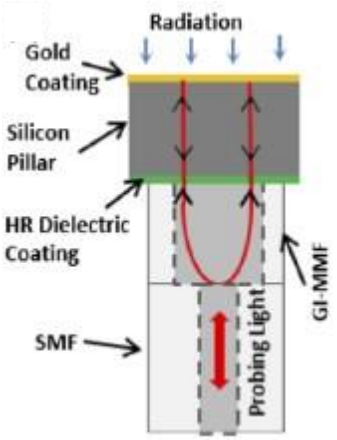

Figure 15 Schematic of the high-finesse fiber-optic bolometer [36].

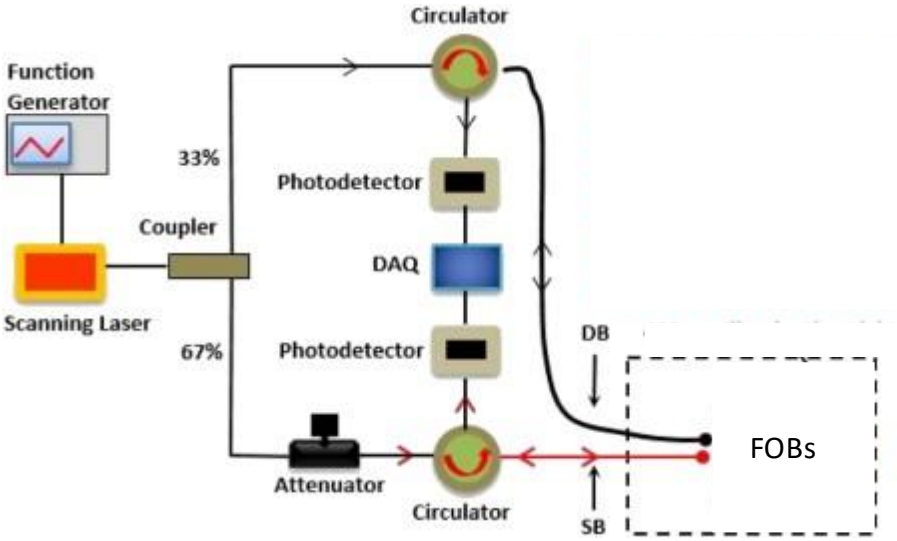

Figure 16 The components for the scanning laser system and their connections [36].

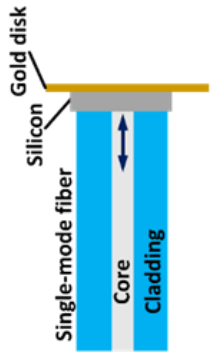

Figure 17 Schematic of the low-finesse fiber-optic bolometer [37].

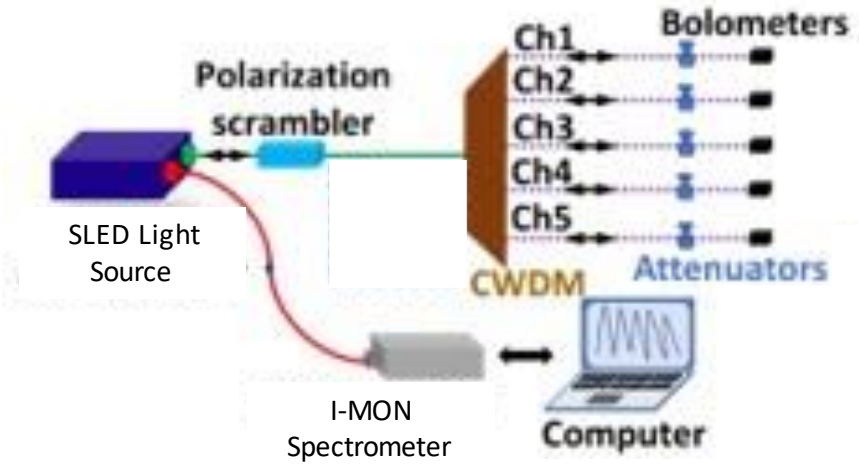

Figure 18 The components for the I-MON spectrometer system and their connections [37].

[37]. The CWDM allows the one interrogator system to accommodate five FOBs by dividing the wavelength range of the spectrometer into sections and appointing each section to a specific FOB [37].

The I-MON spectrometer system results in an interference pattern that consists of multiple interference fringes rather than one notch (Figure 19). The peaks or valleys of the interference fringes shift with the temperature change in the FOB. The shifts of wavelengths are averaged over for a wavelength section dedicated to an FOB. The same temperature sensitivity is used to convert the shifts of wavelengths into the changes of temperature. Again, the temperature change is related to incoming radiation with a calibration process, which will be discuss in the next chapter.

Tomographic Reconstruction

A tomographic reconstruction is a multidimensional inverse problem aimed to estimate a specific system from a finite number of projections. In magnetic confinement fusion, a tomographic reconstruction determines local plasma properties from the measured projections [38]. The measured projection is a non-local measurement like line integrals. For bolometers, the measurements of power from viewing cones passing through plasma are the measured projections. The local plasma property resulted from a tomographic reconstruction/an inversion is plasma emissivity. There are many mathematical methods to solve the multidimensional inverse problem with multiple sightlines. However, the problem is an ill-posed problem [39] such that there is no unique solution because of the finite sampling. Also, a differential operator in inversions could amplify noise from the measured projections [31]

In magnetic fusion environment, the inversion problem is further complicated by plasma machine constraints like port restrictions that prevent measurements in preferred locations or directions. As a result, measured projections can be inadequate making data sparse. This makes the tomographic reconstruction more ill-posed. For instance, even with rather dense measured projections, the actual coverage in the projection space can be still sparse (Figure 20) [40]. However, well-established mathematical methods have been developed to solve the inversion problem with regularization.

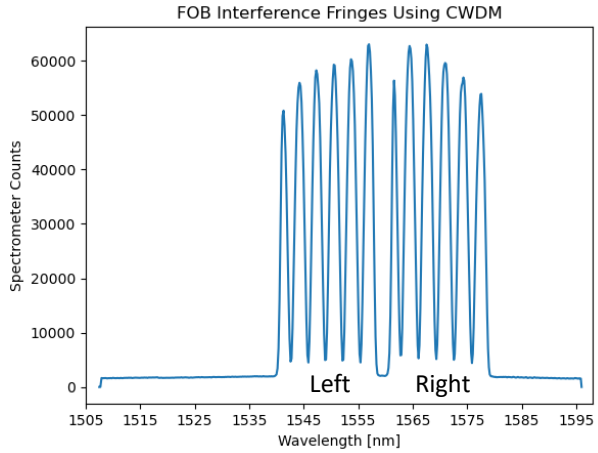

Figure 19 A result of the I-MON spectrometer system with CWDM. The left wavelength section is for a measurement FOB, and the right wavelength section is for a reference FOB.

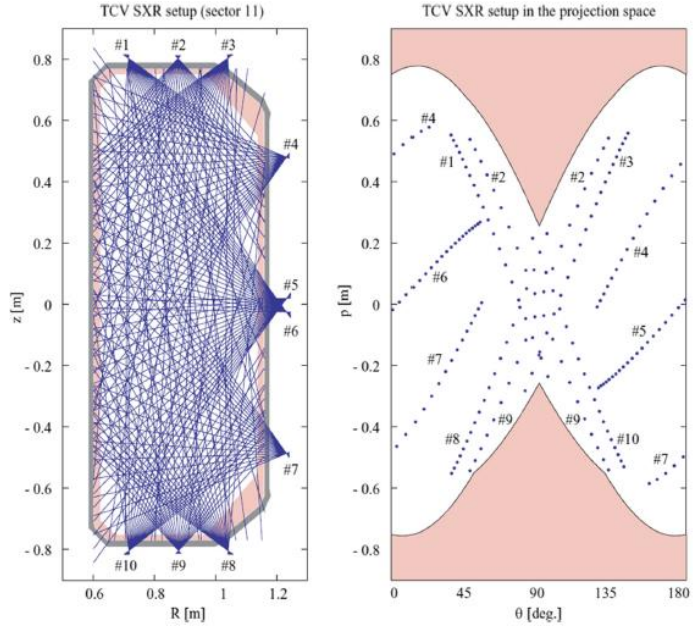

Figure 20 The Soft X-ray tomography setup at tokamak TCV. The number of the measured line integrated projections are rather high (left) for a fusion tomography. However, the coverage in the projection space is still limited (right). [40]

Regularization is a process of adding information to solve an ill-posed problem [41]. The regularization is a trade between a cost on the optimization and making the optimal solution unique. In fusion tomography, regularizations can be isotropic values within a magnetic flux, boundary conditions like zero values outside of a machine, smoothness of magnetic surfaces, constraints like non-negative values, etc. Also, regularization can be effective in limiting adverse effects of noise for a random noise without correlation between neighboring channels [31].

Some of the inversion methods used by bolometers for fusion plasma are simultaneous algebraic reconstruction, non-negative least square, Tikhonov regularization, Bayesian, neural networks, maximum likelihood, etc. Some of the techniques will be used for testing FOBs. This will be discussed more in Chapter 5.

DIII-D Tokamak and Resistive Bolometers

DIII-D is a pulsed tokamak using water-cooled copper magnetic coils [42]. The DIII-D tokamak has performed experiments for understanding of the plasma cross section in optimizing plasma performance for nearly 20 years [43]. The design of DIII-D takes advantage of noncircular shaping of the plasma cross section to optimize plasma performance. Also, the design of DIII-D integrates open divertors for control of heat and particle exhaust needed for a future tokamak (Figure 21). The design of DIII-D allowed different designs of divertor configurations that contributed to better understanding of heat and particle exhaust with the appropriate diagnostics [44]. The table 2 shows DIII-D characteristic parameters.

DIII-D utilized various heating schemes like ohmic heating, neutral beams, electron cyclotron heating, etc. to heat the plasma. Two methods: neutral beams and electron cyclotron heating, will be discussed here since the two methods interfered with the single-channel FOB (Chapter 4). The neutral beam injection is an axillary power system that heats plasma with a beam of neutral particles with high energy [45]. As the neutral beam collides with plasma, the plasma heats up from the energy transfer, and the neutral beam ionizes and confined in the magnetic field of the machine. DIII-D neutral beam injection consists of four beam lines (Figure 22) [43]. Electron cyclotron heating

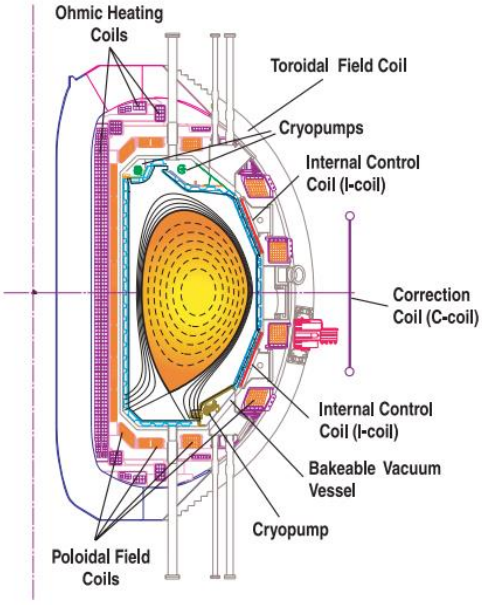

Figure 21 A cross-section of the DIII-D tokamak with a magnetic equilibrium for a single-null discharge. The lower divertor and upper divertors are at the top and the bottom of the inside of the chamber (near the cryopumps). [43]

Table 2 DIII-D Characteristic Parameters [43]

Parameter	Value	Unit
Plasma major radius	1.66	[m]
Plasma minor radius	0.67	[m]
Plasma height	2.8	[m]
Plasma elongation	2.5	
Maximum magnetic field	2.2	[T]
Maximum plasma current	3	[MA]
Plasma ramp rate	1	[MA/s]
Plasma initiation voltage	3	[V]
Fuel gas	D, H, He	
Ohmic flux swing	7.5	[V•s]
Wall material	Carbon	
Wall coating material	Boron	
Vessel leak rate	$<5 \times 10^{-5}$	[torr•l/s]
Baking temperature	400	[°C]

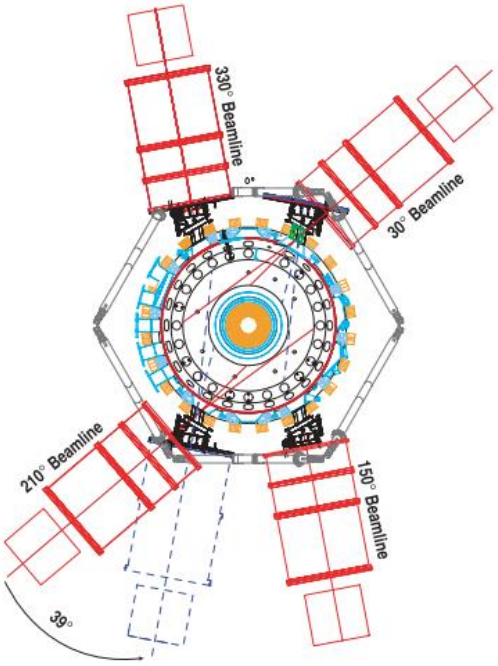

Figure 22 Four neutral beamlines of DIII-D [43]

(ECH) is a radio frequency (rf) heating method, in which electromagnetic waves that have the same frequency as the electron cyclotron frequency of the plasma [46]. The ECH system of DIII-D has six gyrotrons operating at 110 GHz and injecting up to 3.5 MW for pulses up to 5 seconds in length [47].

Arrays of resistive bolometers are installed at DIII-D to measure radiated power profiles in plasma discharges [48]. The arrays consist of four pinhole cameras with 48 channels radially looking at plasma (Figure 23). The absorber of the resistive bolometers are platinum foils that are darkened with a coating of graphite to absorb visible light. The platinum foil resistors are mounted on machined alumina blocks (Figure 24). A channel is cut underneath the active sensor to provide thermal isolation. The reference sensor (incoming radiation blocked) is next to the measurement sensor (with the illuminating aperture) on the same substrate. The reference and the measurement sensors are arranged in a Wheatstone bridge circuit.

Machine Learning Optimization, Neural Network, and Computer Vision

Machine learning is building methods that utilize data to improve performance on a set of tasks [49]. Machine learning algorithms build a model using training data to make predictions or decisions without a user's individual action on the process of the prediction or decision [50]. Machine learning algorithms are used for optimization, inversion, and computer vision due to some advantage over the conventional algorithms. Some machine learning is related to computational statistics to make predictions using computers, and some utilizes the mathematical optimizations. Some implementations of machine learning use neural networks that mimics a biological brain [51].

Bayesian optimization is a global optimization strategy assuming black-box functions [52] for the problem (not having any functional forms). It is used to optimize a function that is hard to or cannot be evaluated. Bayesian optimization is particularly advantageous for a problem function that has high computational cost. The optimization works by creating a posterior distribution for the problem function from the evaluated data. The distribution is updated using Gaussian processes with more evaluations of the

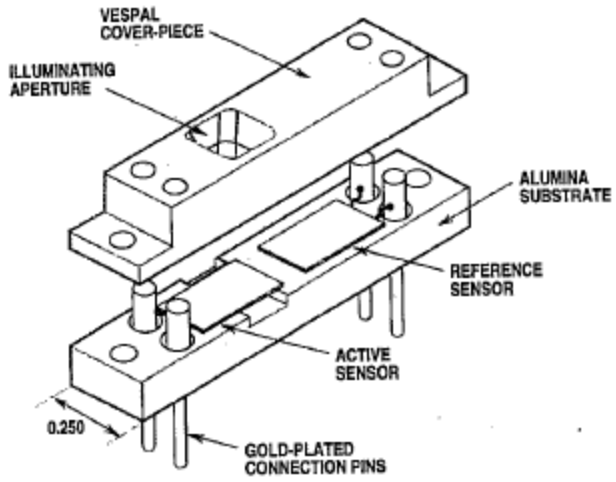

Figure 23 The schematic of DIII-D resistive bolometers. The platinum foil resistors are mounted on an alumina substrate. [48]

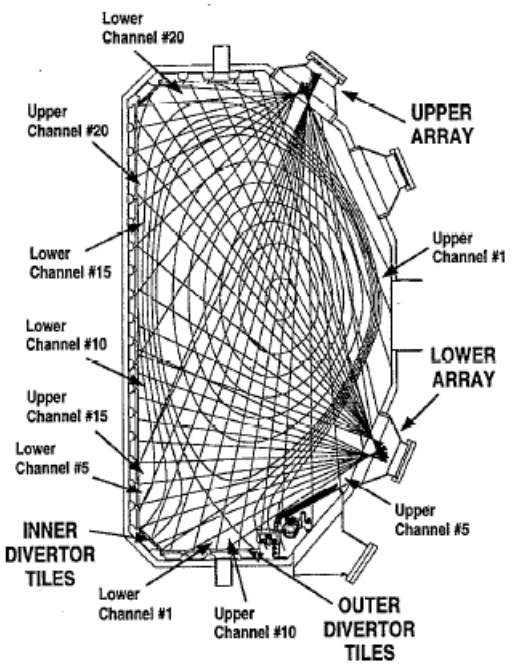

Figure 24 Viewing chords of the two bolometer arrays in the DIII-D vessel. Near complete plasma coverage [48].

function to best describe the function. A Gaussian process is a stochastic process for a selection of random variables if the random variables have a multivariate normal distribution. The algorithm used for this research is the Bayesian global optimization with Gaussian processes [53]. The algorithm balances its needs of exploration and exploitation considering what it knows about the problem function.

A neural network for computers is computing systems mimicing the biological neural networks [54]. A neural network is a collection of connected artificial neurons. An artificial neuron receives, processes, and send signals like the synapses in a biological brain. Each neuron is computed by some non-linear function of the sum of its inputs. Neurons and connections between neurons have a weight that increases or decreases the strength of the signal at a connection. Layers are a collection of neurons that may perform different processes. Signals travel from a layer to a layer that may result in multiple passes. The neural network training algorithm used for this research is TensorFlow - Keras [55].

Computer vision is an algorithm to make a computer result in a high-level understanding of digital images or videos. "Computer vision is concerned with the automatic extraction, analysis and understanding of useful information from a single image or a sequence of images. It involves the development of a theoretical and algorithmic basis to achieve automatic visual understanding."[56] The computer vision library for Python used for this research is OpenCV [57].

Chapter Four

Single-Channel Fiber Optic Bolometer

FOB Benchtop Vacuum Testing

The fiber optic bolometer developed by Michigan State University (MSU) group required testing under vacuum before it could be used in a fusion environment where it will be operated in high vacuum. The task was appointed to the author to be carried out in an experimental plasma laboratory located at the University of Tennessee-Knoxville (UTK). The UTK plasma exposure chamber [58] provided the vacuum pumping system needed to achieve the low base pressure for the bolometer testing. The vacuum chamber used for the testing was designed by ORNL (Figure 25) and was already fabricated. The ORNL vacuum chamber was connected to the UTK plasma exposure chamber by a vacuum bellows, which allowed the ORNL chamber to be pumped down by the UTK chamber's vacuum pumps.

A series of tests was performed at various pressures. The experiment setup details were as follows (Figure 25). The vacuum chamber has a window in the front where a laser, which was used as a radiation source, can be shined through. The laser used was a BlueLyte, diode laser with 405 nm in wavelength (blue) and power below 5 mW. The PDA-36 from Thorlabs was outside of the vacuum chamber to measure the power density of the laser. The distance from the laser to PDA-36 was matched to the distance between the laser and the FOB. Also, the attenuation of the laser due to the window was calculated separately by putting the window between the laser and the PDA-36. The results showed that the window attenuated ~8% of the photons compared to no window. Also, the reflection of the FOB, which had a thin gold plate at the front, was obtain from [59]. The polished gold data was used, which had the reflectance of 0.37582 [59]. The power measured by the FOB was calculated by using the PDA-36 and applying the combined value from the attenuation and the absorption (1 - reflection).

The power density shined on the FOB was determined from the power measured by the PDA-36. The laser was defocused to have the spot size big enough to cover the detection area of the PDA-36. By dividing the power measure by the PDA-36 with the

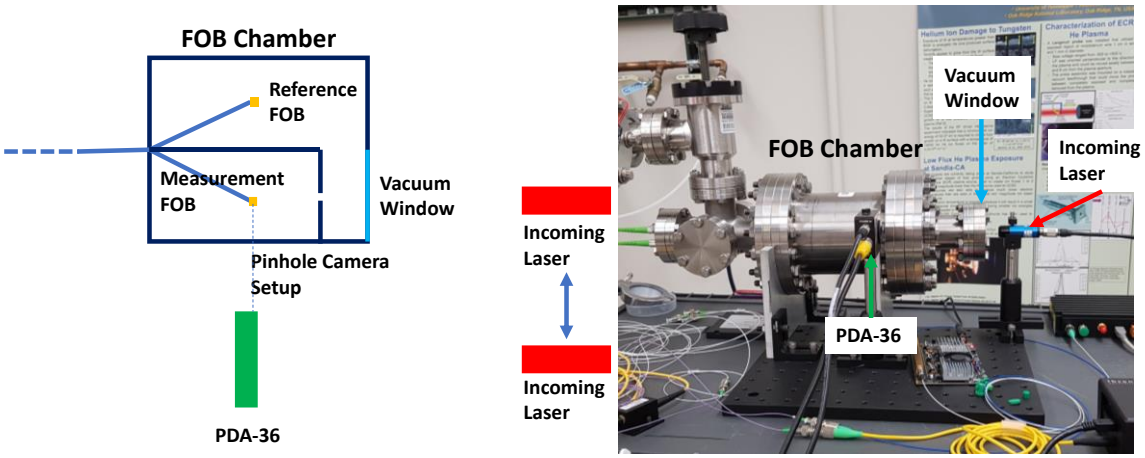

Figure 25 Left: the schematic of the experiment setup. Right: the picture of the setup

area of the PDA-36, the power density was calculated, which will be used for measuring "noise equivalent power density (NEPD)." Also, the laser was controlled by a waveform generator to create an incoming laser with a changing intensity with time. Mostly, a square wave was used to create "on and off" laser with varying power to characterize the FOB.

Initial testing of the FOBs in vacuum was performed with a scanning laser system. The noise equivalent power density (0.77 W/m^2) at UTK was higher compared to MSU group value (0.27 W/m^2) in air. One of the causes could have been the data acquisition, which was performed with National Instrument USB-6210 (digitizer). Both the scan of the system and the interference notch from the photodetector (InGaAs NIR photodetector) were required to measure the temperature change measured by the FOB. However, there was a mismatch between the scanning system and the photodetector in timing. The start of the scan mismatched the detector by several data points, but the values semi-periodically fluctuated. This caused semi-periodic fluctuation of the temperature values calculated from the two measurements. These fluctuations were mitigated by software means during analysis. However, it was impossible to completely remove it from the analysis. Thus, the fluctuation remained as increased noise. In addition, frequency domain analyses showed that the fluctuations cannot be the only reason. The speculation was that the electromagnetic interferences on the digitizer were the second reason. Unfortunately, the problems could not be isolated and eliminated.

Absolute temperature measurements with the scanning laser system for the FOB was envisioned for calibrations. The method utilizes temperature changes of the FOB from the scanning laser itself. First, the absolute wavelength of the scanning laser is measured using a I-MON spectrometer. The resistance of the temperature controller for the laser is set to a certain value and not changed for the next steps. The scanning laser scans a range of wavelength thanks to a small wavelength shift from a change of power of the scanning laser [36]. Due to this fact, there is the maximum measured power in voltage by the photodiode as the wavelength is being scanned. It is reasonable to expect the FOB to be at room temperature with the notch voltage of zero when the lasers are turned off and have zero maximum voltage for the case where the lasers are turned off.

Next, the scanning laser is turned on with two different power levels, which is executed with changing the attenuator. There will be two different maximum voltages and two different temperatures (notch wavelength within the scan) for the FOB due to the two different power levels of the scanning laser. Assuming a linear change of the maximum voltage and the notch wavelength with the changing laser power, one can calculate the ratio between the wavelength change and the maximum voltage change. The temperature sensitivity in voltage is obtained by multiplying the calculated ratio to the temperature sensitivity in °C per pm [36]. The absolute temperature of the set scanning-laser power can be calculated,

$$T = VS + T_{background}$$

T: Absolute temperature of the FOB
V: Measured voltage of the notch
S: Temperature sensitivity in voltage
T_background: Background/ambient temperature

Two values, responsivity [V/W or V/(W/m^2)] and time-constant [seconds] are important in characterizing bolometers. The responsivity is how much the FOB response to a set amount of incoming radiation power. The time-constant is the time required to respond to the incoming power. Commonly, it is assumed that the change is exponential such that the time-constant is the time required for one exponent change (Figure 26). Both the responsivity and the time-constant were measured with changing pressures from atmospheric pressure to 4.2E-5 Torr. The results of pressure vs responsivity and time-constant is present on Figure 27.

The results showed unexpected numbers. The expected asymptotic behavior of the responsivity and the time-constant with pressure was present for the FOB. However, the change was much bigger (~30 times) than expected. The changes are due to changes in major heat- transfer mechanism as the pressure changes. For instance, in air, the air surrounding the FOB acts as a heat sink, which causes lowered temperature variation (responsivity) and lowered time constant. In high vacuum, there is not enough air to act as a heat sink. The heat is mostly transferred through the fiber optic cable attached to the FOB, which is a far less efficient heat-transfer mechanism. This will increase the responsivity and the time constant.

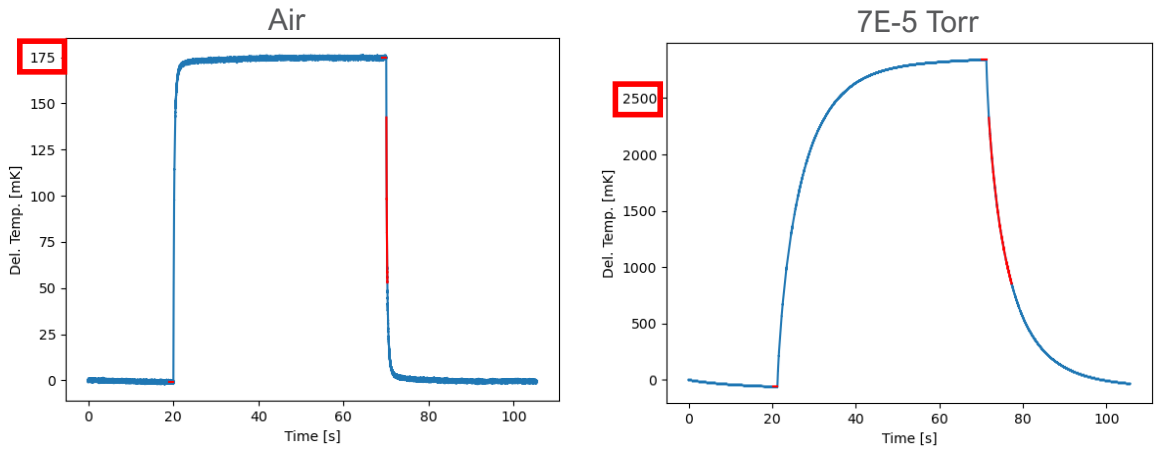

Figure 26 Left: FOB response to constant incoming radiation (on and off) in Air. Right: FOB response in high vacuum. Increased response in high vacuum, but longer transient stages. Vertical red lines are for fitting exponential function to obtain time-constants.

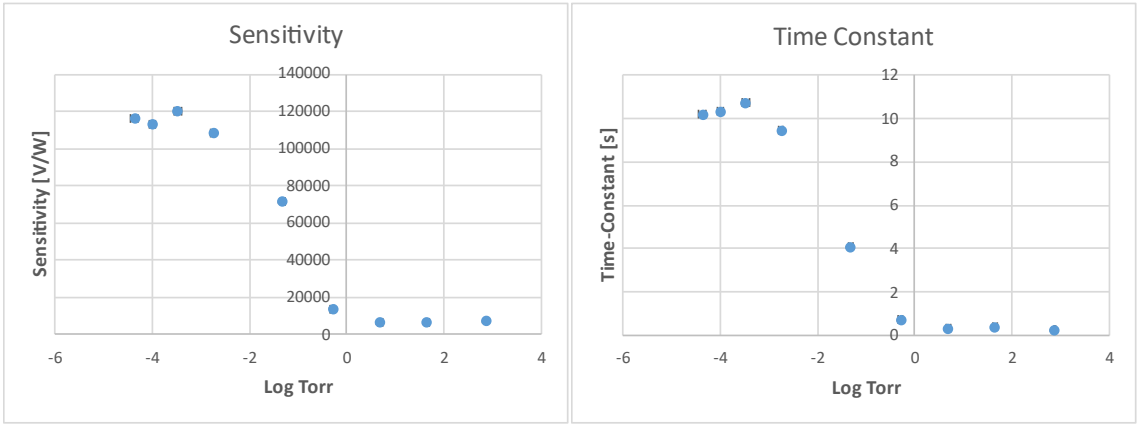

Figure 27 Sensitivity (left) and time-constant (right) of the FOB for the scanning laser system. Short Error bars (barely visible).

The increased time-constant will result in slower response. Since the time-constant is ~10 seconds and the DIII-D plasma shot time is ~10 seconds, the FOB cannot respond to the plasma radiation variations fast enough. The calibrations are used to correct this problem. However, it was reported that it is difficult to calibrate a resistive bolometer to measure timescales faster than the time constant correctly [60].

The increased responsivity is a positive trait as it means that the FOB is more sensitive. However, the increased responsivity resulted in a serious problem for using the scanning laser system. For the scanning laser system, there is a limit to the range of the scan. In high vacuum where the FOB will be operated, the temperature change (the notch movement) in the FOB will occupy a larger section of the scan due to the increased responsivity. A rough estimate of the power density expected for the FOB assuming a similar location as the resistive bolometer showed 200 W/m^2. The power density is estimated to require almost the entire range of the scan. Also, it was tested that the scanning laser showed different responsivities and time-constants depending on where the notch started (determined by the temperature controller (resistance of the scanning laser)) within the scan. For instance, the response (signal) was lower, and the time-constant was higher at the lower wavelength of the scan compared to the higher wavelength of the scan (Figure 28). Due to these problems, it was decided to use the I-MON system rather than the scanning laser system even with an increased noise.

Using the I-MON system has less restriction in the temperature range for the FOB due to the low finesse (broad band-pass) nature of the Fabry–Pérot interferometer and the spectral range of the I-MON spectrometer being wider (up to 1.6nm in range for the scanning system and 85nm for the I-MON spectrometer). In addition, the I-MON system does not require a separate digitizer due to I-MON being a spectrometer and a digitizer, which means that it did not present the noise increase problem due to the mismatch between two signals.

The experiments done with the I-MON system were the same as the scanning laser system with the same incoming laser setup. As done before, the responsivity and the time-constant were measured for different pressures. The results showed the same asymptotic trend (Figure 29). The differences between the air and high vacuum showed

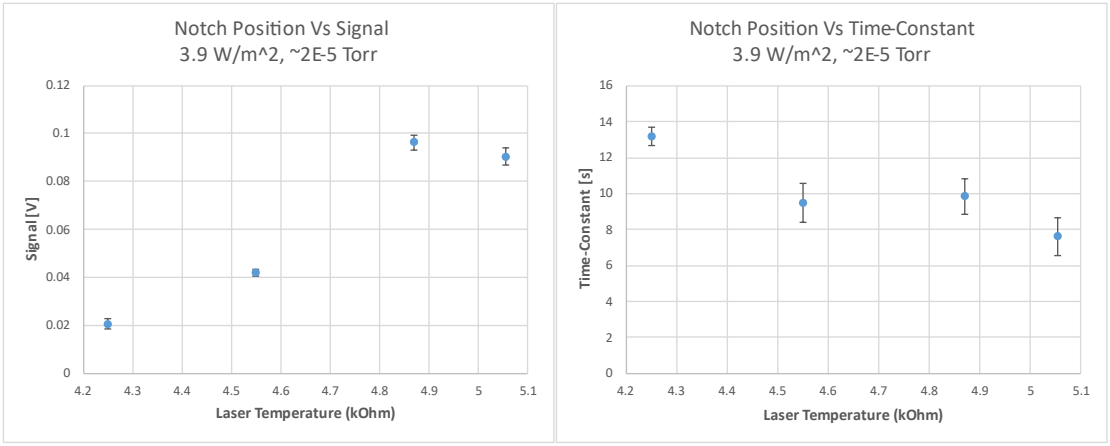

Figure 28 Signal level (left) and time constant (right) changing with the start position of the notch (determined by the temperature of the scanning laser (kOhm)).

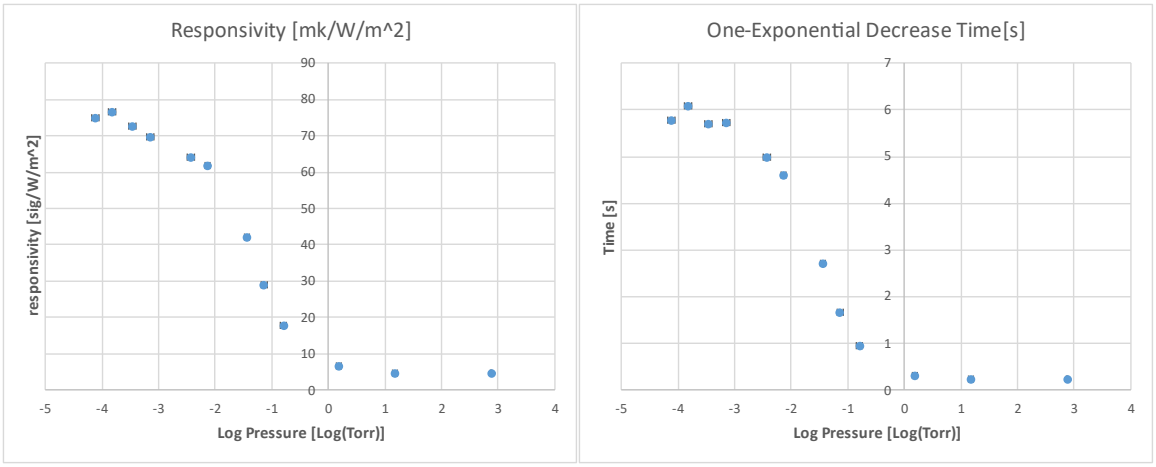

Figure 29 Responsivity (left) and time constant (right) for the I-MON spectrometer system. Short Error bars (barely visible).

the similar order of magnitude difference. However, this problem was not due to the inherent difference between the I-MON system and the scanning laser system. Also, there was no problem of the notch start position within the scan since interference fringes are continuous, and many fringes are present within the I-MON spectrometer range (Figure 19).

Pressure Sensitivity in Resistive Bolometer

Bolometers utilizing temperature changes of sensors to characterize incoming radiation are affected by pressure changes that show up as signal changes, which was detailed by the author in the publication [32]. The publication describes the use of bolometers on a linear plasma device constructed at Oak Ridge National Laboratory (ORNL) known as the Prototype Material Plasma Exposure Stage (Proto-MPEX) [73]. In this research, an empirical model predicts and corrects the pressure-driven bolometer signal. The model requires the two pressure measurements and the raw bolometer signal, and results in a pressure-effect corrected bolometer signal. The model first estimates the pressure inside the pinhole camera using effusion calculations. Second, the two pressure measurements and the effusion pressure estimation of the pinhole camera are matched to the bolometer signal using a time-alignment method. This is performed separately for each correcting case. Third, the pressure measurements, the estimation, and the bolometer signal are standardized using the mean and standard deviation of the data set used for training the empirical model. Next, a regression technique is used to predict the pressure-driven bolometer signal. Finally, the prediction is subtracted from the raw bolometer signal that results in the corrected bolometer signal. In this section, empirical modeling that builds, optimizes, and validates empirical models is described and various applications of the best empirical model are discussed.

The empirical model that predicts and corrects the pressure-driven bolometer signal was built, optimized, and validated using the following procedure and the four deuterium ‘gas-only’ operations data. An estimate of pressure inside the pinhole camera, calculated using the one pressure measurements that was closest to the bolometer and effusion as described in the following subsection, was used as a regression input with two

pressure measurements. Inputs were time-shifted using either the cross-correlation method or the peak-matching method to align with the output or the pressure-driven bolometer signal. The input and output data were divided into training, testing (optimization), and validation sets using the venetian blinds method. The data sets were standardized using the mean and standard deviation of the training data set for PLSR, ridge regression, and LWR. The testing set was used to determine the best regression technique and the best time-delay matching. The performance of the best model was validated and characterized using the validation data set.

Effusion is a gas flow mechanism where the gas escapes from a container through a hole of a diameter considerably smaller than the mean free path of the gas [88]. The pinhole camera was connected to the Proto-MPEX plasma chamber by a 4 mm pinhole, whereas the mean free path of the gas with an average of 2 mTorr in pressure is around 43 mm. The pinhole size is much smaller than the mean free path of gas, which changes the gas flow to the pinhole camera compared to the capacitive manometers for pressure measurements, which were connected to the chamber by an opening approximately 70 mm in diameter. In other words, the vacuum chamber pressure measurements were done through diffusion, whereas the pressure inside the pinhole camera was changing through effusion. Therefore, an estimate of pressure inside the pinhole camera calculated using effusion was required as an additional input for better predictions. The empirical modeling errors were around 2 times higher without the effusion estimation; these results are not presented here due to the superior performance of the models considering effusion estimates of pressure in the pinhole camera.

Time delays between the inputs and output could be due to a delay in measurements, difference in measurement locations, and variation in detectors. For instance, two pressure measurements have different distances to the gas injection locations and pump locations causing delays in physical process being measured at each sensor location, leading to delays in the signals. Two methods for the time-alignment were compared for better pressure-driven signal predictions. The first method was peak matching. This is a simple method of matching peaks of inputs to the output peak and aligning signals accordingly. The second method used cross-correlation of the delayed

signals. This method calculates the cross-correlation coefficient of every possible time-shift between two signals (negative and positive) to identify the time delay that gives the maximum cross-correlation. In the end, inputs were time-aligned to match the output signal.

The empirical model development used three independent data sets to train and test various empirical models and validate the best-performing model. The venetian blinds method was used to divide individual data points of the four deuterium 'gas-only' operations data into training, testing (optimization), and validation data sets. The method avoids possible problems like neglecting regime changes and selecting data points too close to each other in the set. First, the data were divided into 320 blinds with 50 data points. Next, the blinds were evenly shuffled into the three sets. Finally, the minimum value and the maximum value for each variable including the output variable are relocated to the training data set to avoid extrapolations. In the end, the method transformed the time-series data into the three subsets of independent observations that are intermixed data points without time information.

The data sets need to be standardized to have the same importance in variance. The standardized data sets (x_s) were calculated using,

$$x_s = \frac{x - \bar{x}}{\sigma_x}$$

where x is the data set to be standardized, $\bar{x}$ is the mean of the training data, and σ_x is the standard deviation of the training data. In addition, the testing, validation data sets, and any other data set to be used with the model are standardized using the mean and standard deviation of the training data set. This correctly scales the data sets to the empirical models built with the standardized training data set.

Ordinary least squares (OLS) regression assumes inputs are independent (uncorrelated) to ensure stability of the pseudo-inverse solution. The input variables used here are highly correlated to each other since they are time-aligned pressure measurements or pressure prediction of different locations in a closed system. This correlation in the inputs leads to unstable and unrepeatable OLS models. PLSR is a regularization method to solve the stability and repeatability issues by selecting an

appropriate number of latent variables (LVs), which are uncorrelated factors, to replace the original, correlated inputs. The method used was the standard PLSR [89] that performs multilinear regression based on the LVs or uncorrelated factors.

A cross-validation method was used for determining the appropriate number of LVs for the PLSR to include relevant information but exclude noise and confounding information unrelated to the model output. The method is a brute force method, trying one to three LV(s) (three being the maximum possible number of LVs). Root mean squared error (RMSE) of the testing data predictions was calculated and compared for each number of LVs. The best number of LVs was chosen for having the lowest test RMSE.

The best empirical model (the best regression technique and the best time-shift method combined) was determined by comparing both the accuracy (error) and stability (repeatability) using the testing data set. The accuracy was compared using RMSE of the testing data set for each technique and method. For this research, the RMSE or error of modeling needs to be lower than 0.01 V, which is about 10% of the estimated radiated power voltage. If the RMSE is higher than 0.01 volt, the modeling error combined with inherent noise in the signal could overwhelm the radiated power signal. The model stability is evaluated using the condition number of each technique and method. To be considered stable for this research, the models needed to have the condition number near or lower than 100 (a generally-accepted heuristic). Otherwise, the model will be unstable and unrepeatable, meaning that retraining the model with resampled data would lead to significantly different model parameters.

The performance of the best model was validated using the validation data set, a different set of data not used for training and optimization. The model predictions were compared to the pressure-driven bolometer signals of the set. In addition, the modeling error was calculated using the set. The comparison and the modeling error validated the performance of the best empirical model.

The selected best model was applied to data from a different ‘gas-only’ operation than the previous four deuterium ‘gas-only’ operations used for training, optimization, and validation. Unlike the previous data, which were processed to lose time information

due to the venetian blind method, the new data retained the time information to test the model for a time-series of data. The results are compared in both voltage signal and power measurement, which both should be zero due to absence of plasma. The results or corrected bolometer signal were converted to the measured radiated power (P) using (2) [63],

$$\mathrm{P} = \frac{1}{S}\left(\tau\frac{dV_c}{dt} + V_c\right)$$

where S is the sensitivity and τ is the cooling time-constant where both were determined by the calibration of the instrument. V_c is the corrected bolometer signal.

In addition, the model was applied to plasma operation shots, which are more representative of how the model will be used in practice. The radiated power density or the line-integrated brightness ($\int \epsilon dl$) was calculated using [90],

$$\int \epsilon dl = \frac{4\pi {l_{s,p}}^2 P}{cos^2(\theta) A_s A_p}$$

where $l_{s,p}$ is the distance from the sensor to the pinhole, P is the radiated power, A_s is the sensor size, A_p is the pinhole size, and θ is the misalignment angle between the line of sight and the surface of the sensor.

Since the correct bolometer measurement without pressure-driven signal was unknown, the radiated power density of the resistive bolometer was compared with the radiated power density measurement by an absolute extreme ultraviolet (AXUV) photodiode (AXUV100G from Opto Diode Corp) that is not affected by neutral pressure changes to evaluate the consistency of the error-correction method. Although the time-history information can be trusted for AXUV, the absolute values of radiated power will be wrong due to its responsivity problem [91]. Due to a variable responsivity (~0.27 to ~0.1 A/W) over a broad wavelength of the photodiode, the responsivity assuming the high energy plasma radiation will result in a low radiated power. To match and compare measurements of the bolometer and the photodiode, the photodiode measurements were multiplied by a certain value [91] that is specific to the plasma condition. Since this multiplicative factor can vary depending upon the plasma condition (e.g. the amount and type of auxiliary heating), correction of the resistive bolometer measurements is required,

thus justifying the need for this work. The value for each multiplicative factor was chosen comparing the region (4.45 to 4.6 s) where pressure effects were minimal; the neutral pressure dropped to sub-mTorr and stayed near constant. However, this reduction of the neutral pressure is only present in a specific location of the Proto-MPEX. The neutral pressure at other locations either do not reduce to sub-mTorr range or do not stay constant [92], again justifying the need for the developing and implementing the compensations being described here.

The radiated power (P) for the AXUV photodiode was calculated using,

$$\mathrm{P} = \frac{V}{R \times G}$$

where V is the measured voltage from the photodiode amplifier (Thorlabs PDA200C) that converted the current from the photodiode to the voltage, R is the responsivity, and G is the conversion coefficient of the amplifier. Assuming high energy plasma radiation [93], 0.27 A/W was selected for the responsivity, which means the AXUV diode should underpredict the estimated radiation [91].

The AXUV photodiode was used with a similar pinhole camera design. The line-integrated brightness calculation of the photodiode was like the resistive bolometer except that the photodiode was divided into 48 pixels and the brightness was averaged over the pixels [64]. This process was required due to the plasma being smaller than the photodiode field of view. The radiated power was assumed to be homogenous and divided equally among the pixels.

The estimate of the radiated power loss (P_{rad}) of the plasma section where the bolometer was installed was calculated using equation [93],

$$P_{rad} = \frac{\pi}{2} r_p z \int \epsilon dl$$

where r_p is the estimated radius of plasma column (~0.02 m), z is the plasma column length of the section (~0.9 m), and $\int \epsilon dl$ is the line-integrated brightness. It was assumed that the radius of plasma column was constant in the section and represented by the radius where the bolometer was installed, and the emission was uniform and homogenous in the section. These parameters were used to compare with a previous power balance study.

The proposed methodology was applied to the described data. The combined data set for the empirical modeling had 16000 observations or data points covering a broad range of possible inputs and output. The Venetian blinds resulted in three evenly distributed data sets for training, optimization, and validation. The training data set had 5357 observations, the test (optimization) data set had 5341 observations, and the validation data set had 5299 observations. Maximum and minimum for each input and output were verified to be in the training data set to avoid extrapolations beyond the region of the model training.

The cross-validation method was used to select the appropriate number of latent variables for PLSR. The results showed that the first latent variable explained 99.12% of the information. The second and third latent variable explained 0.79% and 0.09% of the information. Although the last two LVs can be treated as noise since they contain less than 1% of the information, the RMSE results of cross-validation showed that including the second LV decreased RMSE significantly. Since using all three LVs is the same as ordinary linear regression, using the first two LVs was the best option.

The better method for time-alignment was the cross-correlation method (Table 3). The cross-correlation method was more accurate (lower RMSE) but less stable (higher condition number). Since the stability highly depended on different regression techniques, the cross-correlation method was chosen for its high accuracy. The best regression technique selected was PLSR (Table 3). Even though the linear regression and LWR had higher accuracies (lower RMSEs), both had condition numbers orders of magnitude higher than 100 making them ill-conditioned or unstable and unrepeatable models. The RMSE of ridge regression was higher than 0.01V, which was the limit set for this research; therefore, the ridge regression was removed from consideration.

The best empirical model (cross-correlation method and PLSR combined) was validated to have a good agreement with the expected values or the perfect predictions over a wide range of possible pressure-driven signal using the validation data set (Figure. 30). This showed that the model had a good accuracy. The validation error or modeling error was 0.0036 V. This was very close to the test data RMSE, which proved that the empirical model was stable.

Table 3 RMSE and Condition Number of Four Different Regressions and Two Different Time-Alignment Mmethods

Regression	Time-alignment	RMSE (volts)	Condition number
Linear regression	Cross-correlation	0.0034	2.30E+04
	Peaks	0.0047	2.06E+04
PLSR	Cross-correlation	0.0035	145.14
	Peaks	0.0047	74.55
Ridge regression	Cross-correlation	0.0094	33.54
	Peaks	0.0113	26.51
LWR	Cross-correlation	0.0025	2.44E+03
	Peaks	0.0031	1.44E+03

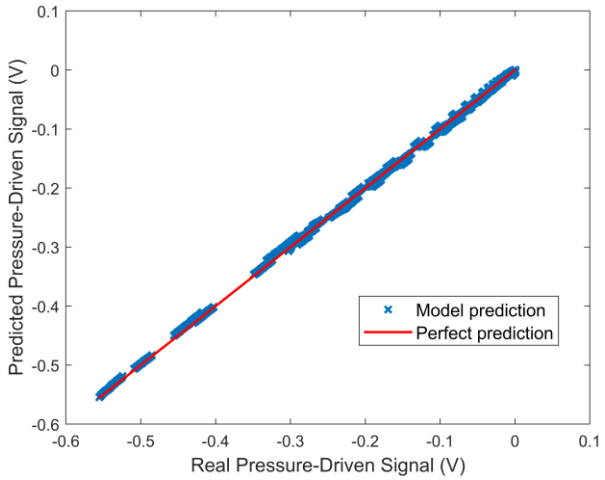

Figure 30 The validation of the best model using the validation data set. The model showed a good accuracy over a wide range of possible pressure-driven signal.

The best model was applied for a different ‘gas-only’ operation data with time information. Since it was a ‘gas-only’ operation, the bolometer was supposed to show zero signal. However, there was a pressure-driven signal (Figure 31 (a), blue line) as previously mentioned. The prediction (Figure 31 (a), green line) matched the actual pressure-driven signal well with only small mismatches. The corrected or prediction-subtraction results showed that the pressure-driven signal has been reduced to near noise level for the voltage signal and the power calculations (Figure 31). The RMSE for the case was 0.0032 V, which was better than the modeling error.

The empirical model was used to investigate data from plasma operations. The presence of plasma radiated power signal in addition to pressure-driven signal was unlike the ‘gas-only’ operation. The pressure-driven signal was corrected from the unprocessed bolometer signal to have only the radiated power signal. The radiated power measurement of the corrected signal was compared to the AXUV photodiode measurement multiplied by each multiplication value calculated from 4.45 to 4.6 seconds. The multiplication values ranged from 0.78 to 1.44. Both the uncorrected and corrected bolometer measurements agreed well with the multiplied AXUV measurement during the period (Figure 32) 4.45 to 4.6 s, as expected. The brightness comparison, during the period when the pressure-driven signal was significant, showed that the corrected bolometer also agreed well with the multiplied AXUV (Figure 32), except when the pressure dropped rapidly (as discussed below). Especially, unphysical negative brightness and very low brightness around the start of the plasma discharge were significantly mitigated for the corrected brightness compared to the uncorrected brightness. In addition, the comparisons of the mean values for the corrected bolometer brightness measurements with AXUV brightness measurements for five different plasma operations showed that the empirical model worked well for the time periods with plasma and pressure effects present in the bolometer signals (4.15 to 4.45 seconds) (Table 4).

Although Figure 32 and Table 4 showed that the model used to correct the pressure-driven signal on the resistive bolometer worked without a significant problem for plasma operations, the model was not perfect. There was a region where the multiplied AXUV and the corrected bolometer measurements partly disagreed. It was

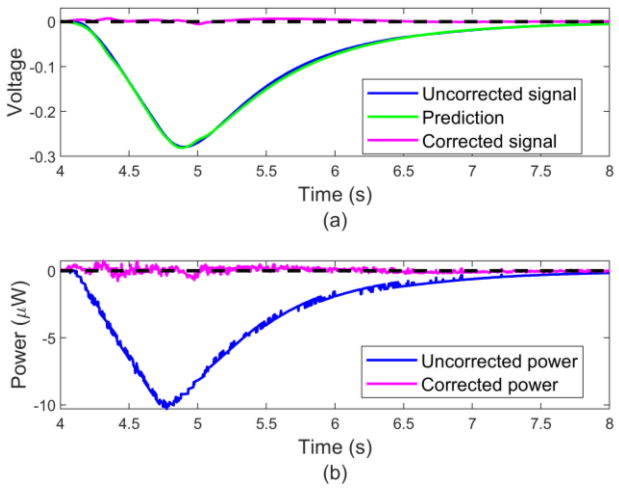

Figure 31 (a) uncorrected (pressure-driven) signal (blue), prediction using the best model (red), and corrected signal (magenta) for a 'gas-only' operation. (b) the corresponding corrected and uncorrected radiated power calculations. The black dotted lines are what noiseless signal or radiated power should be. The prediction subtraction reduced the pressure-driven signal to near noise level.

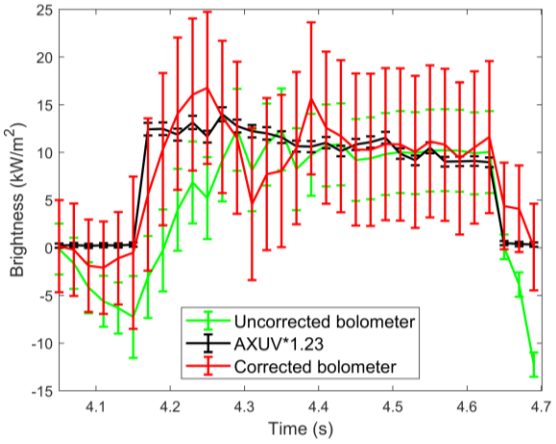

Figure 32 Shot 22817 comparison of radiated power measurements (brightness) for uncorrected and corrected bolometer, and 1.23*AXUV photodiode. The empirical model corrected negative brightness and low brightness where the pressure effects were significant.

Table 4 Mean Values[A)] of Input Power, Uncorrected and Corrected Bolometer Brightness, MV[B)], AND MV*AXUV Brightness

Shot #	Power (kW)	Uncorrected (kW/m^2)	Corrected (kW/m^2)	MV	MV*AXUV (kW/m^2)
22565	41	0.52 ± 0.22	5.06 ± 0.35	0.78	3.35 ± 0.01
22817	53	6.45 ± 0.23	10.75 ± 0.42	1.23	11.35 ± 0.02
22816	55	6.00 ± 0.21	10.52 ± 0.45	1.22	11.69 ± 0.02
22567	58	4.06 ± 0.31	9.73 ± 0.56	1.27	12.22 ± 0.02
22568	64	6.13 ± 0.33	12.37 ± 0.62	1.44	15.58 ± 0.03

[A)] Mean values: averaged over 4.15 to 4.45 seconds
[B)] MV: multiplication value.

where the bolometer measurement had a valley (Figure 32, ~4.3 s). This implied that the pressure-corrected radiated power density dropped and recovered, which was not present in the AXUV measurement and resulted in slightly lower mean brightness (Table 4). This occurred when the neutral pressure dropped rapidly to sub-mTorr range. Therefore, it was speculated that the rate at which the neutral pressure changes, which is non-linear to pressure measurements, affected the pressure-driven signal. In this sense, the discrepancy was understandable since PLSR cannot predict non-linear effects. The LWR, which better predicts non-linear effects, was not comparable for the situation because results for the LWR showed much worse overall predictions, which were possibly due to stability and repeatability issues.

A previous power balance for a similar discharge used Bremsstrahlung radiation, line radiation, and radiative recombination calculations to estimate the radiated power loss in various sections of Proto-MPEX [94]. The estimation was 1.09 ± 0.06 kW of radiated power loss in the plasma section, which includes the installation location of the bolometer, with injected power of 101 kW. This was close to the extrapolation result using the corrected bolometer measurement, 0.87 ± 0.03 kW (Table 5). The difference could be due to magnetic field variation (from ~0.4 T at the bolometer location up to 1T under the magnet coils) in the section. In addition, the lower value could be due to the valley (Figure 32 ~4.3 s) that resulted in slightly lower overall brightness.

Fiber Optic Bolometer as Vacuum Pressure Sensor

The observations mentioned before led to research of using FOBs as highly sensitive vacuum pressure sensors [83]. For this research, the FOB was installed inside a vacuum chamber with a vacuum window (Figure 33). The external laser was shined through the vacuum window onto the gold plate of the FOB. The interrogation system for the FOB consisted of the white light source, a spectrometer (I-MON 512 USB), a polarization scrambler, an attenuator, and a circulator (Figure 33). The chamber was connected to the plasma exposure chamber of the University of Tennessee – Knoxville [58] for controlling vacuum pressure. A convection-enhanced Pirani gauge (Granville-

Table 5 Input Power, Brightness, and Section Radiated Power Loss

Shot #	Input power (kW)	Brightness[B] (kW/m^2)	Section radiated power loss (kW)
22565	41	4.82 ± 0.29	0.17 ± 0.01
22817	53	10.81 ± 0.36	0.31 ± 0.01
22816	55	10.90 ± 0.38	0.31 ± 0.01
22567	58	12.04 ± 0.47	0.43 ± 0.02
22568	64	14.91 ± 0.53	0.53 ± 0.02
Extrapolated[A]	101	30.93 ± 0.90	0.87 ± 0.03

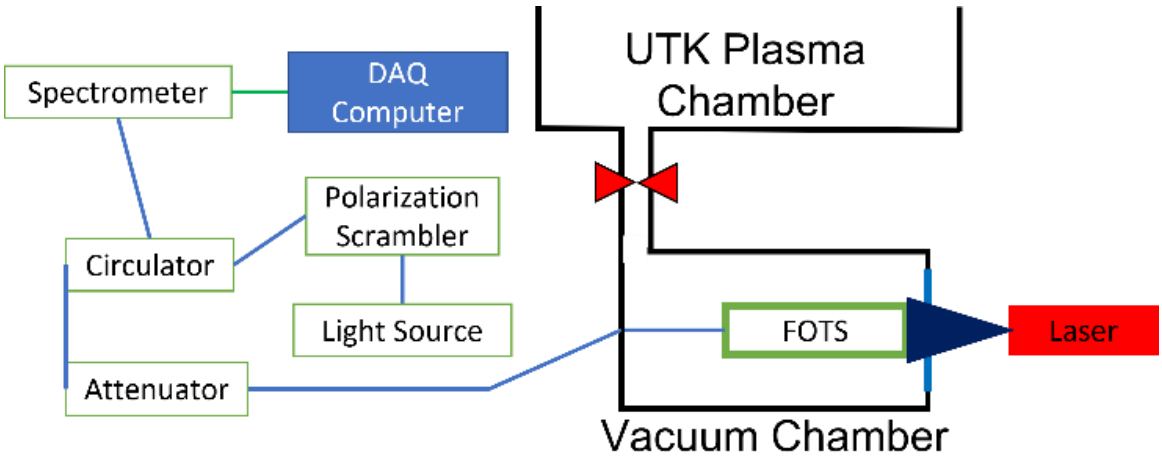

Figure 33 Diagram of the FOB experimental setup and interrogation system.

Phillips® 275 Convectron® Pirani Vacuum Gauge) was used for measuring pressures from 760 to 3E-3 Torr. A Bayard-Alpert Hot Cathode gauge (355001-YG Hot Cathode Vacuum Gauge) was used for measuring from 3E-3 Torr and below. Both gauges agreed with each other at 3E-3 Torr within the error values. The valve connecting to the vacuum pumps was closed for a pressure measurement above 3E-3 Torr. Below 3E-3 Torr, the pressure was controlled by a throttle valve.

The white light source producing the signal carrying light can significantly heat the FOB if it is controlled to have enough power to reach the FOB. It is speculated that the epoxy used to glue the gold plate on the top of the silicon pillar and the silicon pillar on the fiber optic cable was absorbing the power from the light source. Also, it was expected that the gold plate was absorbing some of the power from the light source. The heating power was controlled through the attenuator with fixed values for the power of the light source and the exposure time on the spectrometer. The counts of the highest peak on the spectrometer at 760 Torr acted as a control point for a calibration. The system was left constant during vacuum pressure scans.

The measurements for this method were performed, at least, 30 seconds after the pressure was stabilized in the chamber. This was to compensate for the wait time required for a temperature saturation at a high vacuum (Figure 34, red dotted). The temperature measured by the FOB at different pressures were compared to the temperature at 760 Torr by assuming 0mK at 760 Torr (Figure 35, blue).

The vacuum pressures were divided into different regimes for analysis as mentioned in the introduction. For the medium vacuum regime, a rational function (2nd order polynomial on both the numerator and denominator) and a smoothing univariate spline fits were developed using an optimization data set and used for a pressure measurement. For the high vacuum regime, an exponential function fit was developed from the data set and used to relate the measurement to the vacuum pressure. A separate validation data set was used to validate the fits and the accuracy of the pressure measurement of the method.

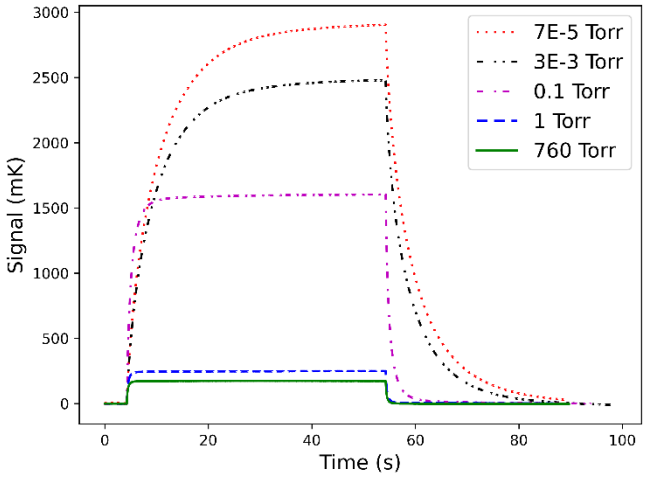

Figure 34 Differences in the response of the FOB between 760 to 7E-5 Torr for the same square wave of incoming radiation. The higher vacuum case showed a higher signal level (increased responsivity), but also a longer wait-time (increased response time) for a temperature saturation.

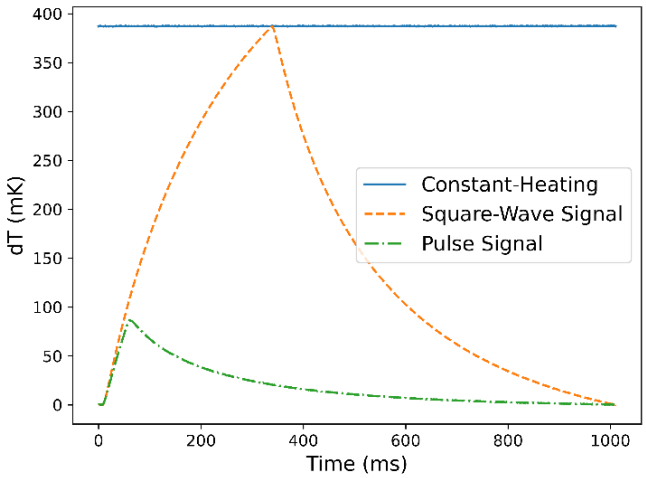

Figure 35 Temperature measurements using the FOB in 1.2 Torr for the three methods. For the constant-heating method, 0mK at 760 Torr was used to calculate the relative temperature at 1.2 Torr. For the square-wave signal method, the amplitude (the peak temperature) of the square wave was measured for each pressure. For the pulse signal method, the decay-constant was calculated from the temperature decay using an exponential fit.

A square wave input to the external laser was used to avoid the wait time for a temperature saturation. The square wave had 33% duty cycle in 1Hz cycle with a fixed power. The laser power level was adjusted to match a certain measured amplitude on the FOB at 760 Torr, which acted as a control point for a calibration. The laser operated continuously during a pressure scan with the constant power.

The measured amplitude of the square wave was calculated from the difference in the temperature between the start and the peak of the temperature increase (Figure 35, orange dashed). An exponential function was used for the low and medium (to 1.5E-2 Torr) vacuum regimes. Again, a separate validation data set was used to validate the fits and the accuracy of the pressure measurement for this method.

A decay constant was calculated from the temperature decay of a pulse coming from the external laser and related to the corresponding pressure. A pulse was better than a square wave due to longer temperature decay with the same cycle. The pulse was 50ms in width in 1Hz cycle with a fixed power. Again, this was to avoid the wait time for a temperature saturation. In addition, this method did not require a control of heating power, which was required for the two previous methods.

The decay-constant was calculated using an exponential function that was fitted to data points corresponding to 82% and 30% of the pulse height on the temperature decay (Figure 35, green dash-dotted). For the medium vacuum regime (to 1.5E-2 Torr), 4th polynomial function and a smoothing univariate spline fits were developed from an optimization data set and used to relate the measurement to the pressure. Again, a separate validation data set was used to validate the fits and the accuracy of the pressure measurement for this method.

The proposed methods were applied to the described data. There were 53 pressure data points ranging from 760 to 1.8E-5 Torr that were equally spread out logarithmically. Each pressure data point had three different FOB measurements of ~5 seconds. Two of the measurements were used for a fit optimization. One of the measurements were used as validation data. RMSE of a fit was calculated assuming that the pressure measurement with the commercial vacuum gauges were exact. A propagated error was calculated using the fit equations and the signal variations of the FOB measurements.

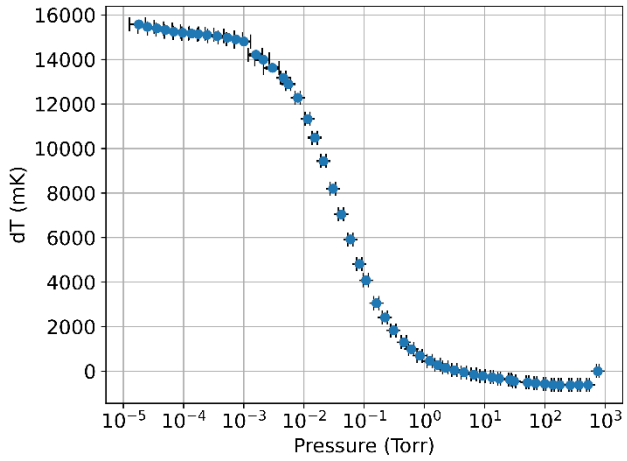

Figure 36 Relative temperature vs vacuum pressure for the constant-heating method. The measured temperature increased with a decreasing vacuum pressure following the increasing responsivity with a decreasing pressure.

The constant-heating method, which utilized the heating from the white light source, showed an increased temperature as the pressure decreased in the vacuum chamber (Figure 36). The measured temperature increased due to the increased responsivity that the constant heating resulted in a higher temperature. This method showed a propagated error of 4.27% and an accuracy of 20.69% in the high vacuum regime with an exponential fit (Figure 37 (a)). Also, the method was capable in the medium vacuum regime (Figure 37 (b)). The pressure values from the rational function and a smoothing univariate spline were in a good agreement with the measurements. The measurements in the low vacuum regime were overwhelmed by a background gas fluctuation.

The square-wave signal method, which exploited the changes in the measured amplitude of the square wave, showed the same trend. The measured amplitude increased with decreasing pressures for a fixed laser input (Figure 38). Again, the trend is due to the changing responsivity with varying pressures. The method showed a propagated error of 4.87% and an accuracy of 14.94% at the low vacuum regime with an exponential fit (Figure 39 (a)). Also, the method was applicable in the medium vacuum regime (Figure 39 (b)). Below 1.5E-2 Torr, the differences in the measured amplitude were overwhelmed by the errors (Figure 38).

The pulse signal method, which measured the decay constant, showed increased decay constants for decreased pressures (Figure 40 (a)). The trend is following the increased response time with decreasing pressure. Only the medium vacuum regime was acceptable for a pressure measurement, where the decay constant differed above the variations (Figure 40 (b)). The other regimes showed a near flat response where the errors overwhelmed the differences in the decay constants.

An overall comparison showed that the different methods were working at different regimes with different accuracies (Table 6). For the low vacuum regime, only the square-wave signal method was operable for a FOB pressure measurement. For the medium vacuum regime, all the methods were acceptable for a pressure measurement. The pulse signal method was the most promising in the regime considering both the accuracy and the advantage of not sensitive to heating power. For the high vacuum

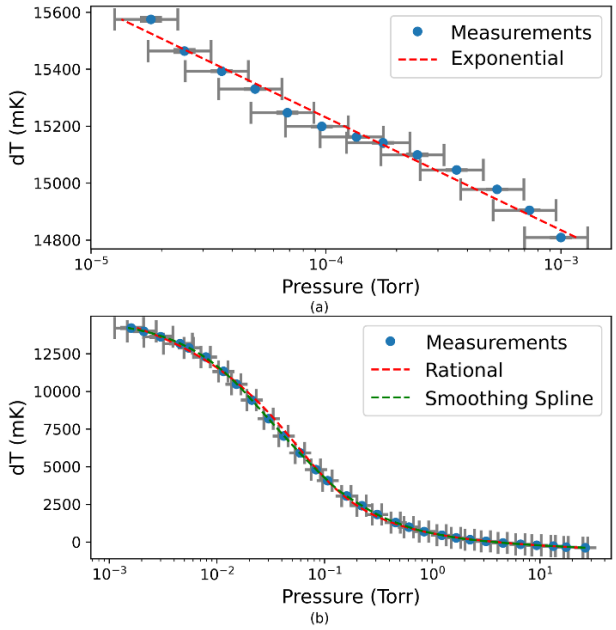

Figure 37 (a) relative temperature measurements at the high vacuum regime with an exponential fit (red dotted line). (b) relative temperature measurements at the medium vacuum regime with a rational function (red dotted line) and smoothing univariate spline (green dotted line) fits.

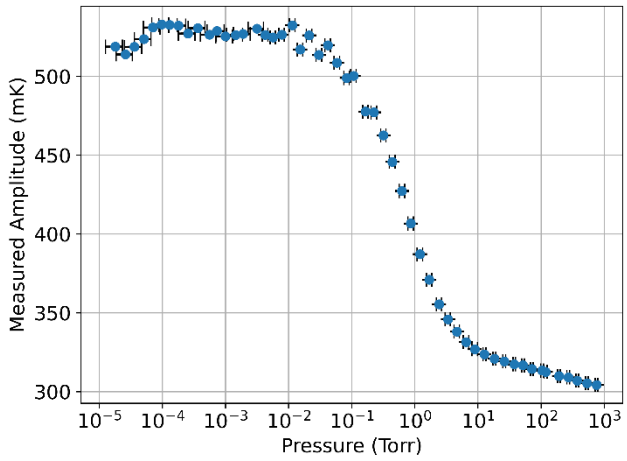

Figure 38 Measured amplitude vs vacuum pressure for the square-wave signal method. The measured amplitude increased with a decreasing pressure due to the increased responsivity. Outliers to the trend in high vacuum could be due to a laser instability or alignment issues.

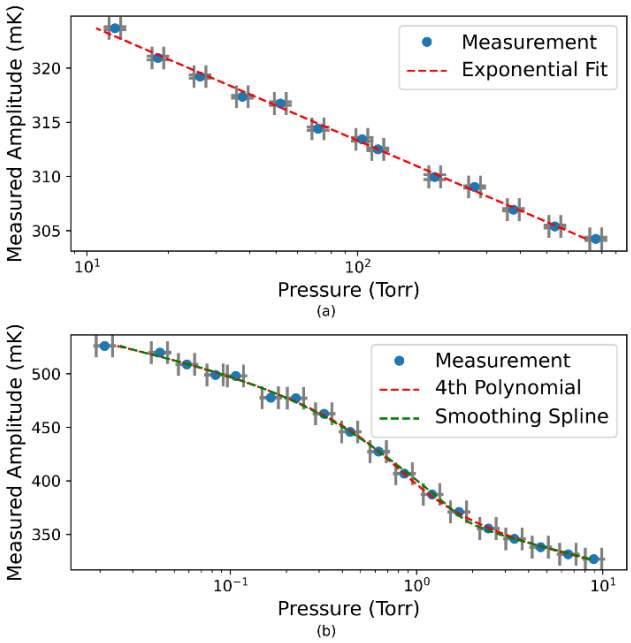

Figure 39 (a) the square-wave signal method measurements at the low vacuum regime with an exponential fit (red dotted line). (b) the square-wave signal method measurements at the medium vacuum regime with 4th polynomial (red dotted line) and smoothing univariate spline (green dotted line) fits.

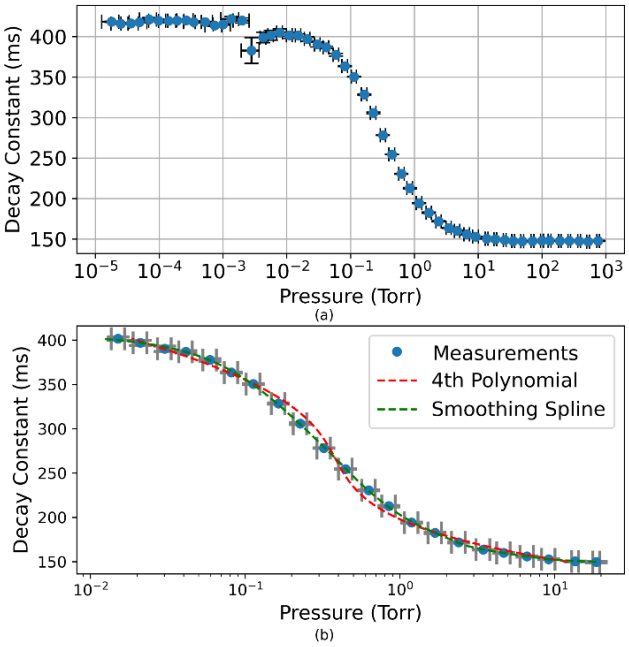

Figure 40 (a) decay constant from the pulse signal method vs vacuum pressure. The decay constant increased as the pressure decreased following the increased response time. (b) the decay constants at the medium vacuum regime with 4th polynomial (red dotted line) and smoothing univariate spline (green dotted line) fits.

Table 6 Accuracy of Three Methods for FOB Pressure Measurements

Methods	Errors	Low Vacuum (760 to 10 Torr)	Medium Vac. (10 to 1.5E-3 Torr)*	High Vacuum (<1.5E-3 Torr)
1. Constant-Heating	Propagated [%]	NA	NA	4.27
	RMSE [%]	NA	5.12 (rational), 1.38 (spline)	20.69
2. Square-Wave Signal	Propagated [%]	4.87	0.30 (4^{th})	NA
	RMSE [%]	14.94	10.83 (4^{th}), 19.09 (spline)	NA
3. Pulse Signal	Propagated [%]	NA	4.25 (4^{th})	NA
	RMSE [%]	NA	28.82 (4^{th}), 5.36 (spline)	NA

NA = not applicable
*: to 1.5E-2 Torr for the square-wave and pulse signal methods.

regime, the constant heating method was the only method possible for a pressure measurement with a good accuracy.

Single-Channel FOB Calibrations

Calibrations Using Heat Transfer Equation

A calibration of bolometers is to convert whatever the bolometer measures (the raw values) like voltage for resistive bolometers and delta wavelength for FOBs into more useful values like measured power (or power density). This is done by doing calibration experiments. The experiment uses the same setup as the previous section. With a known power or power density coming to a bolometer, one can relate raw measurements of the bolometer to the power or power density using various equations.

For resistive bolometers, the system can be simplified as a heating of an insulated enclosure (Figure 41, left). The simple scheme can be turned into a thermal network using thermal-electrical analogy (Figure 41, right) [61]. In the analogy, the incoming heat (radiation) is a current source (Q), the heated element (detector) acts as a capacitor (C), the insulated enclosure (thermal insulation) acts as a resistor (R), and the environment acts as a ground. The electrical analogy is used to calculate a simple heat transfer equation from the scheme. The energy balance of the system is as follows,

$$Heat\ in = Heat\ out + Heat\ stored$$

The equation for the system becomes,

$$Q = \frac{T}{R} + C\frac{dT}{dt}$$

T: the temperature of the heated element (sensor)

The equation for resistive bolometers is [33],

$$\mathrm{P} = \frac{V}{R} + \frac{\tau}{R}\frac{dV}{dt}$$

P is radiated power measured by a resistive bolometer, V is voltage (raw measurement of a resistive bolometer), R is responsivity, and τ is Time-constant. In summary, the calibration parameters are responsivity and time-constant for the resistive bolometers, which can be obtained with the experiments mentioned in the previous section.

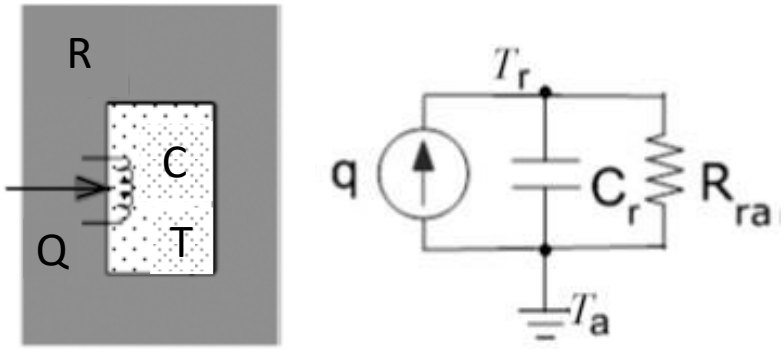

Figure 41 Left: simplified schematic of a resistive bolometer. Right: 1D thermal network corresponding to the left schematic.

FOBs showed a more complex heat-transfer mechanism. The initial sign was that the responsivity and the time-constant changed with different start positions in the scanning range for the scanning laser system. For the I-MON system, it was confirmed that transition sections for a square wave of incoming radiation were not an exponential increase or decrease (Figure 42, left). This meant that the time-constant was not constant (Figure 42, right). Also, this meant that the calibration equation for the resistive bolometers were not viable for FOBs. For example, the transition stages showed unacceptable errors compared to the incoming square-wave radiations (Figure 43). Also, 2D (acceptable due to cylindrical symmetry of the FOBs) finite-element simulations for the FOB were conducted using MATLAB (FEATool) to double-check the problem. Although absolute values were different due to incorrect material properties for the simulation, the results showed similar results as compared to the experiment results if you use the resistive bolometer equation for the resistive bolometers (Figure 44).

Many different attempts were made to overcome this problem. First, the responsivity and the time-constant were treated as variables, not constants for a specific pressure. The responsivity and the time-constant were fitted to a function of the temperature change of the FOBs. However, the parameters of the function changed drastically with pressure. The problem was that it was difficult to characterize the parameters of the function for pressures between the calibration pressures. Thus, the method was not acceptable and discarded.

Second, a new equation for the calibration was applied with an additional term as compared to the equation for the resistive bolometers. The additional term added was the radiative transfer term. This is where the absolute temperature measurements mentioned from the previous section are required. The full equation is,

$$P = A\frac{\partial T}{\partial t} + B\Delta T + C(T^4 - T_0^4)$$

P: Radiated power measured

T: Absolute temperature of the FOB

T_0: Background/ambient temperature

A, B, C: calibration parameters/constants

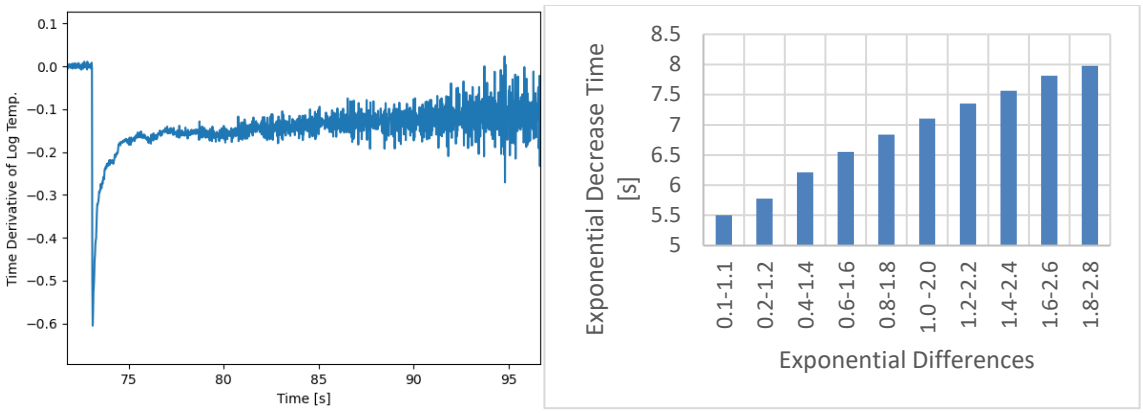

Figure 42 Left: time derivative of natural log of ΔT measured by FOB. If the transition was an exponential decay, the values should have been constant (flat). Right: different time constants at different transition locations.

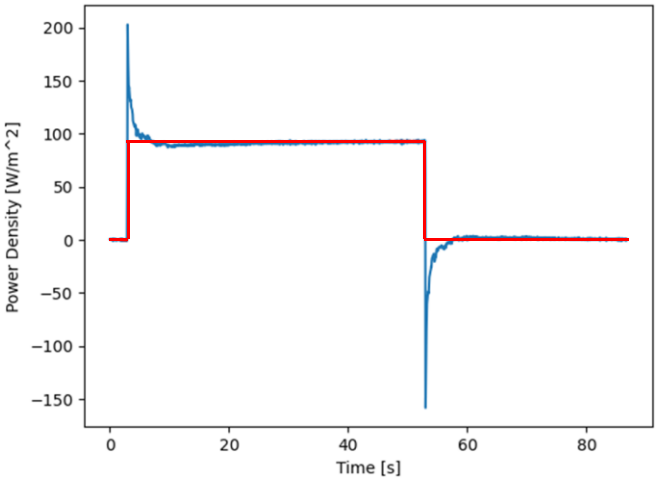

Figure 43 A result from using the resistive bolometer equation for the FOB (blue). Transition stages do not match the incoming radiation (red).

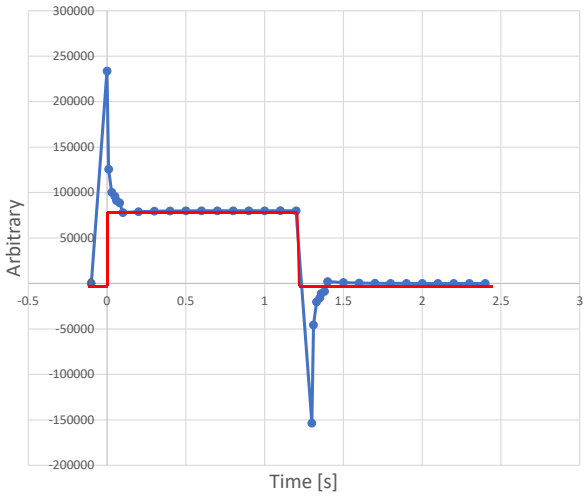

Figure 44 A result from using the resistive bolometer equation for the FOB simulation (blue). Transition stages do not match the input power (red).

Measurements of three different power levels of incoming radiation are required to obtain three different calibration parameters. The results from the equation, however, were not optimal although they were better than using the previous simpler equation. The transition sections were still the problem where it did not show a square wave (Figure 45). Again, this method was discarded due to the performance.

Next, a more complex thermal-transfer scheme was explored for coming up with a calibration equation with possibly constant parameters at a specific pressure. The construction of the FOB can be simplified in 1D heat-transfer scheme. The front part with the gold plate, the silicon pillar behind the gold plate, and fiber optic cables at the back will be the 1D heat-transfer scheme (Figure 46, left). Using the thermal-electrical analogy, the incoming heat (radiation) is a current source (Q), the heated elements (gold plate and silicon pillar) act as capacitors (C), the insulations (between gold plate and silicon pillar, and between silicon pillar and fiber optic cable) act as resistors (R), and the fiber optic cable acts as a ground/thermal sink (Figure 46, right). It was assumed a vacuum surrounding (insulations). The scheme requires two energy balance equations, the heat in and out for the gold plate and the silicon pillar. The two equations are as follows,

$$Q = (q_{rad}^{1} + \frac{T_1 - T_2}{R_{12}}) + C_1 \frac{dT_1}{dt}$$

$$\frac{T_1 - T_2}{R_{12}} = (q_{rad}^{2} + \frac{T_2 - T_a}{R_{2a}}) + C_2 \frac{dT_2}{dt}$$

$q_{rad}^{1\ or\ 2}$: Radiative term for gold plate (1) and silicon pillar (2)

$q_{rad}^{1\ or\ 2} = \epsilon\sigma F(T^4 - T_a^4) \equiv r_{1\ or\ 2}(T^4 - T_a^4)$

ϵ is the emissivity

σ is the Stefan–Boltzmann constant

F is the view factor

r is a simplified constant for multiplication of above three parameters

The only variable measured by the FOB is T_2 (the temperature of the silicon pillar) and its time derivative. Thus, it is required to simplify the equation to be able to solve it.

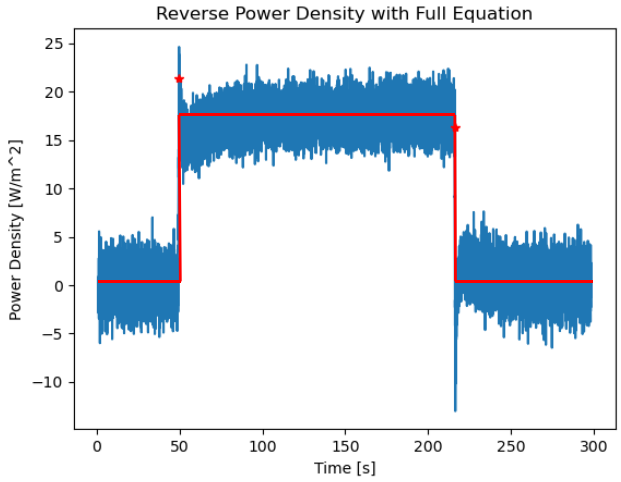

Figure 45 A result from using the resistive bolometer equation + radiative term for the FOB (blue). Transition stages are better, but still erroneous. Incoming radiation (red).

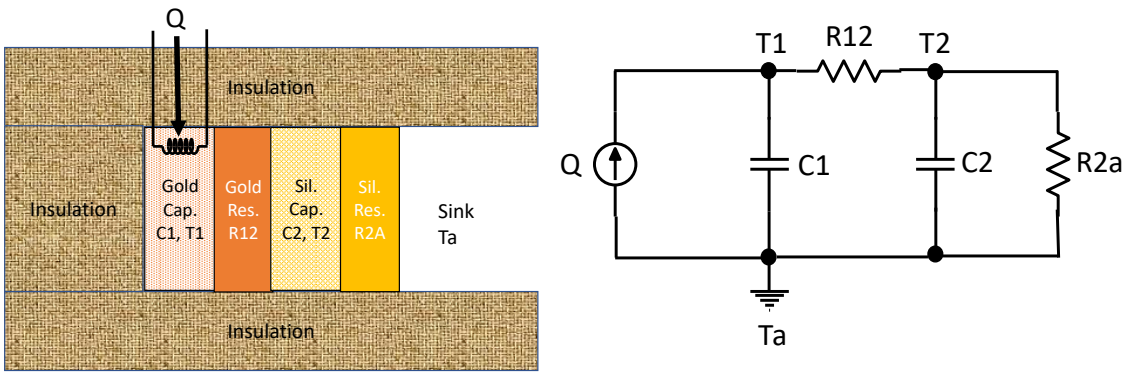

Figure 46 Left: 1D heat transfer scheme of the FOB. Right: thermal circuit corresponding to the left scheme.

The radiative term for the gold plate is ignored considering the emissivity of polished gold is much lower (0.025) than silicon (0.79). With the simplification, two equations can be solved with calibration experiments. The calibration is divided into two parts. The first part is the steady state part where enough time has passed since the start of a constant incoming radiation that the response of the FOB is constant or "steady." In this part, time derivatives in the equation can be ignored since they will be zero. The combined equation to eliminate T_1 is,

$$Q = \frac{T_1 - T_2}{R_{12}} = r_2(T_2^4 - T_a^4) + \frac{T_2 - T_a}{R_{2a}}$$

Since T_a is the temperature of the sink (fiber optic cable), it is considered as constant (an ambient temperature). With the FOB temperature (T_2), one will obtain r_2 and R_{2a} constants (two parameters require two different measurements).

The second part is the transient part with the time derivatives. The combined equation to eliminate T_1 is,

$$Q = \left[r_2(T_2^4 - T_a^4) + \frac{T_2 - T_a}{R_{2a}}\right] + (C_2 + \frac{R_{12} + R_{2a}}{R_{2a}})\frac{dT_2}{dt} + (4C_1R_{12}r_2)T_2^3\frac{dT_2}{dt} + (R_{12}C_2)\frac{d^2T_2}{dt^2}$$

Since the constants in the first bracket are calibrated from the steady-state part, only the other three terms are needed to be calibrated. Rather than trying to find out each constant, one can simplify the constants in the rest of the brackets into single parameters (multiplication of constants) for each term (inseparable variables),

$$Q = \left[r_2(T_2^4 - T_a^4) + \frac{T_2 - T_a}{R_{2a}}\right] + \alpha\frac{dT_2}{dt} + \beta T_2^3\frac{dT_2}{dt} + \gamma\frac{d^2T_2}{dt^2}$$

Now, there are only three parameters requiring three different calibration data. The final equation will transform the temperature measurements into the incoming power or power density.

The results using the equation showed acceptable results in the increase transient part (Figure 47). However, the decrease transient part was unacceptably erroneous. This suggested that the heat transfer problem of the FOB is more complex than the presented scheme. Also, the second time-derivative of the equation made the noise unacceptable

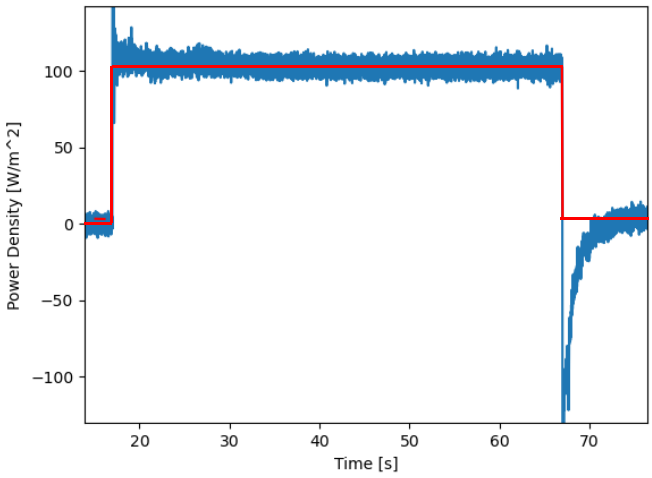

Figure 47 A result from using the complicated thermal transfer equation for the FOB (blue). The increase transition stage matched well, but it was erroneous at the decrease transition stage. Incoming radiation (red).

unless averaged over 100 data points making the data only 10 Hz, which was not acceptable. Again, this method was discarded due to the problems.

Frequency Space Calibration

A novel method of calibrating the FOB was introduced by Dr. Ming Han from the MSU group. The method calibrates the FOB in the frequency space using a deconvolution method rather than in time-series like the methods previously mentioned above. There are two ways to calibrate the FOB in the frequency space. The first one is measurements of discrete frequency components from incoming radiation. The second one is a measurement of a pulse, which will result in continuous frequency components. Both methods require Fourier transforms of the time-series data that result in amplitude and phase data. Both are calibrated by having transform functions that corrects the frequency response (amplitude and phase) of the FOB into the incoming radiation. Then, the corrected frequency response needs to revert to time-series, which is the final data form required for an analysis.

The discrete method requires an incoming radiation of a known frequency. An ideal sinusoidal wave for the incoming radiation was used to obtain the frequency response of the FOB for a specific frequency. Since the amplitude of the incoming radiation is known from the PDA-36, the amplitude of the response of the FOB can be matched to the incoming radiation by a transform function. Also, the phase of the response of the FOB can be offset to the incoming radiation assuming the incoming radiation phase is zero. Several different frequencies of the incoming radiation are used to approximate the response for the frequency components in between the calibrations (Figure 48) for a specific pressure.

The results of using the method to convert the raw measurements of the FOB into the incoming power/power density was somewhat successful (Figure 49). The problematic transient regions were much better than the previous methods that used heat transfer equations. However, it wasn't perfect. There were still systematic errors (not straight for a square wave. in the transient regions) which was thought to be due to the errors in the fits from the discrete data points in calibrations in the frequency space. Also,

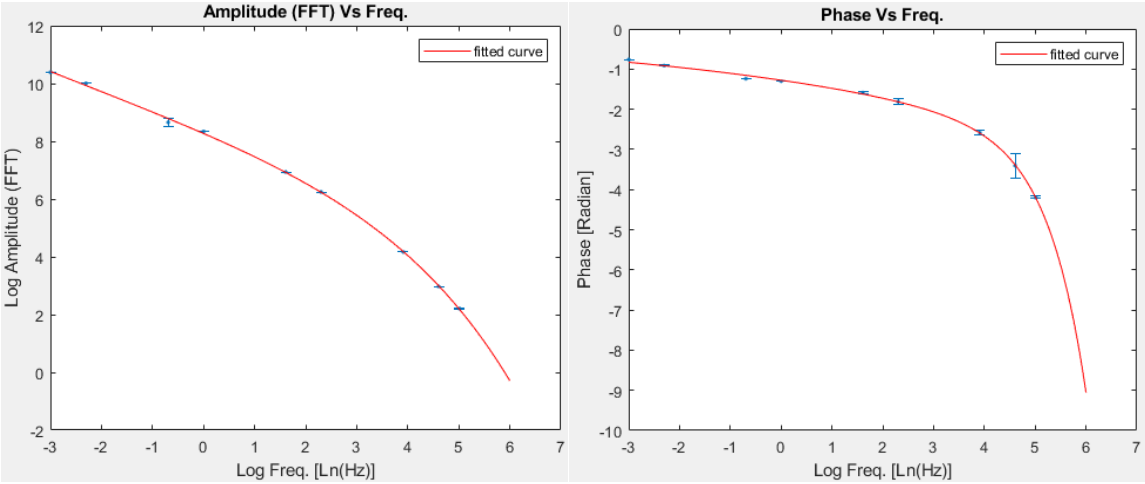

Figure 48 Left: amplitude response of the FOB corresponding to specific frequency components (blue). Right: phase response of the FOB corresponding to specific frequency components (blue). Fitted curve (red) for data in between the frequency components.

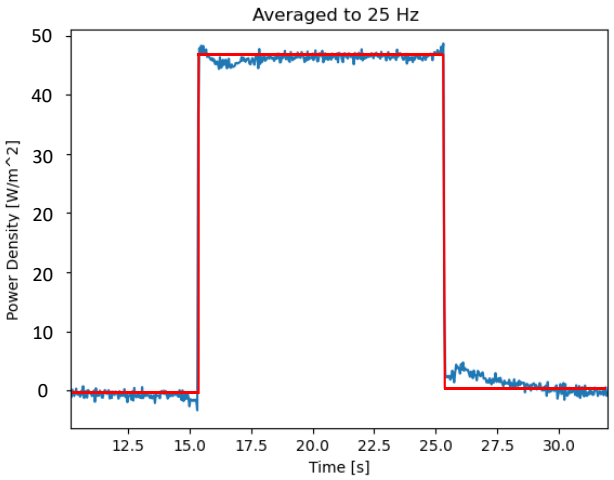

Figure 49 Result of the discrete frequency space calibration that is averaged to be 25Hz (blue). Incoming radiation (red).

the method required too many calibration measurements for a single pressure value that the calibration for air to high vacuum would be very time-consuming.

The pulse method utilizes a pulse of incoming radiation to calibrate the response of the FOB. The pulse width (8.5 milliseconds) was short enough to be considered an ideal pulse for the measurement frequency of 1000 Hz of the FOB. The laser for the incoming radiation had to be focused to a very small spot size. If not, the response of FOB was very small due to the limitation of the laser power. Also, it was impossible to have the laser beam entirely on the FOB through the vacuum windows due to equipment/alignment limitations. These prohibited the measurement of the power density of the pulse. Two-step calibration was required to obtain the power/power density of the incoming radiation from the raw measurement of the FOB.

The first step is to correct the shape of the frequency response by modifying the amplitude and the phase of the FOB using transform functions. Since the incoming radiation is an ideal pulse, the ideal response is well-known. The ideal response of the amplitude is constant for an ideal pulse. However, the amplitude value of the pulse is not known due to not being able to measure the power density of the pulse. Here, the constant value was decided to be 1 with an arbitrary unit for simplicity (Figure 50, left). The ideal response of the phase is zero for all frequency components (Figure 50, right). By reverting the corrected frequency response to time-series, the result showed a correct shape of the incoming radiation with an arbitrary unit (Figure 51).

The next step is to calibrate the arbitrary unit into the power/power density. This is done with several measurements of a square-wave radiation with known power densities. The measurements are processed with the first step. The signal levels in the arbitrary unit differ with different power densities. A power function is fitted to the data that it converts the arbitrary unit to the power or power density (Figure 52). The R-square of the fit was 0.9998 with a root mean square error of 0.7148 W/m^2.

There were some advantages and disadvantages to the frequency-space calibration. The main advantage is that it can calibrate the FOB correctly in transient regions, where other methods could not. The second advantage is that it can resolve timescales much smaller (up to 30 times) than “time-constant” or the transition time

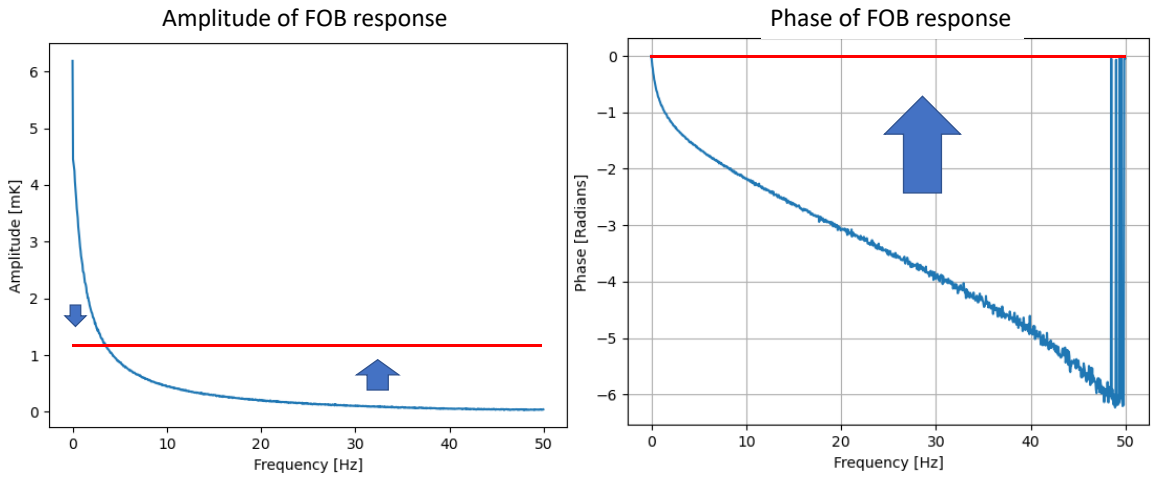

Figure 50 Left: amplitude response of the FOB to an incoming pulse (blue). Right: phase response of the FOB to an incoming pulse (blue). Corrected FOB response assuming an ideal pulse (red). The raw measurement is averaged over 10 data points.

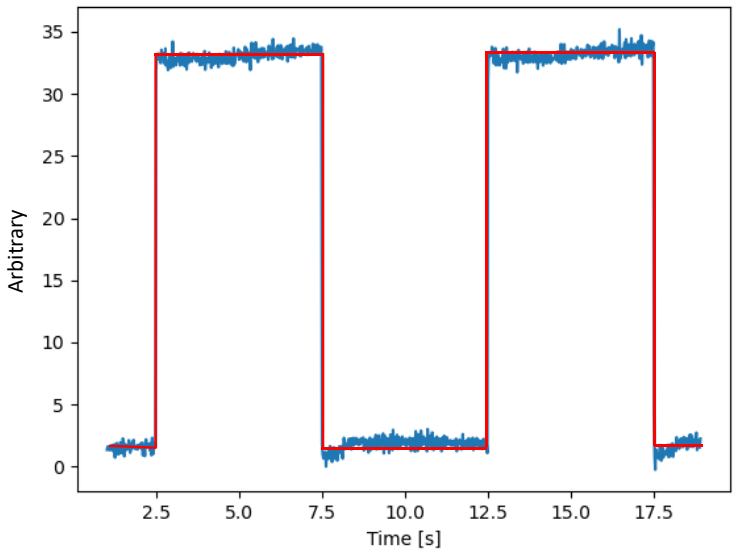

Figure 51 Result of the pulse method (blue). Incoming radiation (red).

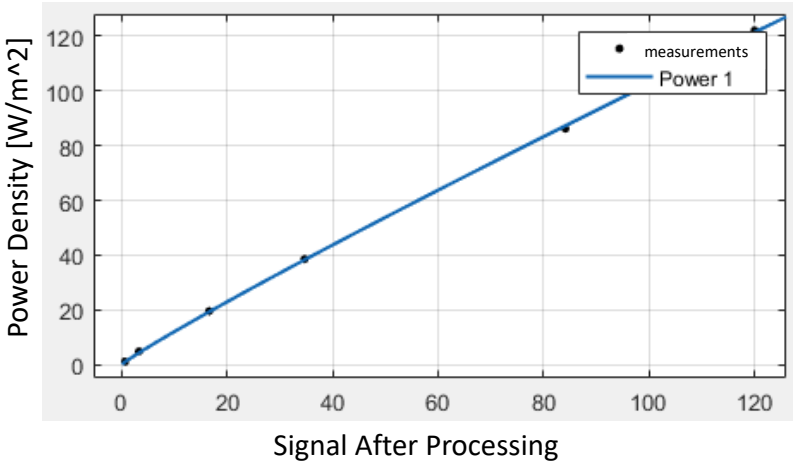

Figure 52 Power function fit (blue) for the calibration data for the power density (black).

(more appropriate since “time-constant” is not constant”). Figure 53 shows an arbitrary shape of an incoming radiation with the time- scale smaller than the transition time with the result of the pulse method. The pulse method was able to resolve the shape near perfectly.

One of the disadvantages is that the noise equivalent power density of the result using the pulse method (0.55 W/m^2) was higher than the reported noise equivalent power density of a resistive bolometer on a benchtop in a noiseless environment (0.2 W/m^2 [62]), although the “apple to apple” comparison is not suitable between resistive bolometer and the FOB due to the calibration methods. Another disadvantage, which was unexpected, was that the noise increased with the power / power density levels. The higher the power density of the incoming radiation, the higher the noise was for the whole measurement (Figure 54). This was thought to be a feature of the method since a testing of a synthetic noiseless signal showed the same result.

Two methods are used to further reduce noise for the frequency-space calibration. The first method is averaging the calibration results. For the discrete method, the frequency response for a specific frequency component is averaged over. For the pulse method, the frequency response of the pulse is averaged with multiple pulses. The averaging showed reduced noise for both. The second method is fitting the response of the amplitude and the phase. This is only available for the pulse method since the discrete method already requires a fitting function. No function could correctly fit the entire response for the amplitude or the phase. It was decided to use the low frequency components as is since they are less noisy. The rest is fit with a fourth order polynomial function (Figure 46). This resulted in reduced noise by about ~38 % (0.55 W/m^2 compared to 0.88 W/m^2).

Single-Channel FOB Demonstration at DIII-D

The single-channel FOB was installed at DIII-D for the first-time plasma testing after all the benchtop testing and calibrations. DIII-D tokamak has preexisting arrays of resistive bolometer (Figure 13), which will be compared with the FOB. Also, as mentioned in the background, DIII-D is a medium sized tokamak that represents a fusion

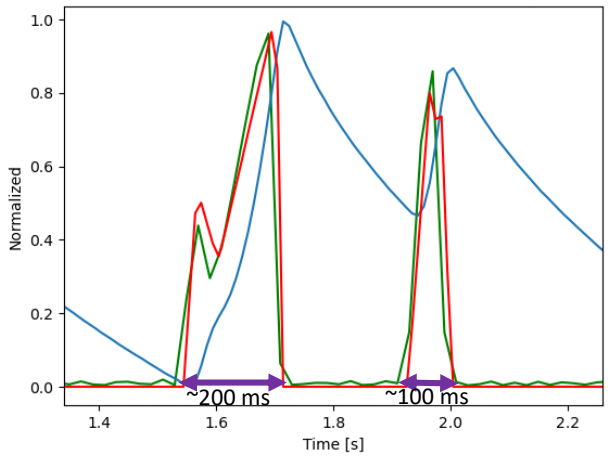

Figure 53 Raw measurements (blue), calibrated measurements (green), incoming radiation (red). The pulse method can resolve arbitrary signal shapes with timescales much smaller than the transition time (~6 seconds).

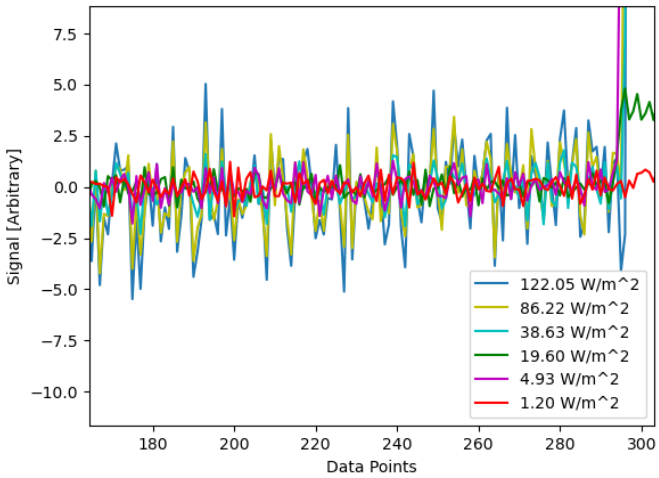

Figure 54 Noise comparisons with different power-density levels. Higher the power density, higher the noise.

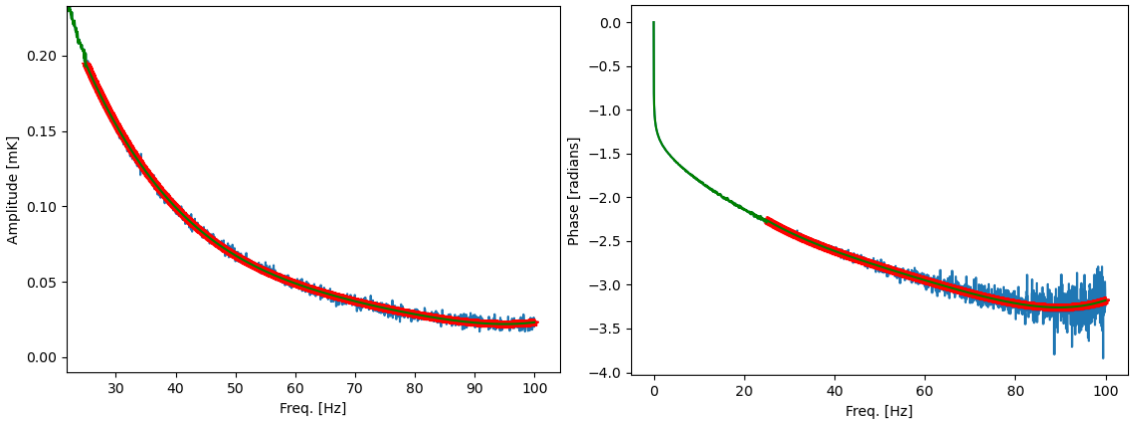

Figure 55 Left: amplitude response (blue) of the FOB with a fit (red). Right: phase response (blue) of the FOB with a fit (red). The low frequency components and the fit combined for noise reduction (green).

environment well. Plasma experiments in a fusion environment are essential to proving the abilities of the FOB. Two major analyses are emphasized to take the experiments as a proof-of-concept. The first is the noise in a fusion environment. The biggest weakness of the resistive bolometer is that it utilizes an electrical circuit for measurements that is prone to electromagnetic interferences, which are severe in a fusion environment. The effects of electromagnetic interferences are increased noise or systematic errors. Since the FOB is theoretically immune to electromagnetic interferences, noise should not increase during DIII-D operations. The second is the comparability of the FOB to the resistive bolometers. Even though the FOB showed good results at the benchtop, it was not tested for a real plasma light that could consist of a very different spectrum compared to the benchtop laser. Especially, the higher energy spectrum like vacuum ultraviolet and X-rays could not be tested in a simple benchtop. As a result, the FOB could react very differently compared to the resistive bolometer, which could be a serious problem for the FOB. Thus, the qualitative and quantitative comparisons of the FOB to the resistive bolometer were performed.

The single-channel FOB chamber was installed at the midplane port of the 285° toroidal location (Figure 56). This was not ideal because the resistive bolometers are located at the R-1 and R+1 ports (Figure 57) and at 45° and 75° toroidal locations. This meant that it is hard to quantitatively compare between the FOB and the resistive bolometers. Also, the port used for the FOB chamber had 18° tilt tangentially. This meant that the viewing cone of the FOB was only partially terminated by the inner wall (Figure 56, left, red lines). This made the quantitative comparison more difficult. The tilt was somewhat offset with a compensating tilt that the viewing cone of the FOB was completely terminated by the inner wall (Figure 56, right, red lines). One advantage present at the installed location was that there was a gate-valve between the DIII-D machine and the FOB vacuum chamber, which made it possible to measure without looking at the plasma light during operations. This was a good way to test the noise level and any abnormal signals measured by FOBs without plasma light confusing the measurements.

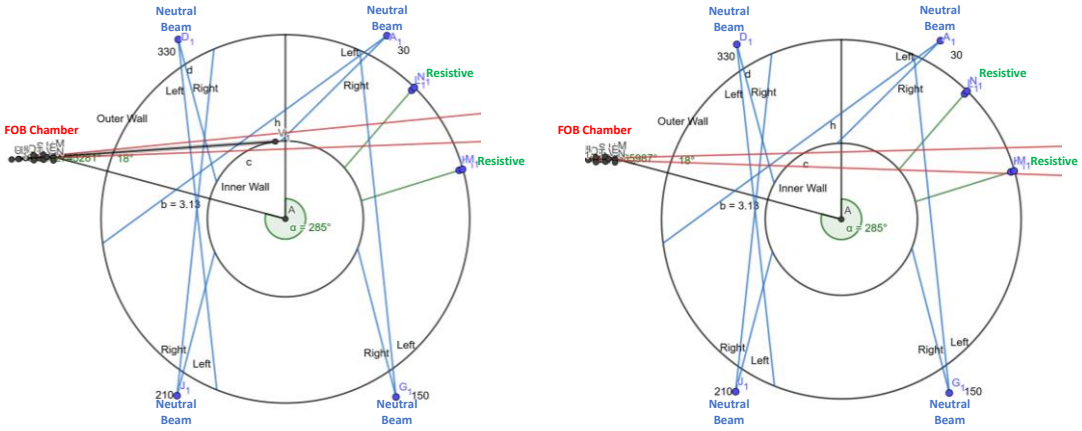

Figure 56 Left: before tilt compensation. Right: after tilt compensation. Red: FOB viewing cone, green: resistive bolometer sightlines, blue: neutral beam injections. Top view.

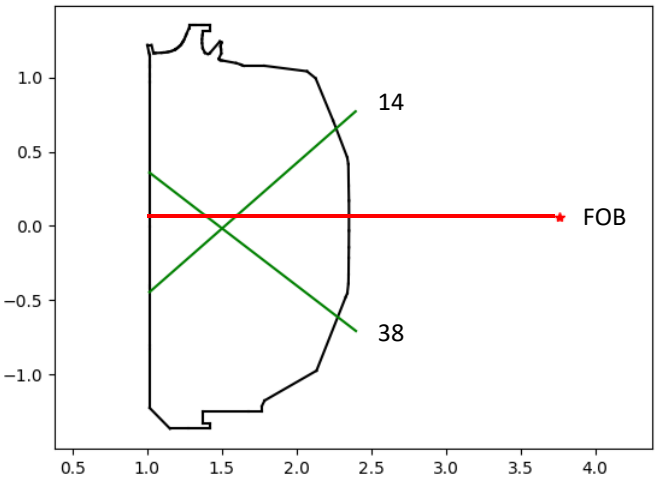

Figure 57 Red: FOB sightline, green: resistive bolometer sightlines. Radial cross-section.

The setup of the fiber optic bolometer is as follows. The measurement FOB and the reference FOB are installed inside the FOB vacuum chamber. The electronic equipment like the SLED light source, the I-MON spectrometer, and the polarization scrambler are positioned inside a remote room away from the fusion environment. This prevents any electromagnetic interferences to the electrical systems from the fusion environment. The major optical components such as CWDM, fiber optic couplers, and attenuators are also inside the remote room. The FOB vacuum chamber is fiber optically connected to the remote room by 100-meter duplex fiber-optic cables. This long connection between a detector and an electronic system is possible due to the nature of fiber optic cables that there is near to no loss in the signal running through the fiber optic cables and no noise pickups, which are difficult for electrical cables.

First, the noise level of both the reference and measurement FOBs were compared during plasma operations with the gate-valve closed to the benchtop results. The benchtop results were 0.30 mK for the reference FOB and 0.39 mK for the measurement FOB. The plasma operation (shot number 187144) results with the gate-valve closed were 0.29 mK for the reference FOB and 0.37 mK for the measurement FOB. Thus, there were no increases in the noise for both FOBs. The theoretical expectation that the FOBs will not suffer electromagnetic interferences due to the nature of the design (no electrical components for the sensor) was validated by this experiment.

Next, the qualitative comparison of the FOB with the resistive bolometers were performed for the single-channel FOB. Since the absolute-value comparison is difficult due to the different installed-locations and different sightlines, the qualitative comparisons were first performed to estimate the FOB performance. The qualitative comparison shows the overall shape of the signal from the plasma light. The channel 14 and channel 38 of the resistive bolometers were averaged. They were crossing the FOB sightline (Figure 57). The results showed that the overall shape of the signal from the FOB was matching well with the signal from the resistive bolometers (Figure 58). This meant that the FOB is measuring what it was supposed to, compared to the resistive bolometers. This was important since the calibration method was completely different and new for the FOB. Also, the qualitative comparisons showed abnormal signals, which

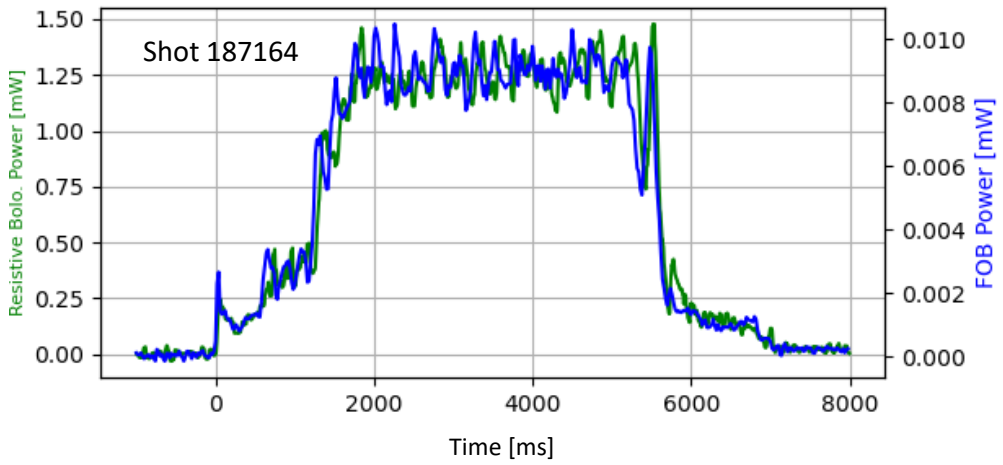

Figure 58 Green: averaged measured power of Ch 14 and 38 resistive bolometers. Blue: measured power of the FOB. The qualitative comparison matched well.

were not present in the resistive bolometers. The first abnormal signal matched the timing of the electron cyclotron heating, and the second abnormal signal matched the neutral beam heating. The third abnormal signal was from the start and the end of a plasma discharge that matched when the plasma is limited at the midplane inner wall.

The ECH of DIII-D heats the plasma using 110 GHz radio frequency (RF) electromagnetic waves [46]. The problem is that the pinhole of the FOB vacuum chamber is big enough that the RF electromagnetic waves pass through the pinhole and are measured by the FOBs. The reference FOB (blocked from plasma radiation) measured signal that matched ECH timing (Figure 59, left). There is no way to distinguish the ECH electromagnetic waves from the plasma light for the measurement FOB. This is a common problem for bolometers used in a fusion environment that the resistive bolometers already implemented measures to block ECH electromagnetic waves. The most common way to mitigate the problem is to install a copper mesh at the pinhole to block RF electromagnetic waves. There was no time to uninstall the FOB vacuum chamber, install a copper mesh, and reinstall the chamber. Thus, the measurements of the FOB during plasma operations with ECH were discarded due to the measurement of ECH electromagnetic waves on the FOBs. However, it was a good experiment to show that FOBs also measure ECH electromagnetic waves like resistive bolometers. Also, it was determined that the signals of the FOBs during ECH were actual ECH electromagnetic waves, not electromagnetic interferences, by closing the gate-valve (Figure 59, right).

Another abnormal signal on the FOB compared to the resistive bolometers from the qualitative comparisons was related to the neutral beam heating. The light emission from collisions of the neutral beams and plasma that is localized in the path of the neutral beam seems to be measured by the FOB due to the overlap of the FOB sightline and the paths (Figure 56). The emission due to the neutral beam collisions with the plasma is, again, not separable from the plasma emission and localized that the resistive bolometers do not measure the emission. The biggest problem of the four neutral beam injections in DIII-D was the 330° beams. However, unlike the ECH, the plasma operations with the neutral beam injections could not be ignored entirely because almost all the plasma shots include the neutral beam injections. Only a handful of the data without the neutral beam

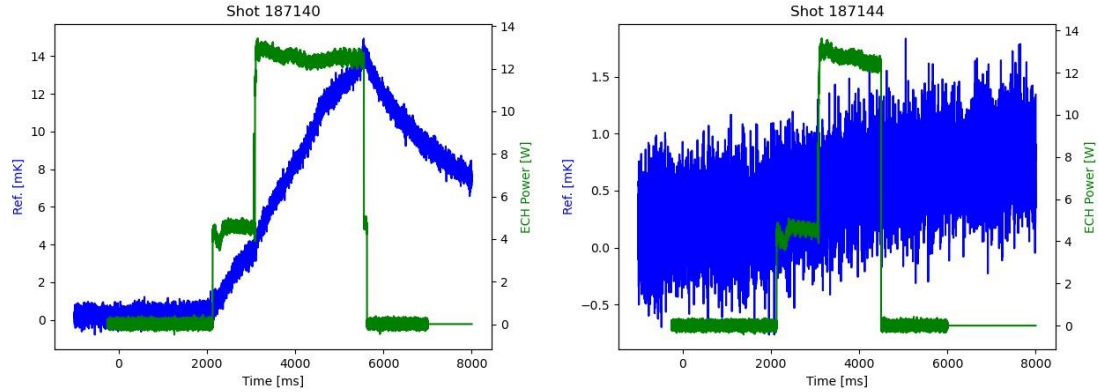

Figure 59 Left: reference bolometer signal (blue) and ECH power (green) with the gate valve opened. Right: reference bolometer signal (blue) and ECH power (green) with the gate valve closed.

injections, especially 330° beams, remained for analyses. After the tilt compensation, there were no plasma shots without the ECH and the neutral beam injections. Thus, the plasma operations with the neutral beam injections and without the ECH (more deleterious to the analysis), were considered for absolute comparisons for the data after the tilt compensation.

The final abnormal signal that was shown in the qualitative comparison with the resistive bolometers matched the plasma being limited by the inner wall at the midplane. DIII-D utilizes the limited plasma during the startup of the plasma discharge and the termination of the plasma discharge. As it can be seen from Figure 60, the plasma core inside the last closed flux surface is intercepted by the inner wall at the midplane. The plasma is interacting with the inner wall that it is creating the plasma radiation like near the divertor. Also, the material is heating up due to the plasma that will be emitting photons. Both interactions are creating emissions that are being measured by the FOB, which is not being measured by the resistive bolometers chosen to be compared due to the sightlines (Figure 60). Other bolometers could be used, but they will only be focusing on the midplane and not crossing the FOB sightline that it will be a worse comparison. Also, they have shorter path lengths (shorter than the FOB). Thus, the start and the end of the discharge are ignored for comparisons.

The absolute value comparisons (the quantitative comparisons) between the FOB and the resistive bolometers were done with three methods. The first method was comparing the plasma brightness measured by the FOB and the resistive bolometers with similar path lengths directly. This method was acceptable since the plasma brightness is a plasma property that is not affected by the locations or dimensions of the bolometers. Although the sightlines for the FOB and the resistive bolometers are different, the path lengths are similar (FOB: 2.18m, Ch. 14: 2.29m, Ch. 38: 2.18m), and the sightlines are passing less localized plasma such that they are comparable. The equation used for the plasma brightness calculation assuming the line-approximation [63] is,

$$Brightness = \int \epsilon dl = \frac{4\pi {l_{s,p}}^2 P}{cos^2(\theta) A_s A_p}$$

ϵ: Plasma emissivity

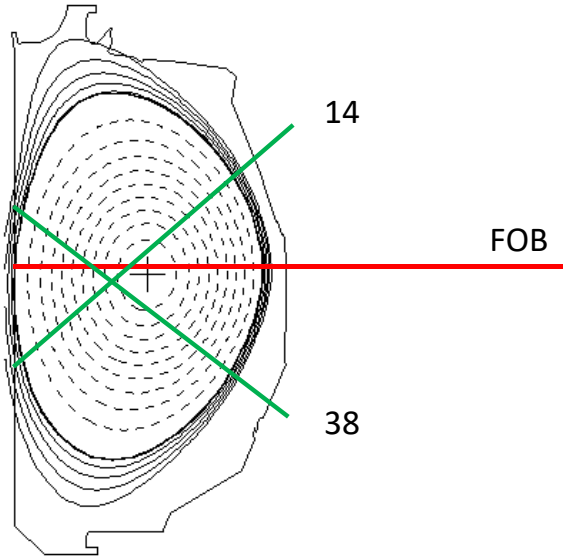

Figure 60 EFIT reconstruction of magnetic configuration during a termination of plasma. Red: FOB sightline, green: resistive bolometer (Ch. 14 and 38) sightlines.

$l_{s,p}$: Distance between the detector and the pinhole

P: Power measured by a bolometer

θ: Misalignment angle between the line of sight and the surface of the sensor

A_s: Area of the detector and A_p: area of the pinhole

The misalignments for the resistive bolometer and the FOB are ignored (0°) since they are small. However, this method was only possible after the tilt compensation.

The second method was a simple and fast integration of the tomographic reconstruction of the resistive bolometers. The FOB sightlines are approximated as a line, which is acceptable since the pinhole is small enough and the distance between the FOB and the pinhole is large enough [64]. The tomographic reconstructions of the resistive bolometer are done with GAPROFILES of DIII-D [48]. The result of the reconstruction is 65 by 65 pixelated emissivity of the plasma in a radial cross-section. The integration was done in Interactive Data Language (IDL). Since the location of the FOB is known radially, the pixels that correspond to the sightline are selected. Then, the length of the sightline for each pixel is calculated and multiplied to the emissivity of the pixel. Adding the multiplied values of all the selected pixels will result in an approximate brightness of the plasma measured by the FOB. Again, this method is only useful after the tilt compensation. However, this method was essential in doing a "sanity" check for the next method since it is a simple method that one can check every step of the calculations.

The third method is more complex integration of the tomographic reconstructions from the resistive bolometers using CHERAB. The CHERAB DIII-D package is ready (the next section). Two other packages were developed for the method. The package for the single-channel FOB simulates a measurement by the FOB from a tomographic reconstruction using the location and the dimensions of the installed FOB setup. The package for importing the tomographic reconstruction is used to have the plasma emissivity imported to CHERAB for the FOB to measure. The 65 by 65 pixels from the tomographic reconstruction are imported as a mesh with emissivity parameters. Assuming a toroidal symmetry, the mesh is made into 3D that is ready for a measurement in CHERAB. The advantage of using CHERAB is that the line-approximation of the simple integration is not needed. The third method will integrate the emissivity for the

entire viewing cone (3D) of the FOB so that the method makes it possible to perform the quantitative comparisons for the data before the tilt compensation. The disadvantage over the simple integration was that this method requires more time to obtain a result.

The plasma brightness measurement of the FOB after the tilt compensation showed a good agreement with the resistive bolometers except for the region (2000 to 5000 ms) where 330° neutral beam is injected (Figure 61). The FOB data is averaged over to be 25 Hz (40ms between data points) to match the resistive bolometer results (averaged over 40ms). This shows that the FOB is comparable to the resistive bolometers. Also, the simple integration method matched with the averaged plasma brightness of the resistive bolometers and the FOB. This confirms that the method is working by comparing with the resistive bolometer. In addition, the FOB is measuring what it was supposed to measure compared to the simple integration method with the correct sightline. However, the start (near 0 ms) and the end (~7000 to ~7500 ms) of the plasma discharge did not match due to the midplane limited plasma. Even the tomographic reconstructions were not working well (bad fits) for the regions with the midplane limited plasma. Unfortunately, there were only two days of operation after the tilt compensation. Also, the experiments for the two days were operated with the midplane limited plasma throughout the entire plasma discharge. Only a few of the shots were available for the analyses. Even then, there were no shots without ECH and 330° neutral beam injection. This was the reason why the CHERAB integration method was required for better comparisons.

From a plasma discharge after the tilt compensation, the CHERAB integration method was validated with the simple integration method (Figure 61). The FOB measurements before the tilt compensation, where there were data without the ECH and 330° neutral beam injections, were compared with the results from the CHERAB method. The results from the CHERAB integration method and the FOB measurements matched well (Figure 62). This confirmed again that the FOB is comparable to the resistive bolometers. These results were cleaner due to the absence of the 330° neutral beam injections. However, the start (near 0 ms) and the end (after ~7000 ms) of the discharge were still ignored due to the bad fits from the tomographic reconstructions.

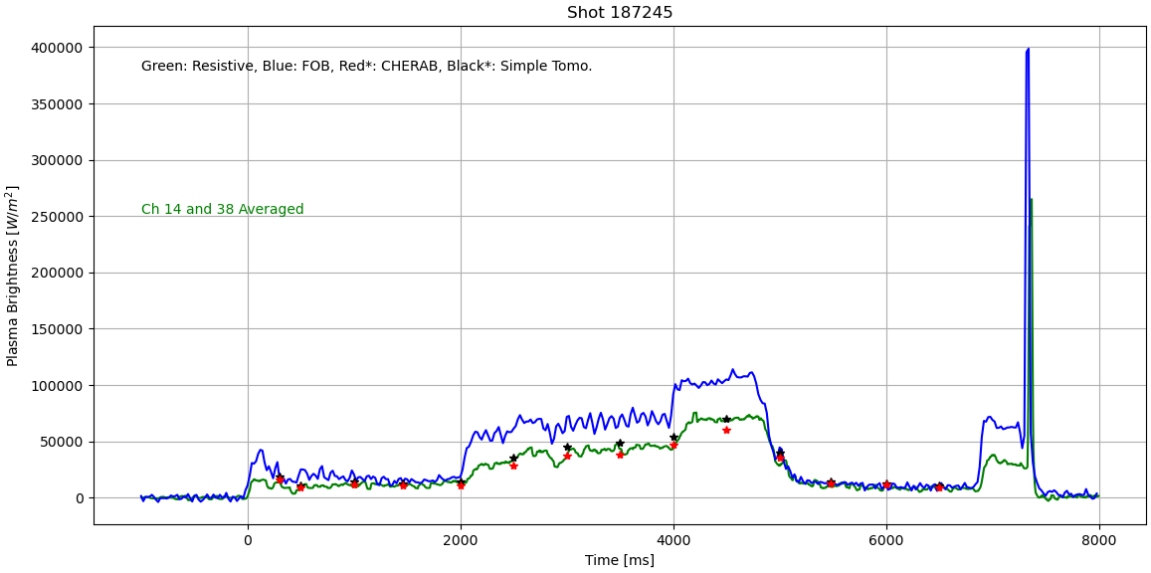

Figure 61 Plasma brightness measurements after the tilt compensation. Green: Ch. 14 and 38 resistive bolometers averaged, blue: FOB, red*: CHERAB integration, black*: simple integration. 330° neutral beam injection from 2000 to 5000 ms.

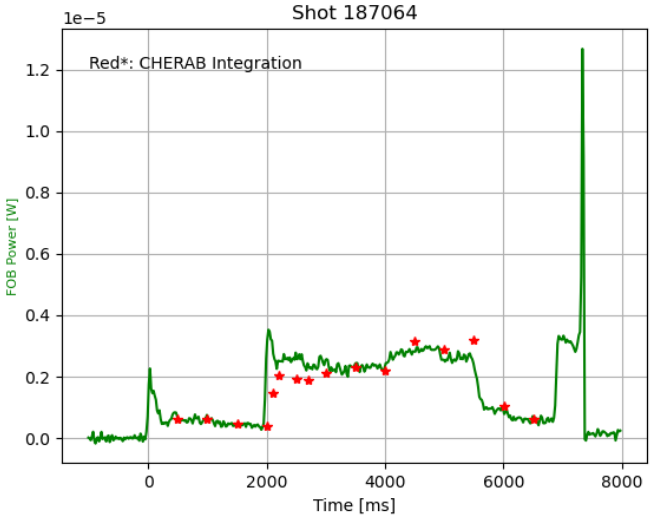

Figure 62 Measured power of the FOB (green) before the tilt compensation. CHERAB integration (red *) matched well with the measurement.

Next, the noise equivalent power density of the FOB and the resistive bolometers were compared since the credibility and the comparability are confirmed from the previous analyses. The resistive bolometers are affected by electromagnetic interferences during a plasma operation that increases noise level (Figure 63). Due to this fact, the FOB (0.40 ± 0.06 W/m^2) resulted in lower noise equivalent power densities compared to the resistive bolometer (2.14 ± 0.21 W/m^2), although the benchtop noiseless results reported for the resistive bolometers [62] were lower than the FOB. However, the noise equivalent plasma brightness was higher for the FOB (~2 times). Also, one thing to note is that the resistive bolometers at DIII-D were old (deployed in 1995 [48]).

The time resolution of the FOB measurements was increased from 25 Hz to 200 Hz to see if the FOB can resolve the plasma radiation at a higher frequency. For the analysis, the frequency response of the pulse is fitted at a higher frequency (the previous section). The results showed that the FOB can resolve the plasma signal up to 200 Hz (Figure 64). Noise increased to 5.44 W/m^2 from 0.32 W/m^2 (25 Hz). Further increasing the time-resolution was possible up to 1000Hz (the limit of the measurement). However, the increase in the noise seemed too much for any advantage. The publication for the results of these demonstration of the single-channel FOB system on DIII-D is under review.

Three interesting technical details were identified during the DIII-D testing. First, there was 290 Hz frequency noise for the measurement FOB (Figure 65). The Fourier transform was done for -1 to 0 seconds of plasma operation where there was no plasma (only noise components). However, the 290 Hz component was not present in the reference FOB, which showed that it was not due to EMI. In addition, the 290 Hz frequency component in the measurement FOB was present in data at the bench (Figure 66). Again, it was only present in the measurement FOB. The 290 Hz component was a problem because the noise level for the measurement FOB was higher than the reference level (Table 7). It was confirmed that the 290 Hz noise component was due to the combination of 1550 nm CWDM, specific attenuator, and specific FOB by testing with different combinations of the components. Changing the attenuator removed the 290 Hz component and reduced the noise level of the measurement FOB to the reference level.

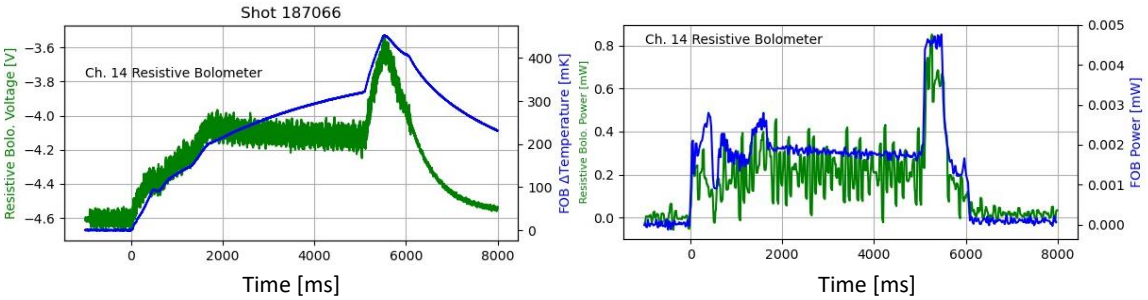

Figure 63 Left: raw measurements of the FOB (blue) and the resistive bolometer (green). Right: raw measurements of FOB (blue) and the resistive bolometer (green). The resistive bolometer demonstrates a higher level of noise compared to the FOB.

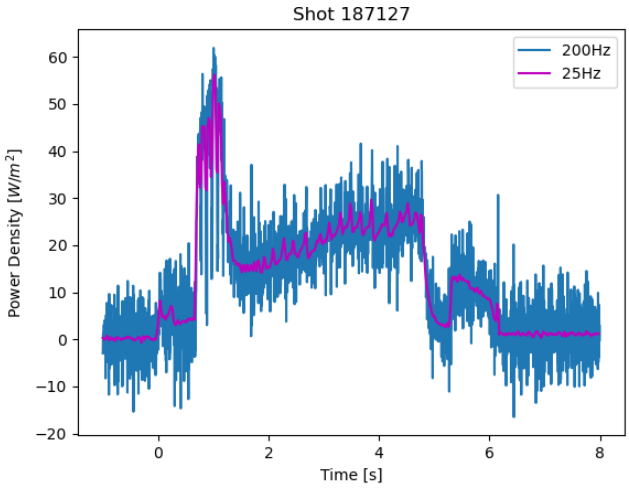

Figure 64 Increased time resolution (200Hz, blue) for the FOB compared to 25 Hz (green). The signal is resolvable but displayed increased noise.

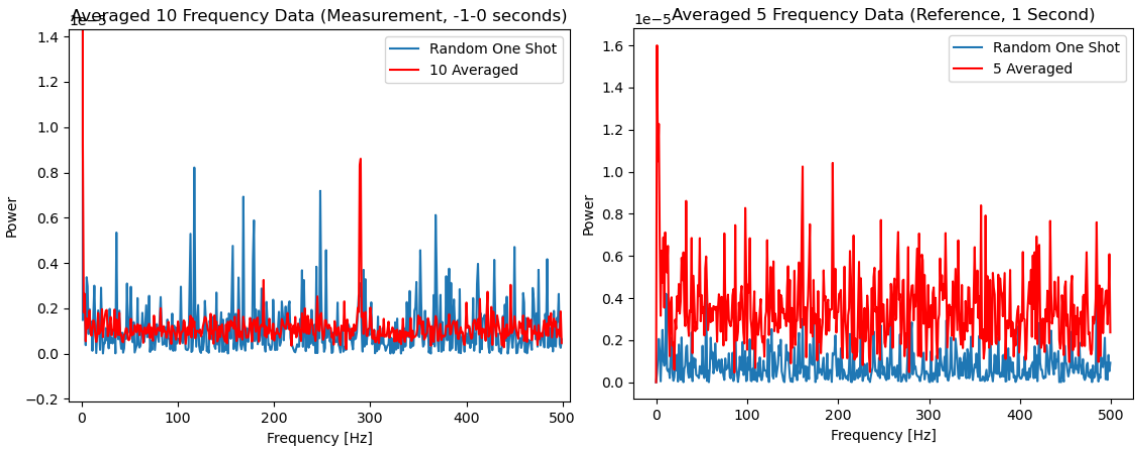

Figure 65 Left: measurement FOB frequency analysis result (blue - random one shot, red – 10 shots averaged) at DIII-D. ~290 Hz frequency component from noise can be seen. Right: reference FOB frequency analysis result (blue - random one shot, red – 10 shots averaged) at DIII-D.

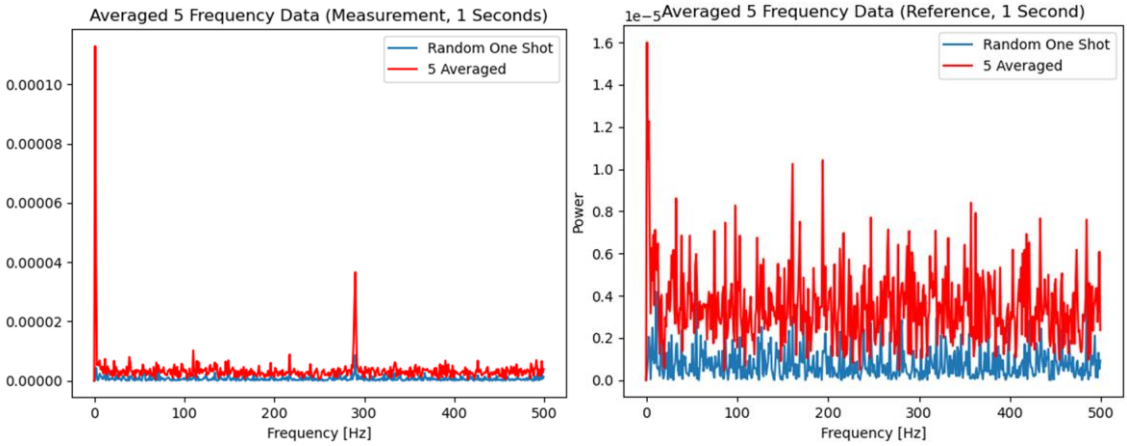

Figure 66 Left: measurement FOB frequency analysis result (blue - random one shot, red – 5 results averaged) at the bench. ~290 Hz frequency component from noise can be seen. Right: reference FOB frequency analysis result (blue - random one shot, red – 5 results averaged) at the bench.

Table 7 Signal Variation Comparison of the FOBS on the Benchtop and on DIII-D

	Measurement Signal Variation (mK)	Reference Signal Variation (mK)
Benchtop	0.381±0.007	0.315±0.008
Shot 187144[a]	0.395	0.304
Before Plasma[b]	0.392±0.031	0.286±0.026

[a] the gate-valve between DIII-D and the FOB chamber was closed
[b] calculated from -500ms to 0ms (right before the start of a plasma)

The second finding was that the overall signal level at the spectrometer decreased as the time passed after the installation (Figure 67). This phenomenon happened for both the reference (Figure 68) and the measurement FOBs. The significant signal jump after 6/22/2021 was due to the reconnection and the adjustment of the attenuators. This could have been a serious problem if it was due to ionizing radiation damage (for instance, neutron). The peak signal degradation was overlapped with the negative of the cumulative density times injected power (Figure 69), which is a good proxy for the high energy photons, and the negative of the cumulative neutron counts (Figure 70). The negative was to show a possible relation to the degradation. The cumulative calculation was started over after 6/22/2021 for both cases. Although both cases seemed to follow the signal degradation in the FOBs, there were obvious disagreement in the trend where the FOB signal counts jumped up after a day (6/17/2021, 6/23/2021) or jumped down and recovered during a day (6/22/2021). Also, the slopes of the cumulative measurements did not match the slopes of the signal degradations. For instance, although the signal degradation was minimal on the day of 6/23/2021, whereas the slopes of the cumulative measurement was like the day of 6/17/2021 where the signal degradation was significant. In addition, the degradation level was much higher than the radiation induced attenuation reported by different experiments [76]. These observations showed that the signal degradations might not be due to the damage from ionizing radiations.

One thing that was noticed from the benchtop experiments was that the attenuators sometimes jump in their attenuation when vibrations were present or physical contacts were made. This was thought to be due to the mechanical operating principle of the attenuators. Mechanically turning the knob on the attenuators adjust the attenuations. So, vibrations, physical contacts, or gravity could change the attenuation in theory. The peak signal level measurement was done on the bench for days without any adjustments to see if the degradation was present. The results showed that the significant signal decrease happed on the bench as well (Figure 71). Although the trend was not a perfect match with the DIII-D testing case, it was shown that the significant signal decrease could happen at the bench where there were no ionizing radiation present. There were no noticeable vibrations or physical contact at the bench, which suggested that the gravity

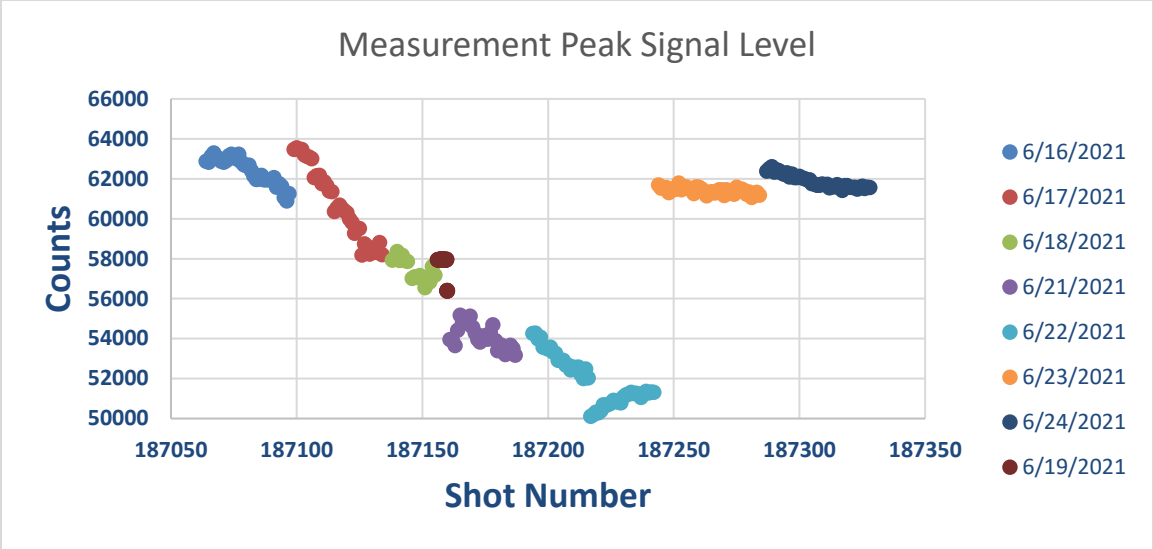

Figure 67 Change in the peak signal level on the measurement FOB during DIII-D testing. The peak signal level decreased. Reconnected and adjusted after 6/22/2021. Error bars are present, but too small to be visible.

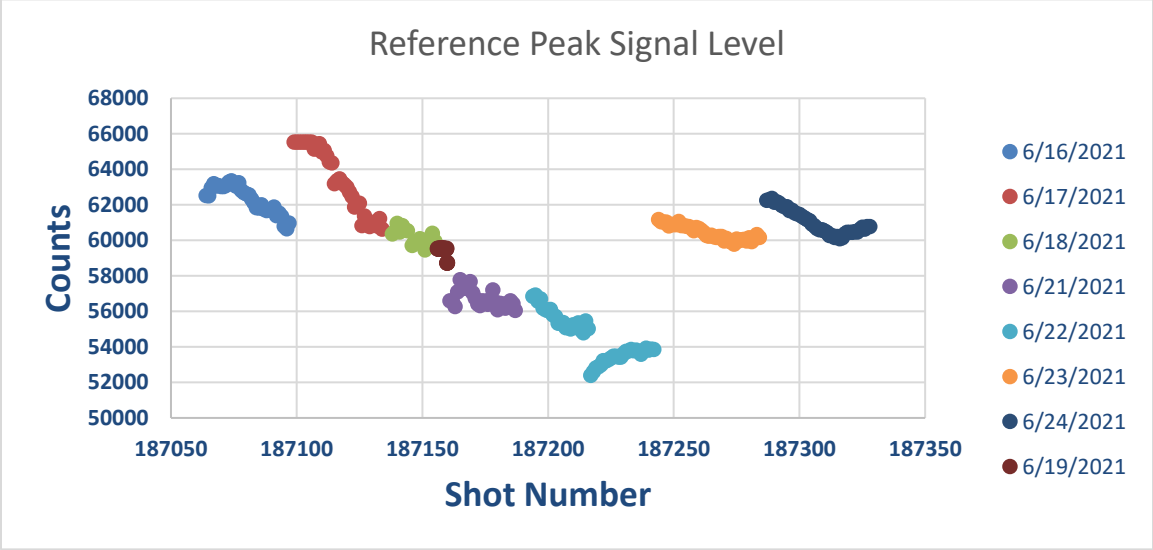

Figure 68 Change in the peak signal level on the reference FOB during DIII-D testing. The decreasing trend was like the measurement FOB suggesting not EMI. Reconnected and adjusted after 6/22/2021. Error bars are present, but too small to be visible

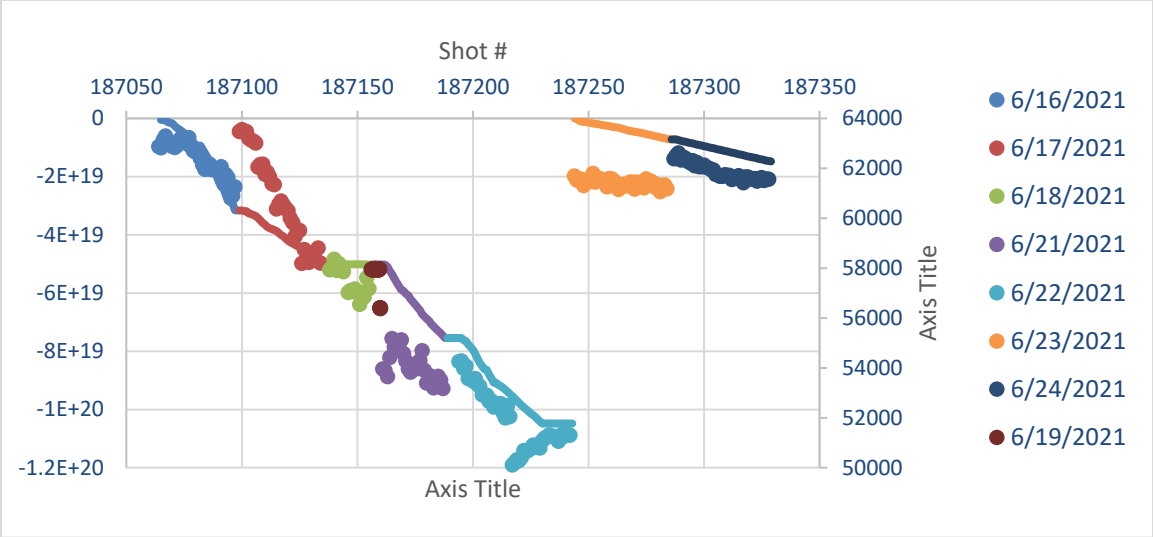

Figure 69 Change in the peak signal level (right Y-axis, dotted, [count]) on the measurement FOB during DIII-D testing overlayed with the negative of the cumulative density * injected power (left Y-axis, line, [kW/m^3]). The cumulative calculation was reset after 6/22/2021.

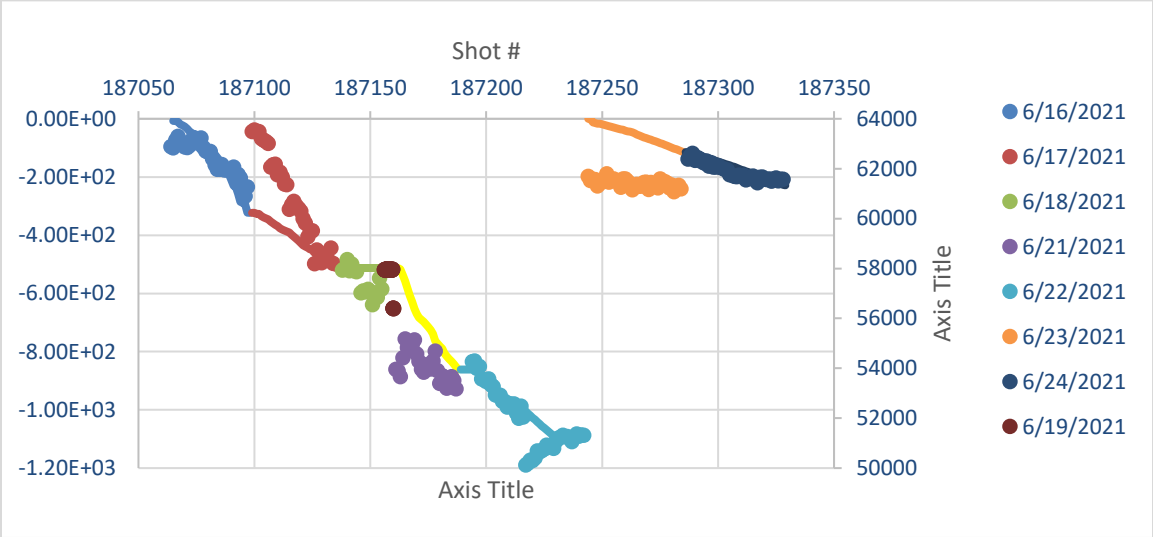

Figure 70 Change in the peak signal level (right Y-axis, dotted, [count]) on the measurement FOB during DIII-D testing overlayed with the negative of the cumulative neutron counts (left Y-axis, line, [count]). The cumulative calculation was reset after 6/22/2021.

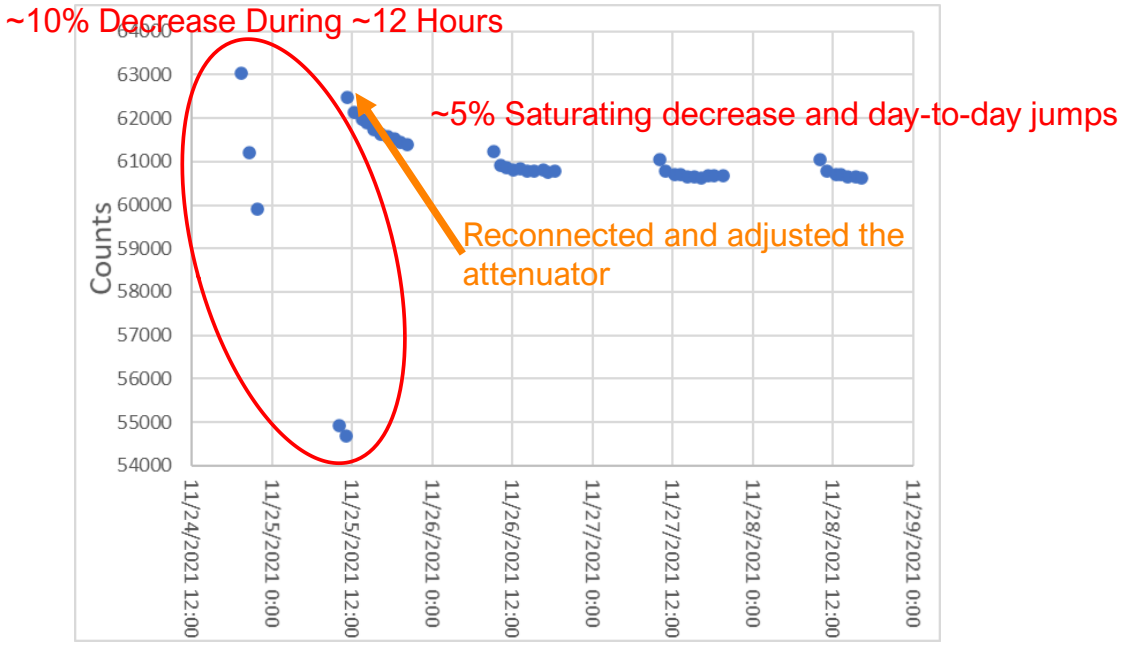

Figure 71 Decreasing signal measurements at the bench. There were no ionizing radiation present unlike the DIII-D testing, but significant peak signal decrease was present at the bench.

could have adjusted the mechanical components of the attenuators. However, it was not possible to pinpoint the problem to the attenuators. Nevertheless, removing the attenuator eliminated the signal decrease (Figure 72) and other components were not suspected of a quick decrease in signal. One thing to note is that the change saturated after a couple of days. It might be possible to setup the system early before an implementation to get the signal level to saturate or a different attenuator could remove the problem. The signal level jump-up at DIII-D after a day was due to the turning off the light source at the end of a day and turning it back on in the morning. The constant operation for 4 days showed that the day-to-day jumps were not present (Figure 72).

CHERAB and Code Development

CHERAB is a python library for forward modelling diagnostics and simulating plasma emissions [65]. CHERAB utilizes a ray-tracing engine called Raysect. In other words, the plasma emission is calculated through raytracing, and the materials/detectors are calculated through mesh. CHERAB is inherently 3D, which is important for complex machine structures and sightlines for a bolometer. Also, thanks to the previous features, CHERAB simulates a bolometer measurement with a full viewing cone rather than with a line-approximation.

A couple of CHERAB packages were developed for FOB purposes. The first essential package was the DIII-D machine package. The second package was the DIII-D resistive bolometer package. The third package was for importing UEDGE results for plasma emissions. The final package was for designing 2D imaging FOB arrays.

The DIII-D machine package requires two parts: an outline and a mesh. The outline is a radial cross-section of the DIII-D machine (Figure 73, left) that act as a mask to exclude CHERAB objects like plasma species, emissive objects, etc. outside of the outline. The mesh is an interacting surface (machine surface) for photons. A Step file of the entire DIII-D machine with the port structures and the wall tiles was used for the mesh. The file is converted to an Obj file due to the limitation of Raysect. Also, the ports were elongated to the outside to accommodate any diagnostics that could be further away from the machine (Figure 73, right). This was essential since the single-channel FOB was

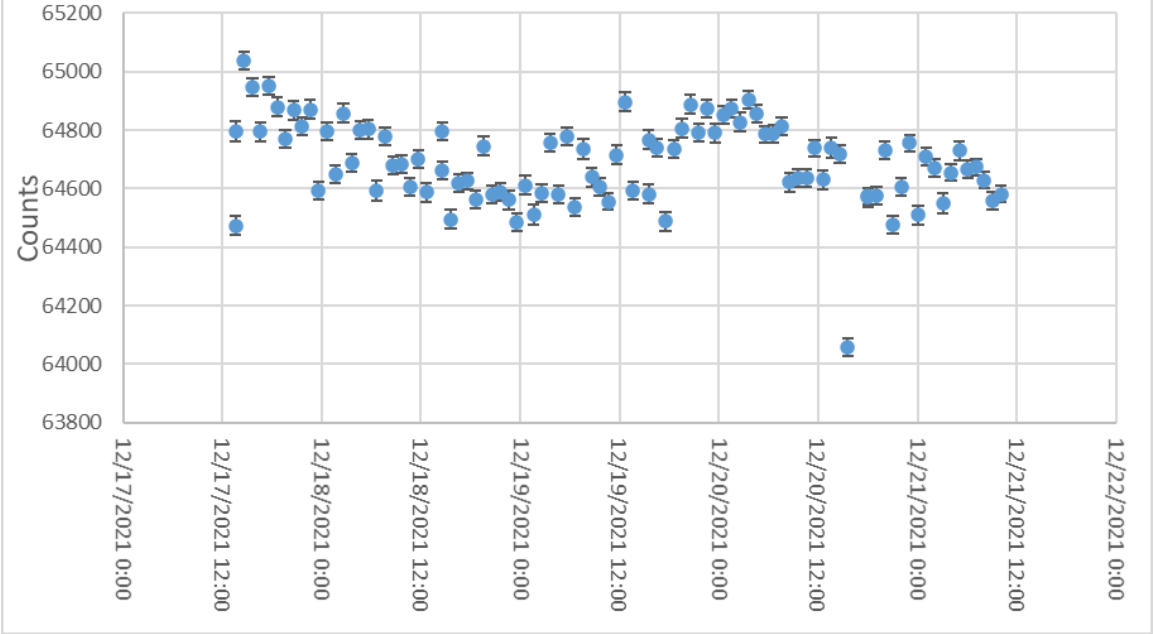

Figure 72 No signal decrease or day-to-day jumps for the constant operations for 4 days without an attenuator.

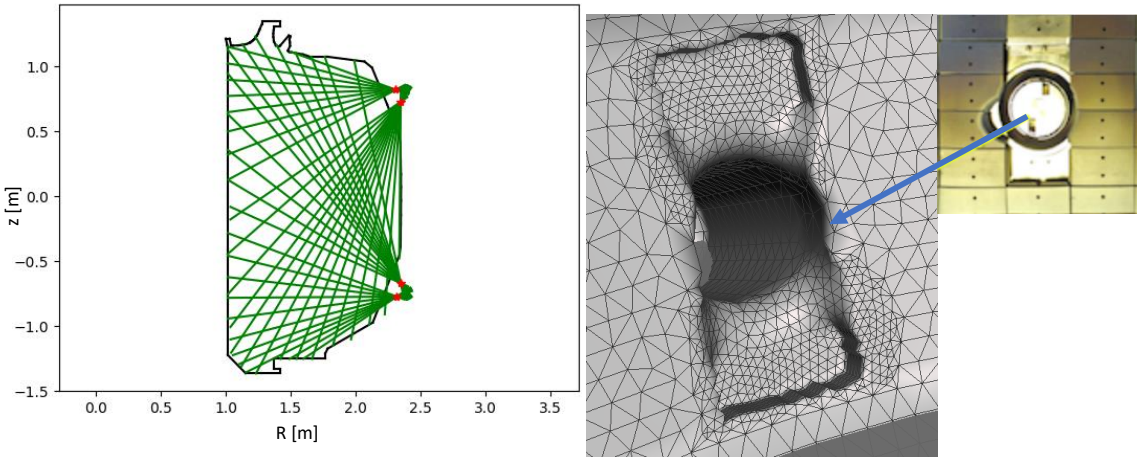

Figure 73 Left: DIII-D resistive bolometer in CHERAB. Right: mesh carved to match the removed wall plate.

installed farther than resistive bolometers. The material property of the mesh was set to "completely absorbing" since the walls of DIII-D is mostly carbon. Carbon made it acceptable to estimate that the plasma emission will be completely absorbed rather than reflected.

The package for the DIII-D resistive bolometers will be used for comparing performances of designs for 2D imaging FOB arrays to the preexisting resistive bolometer arrays. Detailed dimensions and locations of the resistive bolometers were provided by Dr. Leonard and Dr. Moser from DIII-D National Fusion Facility. There are four pinhole cameras with individual pinholes for the resistive bolometer. Therefore, four separate pinhole-camera setups were built into the package with different pinhole sizes, the number of resistive bolometers, and locations/angles (Figure 73, left). Also, the DIII-D machine file for the mesh had to be modified to have correct sightlines for the resistive bolometers. The file did not consider some of the wall plates removed to avoid obstructions, which was the case for the resistive bolometer (Figure 73, right). With the package and a proper emission inside CHERAB, the measurements of the resistive bolometer can be simulated such that the measured power of each resistive bolometer is produced as a result.

The UEDGE package is for importing plasma parameters or emission parameters of UEDGE simulations into CHERAB. UEDGE is a 2D edge-plasma transport code that simulates plasma density, velocity along the magnetic field, electron temperature, ion temperature, electrostatic potential, and emissivity with its own 2D mesh [66]. CHERAB can use the results of UEDGE to simulate plasma emissions that will be measured by bolometers. First, the 2D edge-plasma mesh is imported to CHERAB. Next, the plasma density (plasma species), electron temperature, and ion temperature are assigned to each mesh pixel. Then, the toroidal symmetry is enforced to make the parameters three-dimensional. Finally, the plasma emission is simulated using open-ADAS [74] that will be measured by bolometers. Conversely, the emissivity from UDEGE can be assigned to the mesh pixels rather than the plasma parameters. Again, 2D mesh becomes 3D using the toroidal symmetry. CHERAB can simulate a measurement of a bolometer using only the emissivity data. A comparison of importing plasma parameters and the emissivity is

shown in Figure 74. Higher emissivity for CHERAB compared to UEDGE is due to the different atomic data used for UEDGE (internal [75]) and CHERAB (open-ADAS) to simulate the emission.

The design package for 2D imaging FOB array creates an artificial array using various parameters and measures a given emission. The design consists of a pinhole camera with multiple FOBs. The location of the pinhole camera is a free parameter with three variable (x, y, z) that can be anywhere within any port of DIII-D. Also, there are radial and tangential angles of the pinhole camera to tilt the camera to look at a specific location. In addition, there are the pinhole size (radius), FOB size (radius), distance between the pinhole and the center of the FOB array. The array is divided into subarrays consisting of four FOBs at the edges of a square. Thus, there are the distance between the FOBs within a subarray and the distance between the center of the subarrays. Finally, the number of the FOBs can be adjusted, but it needs to be an even number that will be an integer when it is square rooted. For instance, 36 FOBs (6 by 6) and 64 FOBs (8 by 8) are acceptable. These limitations are not necessary, but the preliminary design was a square array with square subarrays, and the limitation makes the design simpler.

In addition, many tomographic reconstruction codes were developed that can be used with a result from a design that is simulated by CHERAB. Four methods are coded for testing/comparing designs. A regularization is included to alleviate the ill-posed problem. Other than the first method, the regularization is a simple one that smooths the four nearest neighbors.

The first inversion method is a pseudoinversion with Tikhonov regularization, which is the simplest inversion method. The Tikhonov regularization is required due to the singular matrix problem. The equation used is,

$$Emi = (W^T W + \alpha I) W^T P$$

Emi: Emissivity matrix

W: Weight matrix

I: Identity matrix with the size of the grid

P: Vector for FOB measurements

α is adjusted to fix the singular matrix problem.

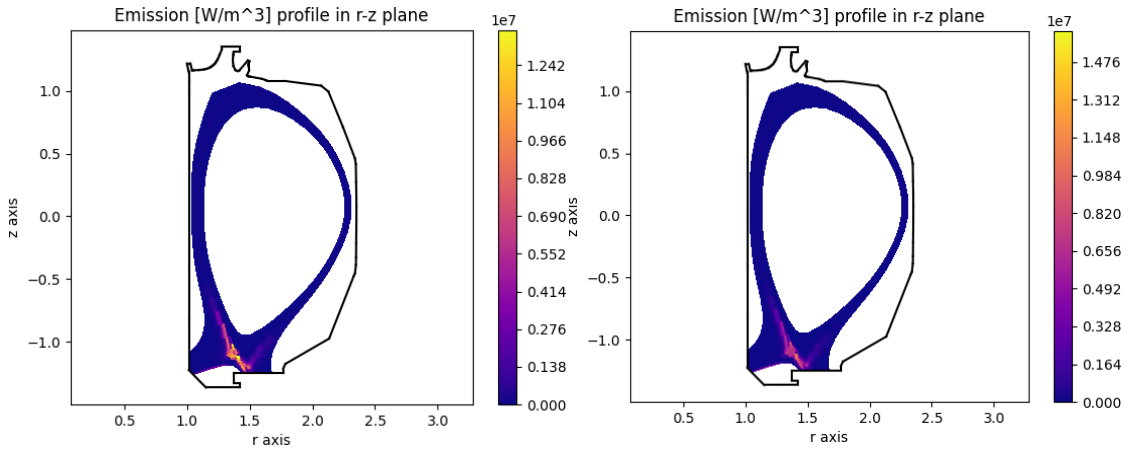

Figure 74 Left: emission profile simulated using UEDGE plasma parameters in CHERAB. Right: emission profile using UEDGE emissivity data in CHERAB. Differences due to different atomic data used for CHERAB and UEDGE for emission.

The next inversion method is Simultaneous Algebraic Reconstruction Technique (SART). SART is an iterative inversion method that simultaneously applies the error correction terms for every iteration [67]. Each grid emissivity is corrected using the equation,

$$Emi_a^{i+1} = Emi_a^i + \frac{1}{W_{tot,a}}\left[\sum_{k=0}^{N_d} \frac{W_{k,a}}{W_{k,tot}}\left(P_k - \hat{P}_k\right)\right]$$

Emi_a^i: Emissivity of a specific grid at i th iterations

$W_{k,a}$: The ray length of a specific FOB in that grid

$W_{tot,a} = \sum_{k=0}^{N_d} W_{k,a}$: The sum of the effective ray lengths crossing that grid

$W_{k,tot} = \sum_{a=0}^{N_g} W_{k,a}$: The total ray length of a specific FOB

N_d: Number of FOBs, N_g: number of the grid pixels

P_k: The power measurement of the specific FOB

$\hat{P}_k$: The forward modelled power of the specific FOB

The error between the measurement and the forward modelled power is weighted to correct the emissivity term. Also, any negative emissivity is corrected to 0 as a constraint. The method is tested with or without the regularization of four nearest neighbor.

The next inversion method is Non-Negative Least Square (NNLS). NNLS is another iterative inversion method that is a least squares problem with a constraint that the emissivity cannot be negative. The algorithm used for the inversion method is from [68] (Appendix 1). Again, the method is tested with or without the regularization of four nearest neighbor. The last method is Maximum Likelihood (ML) reconstruction method. ML estimation is another iterative method that maximizes the likelihood function over the parameter space [69]. The advantage of the ML method over other methods is that variances for the result can be calculated [70]. The error values of a tomographic reconstruction will be crucial for analyses of the plasma radiation structure that need to be more than visual inspections. The variance calculations are not yet implemented in the code. Again, the method is tested with or without the regularization of four nearest neighbor.

An example design of 2D imaging FOB array was used to compare each method. The array was 6 by 6 FOBs with a location shown in Figure 75. The reconstruction grid is 20 by 20 grid near the divertor region with a phantom emission. The phantom emission is a circular emission with a uniform emissivity of 3.5 MW/m^3 (Figure 76). CHERAB calculates total sensitivities of the grid for the design, which are the weight matrix in the inversion calculations There are couple of comparison parameters. The first parameter is an error value calculated between simulated FOB measurements and back-calculated measurements from the tomographic reconstructions. The second parameter is the total radiated power in the grid. The phantom value is 1.12 MW. The last parameter is an error value (root mean square error (RMSE)) calculated from the grid emissivity between the phantom and the inversion. The results show that the simple inversion is the worst for most of the parameters as expected (Table 8). Other methods showed advantages and disadvantages in parameters. Also, the regularization result in higher error in FOBs, but lower error in the total power and the grid emissivity error.

The grid is divided into four sections (inner, outer, core, and private regions) to compare separately (Figure 76). The values for each section are compared between the phantom and the inversions. The results shows that the regularized ML method is the best for the sectional comparison (Table 9). However, the results of the tomographic reconstruction show that the regularized NNLS is the best visually (Figure 77). The inversion back-calculated FOB measurements look all very good except for the simple inversion (Figure 77).

Finally, the design of the FOB array and the resistive bolometers were compared for the grid (Figure 78, left) with the regularized NNLS method. The phantom emission consisted of three circular emissions that are 0.05-, 0.08-, and 0.1-meter radii and have 3.5 W/m^3 emissivity (Figure 78, right). The same comparison parameters were used to evaluate the design compared to the resistive bolometers. The results showed that the FOB design is better in almost every parameter (Table 10 and 11) as expected due to more sightlines. Also, the emissivity profiles using the regularized NNLS method show that the FOB design is much better visually compared to the resistive bolometers (Figure 79).

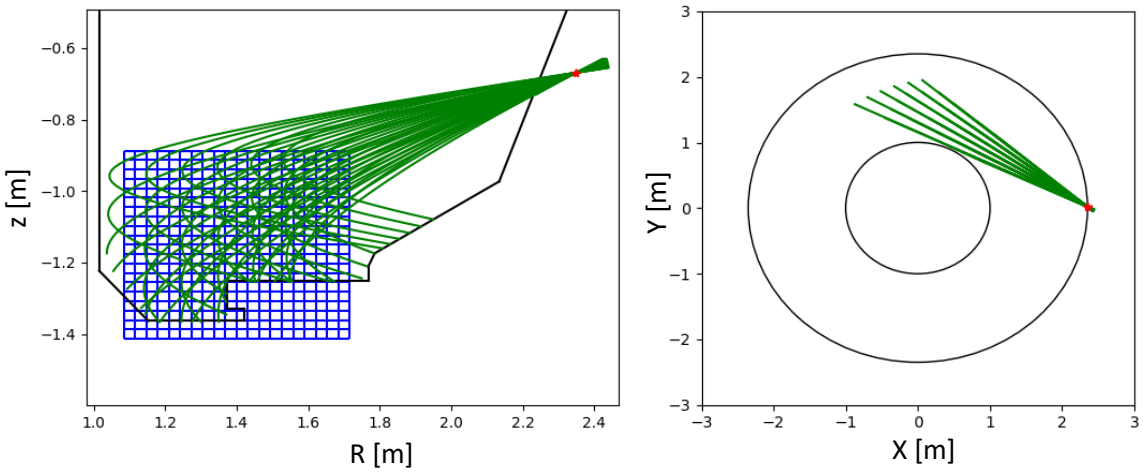

Figure 75 Left: radial view of sightlines (green) of the example 2D imaging FOB array. Right: top view of the sightlines (green). The red star is the pinhole location.

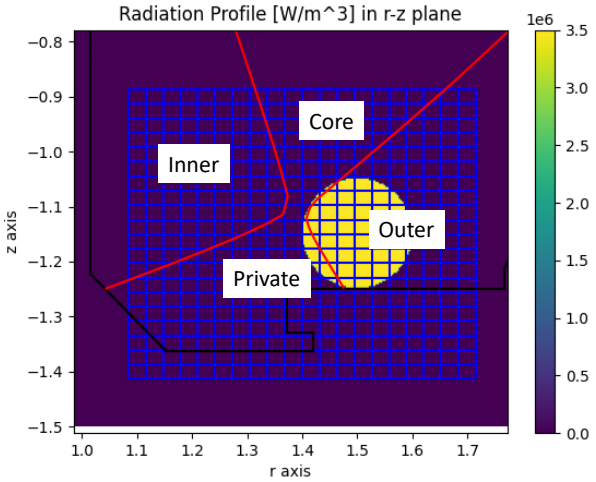

Figure 76 Circular phantom emission with a uniform emissivity of 3.5 MW/m^3 near the outer divertor simulated in CHERAB. The grid is divided into four parts.

Table 8 Comparison between various tomographic reconstruction methods

	Bolo. Errors (%)	Radiated Power Errors (%)	Emissivity RMSE (W/m^3)
Simple	8.72	14.03	1.0604
SART	1.12	4.98	0.6113
Reg. SART	2.96	1.51	0.4421
NNLS	0.41	20.40	1.2804
Reg. NNLS	3.17	4.39	0.3532
ML	0.46	19.25	0.9357
Reg. ML	1.54	0.83	0.6561

Table 9 Sectional power comparisons between various tomographic reconstruction methods. Unit in [W].

	Phantom	Simple	SART	Reg. SART	NNLS	Reg. NNLS	ML	Reg. ML
Inner	0.0	45220	38610	26591	37461	11989	37114	19718
Private	84847	70145	121479	105286	99177	74847	207351	82160
Outer	1023874	840347	1016552	996513	757619	971534	1095535	1023513
Core	14734	9942	2764	12022	0	15723	-320	7405

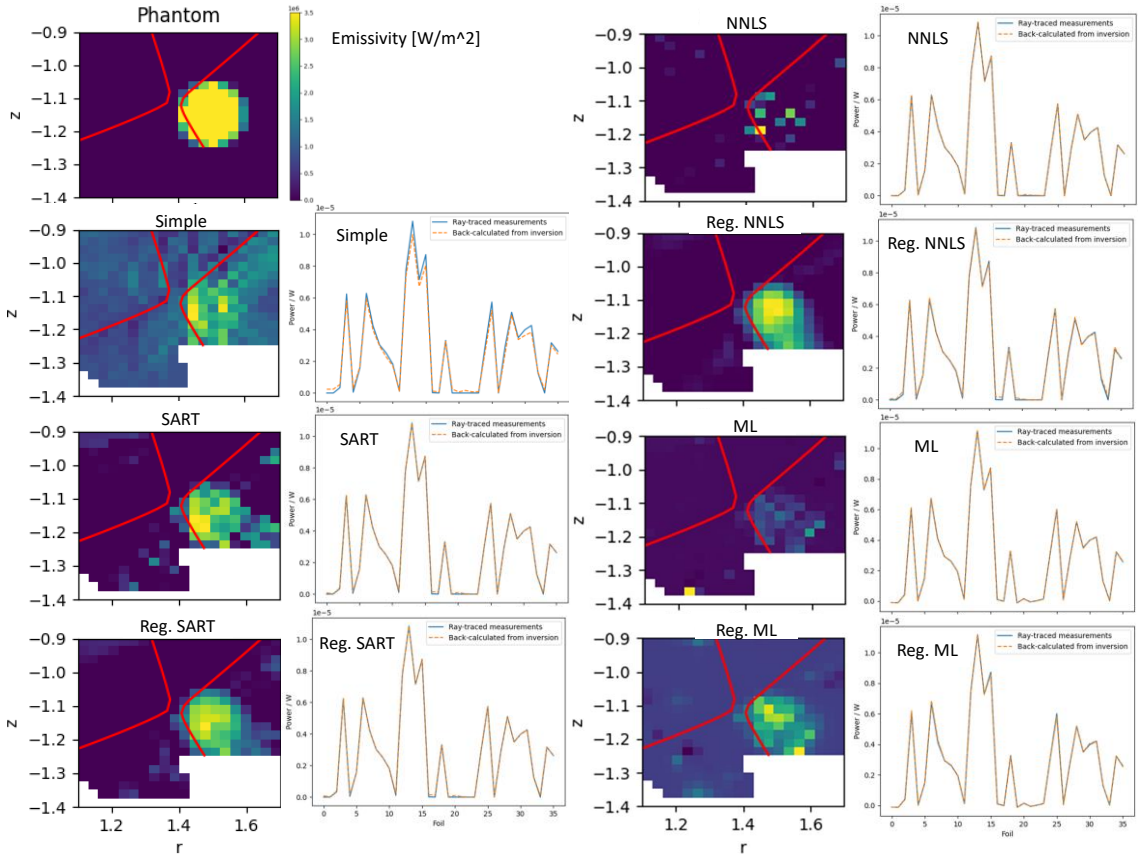

Figure 77 Emissivity profiles of various tomographic reconstruction methods. FOB measurements in CHERAB (blue) and back-calculated values from tomographic reconstructions (dotted orange).

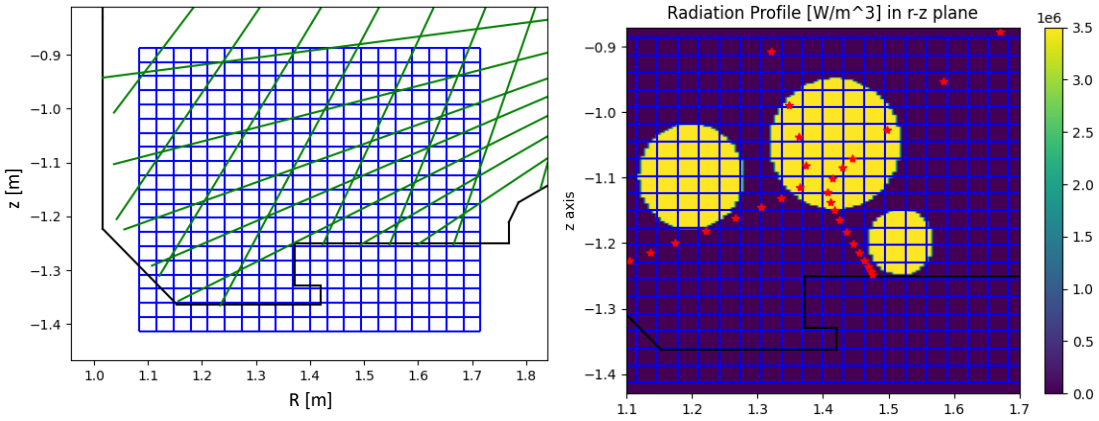

Figure 78 Left: resistive bolometer sightlines in the 20 by 20 grid. Right: phantom emissions for the comparisons between the 2D FOB design and resistive bolometers.

Table 10 Comparisons between the FOB design and resistive bolometers for various parameters.

	Bolo. Errors (%)	Radiated Power Errors (%)	Emissivity RMSE (W/m^3)
Resistive	2.11	8.13	0.7902
FOB	2.21	1.9	0.4865

Table 11 Comparisons between the FOB design and resistive bolometers for different sectional radiated power.

	Phantom [W]	Resistive [W]	FOB [W]
Inner	737873	629819	688844
Private	22062	168769	124143
Outer	583928	432880	588348
Core	575452	531719	554468

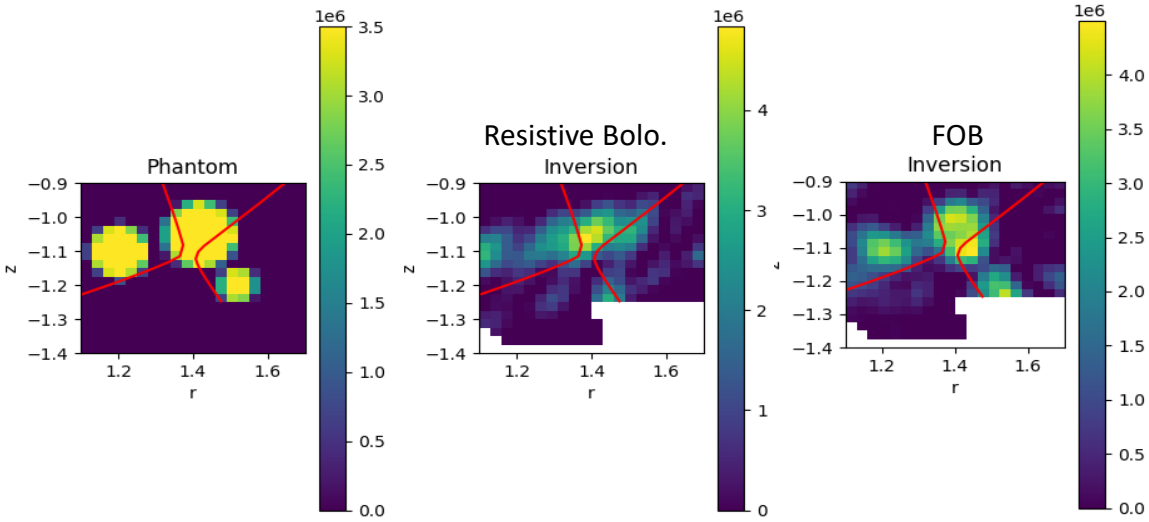

Figure 79 Comparison of tomographic reconstructions (regularized NNLS) for the FOB design and the resistive bolometers. The FOB design matches much better with the phantom profile.

The above process of comparisons was an example that the designing process of the 2D imaging FOB array will use to evaluate a design. More comparison parameters might be required for better evaluations. Also, a more complicated inversion method used by DIII-D will be implemented to Python to be used with CHERAB. These will be discussed in the next chapter.

Chapter Five

2D Fiber Optic Bolometer Array

Machine Learning Optimization of 2D FOB Array

After the successful demonstration of the single-channel FOB, it is planned to implement 2D FOB array at DIII-D to rigorously analyze the divertor region with high spatial resolution. The size of the array, the distance between sensors, the distance between the array and the pinhole, the diameter of the pinhole, the location (ports), the radial tilt, and the tangential tilt are the design parameters for the array. The pinhole radius is traditionally matched to the sensor radius, but it should be equal or bigger than the sensor. The location (X, Y, Z) at DIII-D machine will be determined by the port location allocated by DIII-D. It is most likely be installed at R-1 port, but R+1 port is also a possibility. Also, other parameters will have restraints in the possible values. For instance, the size of the array will be restrained by the budget, but it needs to be big enough to have high spatial resolution. Other physical dimensions need to be possible to fabricate and assemble. Once the parameters are chosen, the selected design will be implemented in CHERAB with the design package mentioned in the previous section. The design can be tested using the codes with synthetic emission profiles and corresponding tomographic reconstructions.

The biggest challenge of optimizing the design parameters is that they are non-linear to each other. For instance, decreasing the distance between the sensors will narrow the viewing cone, which could increase the spatial resolution. However, the covering area will be decreased, which will require a closer distance between the array and the pinhole to compensate the decreased covering area. Now, the tilts will need to be adjusted to accommodate the change. In other case, the pinhole diameter could be reduced to have narrower viewing sightlines, which could result in higher spatial resolution. However, the signal level could be too low or there could be missing coverage between the sightlines. Other parameters will need to be adjusted to accommodate the possible changes. In other words, one parameter that was selected for the best result for a case will not be the best for a case where another parameter has changed.

There are three ways to optimize forementioned design parameters. The first way is to grid-search each parameter. For instance, one can give a range for each parameter and select ten equally spaced values in the range. However, since there are many parameters, the number of the design need to be tested explodes quiet quickly. For example, only optimizing the distance between sensors, the distance between the array and the pinhole, the diameter of the pinhole, the radial tilt, and the tangential tilt will result in 10^5 possible designs. Since testing a design takes about a minute, it will take ~69 days for total, which is not feasible. The second way is trial-and-error with one's intuition. For instance, one can expect that increasing the distance between the array and the pinhole will result in higher spatial resolution, but lower signal, which could result in lower time resolution than is required to overcome inherent noise. However, this is not a systematic approach that could limit the design with one's bias or prejudice. The third approach utilizes the machine learning described in the background section. This approach is more systematic with its principles and fasters. The downside with the approach was that the optimized result could be a local maximum/minimum.

The Bayesian global optimization algorithm that was mentioned in the background was used for the machine learning optimization. The method for the optimization is as follows. First, the design parameters were given a range with lowest acceptable decimal. The Bayesian method results in a set of chosen design parameters. The parameters are fed into the design package to simulate/forward-model the design. A synthetic profile or several different synthetic radiation profiles were used to forward-model the measurements of the design. The tomographic reconstruction is performed with the simple regularization (left-right-up-down smoothing) and SART method. The RMSE is calculated for the inversion result compared to the phantom result for each pixel. The inverse of the root-mean-square error (RMSE) is used as the cost for the optimization to better the optimization. The process repeats according to the Bayesian global optimization principles to maximize the cost.

The optimization method was tested for one parameter and two parameters to see if the optimization code was working. First, the distance between the pinhole and the array center within 0.01 to 0.3 m was optimized with 600 μm diameter sensor, 6 mm

diameter pinhole, 6 by 6 array (the total of 36 sensors), 7 mm distance between sensors, 33° tangential tilt, 15° radial tilt, and at R-1 Port. The result was 0.1581m for the parameter. The data from each iteration showed that the optimization method search the parameter quiet thoroughly (Figure 80). Also, the RMSE calculated by comparing with the phantom image was ~7% better than the first intuition. This showed that the optimization method was working for the single parameters.

Next, the optimization method was tested for two parameters, the pinhole size and the distance between the pinhole and the array center. The pinhole size was bound to the range from 0.004 to 0.014 m, and the distance was bound to the range from 0.13 to 0.33m. Other parameters were 600 μm diameter sensor, 6 by 6 array (the total of 36 sensors), 7 mm distance between sensors, 33° tangential tilt, 15° radial tilt, and at R-1 Port. The data showed that the optimization method search the two parameters quiet thoroughly (Figure 81). The RMSE calculated by comparing with the phantom image was ~10% better than the intuition case. This showed that the optimization method was working for the two parameters as well.

A case for optimizing most of the design parameter with one radiation profile was using an UEDGE simulated result where the radiation was mostly at the top shelf of the divertor (Figure 82). The design parameters for an optimization were the pinhole diameter (from - 0.004 to 0.014 m, round to 0.001m), the distance between sensors (from 0.015 to 0.005m, round to 0.001m), the distance between the array and the pinhole (from0 0.13 to 0.33m, round to 0.01), tangential tilt (from 28 to 38°, round to 1°) and radial tilt (from 10 to 20°, round to 1°). It was set for 6 by 6 array at R-1 port. The optimization result was the pinhole diameter: 0.005m, the distance between the sensors: 0.006m, the distance between the array and the pinhole: 0.25m, the tangential and radial tilts: 35° and 12°. The result showed that the optimization method searched the parameter space thoroughly (Figure 83). Again, the RMSE results were 10% better than the intuition case.

Using one radiation profile for the optimization method showed a problem of focusing on the most radiated region. A synthetic radiation profile with a X-shaped radiation (Figure 84, left) resulted in an optimization of the array mostly looking at the

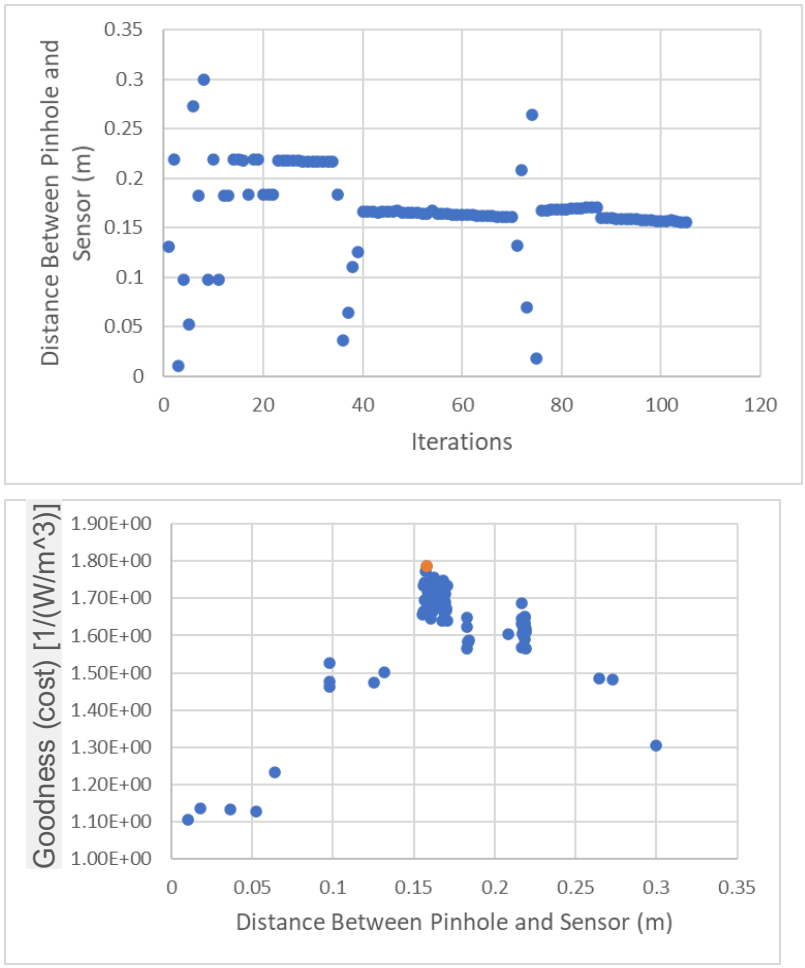

Figure 80 Top: tested values for the design parameter for each iteration. The optimization method searched thoroughly the entire range. Botton: the result of the cost or the goodness of the tested values.

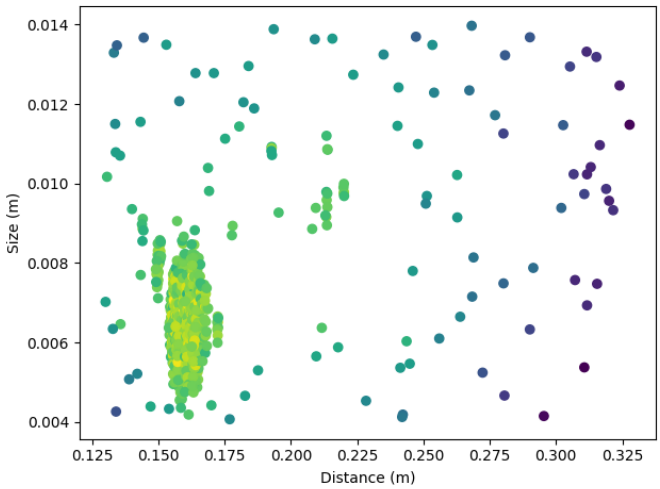

Figure 81 The tested data points in the parameter space. The optimization method searched the parameter space thoroughly. Lighter the color, better the cost.

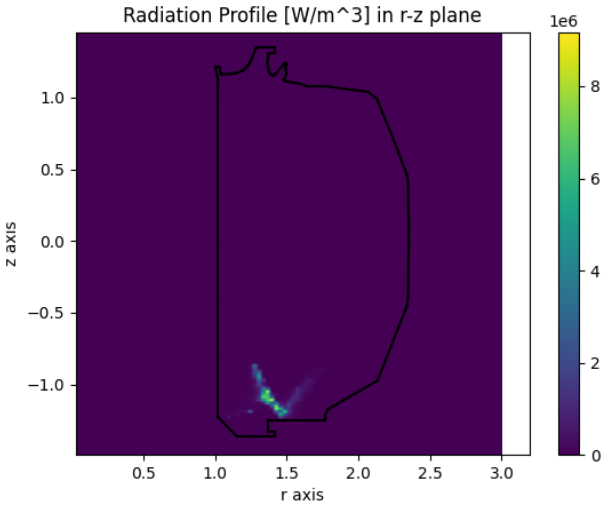

Figure 82 The radiation profile [W/m^3] for optimizing six design parameters.

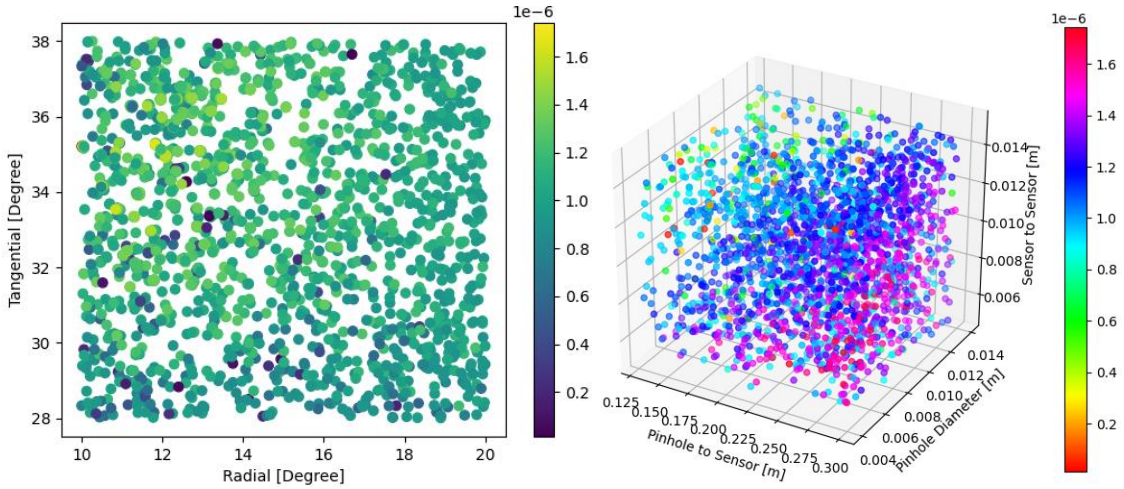

Figure 83 The parameter space searched by the optimization method. Each dot is the tested design parameter. The color bar is the cost value [m^3/W] for the data point.

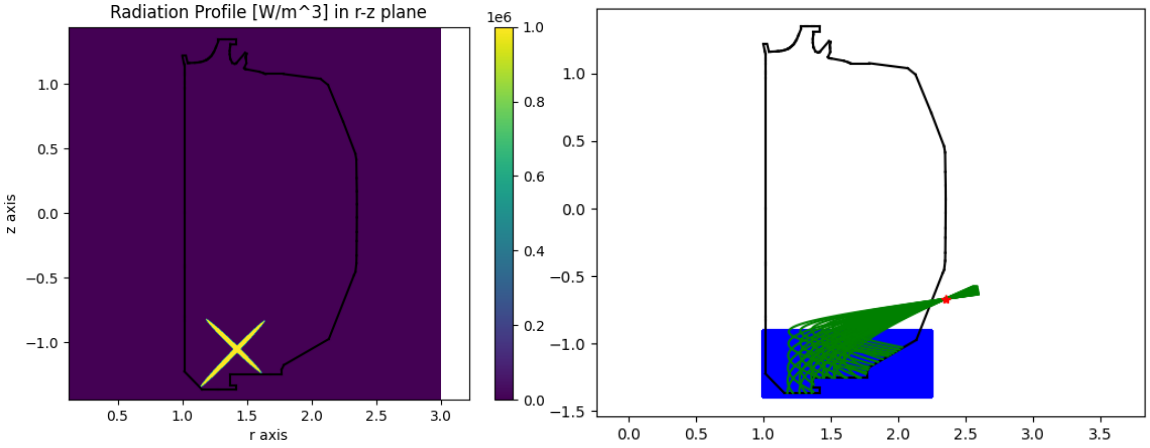

Figure 84 Left: X-shaped radiation profile for optimization. Right: the optimization result that focused on the outer side of the region of interest due to the radiation profile.

outer side (Figure 84, right). The optimizing and set design parameters were the same as before with the same range. The RMSE was ~21% better than the intuition as expected due to the focusing. However, this result is not acceptable since the coverage needs to be the entire divertor region.

To avoid the focusing problem, six different radiation profiles were used to optimize the array design (Figure 85 and 86). The synthetic radiation profiles were constructed following the examples from published papers. In addition, the emissivity of the radiation blobs at the periphery were changed to be higher than the emissivity of the radiation blobs near the center. The optimizing and set design parameters were the same as before with the same range. The optimized results were more spread over the region of interest covering the entire region (Figure 87, blue region).

Another method used to avoid the focusing result was using one radiation profile with four radiation blobs spread out (Figure 88). The emissivity of the radiation blobs at the periphery was higher than the emissivity of the radiation blobs at the center. The optimizing and set design parameters were the same as before with the same range. The result showed that this method also covers the entire range of the region of interest (Figure 89). However, the results were much wilder than the six-profiles optimization (Figure 87) or the intuition case (Figure 90). Some of the sightlines are wasted outside the region of interest for the one-profile optimization. In addition, the inverse of the RMSE (the cost) was worst for the one-profile optimization (Table 12). So, this method was abandoned due to the performance issues.

R+1 port design was explored with the machine learning optimization. If the 2D FOB array is installed at R+1 port, the viewing sightlines will be passing through the core to look at the divertor region (Figure 91). The design parameters were optimized with the six different radiation profiles. It was the same 6-by-6 array. The cost comparison showed that the R+1 port optimized design had lower performance for some radiation profiles (Table 12). In addition, the R+1 port has the problem of subtracting the core contribution / the radiation outside the region of interest, which could increase the error.

For the optimizations and testing cases, the radiation profiles are only present at the divertor region, which is the region of interest. However, the radiations are present

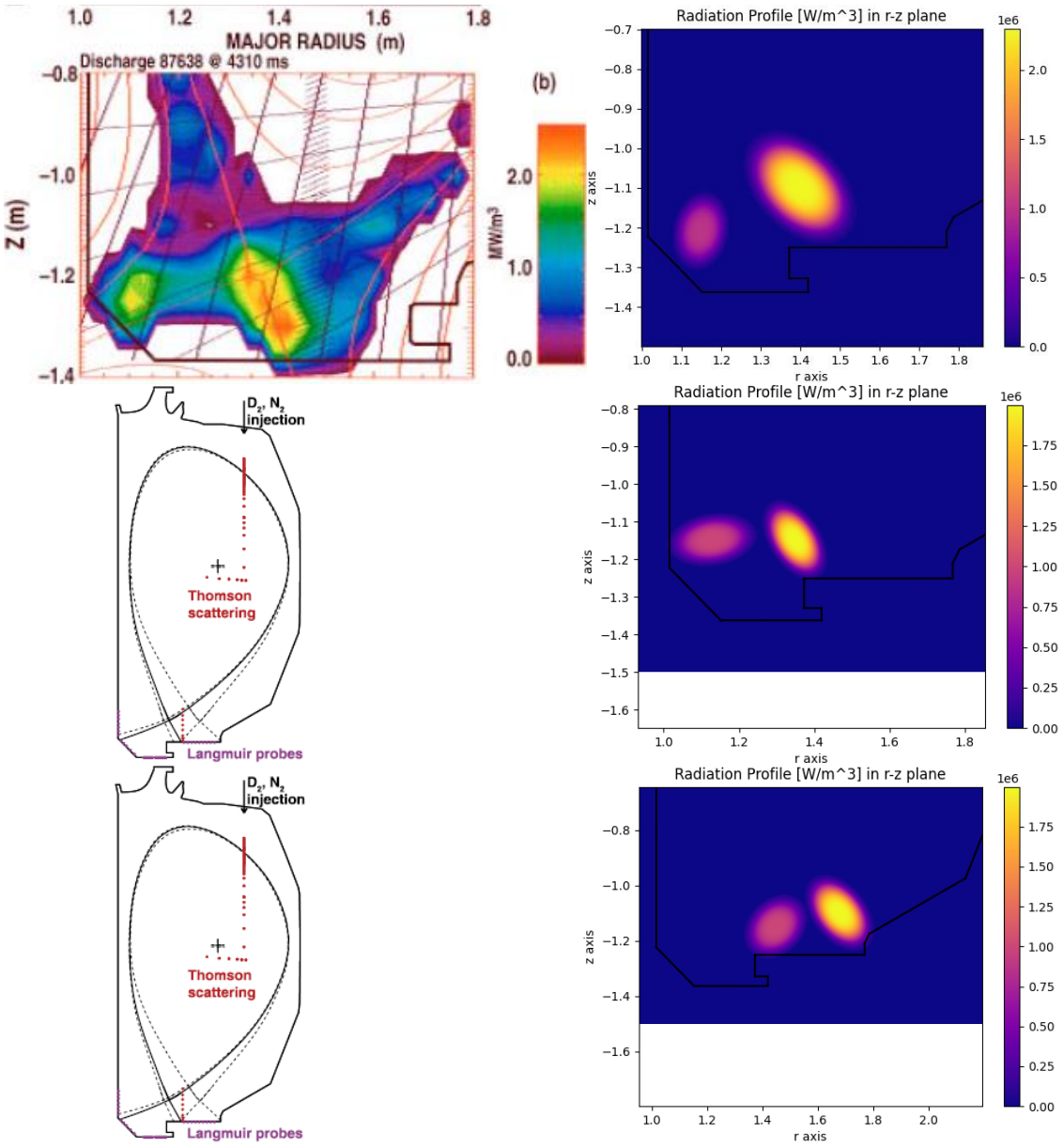

Figure 85 The radiation profiles (1, 2, 3) used for the optimization on the right. The synthetic radiation profiles mimicked the published works on the left [80][13].

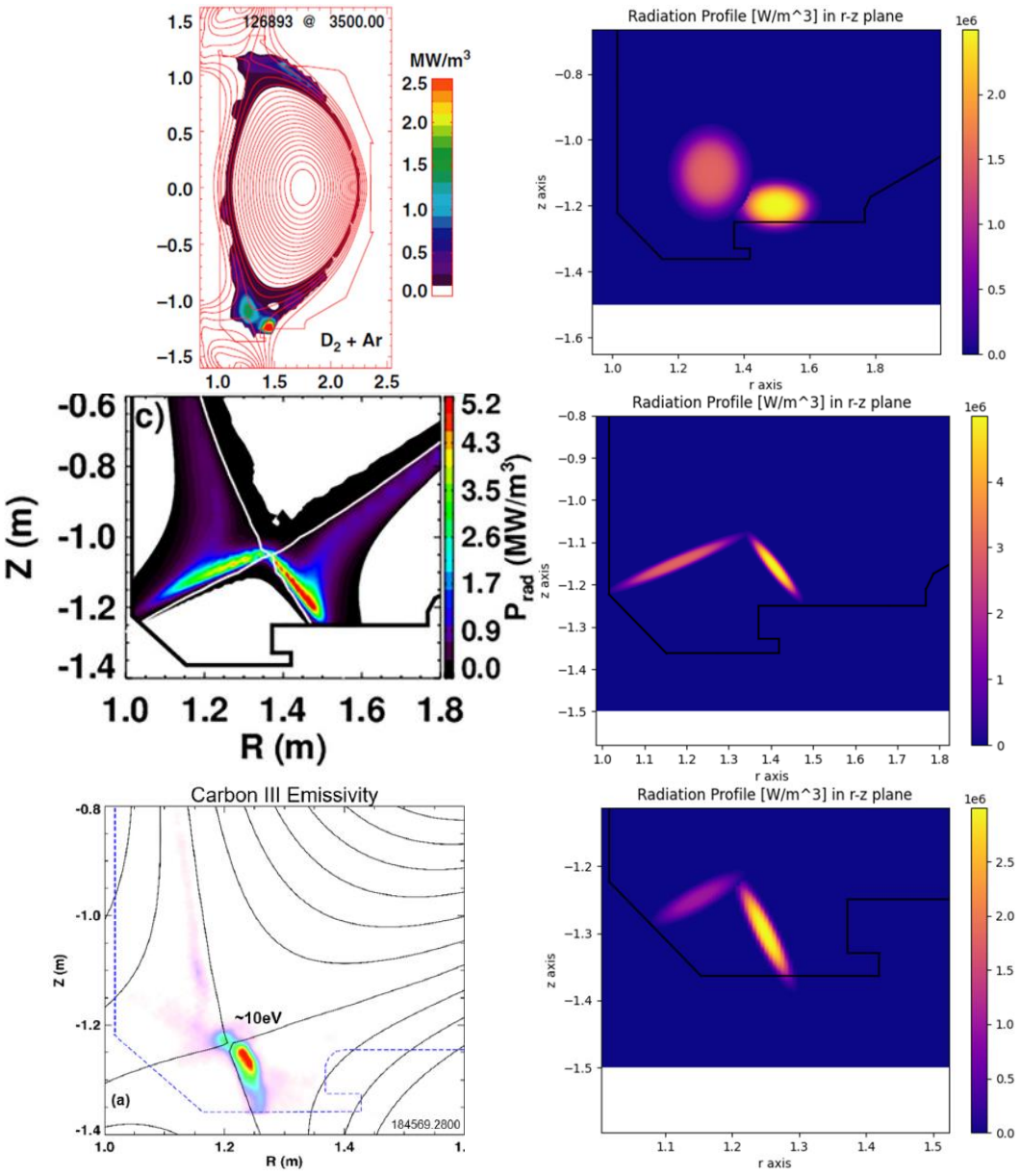

Figure 86 The radiation profiles (4, 5, 6) used for the optimization on the right. The synthetic radiation profiles mimicked the published works on the left [81][12][82].

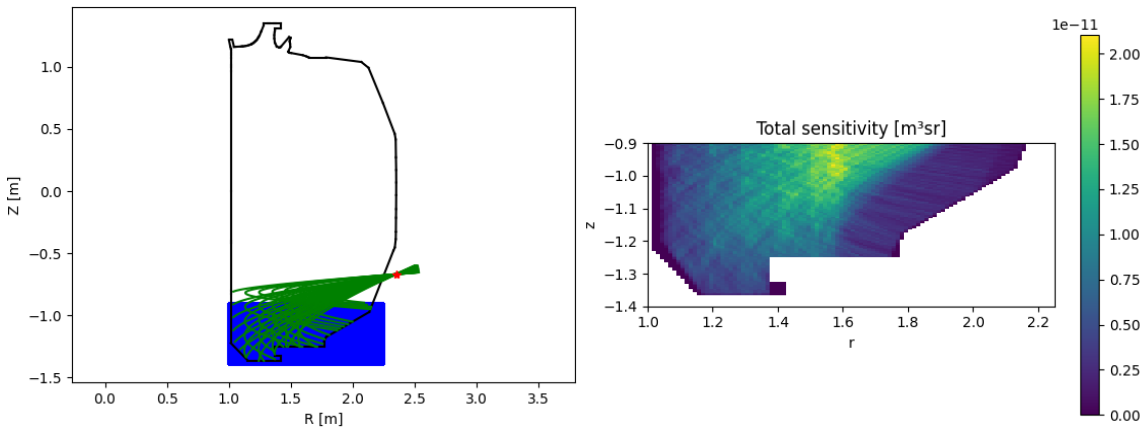

Figure 87 Left: the sightlines of the optimized array with six different radiation profiles. Right: the sensitivity profile of the optimized array. The results are more spread out covering the entire region of interest.

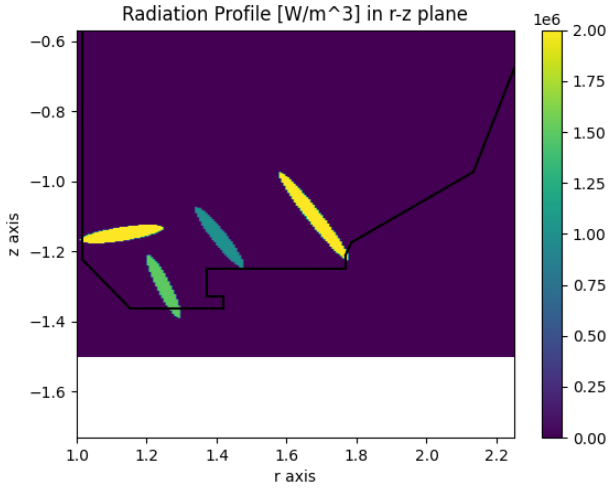

Figure 88 The radiation profile with four radiation blobs spread out to avoid the focusing optimization. The periphery radiation blobs have higher emissivity.

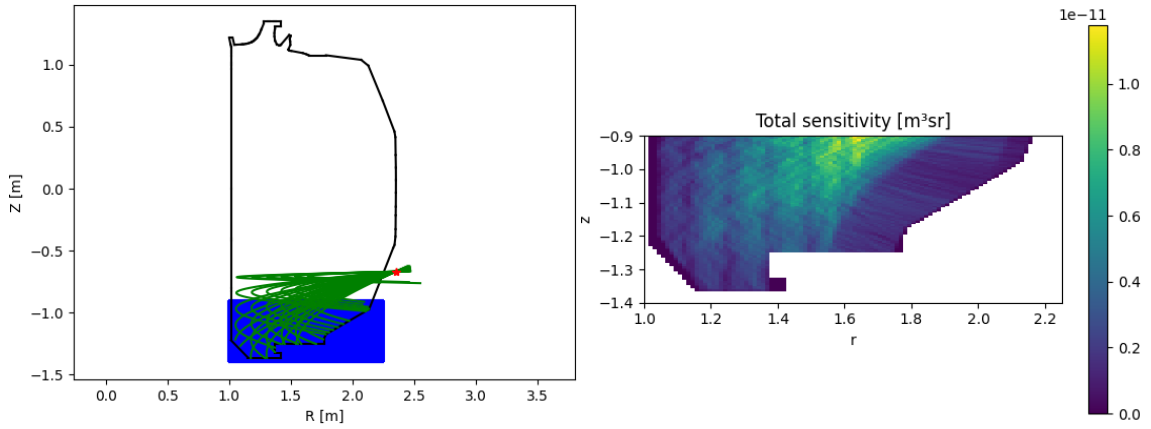

Figure 89 Left: the result of the one radiation profile optimization. Right: corresponding sensitivity profile. Some sightlines were wasted outside of the region of interest.

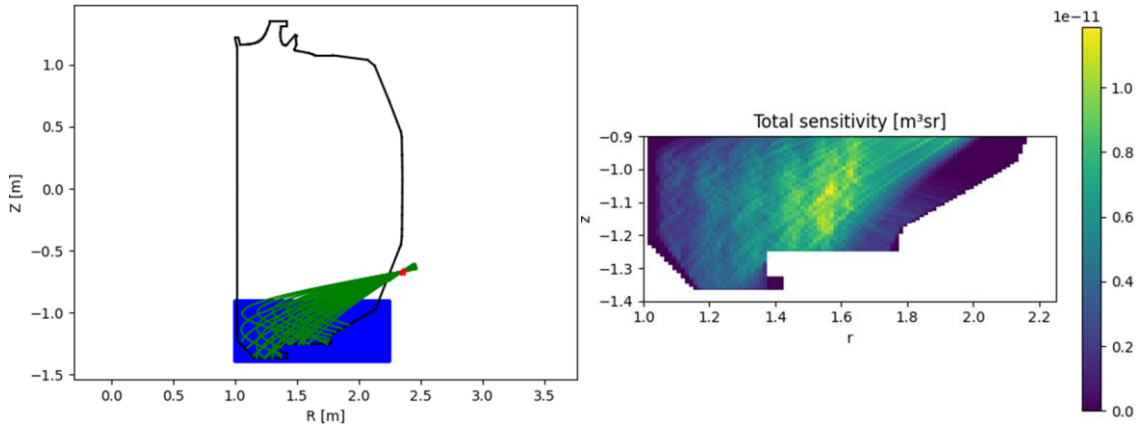

Figure 90 Left: the design parameters selected from my intuition. Right: corresponding sensitivity profile. No sightlines were wasted outside of the region of interest.

Table 12 Cost Comparison for Different Methods of Optimized Design Parameters

	Four Blobs	**Profile 1**	**Profile 2**	**Profile 3**	**Profile 4**	**Profile 5**	**Profile 6**
One Profile	~2.7e-06	4.10e-06	4.54-06	4.96e-06	4.65e-06	2.39e-06	5.63e-06
Intuition	2.47e-06	3.63e-06	3.33e-06	4.41e-06	4.47e-06	2.30e-06	5.15e-06
Six Profiles	~2.7e-06	5.34e-06	4.46e-06	5.80e-06	5.48e-06	2.33e-06	5.60e-06
R+1 6 By 6	3.02e-06	3.14e-06	3.91e-06	4.68e-06	3.00e-06	2.42e-06	5.62e-06

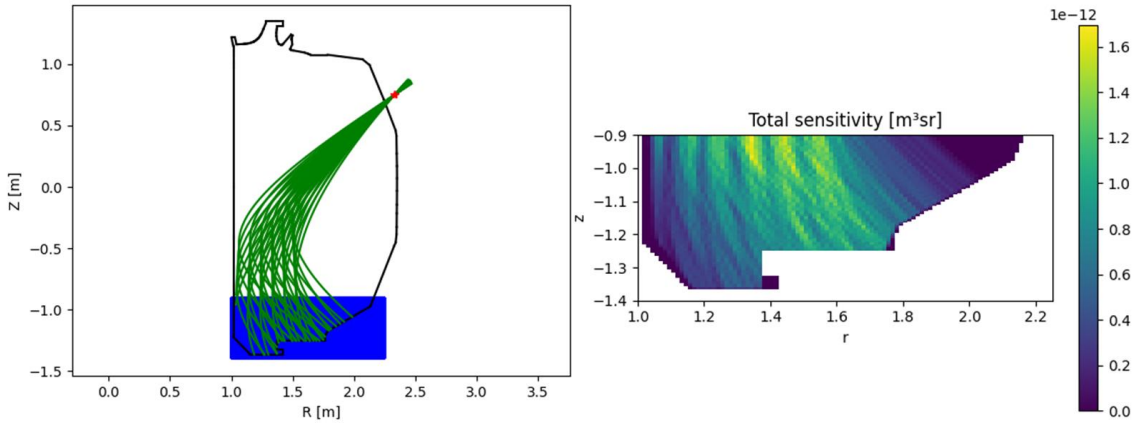

Figure 91 Left: the sightlines of the optimized array at R+1 prot. Right: corresponding sensitivity profile. The sightlines passed through the core.

throughout the entire radial cross section, and the start of the sightlines from the array will measure the radiations, which are outside the region of interest. To avoid the additional measurements from the outside of the region of interest showing up in the inversion results, which only include the region of interest, the portion of the measurement values will need to be subtracted from the total measurements. This will be done in practice by using the inversion results of the resistive bolometers. The inversion results will be limited to the outside of the region of interest (Figure 92). The forward-modeled measured values of the modified inversion results will be subtracted from the total measurements. This process is like the forward-modeled values for the single-channel FOB except that the process will be for the array, with the limited inversion results, and the subtraction.

The next parameter that was explored was the size of the array. It was expected that the bigger the size of the array, better the resolution will be. The results showed what was expected that the bigger size array resulted in higher cost (Table 13). The parameters were adjusted to match the similar structure to the optimized 8-by-8 array. The cost is the obvious problem with increased array size. So, different possible size like 4-by-8 to 8-by-8 were added to the optimization parameters. The results showed that the top ten of the highest costs included two 6-by-8 array showing that the size was comparable to 8-by-8 in some radiation profiles (Table 13). These results will be used in case the budget of the project allows a bigger size array or requires a smaller array due to other expanses.

One design aspect that was not intuitive was that a set line of sightlines was terminated at the inner wall. This was present for both 6-by-6 and 8-by-8 array optimizations (Figure 93). One would assume the best-case scenario would be where all the sightlines are terminated at the divertor (the bottom). So that, each sightline has a longer pathlength into the plasma. Nevertheless, the machine learning optimization results consistently showed that this is not the case. It is believed that the termination at the inner wall results in more packed sightlines at the center. Also, it could be that the termination increases the sightline crossing each other. However, it is not clear why the termination results in better cost since the design parameters are non-linear to each other.

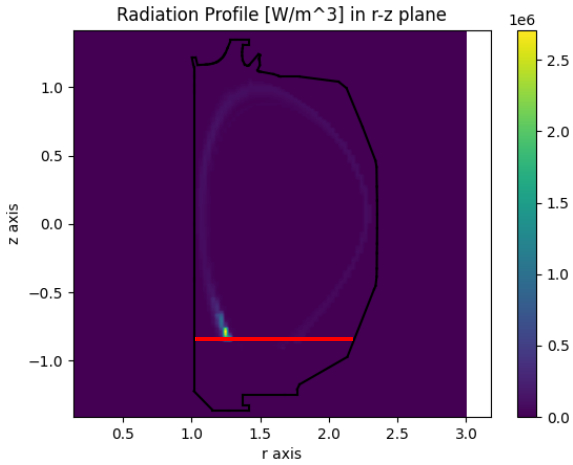

Figure 92 A radiation profile limited to the outside of the region of interest that will be used to subtract the measurement contribution from the outside the region of interest.

Table 13 Cost Comparison for Different Array Size of Optimized Design Parameters

	Profile 1	**Profile 2**	**Profile 3**	**Profile 4**	**Profile 5**	**Profile 6**
6 by 6	5.17e-06	3.81e-06	5.11e-06	5.69e-06	2.37e-06	5.59e-06
8 by 8	5.78e-06	4.35e-06	6.08e-06	5.16e-06	2.69e-06	6.21e-06
10 by 10	7.03e-06	4.40e-06	7.25e-06	6.19e-06	2.94e-06	6.05e-06
12 by 12	9.43e-06	4.28e-06	1.04e-05	5.56e-06	3.02e-06	7.05e-06
4 by 8	3.34e-06	4.15e-06	4.14e-06	3.75e-06	2.42e-06	5.52e-06
6 by 8	7.20e-06	3.19e-06	8.22e-06	5.13e-06	2.85e-06	5.96e-06

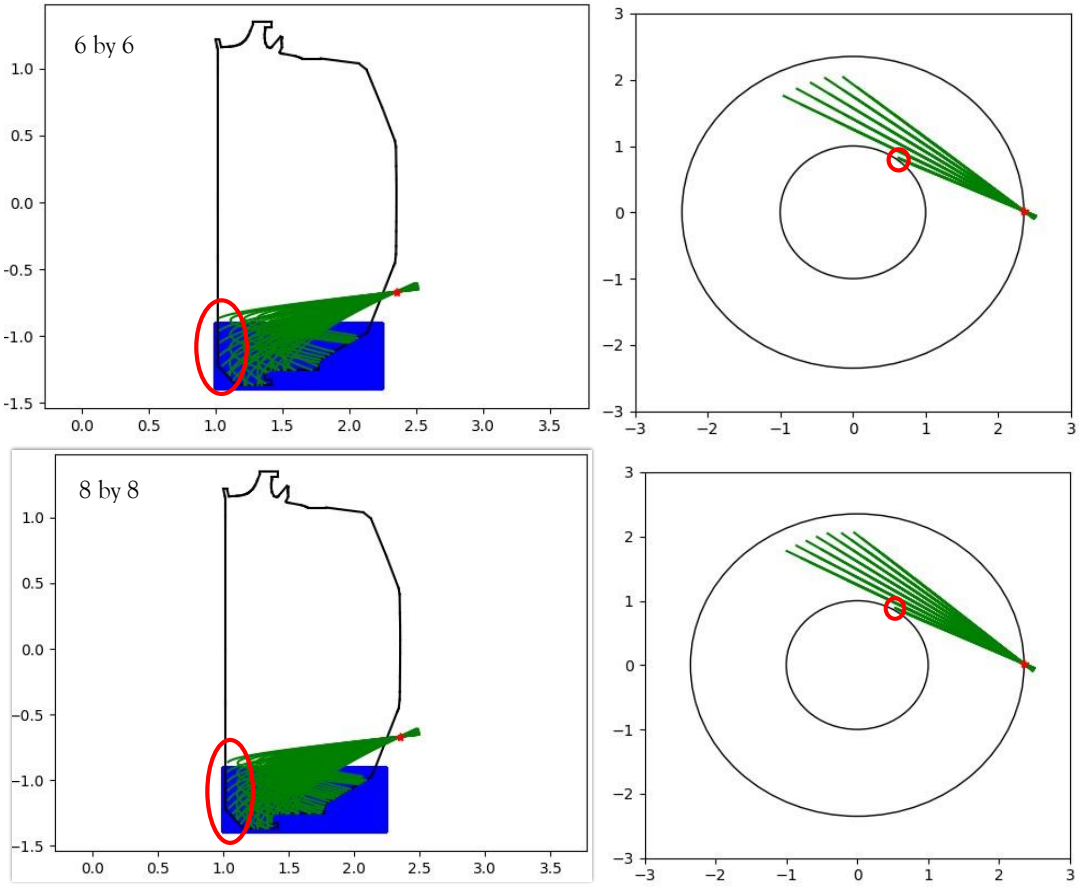

Figure 93 Top: 6-by-6 optimized array. Bottom: 8-by-8 optimized array. Left: radial cross-section. Right: top-down view. Both show a set of sightlines terminated at the inner wall.

Some other aspects that needed to be considered were the R-1 port structure and the finite thickness of the pinhole. The R-1 port has two structures. One is a circular-shaped port and the other is an oval-shaped, which is bigger (Figure 94). For previous optimizations, the bigger oval-shaped port was considered where there were more room at the top or the bottom. However, it should be considered that the port could the smaller circular port. If the optimized design parameters were implemented with the assumption that the center of the pinhole is located at the center of the port than the array could be blocked by the port structure (Figure 95). To avoid the blocking, the sensor spacing was limited to 4 mm or smaller. The cost comparison of the optimized designs showed that the change in the sensor spacing had a minimal effect (Table 14). The result of the design parameters for the 6-by6 and 8-by-8 arrays optimization is shown in Table 15.

The finite thickness of the pinhole results in vignetting. The effective pinhole size reduces for the FOBs at the edge of the array due to the thickness of the pinhole (Figure 96). The thickness calculated to block high energy photons. If the high energy photons pass through other than the pinhole, it could be measured by the FOBs, which result in additional radiation measurements outside the sightline or the viewing volume. Assuming the maximum of 50 KeV photons, 316 stainless steel density of 7.98 g/cm^3, and the mass attenuation coefficient of 1.958 cm^2/g, the thickness required to block 99.9% can be calculated using the below equation.

$$\frac{I}{I_0} = exp\left[-\left(\frac{\mu}{\rho}\right)x\right], x = \rho t$$

$$\frac{I}{I_0} = 0.999$$

μ is the mass attenuation

ρ is the density

t is the thickness.

The result showed that 4.4mm is required to block 99.9% of 50 KeV photons. The effect of the thickness can be seen on Figure 97. The etendue and the sensitivity decrease significantly for 5mm thickness compared to 0.01mm thickness. However, significant amount of 50 KeV photons will be a very special case from runaway electrons. 1mm

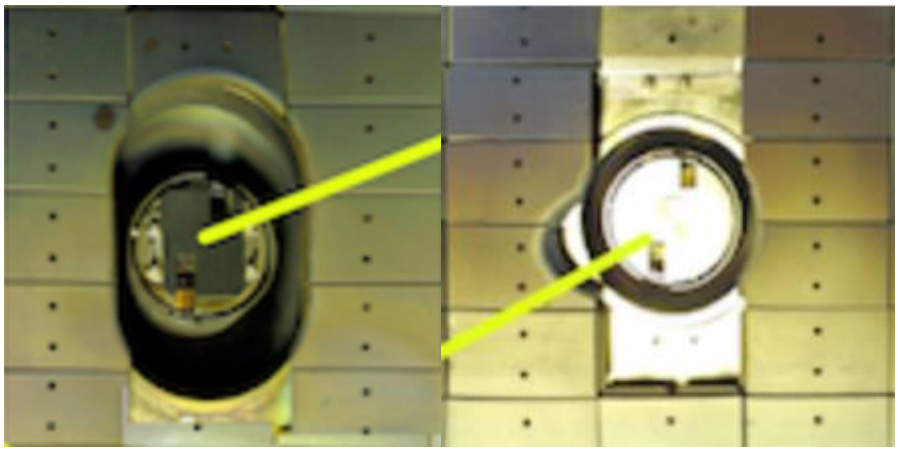

Figure 94 Left: oval-shaped R-1 port. Right: circular R-1 port. Notice the difference in the excessive area above and below the center for the oval-shaped port.

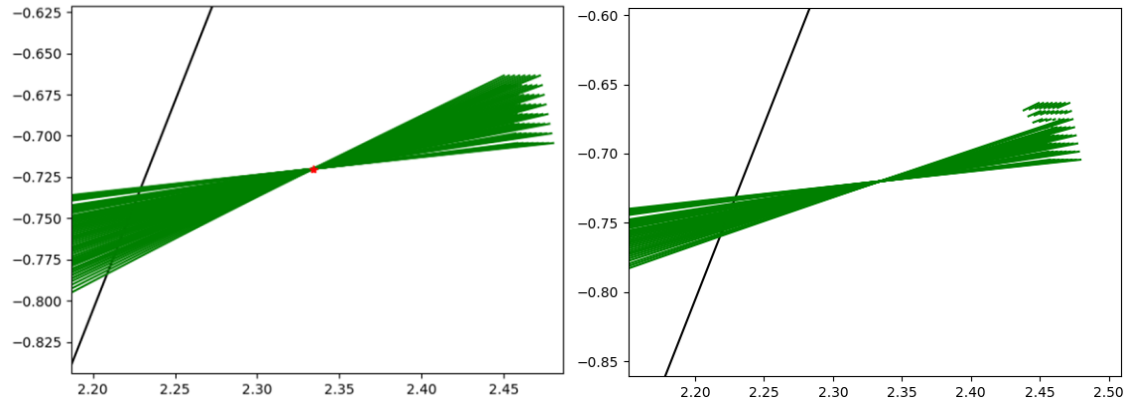

Figure 95 Left: 8-by-8 array sightlines in the oval-shaped port. Right: 8-by-8 array sightlines in the circular port. 1/3 of the sightlines are blocked by the structure of the circular port.

Table 14 The Cost Comparisons for Changed Sensor Spacing

	Profile 1	**Profile 2**	**Profile 3**	**Profile 4**	**Profile 5**	**Profile 6**
6by6 6mm oval	3.57E-06	3.42E-06	5.06E-06	4.02E-06	2.58E-06	5.73E-06
6by6 4mm circular	3.08E-06	3.37E-06	5.05E-06	3.87E-06	2.59E-06	5.86E-06
8by8 6mm oval	5.91E-06	3.38E-06	6.90E-06	4.89E-06	3.04E-06	5.90E-06
8by8 4mm circular	5.80E-06	3.32E-06	7.70E-06	4.84E-06	3.05E-06	6.07E-06

Table 15 The Final Design Parameters

	Sensor Spacing [m]	**Distance between array and pinhole [m]**	**Pinhole Diameter [m]**	**Radial Angle [degree]**	**Tangential Angle [degree]**
6by6 4mm	0.004	0.082	0.0046	12.6	32.1
8by8 4mm	0.004	0.106	0.0037	13.1	33.3

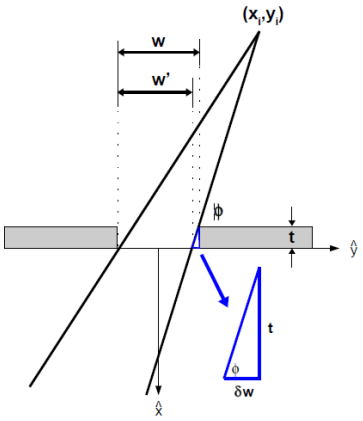

Figure 96 Effect of the finite thickness of the pinhole [64]. The effective pinhole size will decrease for the sensors at the edge of the array.

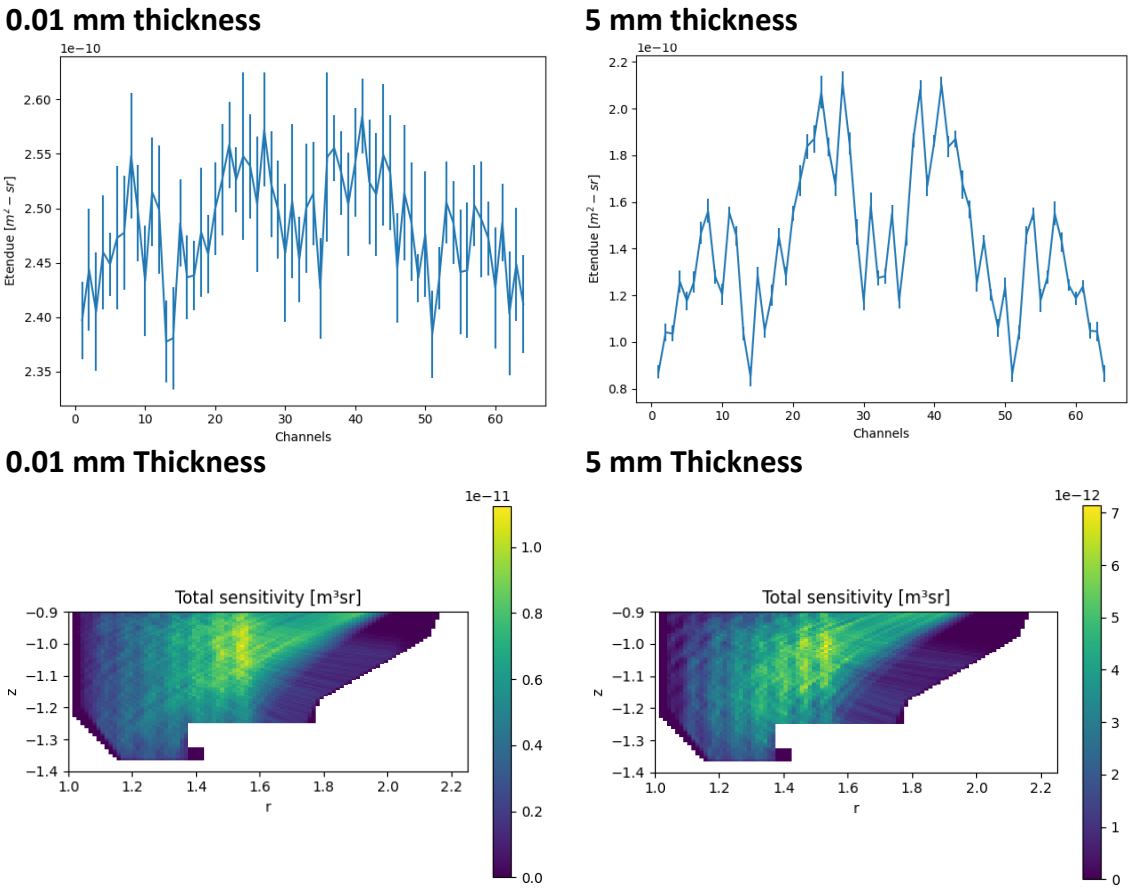

Figure 97 Top: etendue values for the 8-by-8 array. Bottom: sensitivity profiles for the array. Left: 0.01mm thick pinhole. Right: 5mm thick pinhole. Significant decrease in both values can be seem with 5mm thickness compared to 0.01mm thickness.

thickness should be more than enough for couple of KeV photons, which is expected from DIII-D due to the typical plasma temperature of DIII-D. 1mm thickness does not result in a significant vignetting (Figure 98) that there are only minimal changes in the etendue / the sensitivity compared to 0.01mm thickness.

Combining Resistive Bolometers and FOBs

The tomographic reconstruction method for the bolometers is an ill-posed problem where there are more variables than equations. Adding more information will moderate the ill-posed problem. Other than the measurements, additional information is added through regularizations in most cases. Nevertheless, it can be expected to use the resistive bolometer measurements combined with the 2D FOB array measurements for a better inversion since the resistive bolometers can provide additional information. This can be done by adding the resistive bolometer information as the extension of the 2D FOB array information for the inversion process. The sensitivity profile for the resistive bolometers (Figure 91, left) at the same region of interest can be attached to the sensitivity matrix of the 2D FOB array (Figure 91, right). Also, the measurements of the resistive bolometers can be added to the measurements of the 2D FOB array (Figure 100). The example was for the X-shaped plasma radiation profile mentioned in the previous section.

One can quickly see the problem with adding the resistive bolometer information as is. The absolute value difference between the 2D FOB array and the resistive bolometers are more than 50 times due to the differences in the dimensions between the two systems. The overwhelming values of the resistive bolometers overshadow the 2D FOB array information that the inversion results are about the same as only using the resistive bolometers. To mitigate the problem, one can adjust the contribution from the resistive bolometers to the 2D FOB array level. This was done with truncating the resistive bolometer values by multiplying a constant (1/100) (Figure 101). The resistive bolometer values were modified rather than the FOB values since the main information will be from the FOBs. The RMSE of the inversion compared to the original phantom image was 1.8% better than only using the FOB values.

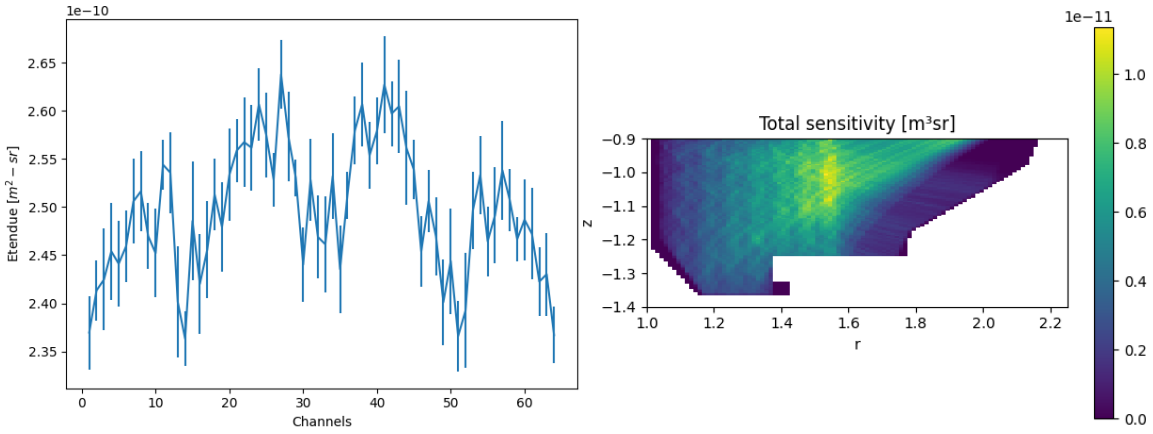

Figure 98 Left: etendue values for the 8-by-8 array with 1mm thick pinhole. Right: sensitivity profile for the array with 1mm thick pinhole.

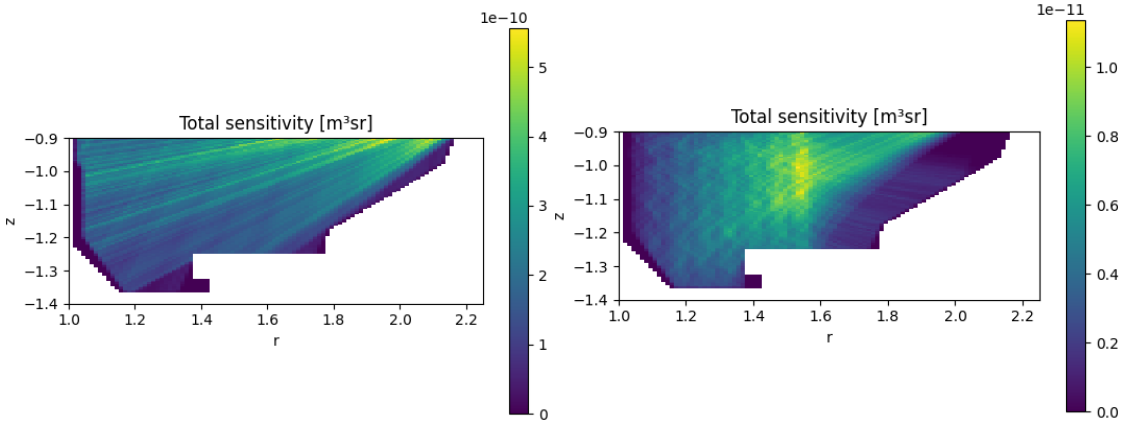

Figure 99 Left: sensitivity profile for the resistive bolometers at the same region of interest. Right: sensitivity profile for 2D FOB array (8 by 8).

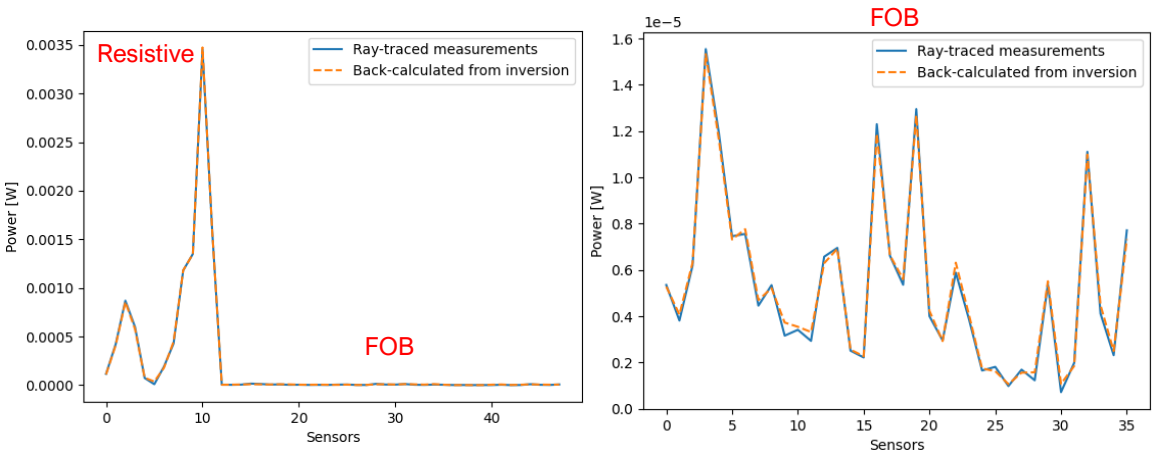

Figure 100 Left: combined measurements of the resistive bolometers and 2D FOB array. Right: measurements of the 2D FOB array

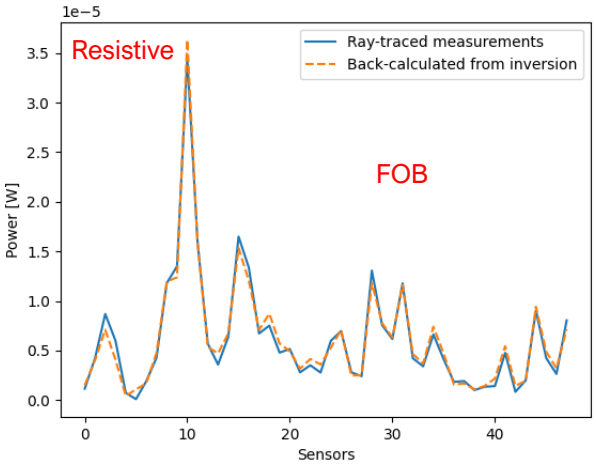

Figure 101 Combined measurements of the resistive bolometers with 1/100 truncated values and 2D FOB array

Another case was tested where the plasma radiation profile had bigger radiation blobs (Figure 102). The radiation blobs were thicker than the X-shaped that the blobs were bigger than the distance between the sightlines of the resistive bolometers. Five different cases were tested to understand the performance of combining the resistive bolometer information. The costs (the inverse of the RMSE) for each case were compared to quantify the performance. The first one was only resistive bolometer where the cost was 1.31e-05. The second one was only 8-by-8 FOB array where the cost was 6.64e-06. The third case was the combination between the resistive bolometers and the FOBs without any reduction for the resistive bolometers where the cost was 2.51e-06. The fourth case was the combination between the resistive bolometers and the FOBs with 0.1 times reduction for the resistive bolometers where the cost was 5.73e-06. The final testing was the combination between the resistive bolometers and the FOBs with 0.01 times reduction for the resistive bolometers where the cost was 7.63e-06. These results showed that the adding FOB information was always better for the resistive bolometers. Again, making the resistive bolometer information comparable to the FOB information resulted in the best result. In addition, the RMSE was more than 10% better compared to only using the FOBs for this radiation profile case. This showed that, if the plasma radiation is better measured by the resistive bolometers (bigger plasma radiation) considering the distance between the sightlines of the resistive bolometers, the effect of additional resistive bolometer information has better impact on the overall result.

More systematic approach to finding the reduction constant was experimented to be less arbitrary. Four different methods were tried. The first method was using the max sensitivity ratio, which was 0.0127, the second method was using the max measurement ratio (0.0613), the third method was using the mean sensitivity ratio (0.0400), the final method was using the mean measurement ratio (0.0111). Also, a grid searching the values (trial and error) resulted in the best RMSE with 0.016. The RMSE result of using the max sensitivity ratio (0.0127) had only 1% difference compared to 0.016. From this, it was concluded to use the max sensitivity ratio to be more precise.

The previous testing with the resistive bolometers ignored the possible noise level in the resistive bolometers. As mentioned before, the problem with the resistive

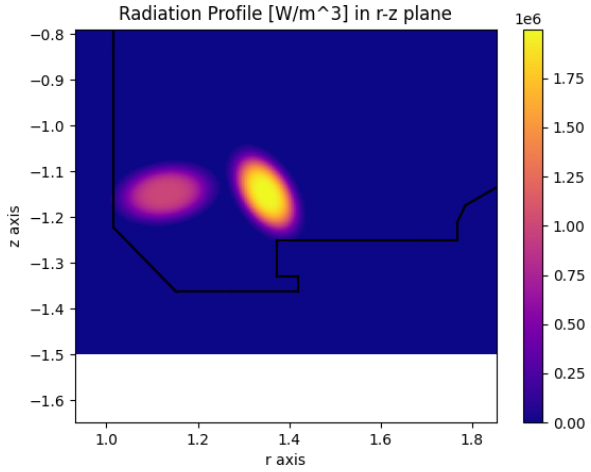

Figure 102 Different plasma radiation profile tested for combining the resistive bolometer information. The radiation blobs are bigger / thicker compared to X-shaped profile.

bolometers is that they are prone to EMI. EMI could result in high noise level. So, the random noise was added to the resistive bolometers that were measured from the stand deviation of -500 to 0 ms for DIII-D data (shot 187064, 187138, 187162, 187170, 187195, 187240, 187245, and 187288). There were some channels of the resistive bolometer with significant noise level. These channels were excluded from the combination of the resistive bolometers and the FOBs.

The plasma radiation profiles 1 to 6 mentioned in the previous section were used to test the combination of the resistive bolometers and the FOBs. The resistive bolometer information was added to the 6-by-6 optimized FOB array with or without the noise and to the 8-by-8 optimized FOB array with the noise. The results showed that adding the resistive bolometer information bettered the cost values for the plasma radiation profiles with larger radiation blobs (profile 1, 2, and 4) (Table 16). Again, this showed that, if the plasma radiation is better suited for the resistive bolometers considering the distance between the sightlines of the resistive bolometers, the additional resistive bolometer information better the inversion results. Other plasma radiation profile cases had about the same cost or reduced cost due to the noise in the resistive bolometers. The biggest advantage of adding the resistive bolometer information was that the cost values for the 6-by-6 FOB array combined with the resistive bolometer information were compared to the 8-by-8 FOB array and the cost values for the 8-by-8 FOB array combined with the resistive bolometer information were compared to the 10-by-10 FOB array for the profiles with bigger radiation blobs.

Fourier Transform Analysis of Raw Spectra Data

When analyzing the raw spectrum data (Figure 103, left) of the FOB, a sinusoidal function is fit to a valley to calculate the wavelength value of the minimum count in the function. This is done for 4 or 5 valleys, and the values are averaged over to be represent the wavelength of a raw spectra data point. The wavelength changes correspond to the temperature changes with the temperature sensitivity (constant). However, it was found that the wavelength values / the temperature changes for the different valleys show different results (Figure 103, right). These deviations showed up in different heating

Table 16 The Cost Comparison for The Combination of The Resistive Bolometer Data and The Different FOB Array Size

	Profile 1	**Profile 2**	**Profile 3**	**Profile 4**	**Profile 5**	**Profile 6**
6 by 6	4.35E-6 ±0.32E-6	3.57E-6 ±0.07E-6	5.64E-6 ±0.21E-6	4.58E-6 ±0.45E-6	2.56E-6 ±0.01E-6	5.40E-6 ±0.06E-6
6 by 6 with resistive	5.96e-06	5.421e-06	5.52e-06	6.19e-06	2.49e-06	5.29e-06
6 by 6 with noise in resistive	6.29E-6 ±0.27E-6	5.15E-6 ±0.14E-6	5.61E-6 ±0.22E-6	5.67E-6 ±0.26E-6	2.51E-6 ±0.02E-6	5.29E-6 ±0.06E-6
8 by 8	6.05E-6 ±0.31E-6	4.30E-6 ±0.11E-6	6.31E-6 ±0.24E-6	5.41E-6 ±0.22E-6	2.72E-6 ±0.05E-6	6.34E-6±0.15E-6
8by8 with noise in resistive	7.26E-6 ±0.16E-6	5.89E-6 ±0.17E-6	6.28E-6 ±0.36E-6	6.48E-6 ±0.40E-6	2.71E-6 ±0.04E-6	5.94E-6 ±0.14E-6
10 by 10	7.03e-06	4.40e-06	7.25e-06	6.19e-06	2.94e-06	6.05e-06

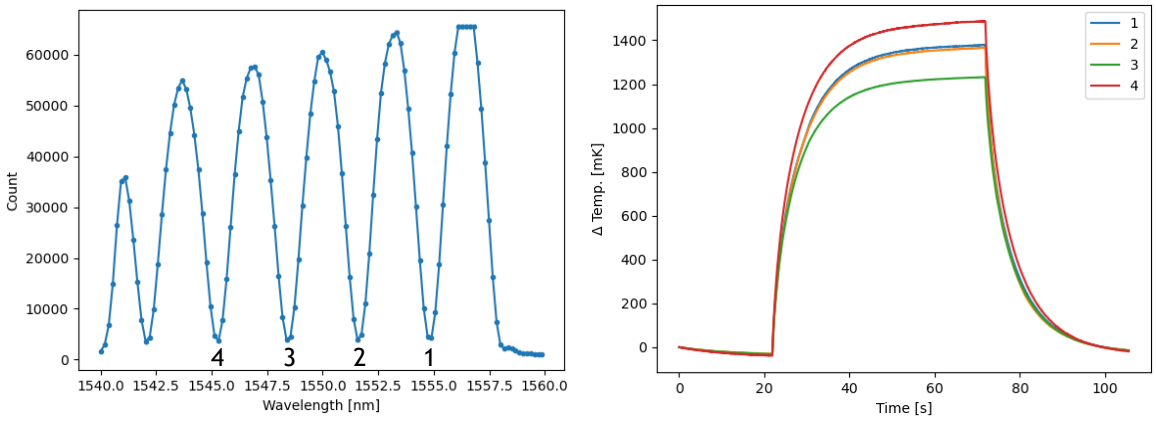

Figure 103 Left: raw spectra data of a time-series data point. Right: entire time-series data of the raw spectra processed to be the temperature changes. Different valleys show different results.

cases, for different FOBs, with different equipment, and at DIII-D testing data. Although this should be accounted for in the calibration from the averaged values, it could have unforeseen consequences to the results. In addition, it is not clear why different valleys have different result to the analysis.

A linear regression on different valleys was tried to match the results. One of the valley values were set as a reference to be aligned with. However, the method did not work at all where the deviations become significant after heating / temperature changes. Also, the differences seem to depend on the time as well as the values. A neural network regression on different valleys was tried to match the results as well. This was done to account for the possible non-linear aspects of the problem. However, the method did not work well like the previous method. The time dependance was difficult to account for.

A new analysis technique for raw spectra data was developed to avoid the problem of having the different results for the different valleys. This method utilized the Fourier transform of the raw spectra data. This is possible since the raw spectra data is an interference spectrum showing a periodic feature. The result of the Fourier transform of the raw spectra is data (amplitude and phase) in cycle/nm or 2π/nm space (Figure 104). One can see the major component with a determined cycle/nm value. Also, there are noise and other components present that could be resulting the differences between the valleys. If one follows the phase change of the major component, the phase change can be related to the wavelength change by using the determined/component cycle/nm. The phase change [radian] in radian transforms to the wavelength change by multiplying the inverse of the determined/component cycle/nm [nm/radian] (Figure 105). The wavelength change in the time-series will be related to the temperature change with the temperature sensitivity, which is the same as the valley fitting method.

Since there is only one major component, the problem of having different results for the different valleys is not a problem anymore. Nonetheless, using different equipment or settings was tried to see if the noise or the other components were eliminated to pinpoint the problem of deviations between the valleys. Removing or changing ports in CWDM, removing/changing the attenuator, changing the environment pressure, changing the light source power, changing the FOB, and changing the exposure

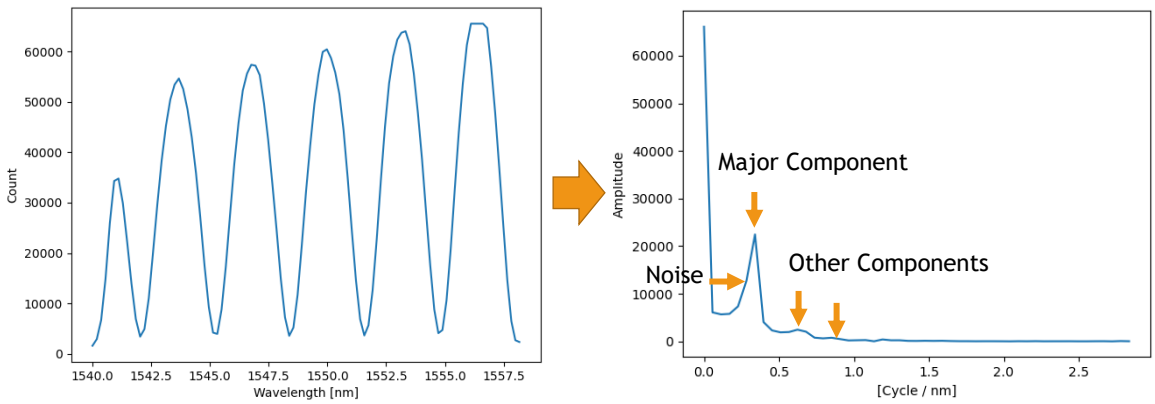

Figure 104 Left: raw spectra data of a time-series data point. Right: amplitude data of the Fourier-transformed spectra. The major component can be determined with the highest peak. Noise and other components are the suspects of the deviating results for the different valleys.

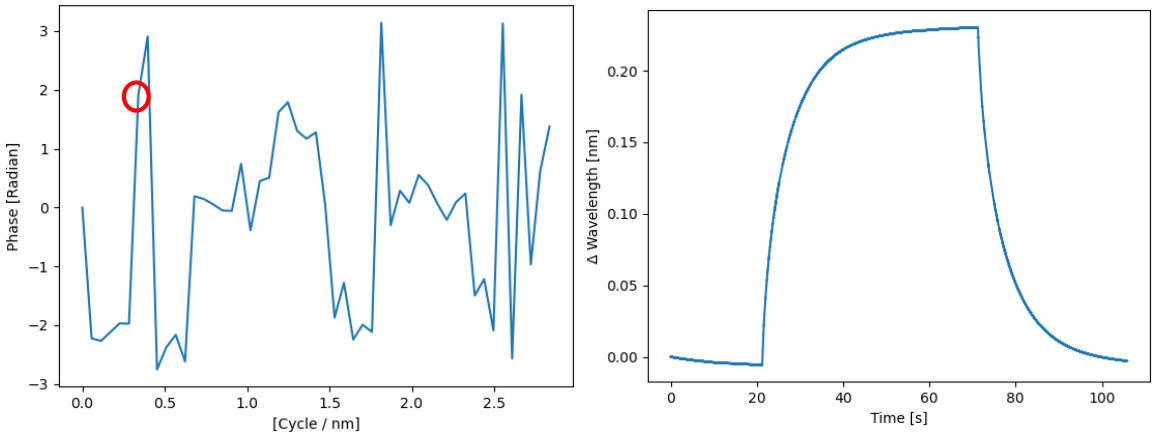

Figure 105 Left: phase data of the Fourier-transformed spectra. The major component in the red circle. Right: the phase change processed into the wavelength change using the major component cycle/nm for the entire time-series.

time on the spectrometer did not mitigate the problematic components. However, the longer silicon pilar FOB had higher major component or lower noise and amplitude of other components compared to the shorter FOB (Figure 106). Also, the longer silicon pilar FOB had the lower deviations (~6 mK) between the valleys compared to the short pillar FOB (~60 mK) with a similar heating. These results suggest that the noise and the other than major component are the reasons for the deviations between different valleys. In addition, the results suggest that the problem is inherent in the FOB rather than due to other equipment.

The Fourier transform method was much faster than the valley fitting method. For a data with 120 seconds, the valley fitting method took 14 minutes to analyze whereas the Fourier transform method only took about 1 minutes. This is a huge advantage for a between-shot (~10 minutes) analysis, and even a real time analysis is possible. Considering the number of FOBs for the 8-by-8 array (80 FOBs including the reference FOBs), this analysis method will be crucial for the between-shot analysis for the 6-by-6 or 8-by-8 FOB array. A LabVIEW code was developed to have a real time analysis of the raw spectra using the spectrometer recording code (Figure 107). The fast Fourier transform (FFT) code in LabView was used for the analysis. The latency between the data recording and the analysis was only around 1 ms, which showed that the real-time analysis using the Fourier transform method is possible.

However, the noise level of the Fourier transform method (~0.55 mK) was higher than the valley fitting method (~0.35 mK). Different FFT methods with different window functions were experimented to see if the noise level can be reduced to the valley fitting method level. Only non-uniform discrete Fourier transform (NUDFT) had a significantly lowered noise level (~0.4 mK). However, although NUDFT method removes the problem of having deviations in different valleys with acceptable noise level, it takes more 30 minutes for 120 seconds of data, which eliminates the biggest advantage of the Fourier transform method.

Fortunately, the noise equivalent power density (NEPD) does not seem to be affected by the noise level increase with the FFT method. The entire process of the analysis and calibration was done with the FFT method to calculate the NEPD in

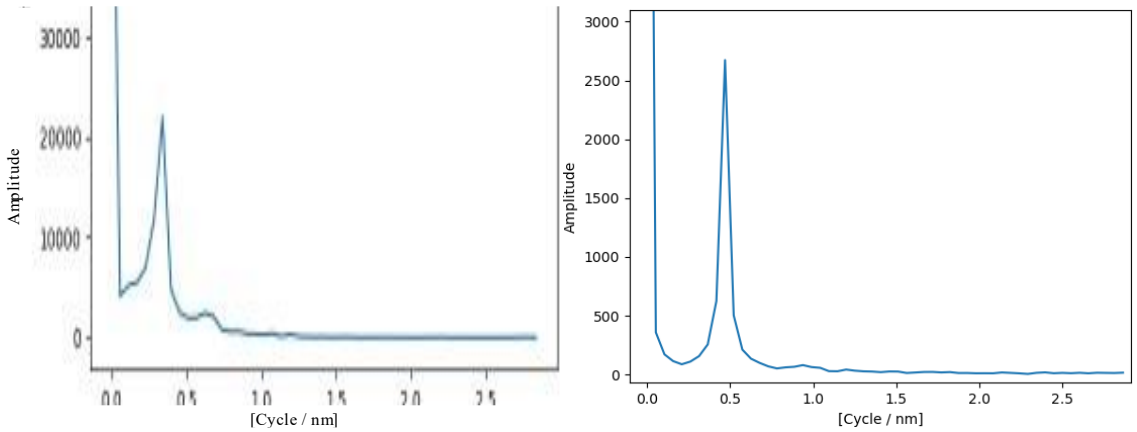

Figure 106 Left: amplitude data of the Fourier-transformed spectra of the short pillar FOB. Right: amplitude data of the Fourier-transformed spectra of the longer pillar FOB. The longer pillar FOB has a sharper major component with less noise and other components respectively.

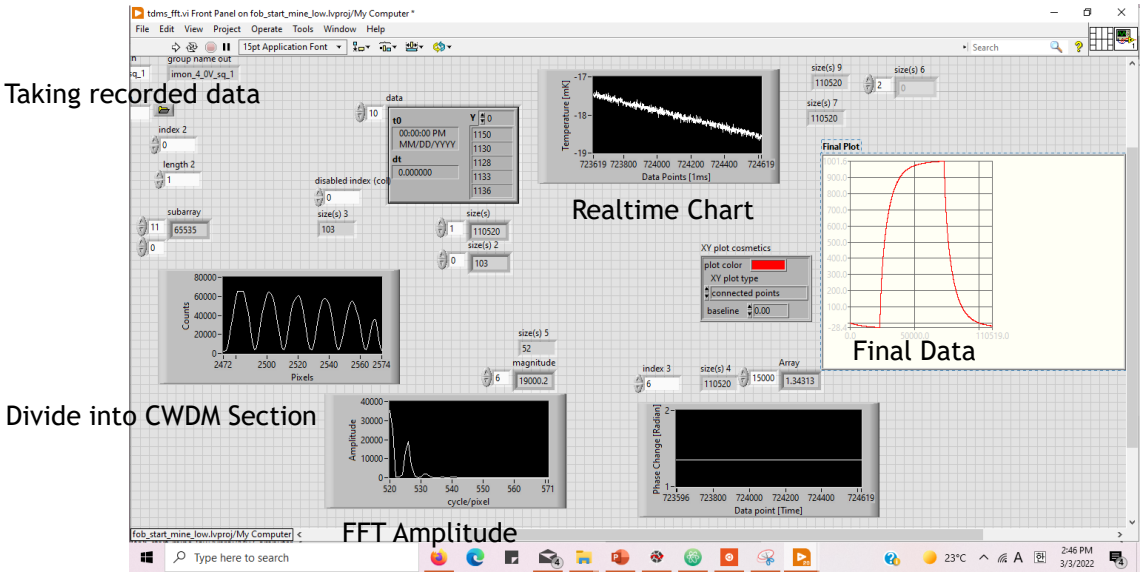

Figure 107 Real-time analysis LabVIEW code using the spectrometer recording code and the LabVIEW FFT. The latency between the recording and the analysis was only ~ 1ms.

comparison with the valley-fitting method (Figure 108). The results showed that the NEPD values are about the same (Table 17). This could be due to the FFT method removing interferences from the deviations of different valleys (the noise and other components), which compensated increased noise level, or it could be that the deconvolution calibration noise is overwhelming the noise from the raw spectra analysis. In addition, it can be seen from Figure 109 that the shapes of the calibrated results are the same for the two methods with a bit higher signal level for the FFT method.

The final method for the raw spectra analysis was a neural network regression using the entire raw spectra to result in one wavelength value. The input was the entire raw spectra, and the output was the corresponding averaged valley-fitting value. Even though the analysis speed (only 2 seconds for 120 seconds of data) was much faster than all other analysis methods, the noise level was the highest (1.5 mK). Also, this method does not fix the problem of having deviations for the different valleys because the method uses the averaged value for training.

Complex Regularization

A lower noise equivalent power density of a bolometer and more bolometer sightlines are the parameters to show that a bolometer system is better than the compared one. Both parameters would mean that emission profiles are better resolved by the system compared to the other. It has been shown that the FOB result in a lower noise equivalent power density compared to the resistive bolometer at DIII-D in the nuclear fusion environment. Also, the designs have more sightlines near the divertor, and were optimized for the 2D FOB array. The system will better resolve emission profiles near the divertor.

Another method to show that emission profiles are better resolved is comparing tomographic reconstruction results. A synthetic emission profile can be used for a new system with the same tomographic reconstruction method. As mentioned at the end of the last chapter, DIII-D has a long-used tomographic-reconstruction code that has been the "workhorse" to get the emissivity profile for the resistive bolometers. The DIII-D code reconstructs an emission profile with the following steps [48]. First, the code fits the core

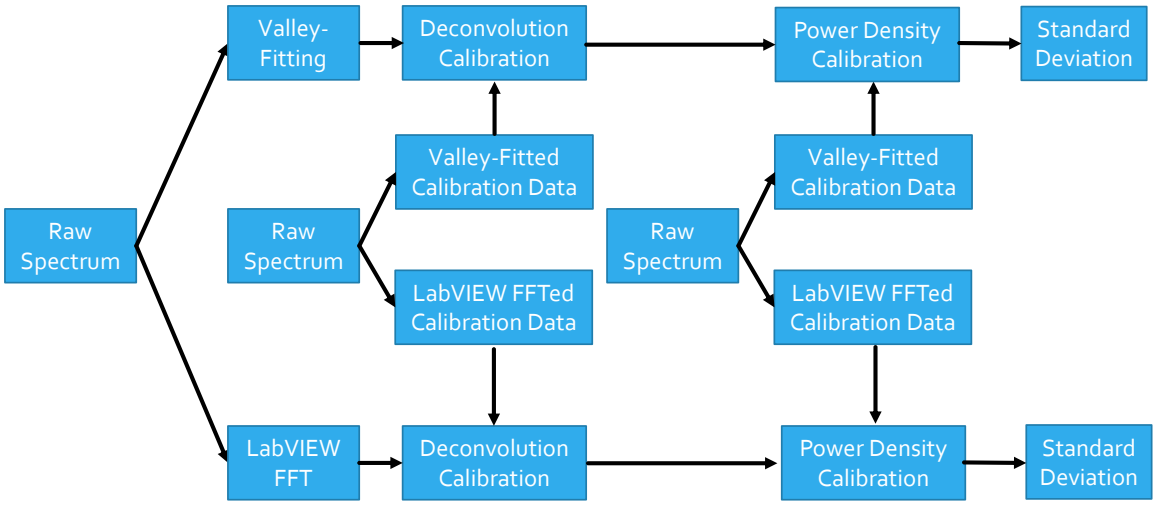

Figure 108 Entire flow chart for NEPD calculations comparing between the valley-fitting method and the FFT method.

Table 17 NEPD Value Comparisons Between the Valley Fitting Method and FFT method

Averaging Time	**Valley Fitting NEPD [W/m^2]**	**FFT NEPD [W/m^2]**
20 ms	0.4662	0.4664
40 ms	0.2643	0.2607

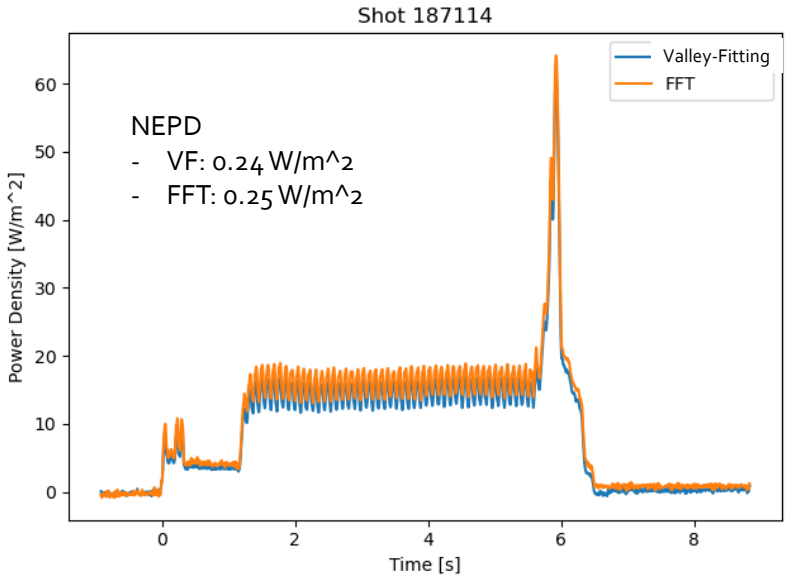

Figure 109 Comparison of calibrated results for the valley-fitting method and the FFT method for shot 187144. The shapes are exact match, but a difference in the signal levels.

radiation to a spline function of magnetic flux with least squares fit. The result is then subtracted from the divertor viewing chords. A similar process will be conducted for the FOB array as well that was mentioned in the first section of this chapter. (The tomographic reconstruction results from the resistive bolometers will be implemented with the limitation of above the region of interest. The FOB array measurements will be forward-modelled and subtracted from the total measurements to exclude the plasma radiation contribution from above the region of interest.) The divertor profile is then fit to a 2D spline as a function of magnetic flux and distance from divertor floor. The magnetic-flux structure for the process is reconstructed by EFITD code [62]. The code is built using Interactive Data Language. Using the method for the 2D imaging FOB array will required new code developments. Since synthetic emission profiles and forward-modelling FOB measurements are done with CHERAB, which is built using python, the IDL script will need to be translated into Python to be exact.

Rather than copying the code to Python, the author developed a tomographic reconstruction code using the FOB array measurements. Using the CHERAB package with the optimized design, the sensitivity matrix is calculated for the region of interest. For each shot, the EFIT profile from EFITD code will be used to create an intricate regularization relating to the magnetic fields. First, the flux data from the EFIT profile, which has a coarse grid, will be linear interpolated to the finer grid of the sensitivity matrix, or the EFIT flux profile with the finer grid matching the sensitivity matrix will be produced from the EFITD code. Using the flux data for the finer grid, the regularization will be created where the emissions are more likely to be along or parallel to the magnetic field lines. Then, using the sensitivity matrix, the FOB measurements, and the regularization will be used for an iterative inversion algorithm mentioned in the previous chapter to get the inversion result. The non-negative least square method was chosen because it was the method used for the DIII-D resistive bolometer inversion process and it had an acceptable performance from the testing. In addition, a limitation where the sensitivity is zero at after normalized magnetic flux was imposed to have no radiation at the locations with higher than 1.3 normalized magnetic flux (Figure 110).

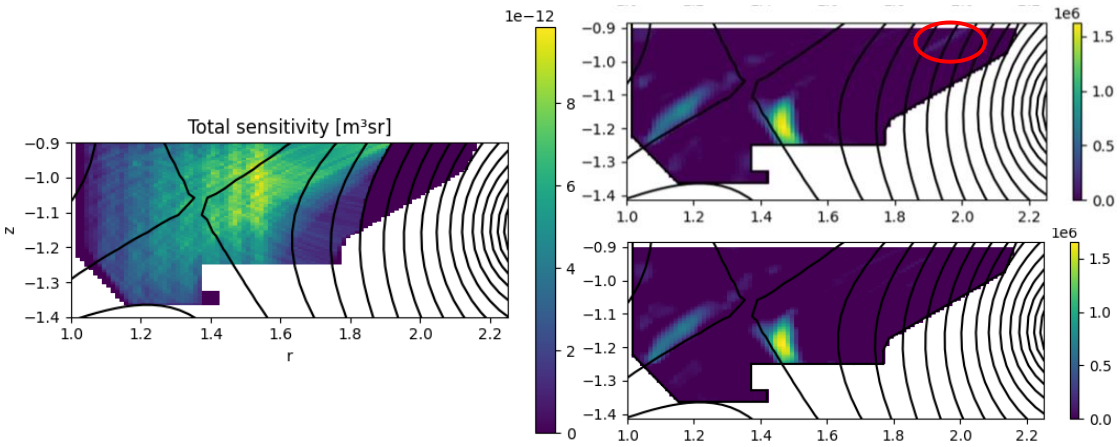

Figure 110 Left: zero sensitivity limitation at higher than 1.3 normalized magnetic flux. Right: inversion results with top – without the limitation and bottom – with the limitation. The emissivity present at the region with higher than 1.3 normalized magnetic flux is gone with the limitation.

More details on the complex regularization are as follows. With the normalized magnetic flux data on the finer grid, the algorithm selects a pixel in the grid and searches nearest 11 by 11 pixels with less than 0.5% difference in the normalized magnetic flux. The regularization is built to spread the emissivity of the selected pixel to the pixels with 0.5% difference (Figure 111). Using the regularization, the spread will be along or parallel to the magnetic fields. Another regularization investigated was to have a similar effect to the limitation. The pixels with higher than 1.3 normalized magnetic flux had higher costs to be less likely to have an emission whereas the pixel with below 1.3 normalized flux had lower cost to be more likely to have an emission (Figure 112). The private flux region and the core had zero cost to be neutral. However, this regularization did not work well to remove the emission from the region with higher than 1.3 normalized magnetic flux. In addition, the regularization broke the iterative inversion algorithm to have completely wrong results. So, this regularization was abandoned.

The first problem with the complex regularization and the iterative inversion algorithm was that it required a regularization strength for the inversion. Although "along the magnetic field line" regularization itself and the limitation have physical reasons, the regularization strength is arbitrary. The regularization strength value is determined by trial and error to find the best value. Synthetic or example emission profiles was used to forward-model the measurements of the FOBs. Different regularization strengths were tried for the inversion process. The inversion results with different regularization strengths were compared to the original synthetic emission profiles to quantify the performance and select the best regularization strength. The strength value of 1E-14 showed the best performance. In any case, the value has no physical ground.

The second problem with the complex regularization and the iterative inversion algorithm was the time required for one data point in time-series. Although the iterative tomographic reconstruction algorithm relatively optimized, it takes about 30 seconds with the finer grid and the regularization, which means that only about 20 data points in the time-series will be analyzed during between shots. The biggest bottleneck in time is due from creating the regularization. It takes couple of minutes to create the regularization from one EFIT profile. The EFIT profiles during a plasma operation could change

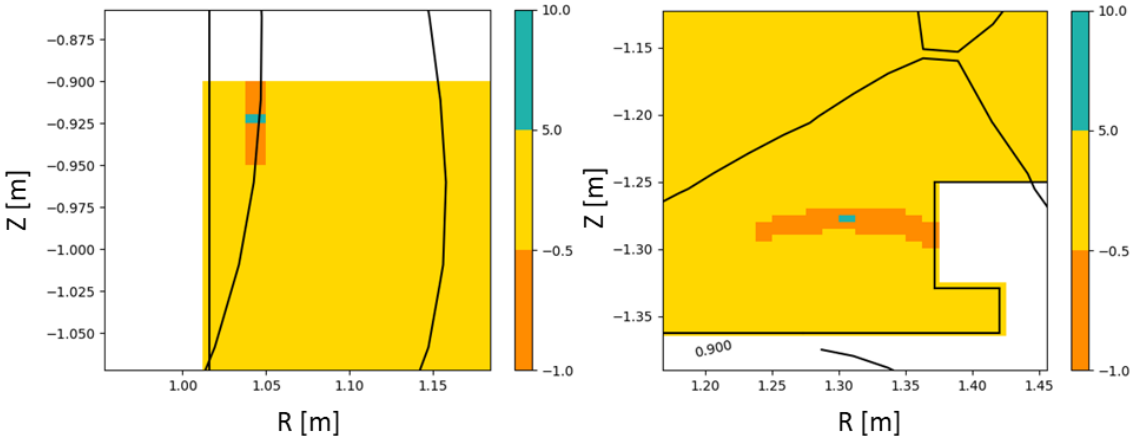

Figure 111 Examples of the “along the magnetic field line” regularization.

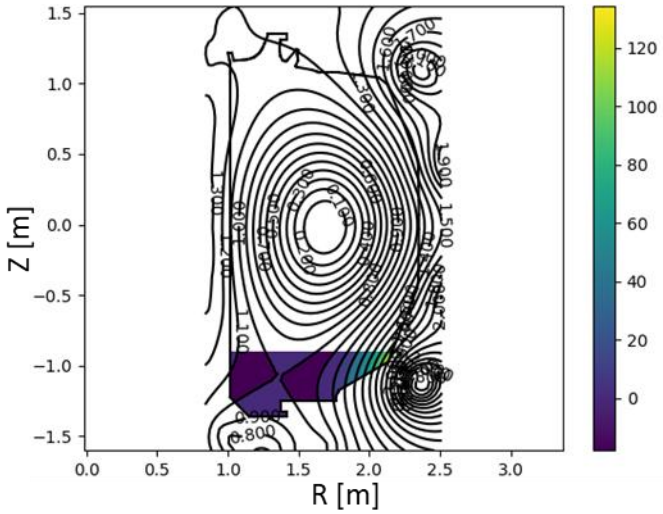

Figure 112 Regularization to limit plasma emissions at pixels with higher than 1.3 normalized magnetic flux.

significantly that one regularization from one EFIT profile will not be enough. This means that there will be only two to three inversion results will be possible between shots. To avoid the two problems, the neutral network inversion methods were explored, which will be discussed in the next section.

The original plan was to implement the variance calculations of the maximum likelihood method. The work at JET tokamak successfully implemented the ML reconstruction method with the variance calculations (Figure 113) [70]. The variance is critical discussing the plasma radiation structures since the tomographic reconstruction process is an ill-posed problem without a unique solution. With variances, it will be possible to convince any aspects related to plasma radiation structures that they are real. For instance, a location shift (change in distance) of a substructure outside the variance will be accepted as a real change. Also, the variance will help determine if the smaller details like shape (or corresponding volume) is an artifact of noise or a real measurement. However, there are the variance due to the random noise and the variance due to the inversion. The variance due to the random noise will be able to be determined by injecting random noise values to the measurements and performing the inversions. The multiple inversion results with different noise values will show the variance. However, the variance due to the inversion is much harder to quantify. This is because the inversion results will change significantly with the plasma radiation locations and shapes. It wasn't clear if and how the ML method could predict the variance due to the inversion process. So, the variance from the inversion was left as unknown of the current inversion method.

Neural Network Inversions

Neural network inversions are investigated to overcome the two problems with the regularized iterative inversion method. The neural network inversion method does not require any arbitrary parameter. As the neural network is trained with the training data, the inversion results from the neural network are automatic that nothing can be changed. In addition, the neural network is very fast at predicting results from an input as seen previously. As a tradeoff for the fast prediction, the neural network requires training, which usually takes a long time and requires a huge set of training data. As mentioned in

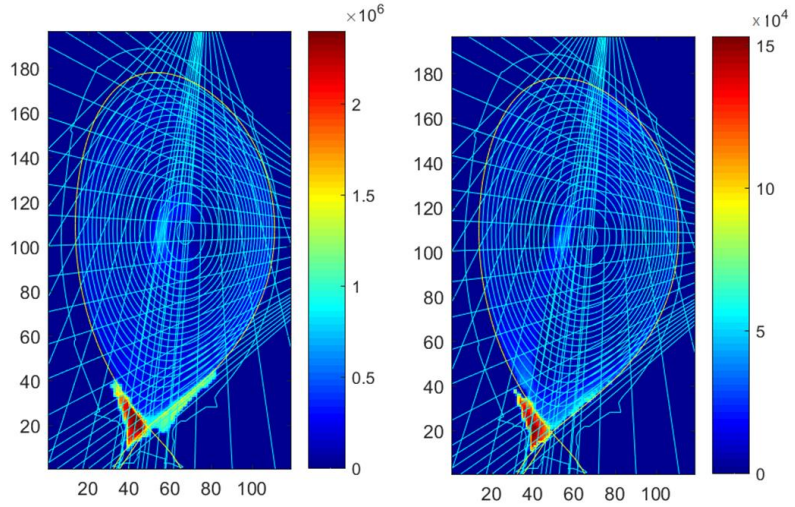

Figure 113 ML reconstruction (left) and the corresponding variance image (right) [70]

the background, the neutral network inversion for this research was performed with TensorFlow Keras library in Python

The neural network inversion was performed for bolometers at other fusion plasma machines such as JET [77] and C-2W [78]. The JET case was trained with tomograms from the iterative inversion results from the resistive bolometers, ~3000 training data, the resistive bolometer measurements as the inputs. The neural network consisted of several "up-convolution" layers with the sublayers consisting of up-sampling, convolution layers, etc. The result showed 2-4% average error on each pixel. The C-2W case used simulated 2D profiles (simple annular structure), 2000 training data, the synthetic diagnostic measurements as the inputs. The neural network consisted of 2 dense layers and 5 convolution layers. The result showed ~98% accuracy for similar 2D profiles, but only 60% accuracy for exotic profiles.

One thing noticed from the previous work is that both never mentions the use of the sensitivity matrix, which is used in the iterative inversion methods and holds a vital information about the measurements. Rather than following the previous cases, two different methods utilizing the sensitivity matrix were investigated for the 2D FOB array. The different methods were required due to the different situation for the 2D FOB array. First, there were no detailed tomograms from DIII-D resistive bolometers to satisfy the high spatial resolution planned for the 2D FOB array. Also, the neural network inversion for the 2D FOB array is not trying to replicate the resistive bolometer inversion results. Synthetic 2D plasma radiation profiles need to be created to train the neural network inversion for the 2D FOB array. However, the variety and the complexity of the plasma radiation profiles at the divertor of the DIII-D need to be higher than the C-2W case.

The first method utilized the sensitivity matrix by turning the sensitivity matrix into a pseudo inverse matrix. The relationship between the sensitivity matrix, the emissivity profile, and the measurements is shown by the equation,

$$[Sensivitity\ Matrix][Emissivity\ Profile\ Matrix] = [Measurements]$$

Since the sensitivity matrix can be a singular matrix, the pseudo inverse matrix of the sensitivity matrix was used to include the sensitivity matrix with the measurements as the inputs. The pseudo inverse matrix was calculated using the equation,

$$([Sens.Matrix]^T[Sens.Matrix])^{-1}[Sens.Matrix]^T$$
$$= [Sens.Matrix\ Pseudo\ Inverse]$$

The output for the method was the phantom (synthetic) plasma radiation profile. The neural network for the method included three dense rectified linear unit (ReLU) layers (Figure 114).

The second method utilized the sensitivity matrix by using the iterative inversion method. Rather than using the complex regularization that takes a long time to create, a simple (left-right-up-down smoothing) predetermined regularization was used for the iterative inversion process. The results from the iterative inversion process were the input for the neural network. The output was the same phantom (synthetic) plasma radiation profiles. For this method, the neural network consisted of two convolution layers and two dense ReLU layers (Figure 115).

The training data consisted of three different types of the synthetic plasma radiation profiles (Figure 116). The first type was the synthetic plasma radiation profiles with two radiation blobs. The central locations, the width/length of the blobs, and the emissivity levels were randomized. The second type was the same as the first type except that it had three radiation blobs. The third type was completely randomized radiation profiles for each pixel. 6000 training data were created for each type resulting in 18000 total training data. The training was performed with the epochs value of 100 (using the training data 100 times) and the batch value of 300 (300 training data at a time through the neural network for the training speed and the averaging effect).

Several measures to prevent overfitting was taken into place because of severe overfitting for earlier attempts. The overfitting was detected by comparing the accuracy for the training data and the validation data, which was not used in the training. After certain training iterations, the accuracy for the training data surpassed the accuracy for the validation data, which becomes steady or starts decreasing after certain iterations (Figure 117). This showed that the neural network started to overfit when the accuracy for the validation data reached the peak where the accuracy for the training data kept increasing. The result of the overfitting is that the accuracy of the neural network decrease for the data other than the training data, which can be seen as the accuracy for

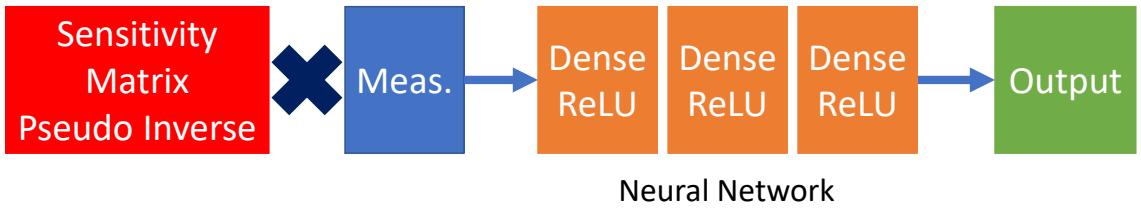

Figure 114 Neural network inversion method using the pseudo inverse of the sensitivity matrix and three dense ReLU layers.

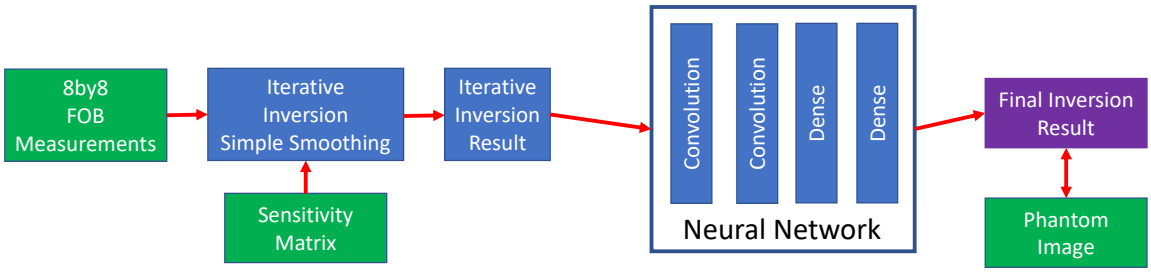

Figure 115 Neural network inversion method using the simple regularized inversion results and two convolution layers and two dense ReLU layers.

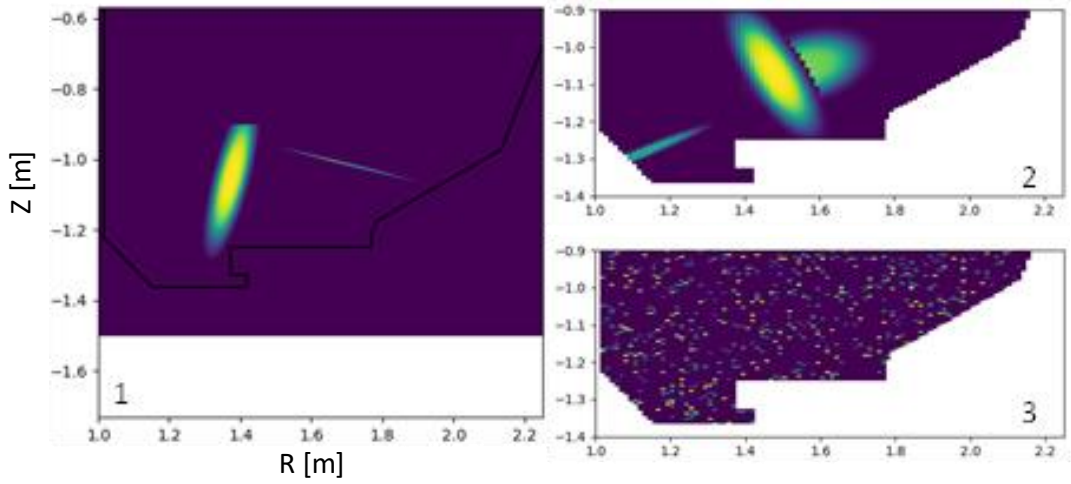

Figure 116 1: training data with two randomized radiation blobs, 2: training data with three randomized radiation blobs, 3: completely randomized training data.

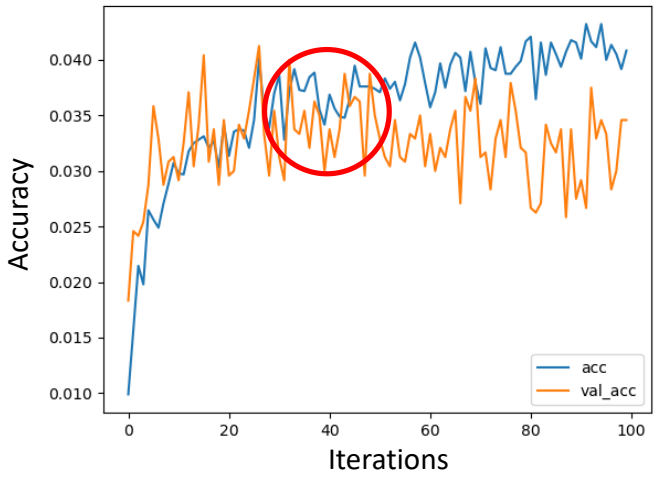

Figure 117 Evolution of the accuracy for the training data (blue) and the validation data(orange) with increasing training iterations. Can be used to detect the start of overfitting (red circle).

the validation data started to decrease. To avoid the overfitting, the training data number increased from 4000 to 18000. Increased the batch size from 100 to 300 that the overfitting was mitigated by the averaging effect. The dropout rate of 0.3 was used that the 30% of the neuron values were zeroed, which can mitigate the overfitting problem [79]. In addition, the training was stopped early when the accuracy of the validation data did not change for 10 iterations.

The preliminary results were promising using the two neural network inversion methods. The two methods were tested with the six plasma radiation profiles mentions before. The plasma radiation profiles were resolved relatively well with the two methods (Figure 118 and 119). The total radiated power calculations for the methods matched well with the phantom values within 10-20% (Table 18). The figures and the values were compared with the regularized iterative inversion method (simple up-down-left-right regularization). In addition, the variance map (Figure 120) for the entire region of interest including the random noise and the inversion process calculated using the validation data.

The two neural network inversion methods started to fail when the plasma radiation profiles were very different from the training data. Using the CIII measurement where there were long tails to the radiation, the neural network inversion methods could not predict the long tail of the plasma emission (Figure 121). This was believed to be due to the neural network biasing to the shape of an oval, which the training data followed. The next testing case was where the shapes were like the training data, but the emissivity distribution was different from the training data. The neural network inversion methods were only predicting the highly radiating part of the profiles (Figure 122). In addition, the total radiated power values were underestimated for the two neural network methods (phantom: 103344W, iterative: 108429 ±3431.8W, neural network 1: 67585 ±6051.0W, neural network 2: 7966699145 ±4643.5W). This was believed to be due to the neural network biasing to the distribution of the training data.

To avoid the biasing on the shape and the distribution of the plasma emission, the completely randomized radiation profiles (Figure 116, 3) were exclusively used to train the neural networks. The first method utilizing the pseudo inverse resulted in a background radiation (Figure 123, 2). This was possibly due to 300 batch size (averaging

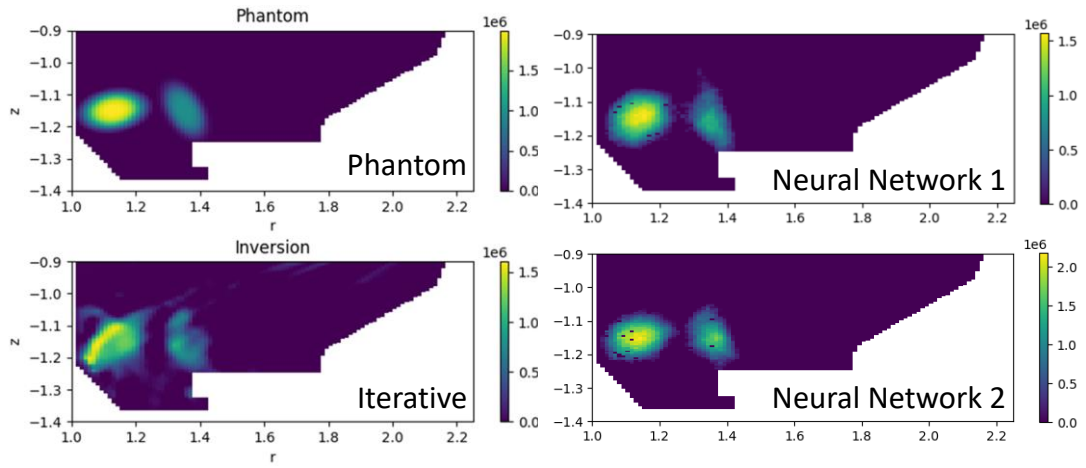

Figure 118 Inversion results for different methods including the phantom / original

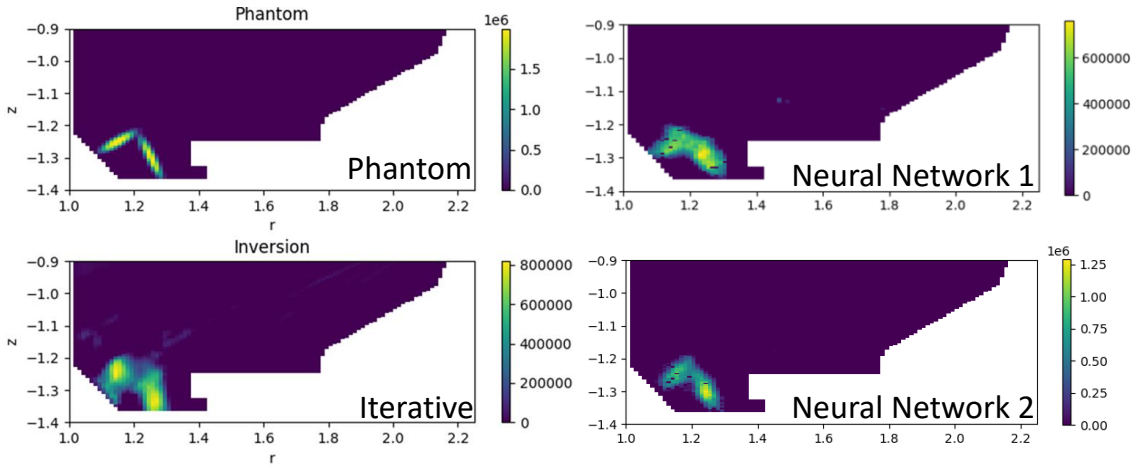

Figure 119 Inversion results for different methods including the phantom / original

Table 18 Total Radiated Power [W] Calculations for Different Inversion Methods

	Profile 1	**Profile 2**	**Profile 3**	**Profile 4**	**Profile 5**	**Profile 6**
Phantom	196661.2	663721.9	291240.8	407372.3	113019.9	80092.77
simple Iterative	218640.8	790982.5	312735.4	451954	130681.5	85627.88
Neural Network 1	190726.3	586271.9	240250.1	419706.8	73154.38	63680.58
Neural Network 2	180296.6	461764	300441.3	393715	108482.1	68056.03

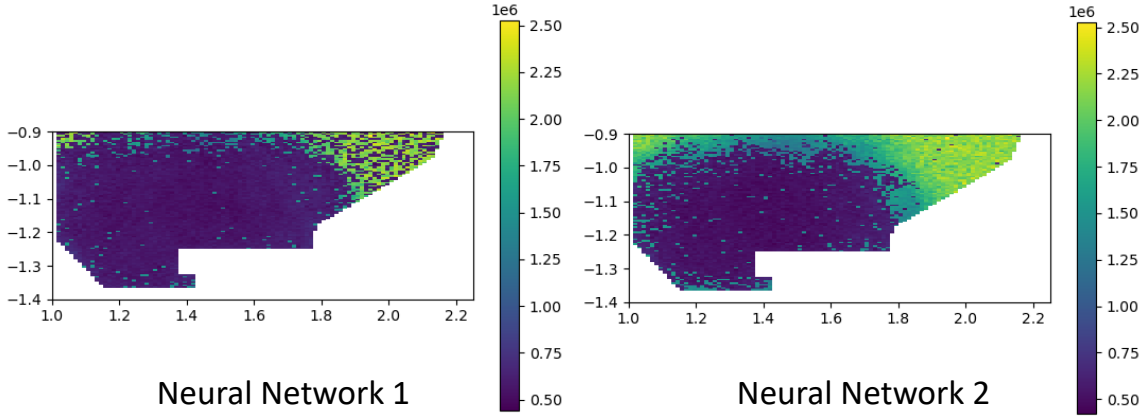

Figure 120 Variance maps [W/m3] for the color bars] for the two neural network methods. using the validation data.

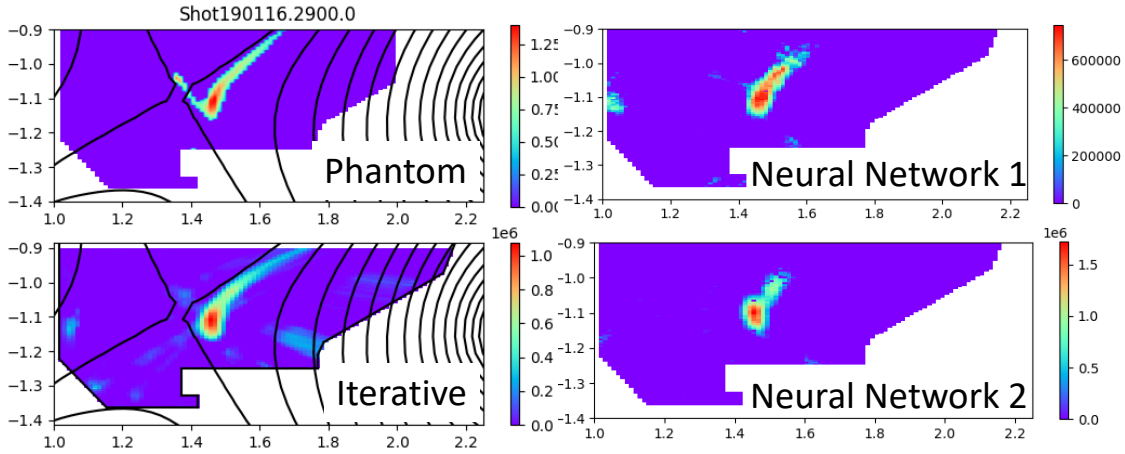

Figure 121 Inversion results for different methods including the phantom / original image created using CIII data.

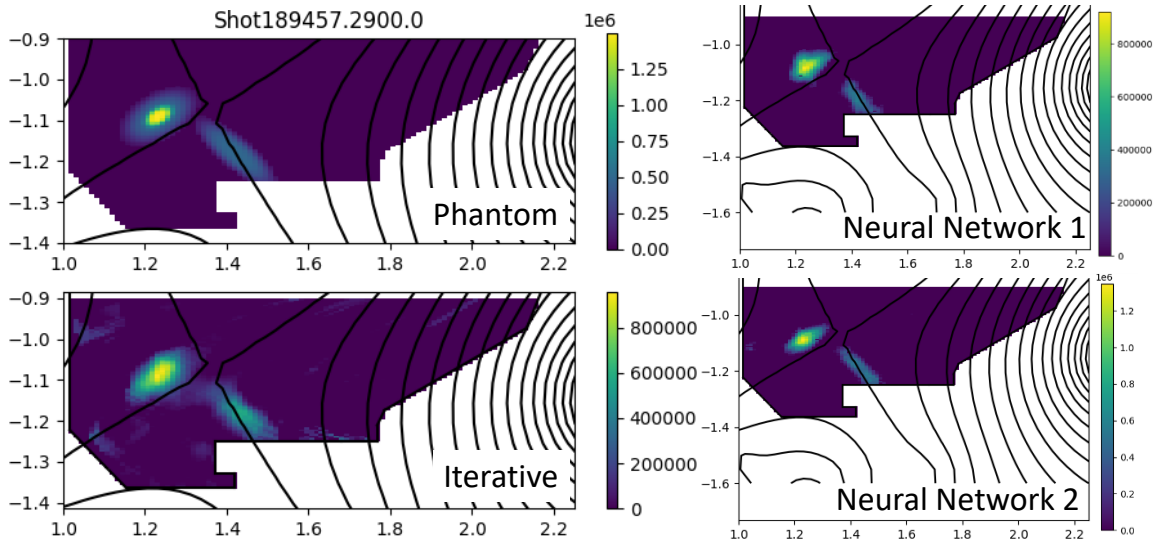

Figure 122 Inversion results for different methods including the phantom / original image created with different plasma emission distribution compared to the training data.

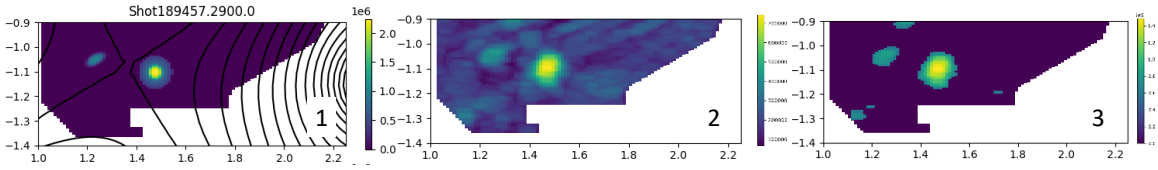

Figure 123 1: phantom image, 2: neural network inversion result from completely randomized training data, 3: post-processed data from the result.

effect) for the neural network training. Unfortunately, reducing batch size lower than 100 made the neural network not getting better after each iteration, which is possibly due to the training data being too random. As a jury-rigging fix, a threshold was imposed where any values lower than the threshold were truncated to zero. Next, the cleaned values were multiplied to match the peak value in the phantom (Figure 123, 3). The total radiated power values for the fixed data were within 30% of the phantom values. Also, the total radiated power values were not always underestimating like before. However, having the threshold and the multiplication constants was against the reason for using the neural network inversion method because the constants were arbitrary.

The second method of utilizing the simple regularized inversion method did not fix the problem. Also, other various means were tested to fix the problem. The tried means were changing the batch size, adding more layers to the neural network, standardizing the training data, using the FOB measurements as the input (like the previously reported cases), changing the loss function to match the FOB measurements rather than the phantom image, and a combination of the mentioned means. However, none of them fixed the problem, and most of them did not work at all (the neural network not getting better after each iteration). A better way of creating the training data that are more random, but still retains the possible emission structures and distribution will be required for the neural network inversion of the 2D FOB array.

Sectional Radiated Power Analysis

The radial cross section of the divertor region can be divided into four sections: inner leg, outer leg, core, and private flux regions (Figure 124, left). Analyzing the plasma radiated power into four different sections with details have important aspects to understanding the fusion plasma. As mentioned before, a plasma radiation profile is unique to the operating/plasma conditions. A difference in the radiated power at different sections show different operating and plasma conditions. For instance, the total radiated power could be similar, but where most of the radiated power is located could mean a completely different scenario. If most of the radiated power is located at the core, the core could be cooling due to the impurities that the performance of the fusion plasma

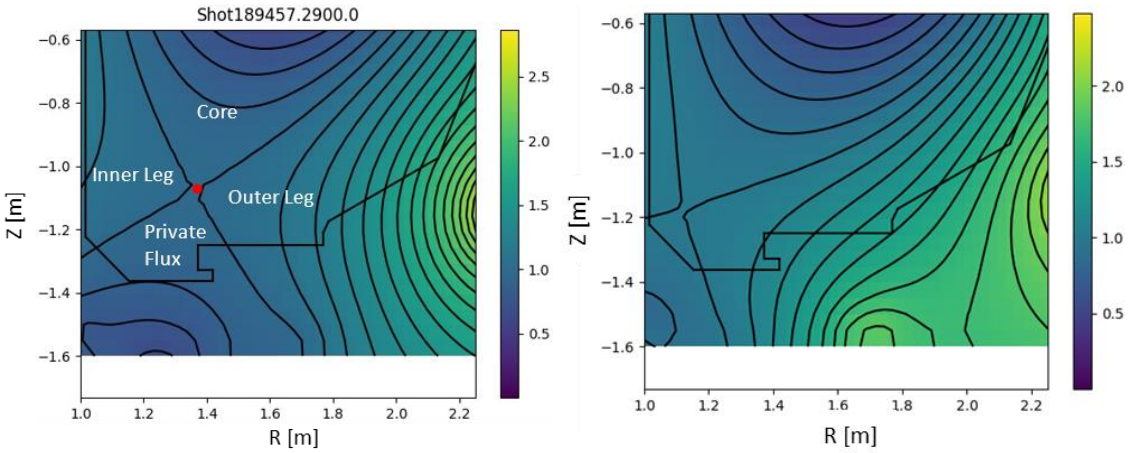

Figure 124 Left: EFIT magnetic reconstruction profile for the shot 189457 at 2900ms. Right: synthetic EFIT magnetic reconstruction profile for future experiments. Color bar: normalized magnetic flux value

might be deteriorating. Even with a within the divertor region without the core, where most of the divertor radiated power is located will mean a completely different scenario. A precise value for the sectional radiated power will help better analyze the plasma and operating conditions. Only a small change in the radiated power at the outer leg could have important implications to the divertor or the fusion plasma performance. In addition, it would be interesting to see in detail the radiated power during impurity injections at the private flux region where it is usually ignored.

Two EFIT magnetic reconstruction profiles were used to divide the plasma radiated power into four different region and have more plausible emission profile related to the magnetic reconstruction profiles. The first one is a common magnetic reconstruction profile, which is from the shot 189457 at 2900ms (Figure 124, left). The second one is a synthetic magnetic reconstruction profile that is a special case and will be used for future experiments (Figure 124, right). The second one is more extreme case where the outer leg is on the lower shelf with smaller divertor sections and private flux region. For dividing the sections, the normalized flux data from the EFIT profiles, which has a coarse grid, was linear interpolated to the finer grid of the region of interest, or the EFIT flux profile with the finer grid matching the region of interest can be produced from the EFITD code. The sections are divided by the rules: the inner leg is $r <$ X-point with the normalized magnetic flux > 1, the outer leg is $r \geq$ X-point with the flux > 1, the private flux region is $z <$ X-point with the flux ≤ 1, and the core is $z \geq$ X-point with the flux ≤ 1.

The first test case was where a circular radiation blob moved from the private flux region to the outer leg to the core (Figure 125). In addition, there was a small and low emitting radiation blob present at the inner leg. The moving blob did not change while moving through the different sections. The movements were divided into 30 steps. The performance of the optimized 8-by-8 FOB array, which is the most likely design to be implemented, was tested using the changing radiation profile. Four different inversion techniques were tested to see the performance. The first technique was the simple (left-right-up-down smoothing) regularized iterative method, and the second technique was the

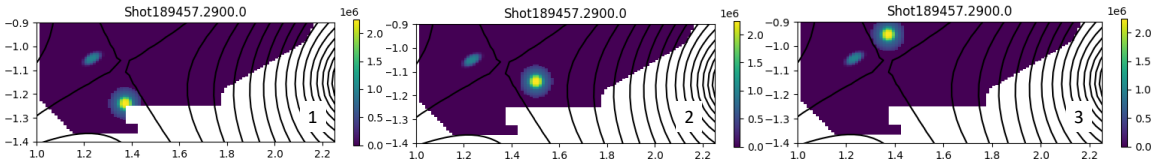

Figure 125 Synthetic plasma radiation profile changing from 1 to 2 to 3 with 30 steps.

complex (“along the magnetic field”) regularized iterative method. The other two were the two neural network inversion methods.

The iterative methods showed near perfect match to the phantom image radiated power divided into the four sections (Figure 126 and 127). The results showed that the optimized 8-by-8 FOB array has a high spatial resolution for analyzing the radiated power that are divided into the sections. The moving emission was circular that had no relation to the magnetic field other than the location. Still, both methods predicted the radiated power in great details. When a detailed analysis on the radiated power is required for a plasma radiation profile predicting highly emitting emission with the location like the moving blob, the iterative methods will be used with a good confidence.

Unlike the iterative methods, the neural network methods did not predict the radiated power well (Figure 128 and 129). The total radiated power values were underestimated for the most case as expected from the previous testing. Since the moving emission had different emissivity distribution than the training data, the results are understandable. The sectional radiated power values were sometime matching, but a lot of cases were underestimated. These results show that the neural network inversion methods cannot be used for the radiated power analysis. Again, this was expected from the discussion from the previous section, but the moving emission confirmed the expectation with more thorough testing.

The second test case was using the different EFIT magnetic reconstruction profile where the radiation blob moved from the outer leg to the core and up (Figure 130). In addition, there was a small and low emitting radiation blob present at the inner leg. The moving blob did change while moving through the sections. The movements were divided into 20 steps. It was to see the performance of the optimized 8-by-8 FOB array in more extreme cases. Only the iterative inversion techniques were tested for this case.

The iterative methods for this case did not result in as perfect match to the phantom image radiated power as the previous case (Figure 131 and 132). The inner leg sectional radiated power values did not match well, although the total and other sectional radiated power values matched well. This was possibly due to the inner leg emission too close to the wall. This can be seen from the sightlines plot and the sensitivity plot (Figure

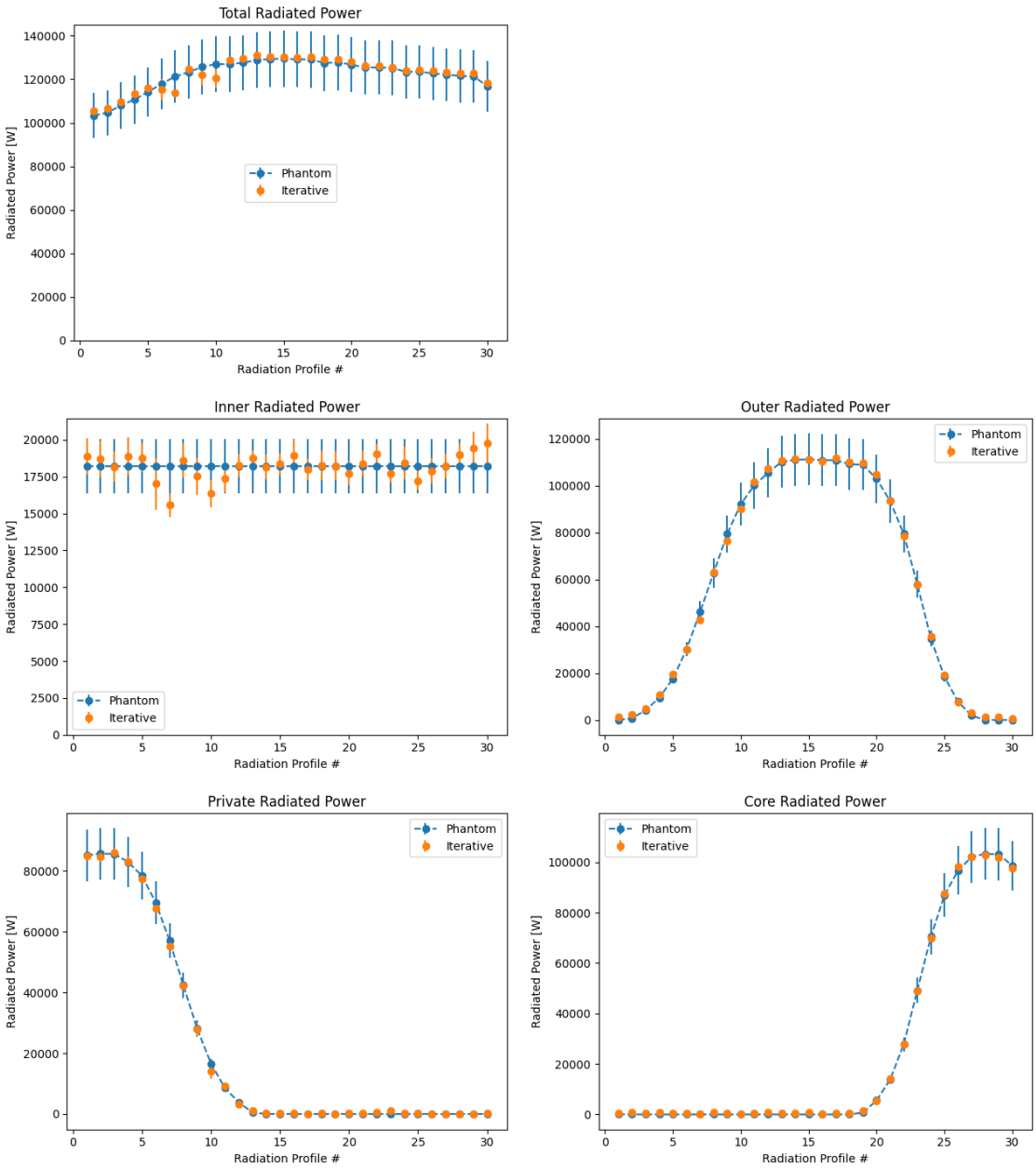

Figure 126 Radiated power analysis for the moving emission using the simple regularized iterative method. The total radiated power and the sectional radiated power compared with the phantom (exact) values. The phantom values included 10% error bar.

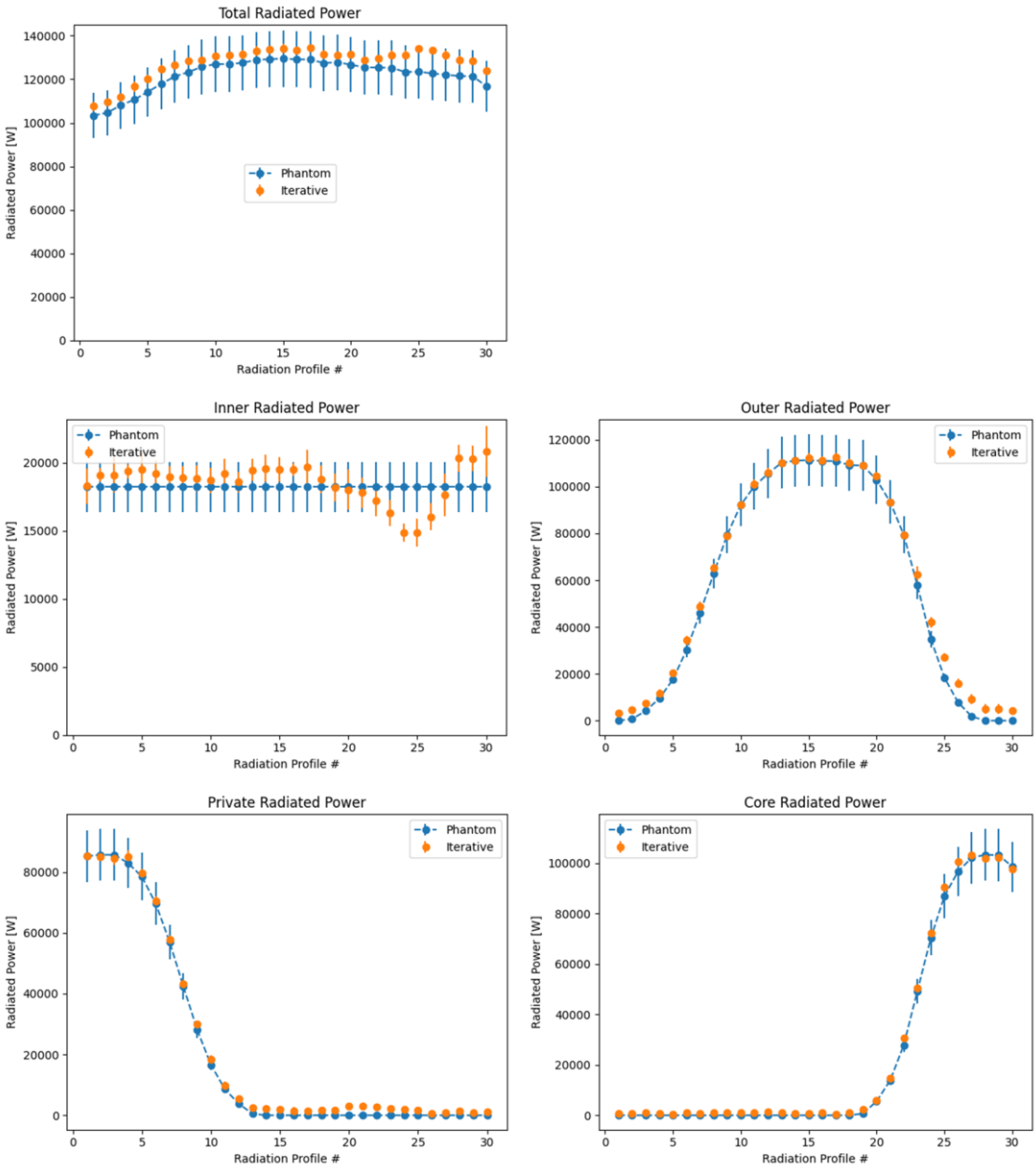

Figure 127 Radiated power analysis for the moving emission using the complex regularized iterative method. The total radiated power and the sectional radiated power compared with the phantom (exact) values. The phantom values included 10% error bar.

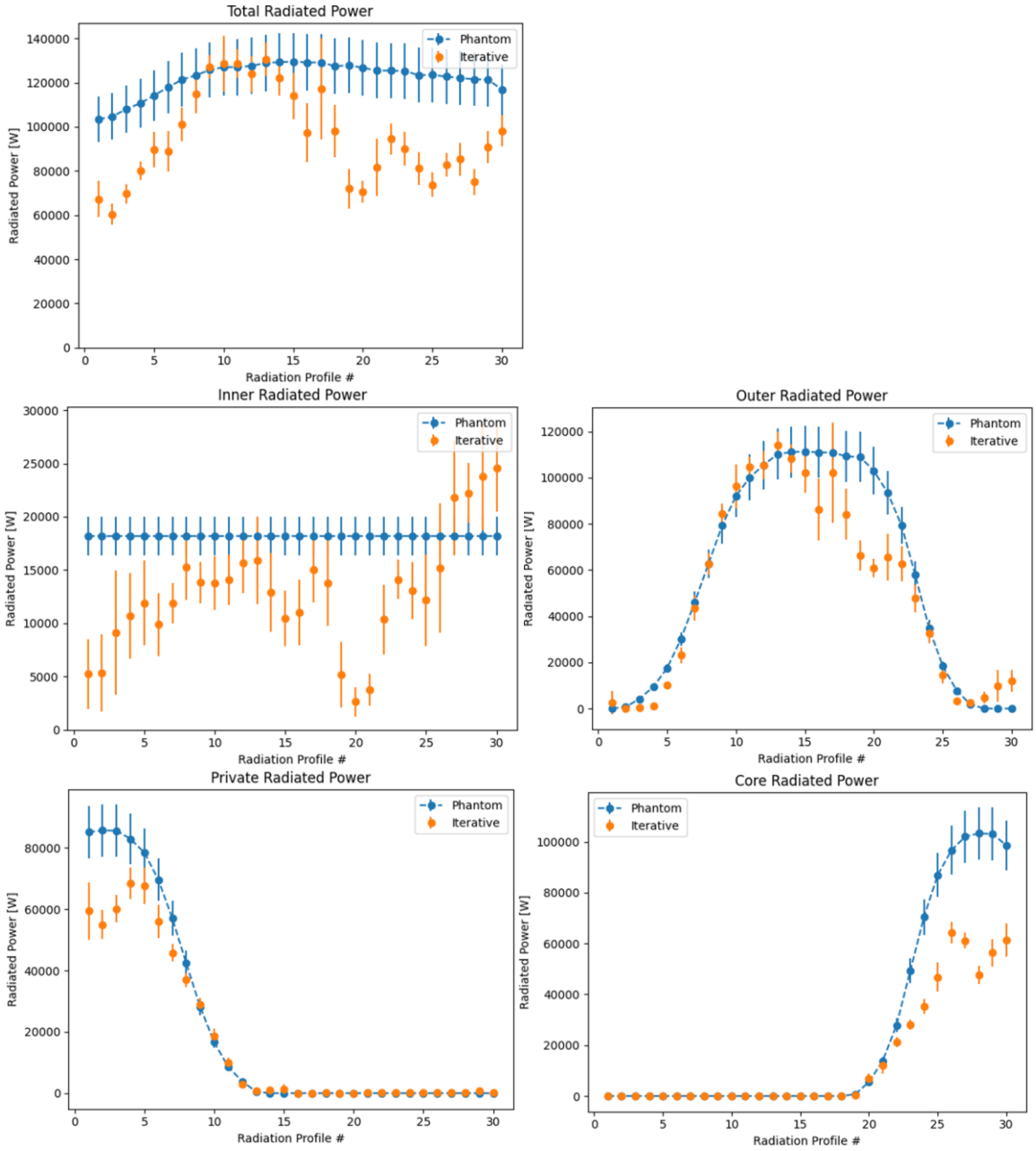

Figure 128 Radiated power analysis for the moving emission using the neural network method 1. The total radiated power and the sectional radiated power compared with the phantom (exact) values. The phantom values included 10% error bar.

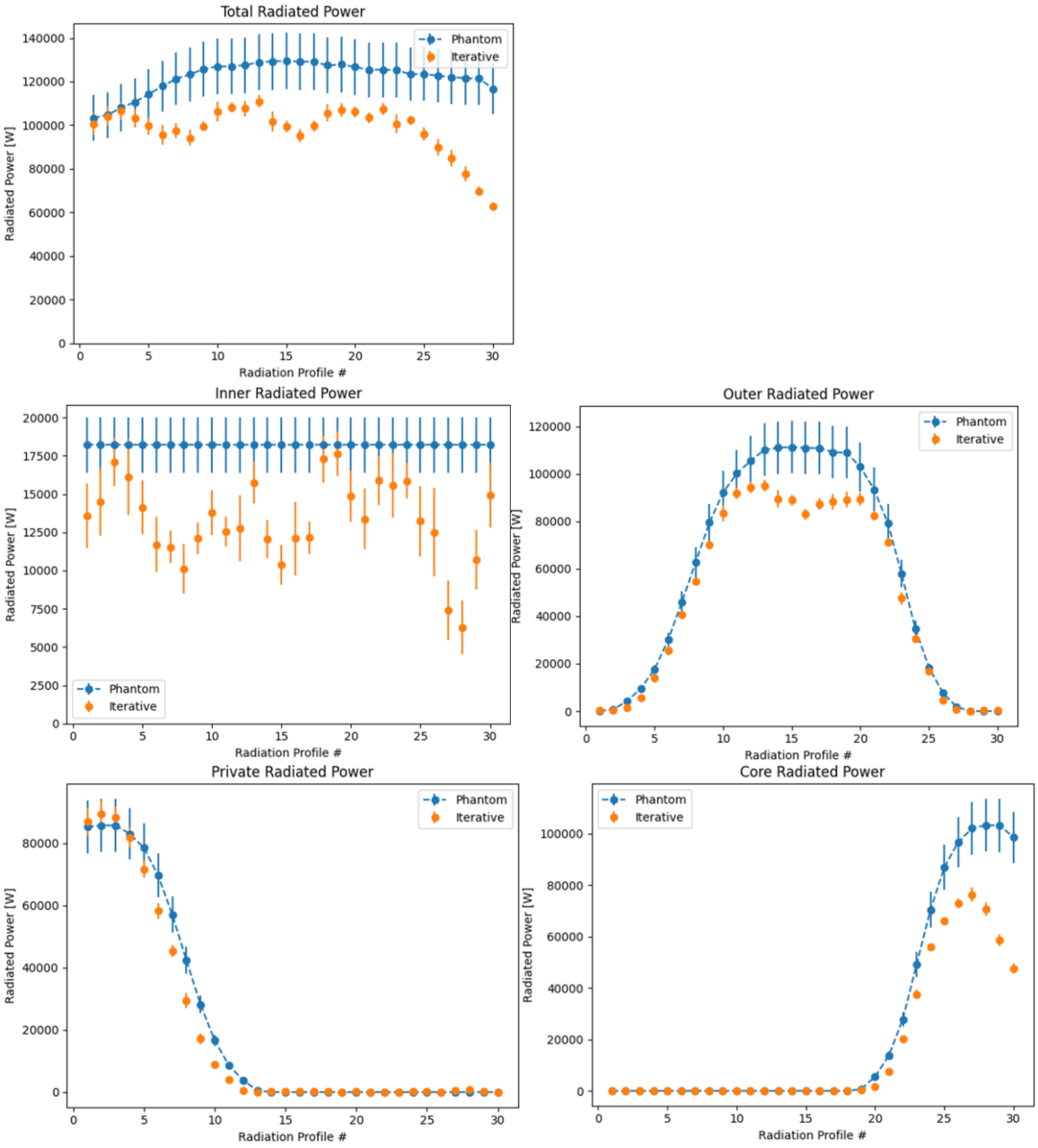

Figure 129 Radiated power analysis for the moving emission using the neural network method 2. The total radiated power and the sectional radiated power compared with the phantom (exact) values. The phantom values included 10% error bar.

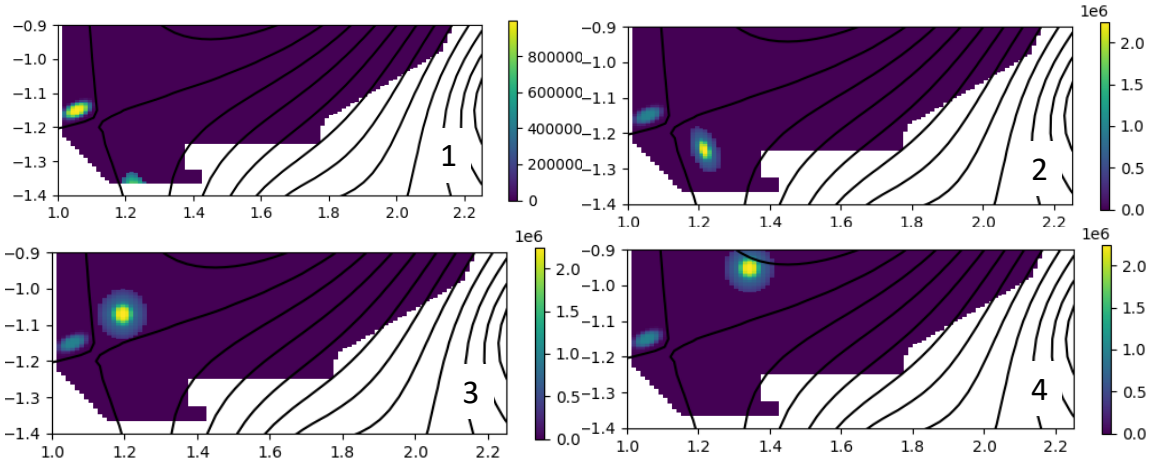

Figure 130 Case 2: synthetic plasma radiation profile changing from 1 to 4 with 20 steps.

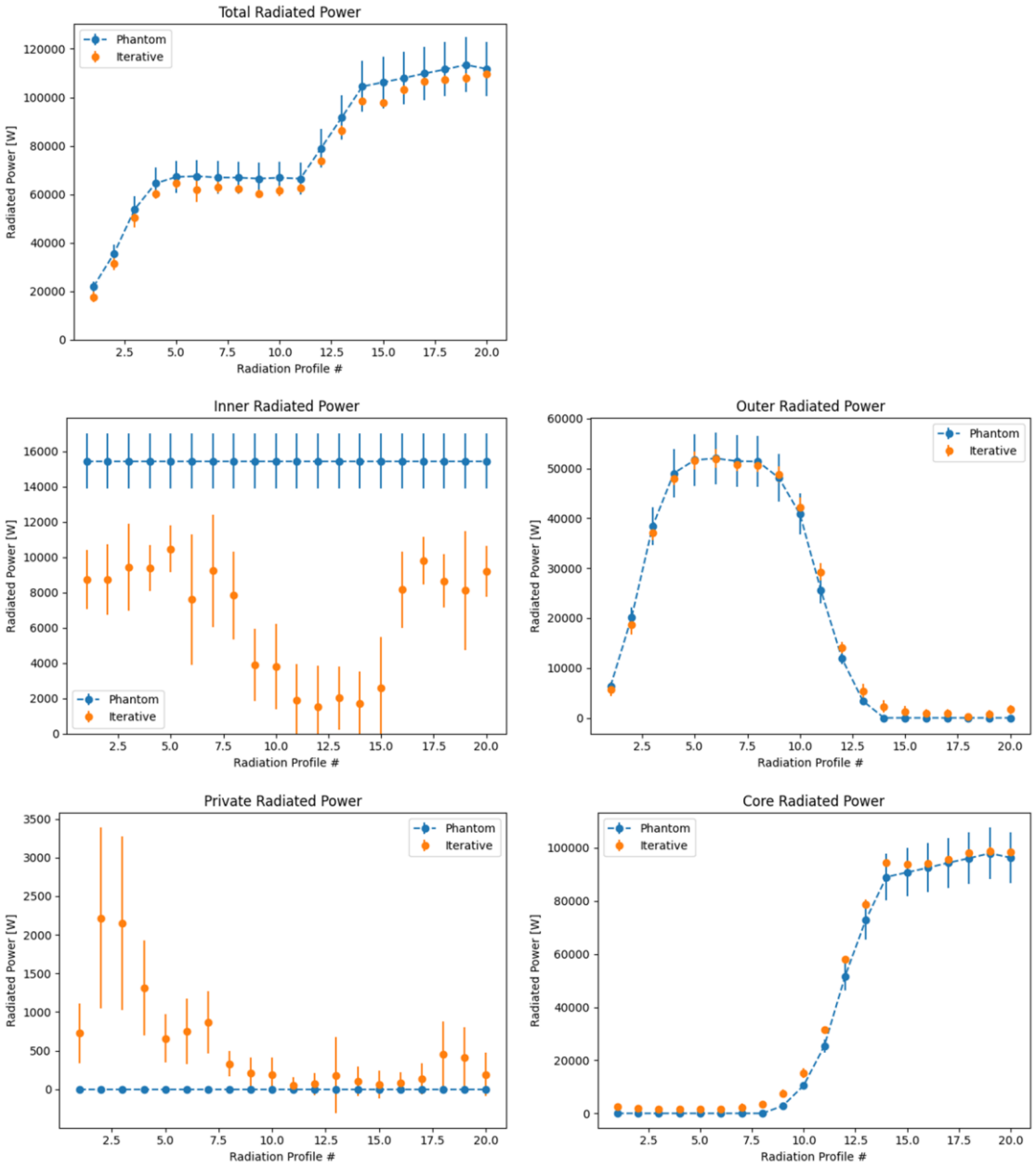

Figure 131 Radiated power analysis for the second case using the simple regularized iterative method. The total radiated power and the sectional radiated power compared with the phantom (exact) values. The phantom values included 10% error bar.

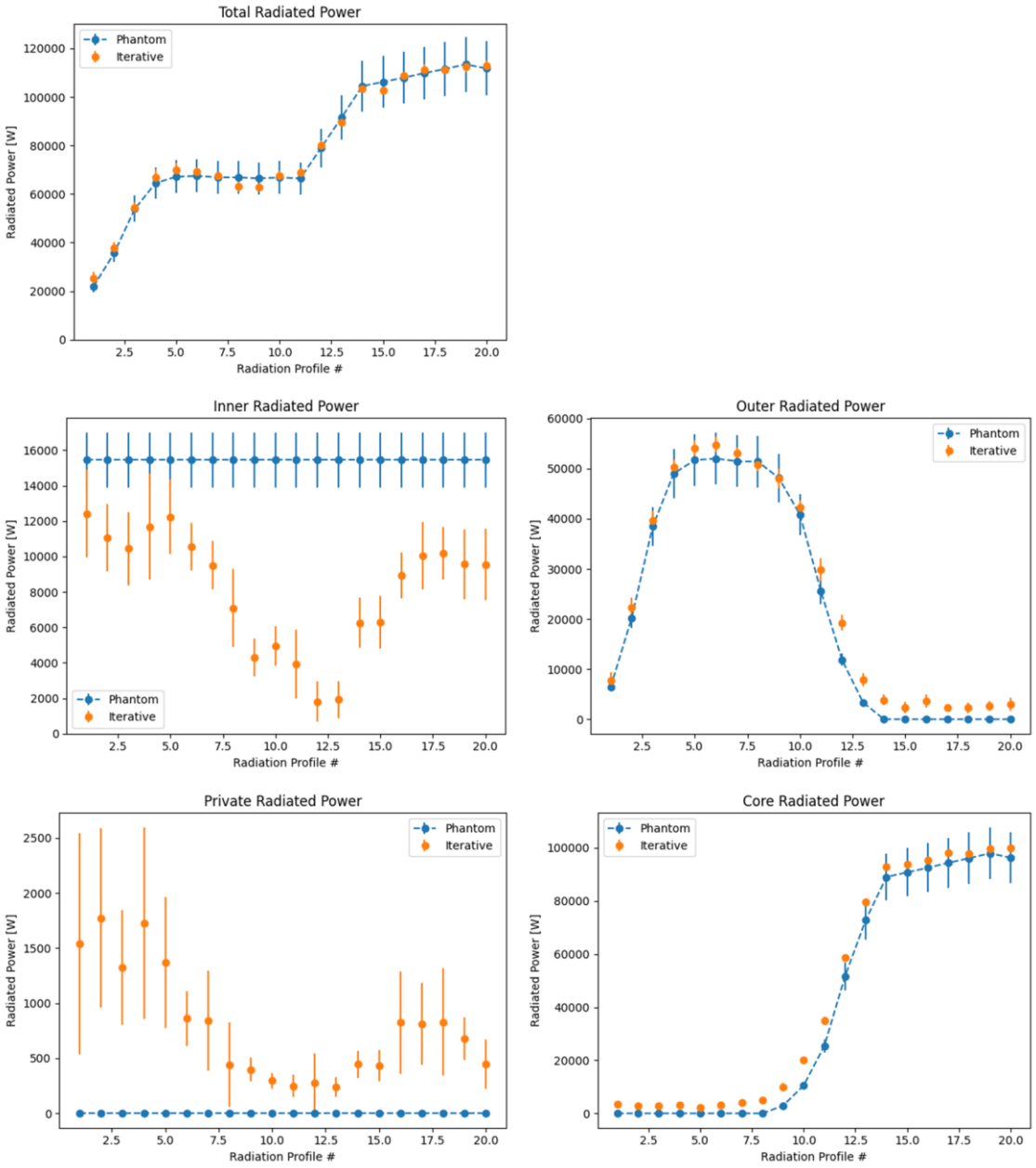

Figure 132 Radiated power analysis for the second case using the complex regularized iterative method. The total radiated power and the sectional radiated power compared with the phantom (exact) values. The phantom values included 10% error bar.

133). There are only one sightline looking at the small radiation blob at the inner leg section, and the sensitivity value at the location is much lower than other places. In addition, the private flux section had some erroneous radiated power. However, the values were small compared to other sectional values that the error could be due to the random noise or the results from the inner leg error. From these results, it should be noted that the emissions too close to the wall or at places without enough coverage of the 2D FOB array will result in a systematic error.

The final test case was using the first EFIT magnetic reconstruction profile where the radiation blob did not move from the outer leg section. However, the size decreased to a thin plasma emission (Figure 134). There was a small and low emitting radiation blob present at the inner leg again. The emission width changed from 10 cm to 1 cm with 10 steps. It was to see the performance of the optimized 8-by-8 FOB array for thinner radiation blobs. Only the iterative inversion techniques were tested for this case as well.

The iterative methods for the final case showed a great match to the phantom image radiated power divided into the four sections (Figure 135 and 136). The total radiated power values for both iterative techniques matched near perfectly with the phantom values. The values from the inner and outer leg sections where there were radiation blobs matched well with the phantom values. The core and the private flux sections had some results outside the 10% of the phantom values. However, the phantom values were zero and the iterative values were small. The errors are more likely be due to the random noise since other sections with the emissions did not have a noticeable error. The results showed that the optimized 8-by-8 FOB array can resolve the thin emissions for analyzing the radiated power.

Structural Analysis Using Computer Vision

Structural analysis of the radiation profile will be essential for investigating the open questions mentioned at Chapter 2. For plasma radiation structures due to plasma turbulence, the difference between simulations without and with plasma turbulence resulted in 2-3 cm in width estimated by heat flux to the divertor (Figure 7). The difference between UEDGE simulations and resistive bolometers showed ~5 cm in width

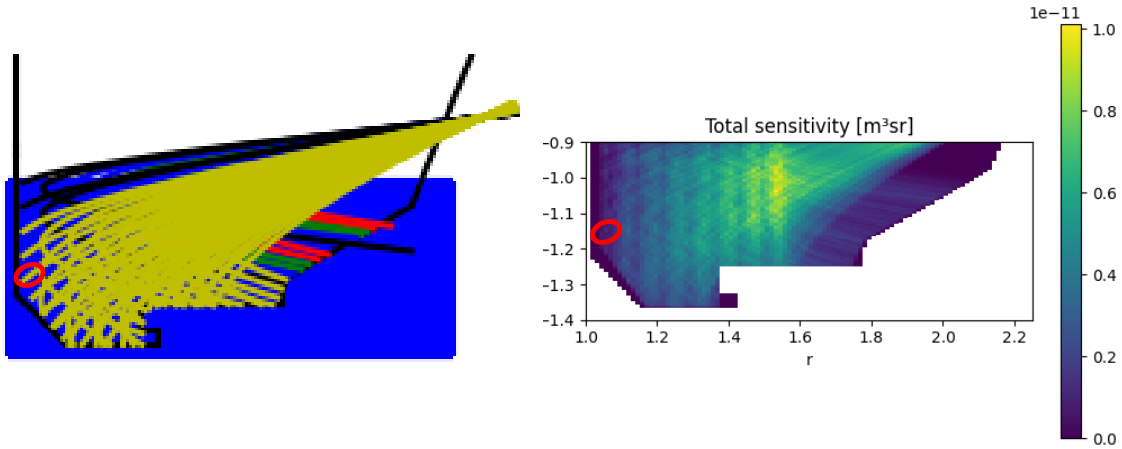

Figure 133 Left: the 2D FOB array sightlines. Right: the sensitivity profile of the 2D FOB array. The small emission located at the inner leg section (red circle). Only one sightline measuring the emission and the low sensitivity due to too close to the wall can be seen.

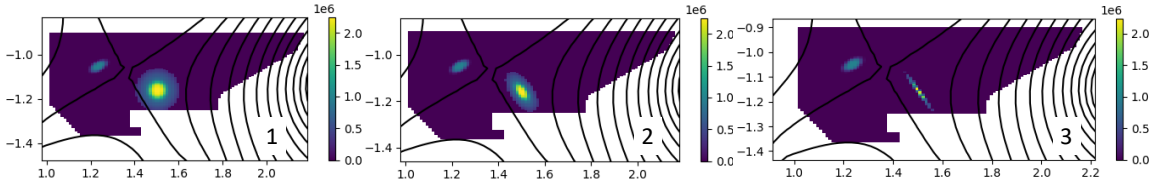

Figure 134 Case 3: synthetic plasma emission profile changing from 1 to 3 with 10 steps.

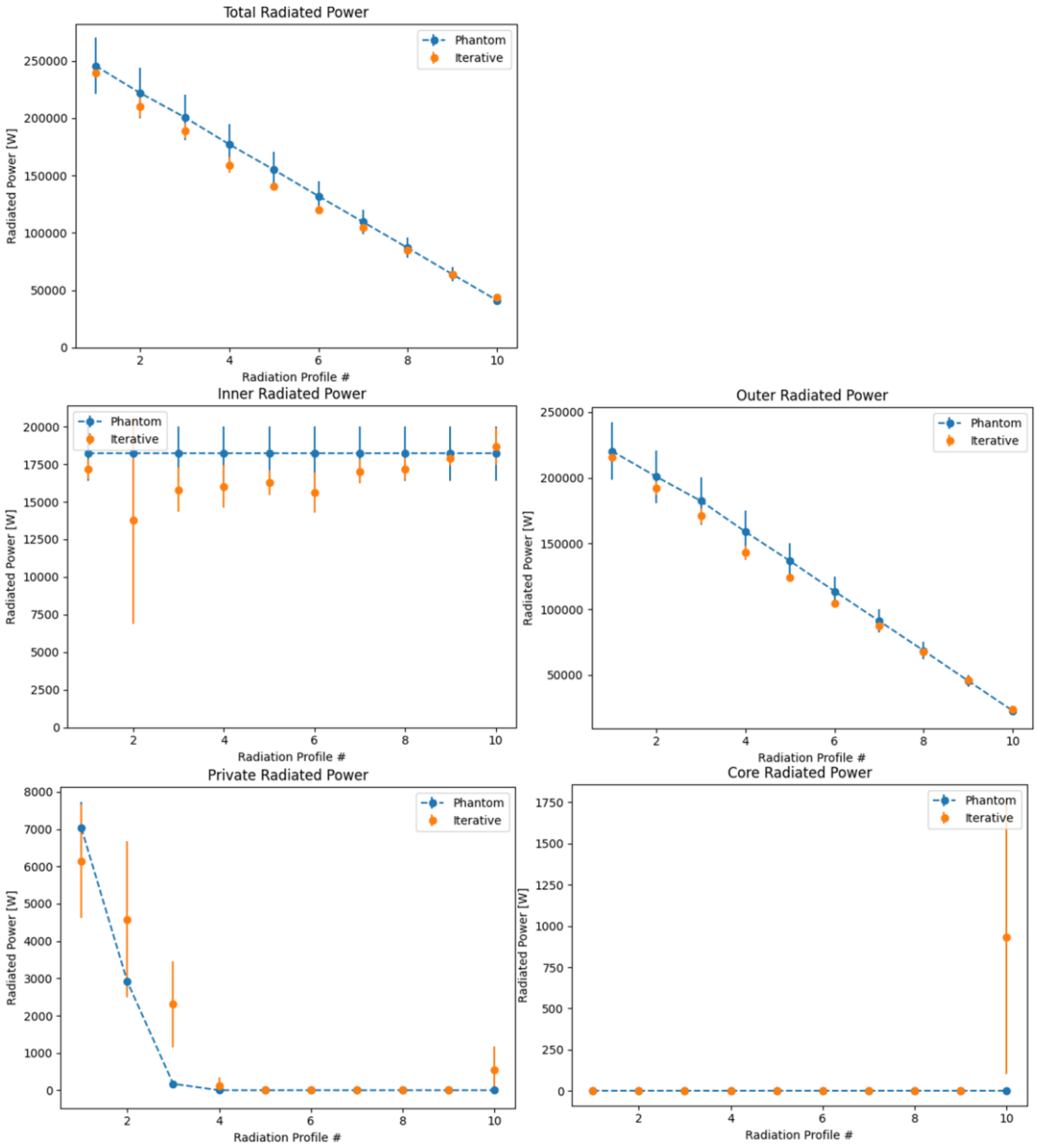

Figure 135 Radiated power analysis for the third case using the simple regularized iterative method. The total radiated power and the sectional radiated power compared with the phantom (exact) values. The phantom values included 10% error bar.

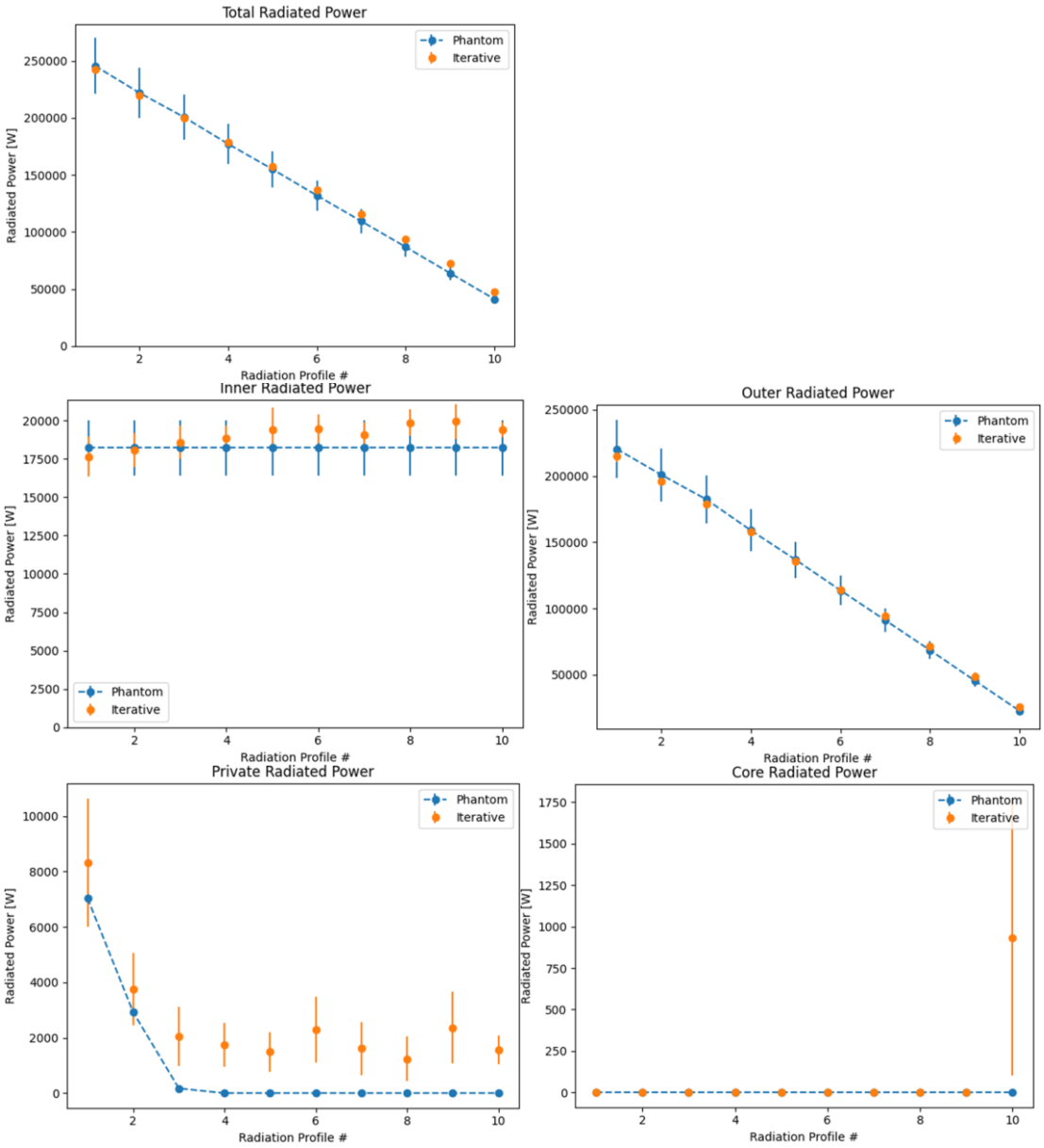

Figure 136 Radiated power analysis for the third case using the complex regularized iterative method. The total radiated power and the sectional radiated power compared with the phantom (exact) values. The phantom values included 10% error bar.

of plasma radiation substructures (Figure 6). The difference between plasma turbulence levels (lowest and highest) due to the plasma density resulted in ~1.5 cm difference in heat flux profile at midplane (Figure 137), which should result in the different width on the plasma radiation structure. For magnetic divertor configurations, the volume of the substructures, which can be approximated with the width and the length, will be important. For the evolution of the plasma radiation structure, the plasma radiation structure can move few cm/second for the experiments with the plasma radiation at a certain height above X-point [27]. Thus, following the center of a radiation structure with few-centimeter resolution will be beneficial. For comparison, the resistive bolometers at DIII-D could have about 3 to 10 cm spatial resolution (distance between sightlines) near the divertor depending on the location (Figure 78, left). In addition, there are no data on the size of the substructures due to the coarse grid of the resistive bolometers.

Rather than using each sightline as the spatial resolution like the resistive bolometer cases, the inversion results of the 2D FOB array can be used for the structural analysis due to the finer grid and the high spatial resolution. To verify this, the computer vision library mentioned at Section 4.6 in Python was used for more automated and strict structural analysis. The first step for using the computer vision is importing the inversion results in Python. The second step is to use a threshold value to outline the image of the inversion result (Figure 138, 2). The threshold used for this research was 0.05E6 W/m3. The next step is to find the contours of the outlined image using the computer vision library. The result (Figure 138, 3) is ready for the structural analysis.

The center location of a contour is calculated by using the image moment, which is a particular weighted average of image pixel intensities. The calculated center location for the prepared image is shown in Figure 139. The calculated center locations were near exact match to the original values. The center locations will be used to analyze the evolution of the radiation structure and the relative position to the X-point.

The center location analysis for the case 1 and 2 plasma radiation profiles were carried out to follow moving emission. The iterative methods for the case 1 showed that the center locations were well predicted (Figure 140). The deviations from the original

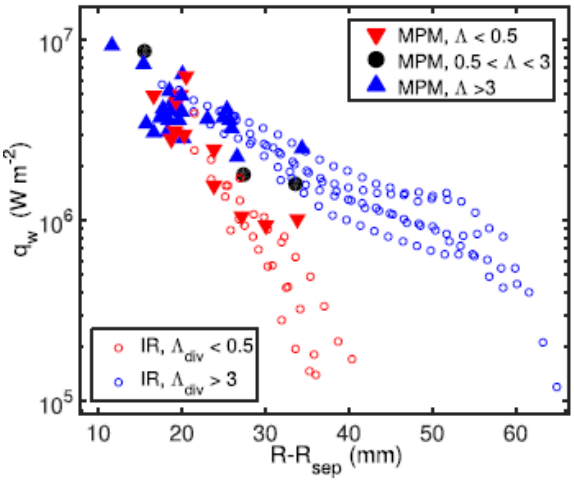

Figure 137 Heat flux profile at midplane (blue: highest plasma turbulence, black: middle, and red: lowest). Open symbols are calculations from IR camera. Close symbols are calculations from a midplane probe [21].

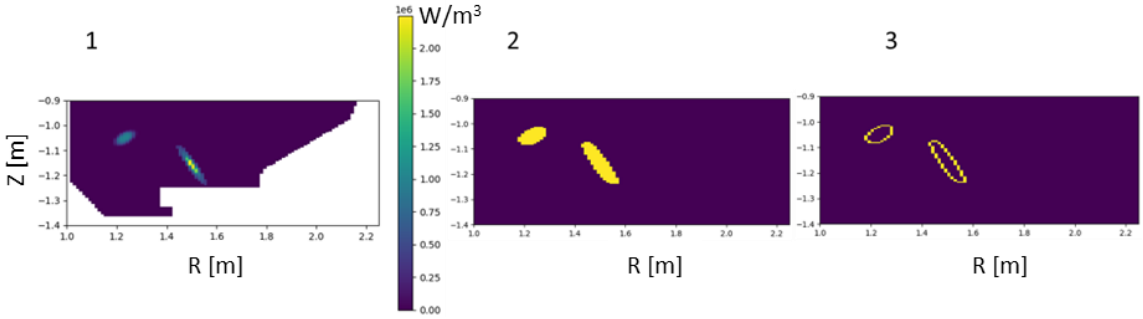

Figure 138 1: phantom image for the computer vision processing, 2: outlined image with the threshold, 3: found contours from the outlined image.

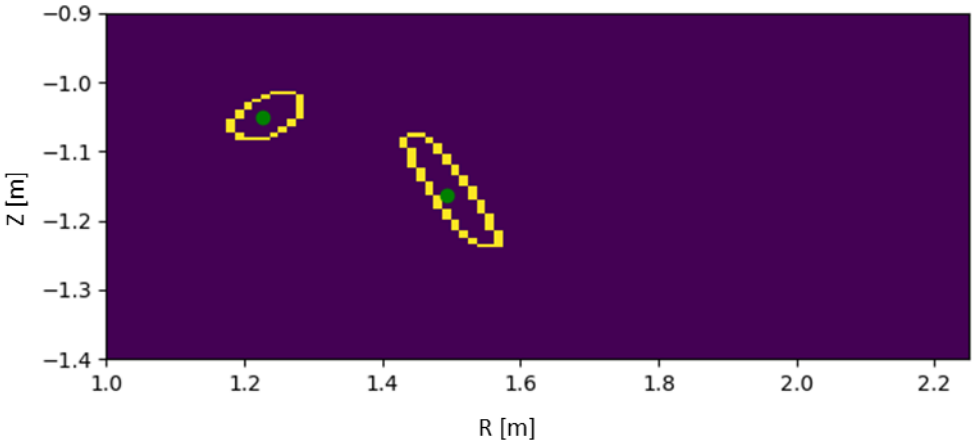

Figure 139 Center location (green dots) calculated for each contour.

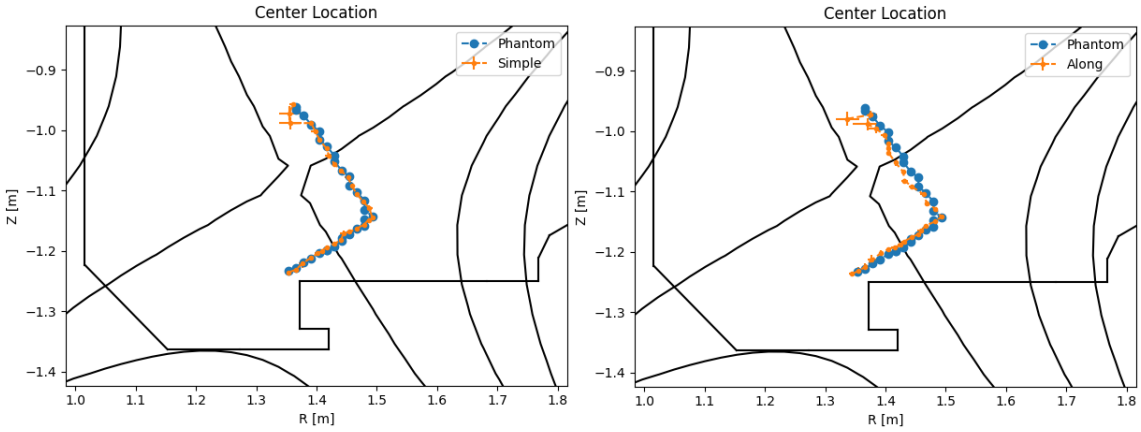

Figure 140 Left: the center locations of the simple regularized iterative method for the moving emission of case 1. Right: the center locations of the complex regularized iterative method for the moving emission of case 1.

location were 5 ± 5mm for the simple regularized iterative method and 10 ± 7mm for the complex regularized iterative method. The error values due to the random noise were (4 mm, 4 mm) for the (R-axis, Z-axis) of the simple method and (6 mm, 4 mm) for for the (R-axis, Z-axis) of the complex method. The complex method having worse results are most likely due to the moving emission not related to the magnetic fields.

The iterative methods for the case 2 showed that the calculated center locations were bit worse than the case 1 (Figure 141). The deviations from the original location were 9 ± 8mm for the simple regularized iterative method and 17 ± 15mm for the complex regularized iterative method. The error values due to the random noise were (4 mm, 6 mm) for the (R-axis, Z-axis) of the simple method and (8 mm, 6 mm) for the (R-axis, Z-axis) of the complex method. This is understandable since the 2D FOB array coverage for the case 2 is worse than the case 1. Again, the complex method having worse results are most likely due to the moving emission not related to the magnetic fields.

The shape/size analysis required more complicated approach due to the angle/tilt of the magnetic field. The angle or the tilt was calculated by using the center location and the magnetic flux data. First, the algorithm searches the nearest 11 by 11 pixels to the center location to find the pixels with less than 0.5% difference in the normalized magnetic flux compared to the pixel of the center location. Then, the farthest pixel to the center location pixel is used to make a line from the center location. The angle of the line compared to the X-axis is used as the angle or the tilt of the magnetic field (Figure 142, left). The length of the structure would be the distance from the center location to the farthest point parallel to the magnetic field (Figure 142, right, red). The width of the structure would be the distance from the center location to the farthest point perpendicular to the magnetic field (Figure 142, right, green).

The shape/size analysis for the case 3 plasma radiation profiles were carried out to analyze the changing shape. The simple regularized iterative method for the case 3 showed that the length was not well predicted, but the width was acceptable until 4 cm (Figure 143). The deviations from the original length were 25 ± 12 mm and the deviations from the original width were 11 ± 8 mm for the simple method. The errors

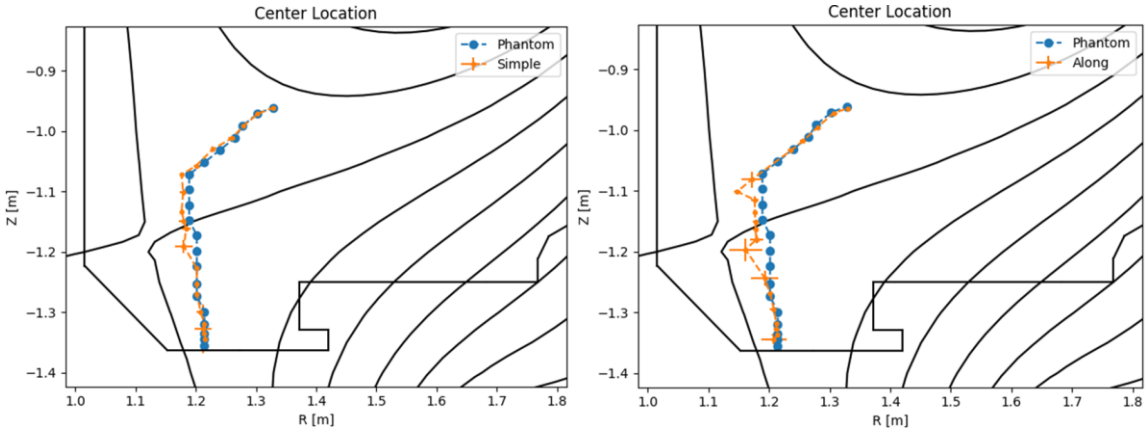

Figure 141 Left: the center locations of the simple regularized iterative method for the moving emission of case 2. Right: the center locations of the complex regularized iterative method for the moving emission of case 2

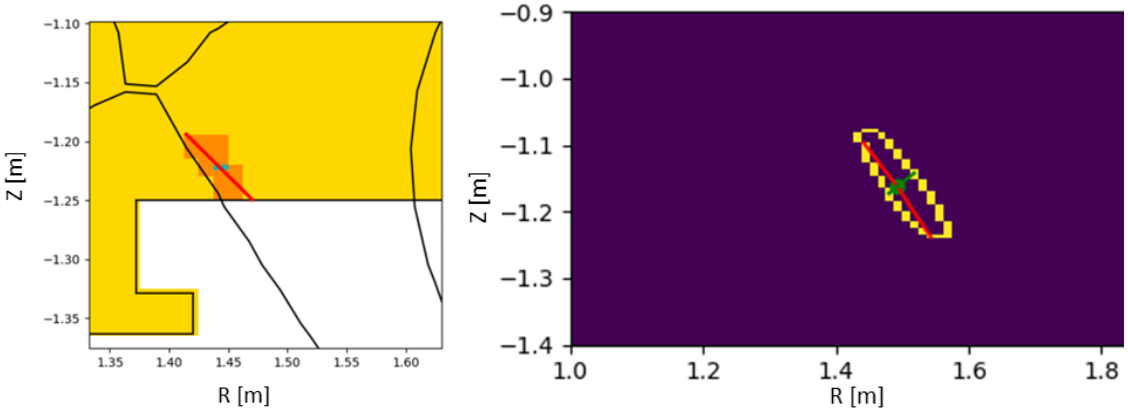

Figure 142 Left: example of finding the angle of the magnetic field at a center location (blue rectangle). Orange pixels have less than 0.5% difference in the normalized magnetic flux. The red line is created by connecting the farthest orange pixel from the center location to the blue pixel. The angle is calculated from the line and the X-axis. Right: length (red) and width (green) shown for the magnetic field angle calculated from the center location.

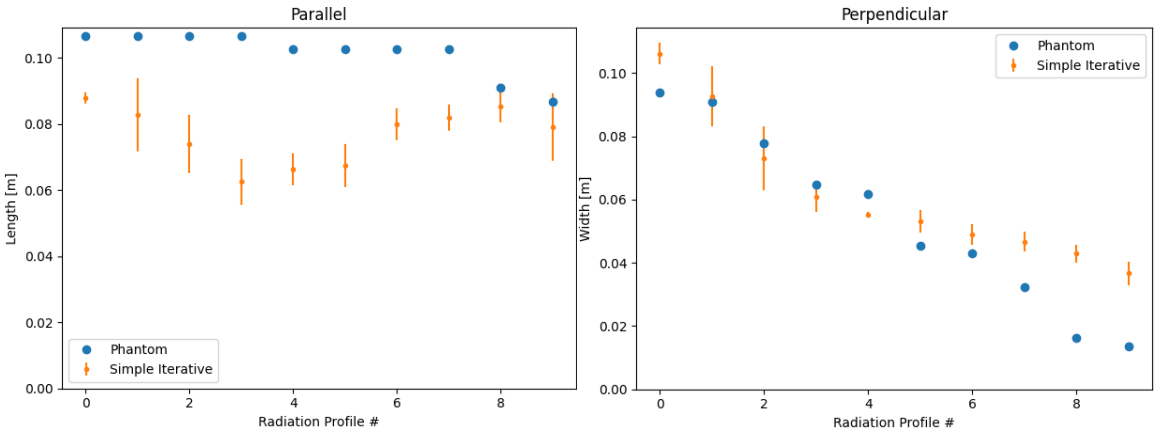

Figure 143 Left: length calculations for the simple regularized iterative method and the case 3 comparing with the phantom value. Right: width calculations for the simple regularized iterative method and the case 3 comparing with the phantom value. The simple regularization is not related to the magnetic field.

from the random noise were 6 ± 3 mm for the length and 4 ± 3 mm for the width. It is understandable the length is not well predicted since the simple regularization is not related to the magnetic fields. In addition, there seems to be a threshold for the width below 4 cm where the deviation is >1 cm.

The complex regularized iterative method for the case 3 showed that the length was well predicted, and the width was acceptable until 3 cm (Figure 144). The deviations from the original length were 6 ± 4 mm and the deviations from the original width were 8 ± 6 mm for the complex method. The errors from the random noise were 5 ± 1 mm for the length and 5 ± 2 mm for the width. When the radiation profile is following the magnetic fields, the complex method is clearly better than the simple method. The length deviations for the radiation profile # 0 to 2 could be due to more circular emission, which are less related to the magnetic fields. In addition, there seems to be a threshold for the width below 3 cm where the deviation is >1 cm. It should be noted that the accuracy of the structural analysis will change depending on the location of the plasma radiation structure due to the different coverage in the region of interest for the 2D FOB array.

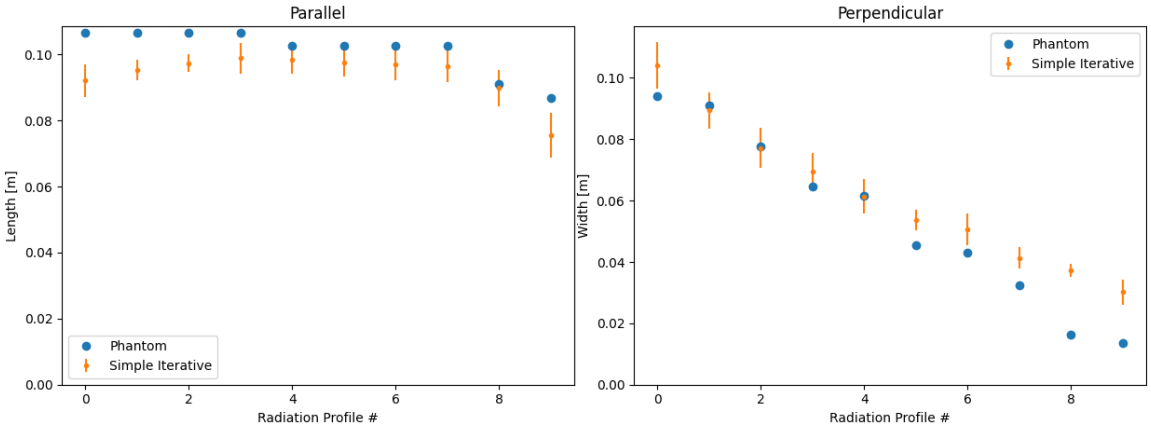

Figure 144 Left: length calculations for the complex regularized iterative method and the case 3 comparing with the phantom value. Right: width calculations for the complex regularized iterative method and the case 3 comparing with the phantom value.

Chapter Six

Conclusion

The plasma radiation profile contains the information on the condition of the plasma operation. The details in the plasma radiation profile will help understand the physics behind the plasma phenomenon. Analyzing the plasma radiation profiles with a detailed structure has been limited due to the limitation on the diagnostic equipment. Especially, diagnosing the plasma radiated power on a wide spectrum of the plasma emission has been limited due to the disadvantage of a bolometer where it is utilized. The resistive bolometers, which are a typical bolometer used on fusion plasma, are limited in resolution from its susceptibility to the electromagnetic interference. Analyzing the details of the plasma radiation structure in combination with the plasma radiated power will require high spatial resolution enough to resolve the information embedded in the details.

The plasma radiated power is an important measurement for the fusion plasma for the balance between the injected power and that absorbed by the wall armor and the level of impurities accumulating in the plasma core. The radial cross section of the fusion plasma is divided into different sections depending on the structure of the magnetic field configuration. Where the plasma-radiated power is located relating to the different sections and how much is the radiated power are an important piece of information. The differences in the information can have significant implications on the performance of the plasma conditions and operations. The radiated power in the core and the divertor leg need to be distinguished in detail to see if the plasma is detaching to protect the divertor or the plasma core is accumulating impurities, which is typically unfavorable. A bolometer with high spatial resolution will be required to comprehensively analyze the information.

The plasma radiation structure is another important piece of information that is usually ignored due to the lack of resolution in the data. The plasma turbulence has been known to affect the plasma radiation structure at the divertor. The discrepancies in the structure of the plasma emission between the measurements, which are usually coarse in spatial features, and the simulations could be due to the plasma turbulence, which is not

usually included in the simulations. The discrepancies are on the order of few centimeters in the radial direction, which requires high spatial resolution to resolve the possible differences.

The different divertor magnetic field configurations result in difference for important parameters like the flux expansion and the connection length. The changing two parameters will result in change in the structure of the plasma radiation. It was reported that with a limited resolution bolometer system, the change in the structure did not result in a change in the radiated power. Since increase in the flux expansion and the connection length will result in increased plasma volume at the divertor, it could be expected that the size of the plasma emission should be bigger. However, the flux expansion could spread out plasma that the density could be lowered, which will result in lowered plasma emissivity. If the size can be accurately determined with the corresponding radiated power, it can be determined whether the plasma volume and the corresponding plasma emission volume increased with decreased emissivity due to the decreased plasma density that the radiated power stayed the same.

The structure of the plasma emission evolves with the changing plasma condition during a plasma operation. It is important to see the change in the structure relates to the change in the performance and the condition of the plasma. As the detachment of plasma from the divertor progress due to the increased impurities, the central location of the highly emitting structure moves toward the X-point and into the plasma core. The location of the structure is closely related to the plasma performance during the detachment experiment that at a certain position inside the plasma core, the performance was better, which was not expected. Quantifying the central location of the highly radiating structure with high spatial resolution will be important in understanding the performance of the plasma. In addition, the shape of the structure should change during the evolution of the plasma for a plasma operation. Determining the shape change of the structure and relating to the performance will be an interesting study that will require high spatial resolution.

Before this dissertation, the FOB was never tested in vacuum and never calibrated to an incoming radiation. Also, the FOB operating/analyzing principles were still in

development. It was from the benchtop experiments in this dissertation that showed the significant increase in the responsivity and the time constant of the FOB, which was not expected, and the measurement range of the scanning laser system is not adequate due to the increase.

A single-channel FOB was demonstrated with a fusion plasma on DIII-D. The reference and measurement FOBs showed negligible increase in the noise level for the raw temperature measurements during plasma operations compared to the values at the bench. Therefore, it can be concluded that the FOB in a fusion environment is insignificantly affected by EMI.

The new calibration method for the FOB worked well with a good response time. The calibrated results from the impulse deconvolution method showed a decay constant of 14 ms, whereas it was ~6 seconds for a raw temperature measurement at 7E-5 Torr. The time response will depend on the averaging time. For instance, it is expected to be ~20 ms considering the 50 Hz cutoff and 20 ms averaging time.

A comparison to traditional resistive bolometers on DIII-D showed that the temporal trend of measured plasma brightness from a single channel with a similar view through the plasma agreed with the temporal trend of the FOB result. Channel 14 of the DIII-D resistive bolometer had a comparable sightline with a similar pathlength to the installed FOB. This comparison showed that the FOB and the calibration method were working as anticipated compared to a resistive bolometer.

A quantitative comparison required more complex processing due to the different dimensions, installed radial location, and the tangential tilt present at the installed port. The forward-modeled FOB results employing a CHERAB 3D simulation and a tomographic reconstruction from the DIII-D resistive bolometers agreed with the actual measurements of the FOB. This demonstration confirmed that the FOB is comparable to a resistive bolometer. In addition, the FOB showed a satisfactory NEPD value in the fusion environment. This will make high spatial resolution possible for a FOB array design. The comparisons of resistive, infrared video, and fiber optic bolometers for various criteria are shown in Table 19, which showed that the FOB is very competitive considering an actual implementation (in fusion environment).

Table 19 Comparisons Between Resistive, Infrared Video, and Fiber Optic Bolometers

Criteria	Resistive Bolo.	IRVB	FOB
NEPD* [W/m^2]	0.28 [97]	3 (0.29**) [98]	0.64
Susceptibility to EMI	Very susceptible (typically a factor of 10 higher NEPD [99])	Less susceptible (depending on the location and the shield)	Negligible
Compactness	Less compact (sizable sensor)	Big (due to the IR camera, lenses, and mirror)	Compact
Port flexibility (where it can be deployed, related to compactness)	Less flexible (due to the sensor size and cooling)	Limited (due to the infrared periscope, IR camera, and shield)	Flexible

*: 10 ms resolution assuming Gaussian distribution of noise
**: ideal calculation value, not from measurements.

Two design considerations were identified during the testing at DIII-D. The first consideration was an interfering measurement from a neutral beam interacting with a plasma, which will be measured by any kinds of bolometers since some of the interaction emissions will be within the measuring spectral range of a bolometer. The sightline of a bolometer should not overlap or cross the path of a neutral beam. This will also be a consideration for future FOB implementation. The second consideration was an interfering measurement from stray ECH radiation. An ECH radiation shield will be needed for implementation in a device with ECH injection.

The "darkening" of fiber optic cables will be the major potential effect of ionizing radiation for the FOB in D-T or long-pulse D-D magnetic confinement fusion devices [35]. Attenuation from the effect could reduce the interference spectrum count level and will result in increased noise [37]. This can be compensated by increasing the light-source power or adjusting the attenuator. The measurements of the FOB rely on the shifts of the interference spectrum so they should be minimally affected by radiation-induced attenuation, radiation induced-emission, or compaction due to ionizing radiation [76]. The effects of ionizing radiation in the FOB will require further experimental studies.

Additionally, the FOB was demonstrated as a sensitive pressure sensor in a wide range of vacuum pressure. The changes in the responsivity and the response time of the FOB in different pressures were the basis for the pressure measuring operation. The constant-heating method, where the FOB was heated using the white light source, showed good results in the medium (~10 to ~1.5E-3 Torr) and high vacuum (below ~1.5E-3 Torr) regimes. The method was possible for a pressure measurement due to the changing responsivity with the vacuum pressure, which resulted in a varying temperature to a constant heating. This method was the only method possible to operate in the high vacuum regime with ~20% accuracy. The disadvantage of the method was that it required ~30 seconds of a wait-time for a temperature saturation. The design of the FOB could be optimized for a faster response with a lesser thermal isolation of the FOB that would decrease thermal response time.

The square-wave signal method utilized the measured amplitude of the square wave from the external laser. Again, the method was possible for a pressure measurement

due to the changing responsivity with the vacuum pressure, which resulted in a varying amplitude to the same square wave radiation. The method did not require the wait time due to 1 Hz laser cycle (1 Hz pressure measurement). The method was working well in the low (760 to ~10 Torr) and medium (~10 to ~1.5E-2 Torr) vacuum regimes with <20% accuracy. This method was the only method possible to measure in the low vacuum regime.

The pulse signal method exploited the changing decay constant with different pressures. The changing decay constant relates to the changing response time from varying vacuum pressure. This method did not require the wait time and was not sensitive to the heating power since the measurements were from a temperature decay of a pulse. The method only worked for the medium vacuum regime (~10 to ~1.5E-2 Torr) with a good accuracy (<20%).

The operating range of the square-wave signal method and the pulse signal method could complement the ASDEX type gauge [84] or miniature Penning gauge [85], which has a limit at ~0.1 Torr, deployed in the divertor region where the neutral pressure could increase drastically [86]. In addition, the FOTS does not have the disadvantage of capacitance manometer-type gauges that need to be further away from the divertor region. The capacitance manometer-type gauges are often installed further away from the divertor due to the sensitivity to vibrations and stray magnetic fields, and the membrane of the gauges requires a thermal stabilization [87]. Other advantages include negligible susceptibility to EMI and the compact design that could make the FOTS a beneficial neutral pressure diagnostic in a fusion environment.

A pig-tailed laser incorporated inside the fiber-optic circuit of the interrogation system could be the next step for the research. This will make the system more practical and avoid laser alignment issues. In addition, an optimized design of the FOB could result in a better accuracy for a specific method and at a specific pressure range. Different designs could be envisioned with a better or lesser thermal isolation of the FOTS for a more precise measurement due to increased or decreased thermal responsivity and response time.

2D FOB array is planned for an implementation at the DIII-D tokamak to observe the radiate power rigorously at the divertor region. The design needed to be optimized to fully take advantage of the FOB. The design parameters were the pinhole size, the distance between the sensors, the distance between the pinhole and the array, the radial tilt, the tangential tilt, and the array size. Since the parameters are non-linear to each other, the simple method of grid searching would have taken too long. For a systematic optimization, the machine learning optimization approach (Bayesian global optimization) was used to efficiently optimize the design parameters. Six different synthetic radiation profiles were used to test a set of the parameters and to obtain the root mean squared error calculated from the simple inversion using the forward-modeled measurements compared to the phantom image. The currently selected design is 8-by-8 FOB array at R-1 port looking tangentially at the divertor region.

Rather than using the FOB array alone, the resistive bolometer measurements can be added to the FOB array data for more information on the plasma. This is advantageous since the inversion process is an ill-posed problem. The sensitivity information and the measurements are added to the FOB array data. The magnitude difference in the absolute values of the resistive bolometers due to the differences in the dimensions were the problem with adding the resistive bolometer information. The peak sensitivity ratio between the resistive bolometers and the FOB array was used to modify the resistive bolometer information to the FOB array level. The results showed that the adding information is advantageous when the radiation structure is big enough to be resolved by the resistive bolometers. For these cases, adding the resistive information resulted in the performance boost like increasing the FOB array size. The other cases where the radiation structures were small compared to the resistive bolometer resolutions did not have an advantage over using the FOB array alone.

A new method for analyzing the raw spectrum data of the FOB was developed to overcome the tricky problem of having different wavelength values for different valleys. Although the wavelength values were averaged over and the calibration possibly tended the problem, the Fourier transform method was able to remove the problem entirely. The method used a Fourier transform on the raw spectra to analyze in the cycle/nm space,

since the raw spectra was the interference pattern (a sinusoidal shape). The major component in the amplitude was selected to follow the phase change, which can be transformed to the wavelength change. The noise and the other minor components were thought to be the cause of the difference in wavelength for the different valleys. The advantage other than the removal of the problem was that the method was much faster than the valley-fitting method. It was fast enough to have real time analysis. However, the noise level of the new method was bit higher than the valley-fitting method. The noise equivalent power density of the calibrated results was the same as the valley-fitting method. This was thought to be due to discarding the noise and other minor components or the calibration noise overwhelming the data noise.

A complex regularization for the iterative inversion method was developed for the 2D FOB array. The regularization utilized the magnetic reconstruction data from EFIT. The algorithm searches, for each pixel, the nearby pixels that have similar flux values and created the regularization that results in smoothing the emissivity profile along or parallel to the magnetic fields. In addition, a limitation was imposed where the pixels with higher than 1.3 normalized magnetic flux values to have zero sensitivity that there was no emission in the pixels. The issue with using the complex regularized iterative inversion method was selecting the regularization strength. The regularization had a physical basis for the construction, but the regularization strength was arbitrary that it was chosen from trial and error.

The neural network inversion methods were experimented to overcome the regularization strength issues. Two different methods were tried to utilize the sensitivity matrix, which was not in use for the previously reported studies. The first method used the pseudo inverse of the sensitivity matrix multiplied to the measurements as the input, and the second method used the simple regularized result, which requires the sensitivity matrix, as the input. 18000 training data were created having randomized radiation blobs or having a completely randomized emissivity for each pixel. The results worked well for the radiation profiles with radiation blobs having the similar shape and the emissivity distribution. However, if the shape and the distribution were different, the two methods underestimated the shape size and the total radiated power. Using only the completely

randomized pixel training data did not work to the iterative method level. Most cases the neural network failed to train with the completely randomized data. For the cases where the training was possible, there were background radiations that required a post processing, which defeats the purpose of using the neural network inversion method. A more randomized, but still retaining plausible radiation structure and distribution, method of creating synthetic radiation profiles will need to be developed to use the neural network for inversion of the 2D FOB array data.

The radiated power analysis divided into different sections according to the magnetic reconstruction profiles were used to demonstrate the performance of the optimized 2D FOB array and the inversion method. Two different magnetic reconstruction profiles and synthetic radiation profiles with moving/changing structures were used to test the 8-by-8 FOB array with the simple and complex regularized iterative inversion methods. The results showed that the system predicted near perfect total and sectional radiated power compared to the phantom values (the synthetic profiles). There were exceptions where the radiation blobs were located too close to the wall where the sightline coverage of the 2D FOB array were sparse. In any case, the resulted demonstrated the FOB system can resolve the radiated power in different section with great details.

The radiation structure analysis using the computer vision library demonstrated the performance of the optimized 2D FOB array and the inversion method. The center location analysis of the two different magnetic reconstruction profiles and synthetic radiation profiles with moving/changing structures showed that the system matches well to the original values. This showed that the system has high spatial resolution for analyzing the central location of highly emitting radiation structure. The error values were 10 ± 7mm for the complex regularized iterative method with the random error of (6 mm, 4 mm) for the (R-axis, Z-axis). The shape analysis results showed that the system predicted the length and the width related to the magnetic field angle well compared to the phantom values. However, there seems to be a threshold of below 3 cm where the error values increase more than 1 cm. The error values for the length were 6 ± 4 mm and

the width were 8 ± 6 mm for the complex regularized iterative method. The random errors were 5 ± 1 mm for the length and 5 ± 2 mm for the width.

The demonstrations of the sectional radiation power and the radiation structural analysis showed that the optimized 8-by-8 FOB array with the complex regularized iterative inversion method have high spatial resolution. The capability of the detailed predictions of the sectional radiated power will benefit the study of implications of the sectional radiated power on the performance of the plasma conditions and operations. The FOB system will result in more details since the DIII-D resistive bolometers have a coarse resolution. The capability of the detailed predictions of the radiation structures will be adequate to study the plasma phenomena. The high resolution for resolving the central location will reveal the details of the plasma radiation structure evolution, which closely relates to the plasma performance during the detachment experiment. The high resolution for resolving the radiation shape will be able to answer the effects of the plasma turbulence and the different divertor magnetic configurations.

Chapter Seven

Future Work

Radiated Power Analysis of Emissions from Neutral Beam Interacting with the Plasma

From the single channel demonstration, it was shown that the emissions from the neutral beam interacting with the plasma was being measured by the FOB (Figure 61). This could be a unique chance to address the assessment of the power balance of the neutral beam injected power. The resistive bolometers of DIII-D did not measure the emissions due to the different installed locations that the sightlines did not intercept the neural beam injection line. The difference between the FOB measured power and the forward-modeled FOB power from the resistive bolometers will be due to the emissions from the interaction.

The radius of the neutral beam will need to be determined to find the intercepting length of the FOB sightline and the neutral beam. Subtracting the forward-modeled FOB plasma brightness from the FOB measured plasma brightness will results in the plasma brightness from the emissions of the interaction. The subtracted brightness divided by the intercepting length will result in the average emissivity of the emissions. The intercepting volume between the FOB viewing cone and the neutral beam multiplied by the average emissivity will be the radiated power of the emission measured by the FOB. It will be interesting to see what the absolute value of the radiated power of the measured emissions is.

In addition, the total radiated power of the emissions from the neutral beam interacting with the plasma can be approximated by assuming uniform emissivity. The total volume of the neutral beam into the plasma can be calculated by calculating the neutral beam path length into the plasma and multiplying it to the size of the neutral beam. The average emissivity multiplied by the total volume will be the approximate total radiated power of the neutral beam that is not being measured by the resistive bolometers. However, the value will be a rough estimate since the emissivity will not be uniform. This is because the density of the plasma will not be uniform. Also, the neutral beam will not have the same energy and density as it penetrates the plasma. Nevertheless,

it will be interesting to see the total radiated power of the neutral beam compared to the injected power of the neutral beam.

New FOB Design Benchtop Vacuum Testing

One of the unexpected features of the FOB was a significant increase in the transition time (~0.4 seconds to ~8 seconds) from air to high vacuum. Although the problem was mitigated by the frequency space calibration, the performance of FOBs could be improved by decreasing the transition time in high vacuum. The MSU group is working on decreasing the transition time by adding a bigger thermal sink behind the silicon pillar. The material of the thermal sink is silicon, and it wraps around the fiber optic cable. Silicon has high thermal diffusivity that the heat will spread out well. The initial results showed the decreased transition time to few tens of milliseconds in air but with increased noise equivalent power density. With the low transition time, the frequency space calibration might not be needed. A linear calibration that will relate the temperature change of the FOB to the power/power density of the incoming radiation might be enough. The design is expected to have a transition time increase about 2-3 times in high vacuum compared to in air, but it has not been tested.

The preliminary design of the 2D imaging array consisted of subarrays with four measurement FOBs and one reference FOB in a common substrate (Figure 145) [71]. The MSU group is planning to use one silicon thermal sink behind the silicon pillars for four measurement FOBs and one reference FOB (maybe not be behind the silicon pillar) like the initial design. The common substrate acts a common sink to all the FOBs in the subarray. The common sink will link the FOBs with the same ambient changes, which will be measured by the reference FOB. By subtracting the signal of the reference FOB, the ambient changes should be subtracted from the measurement FOBs. However, MSU group reported some time delays between FOBs from the changes in the common substrate.

As the huge increase in the transition time was not expected for the single-channel testing, there could be other features that cannot be easily expected for the subarray designs. The vacuum testing of the designed subarray is planned to be performed at MSU

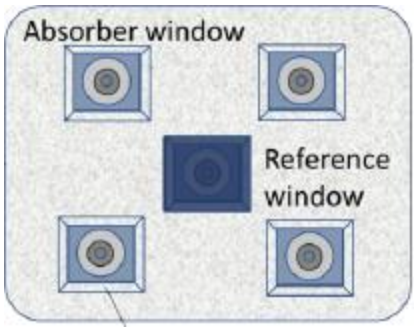

Figure 145 Preliminary design of 2D FOB subarray consisting of four measurement FOBs and one reference FOB. [71]

and UTK. The testing like the benchtop testing of the single-channel FOB will be performed for UTK testing. The single-channel vacuum chamber will be reused with some component changes. The FOB mount inside the vacuum chamber needs to be redesigned to hold the subarrays. The corresponding pinhole camera attached to the mount will be needed as well. Also, a dedicated vacuum pump for the testing will be beneficial. The single channel FOB was attached to the plasma exposure chamber (second-hand vacuum pumping) that the vacuum pressure (low 10^-5 torr) in the single channel chamber was not low enough (< 10^-6 torr) for DIII-D reviews.

Experiments for the designed subarray will be like the experiments performed for the single-channel FOB. The responsivity, the transition time, and the noise equivalent power density for each FOB will be measured for different pressures. The time delays will be tested by shining a laser at a localized location of the substrate. The delays will need to be tested at different pressures since they could be changing with pressure. Since the delays could distort the signal in the measurement FOBs, it would be a good experiment to look at the measurements by the measurement FOBs with a defocused laser that is shining all four FOBs. If subtracting the reference FOB is working for the designed subarrays, all four FOBs should have the same signal structure as a square wave. In addition, a misalignment between the pinhole and the FOBs (angle between the perpendicular line from the FOB and the perpendicular line for the pinhole) could influence measurements. The single channel FOB is nearly perfectly aligned with the pinhole (0° angle). For the 2D array and the subarrays, this will not be possible since there will be only one pinhole that will most likely be centered at the 2D array or the subarrays. Angled incoming radiation could result in reduced signal due to a different reflection than the right-angle reflection. This might not be captured during the responsivity testing because the testing will be done without a pinhole to overcome the difficulty in laser alignments.

DIII-D Reviews for Installation

There are three review processes that need to be passed to install a diagnostic at DIII-D. The processes are to validate a need/worth and a design of a project. However,

these processes can be time consuming. They delayed the installation of the single-channel FOB to the end of a DIII-D operation campaign. It is critical to pass the review processes as soon as possible to be able to reach these thesis goals. Thus, the reviews are important part of the future research.

The first review is called Physics Validation Review (PVR). Why 2D imaging FOB array should be installed at DIII-D will be the question for the review. The importance of the physics questions (chapter 2) will be emphasized during the review with the fact that the higher resolutions are required to answer the questions. The results of the single-channel testing and a plan for the 2D FOB array will show that the resolutions of the 2D FOB array will surpass the resistive bolometers and satisfy the requirement for the questions. The second review is called Critical Design Review (CDR). The review is for the protection of the DIII-D tokamak and operations. A design (possibly already constructed) for the 2D imaging FOB array will be presented in detail with where and how it will be installed. Important considerations are vacuum materials, vacuum level, and temperature tolerance of the array. The final review is called Final Design Review (FDR) where any concerns pointed out during CDR will need to be resolved.

Fabrication/Construction and Calibration

The 2D imaging FOB array will consist of similar components as the single channel FOB, but upscaled or bigger. The array will be housed in a vacuum chamber with a mount for subarrays and a mount for the assembled subarrays. The array will be inside a pinhole camera. A vacuum feedthrough for fiber optic cables is required for FOBs. The vacuum chamber and the vacuum feedthrough (or feedthroughs) can be commercial products. The mounts and the pinhole camera will be custom fabricated. Some concerns for fabrications/construction are as follows. The metallic components need to be non-magnetic metal due to the regulation from DIII-D. The vacuum components require 350°C temperature tolerance due to the baking of DIII-D machine. The components that require attention are fiber optic connectors from FOBs (180°C limit) and the vacuum feedthrough (250°C limit). Cooling might be required at the

outside of the vacuum feedthrough to cool the feedthrough and the connectors that are connected to the feedthrough. The vacuum pressure needs to reach below 10^-6 Torr, which means that materials with high vapor pressure need to be avoided. The only component that is of concern for the pressure is fiber optic cables inside vacuum, but they will be tested at DIII-D.

It will be beneficial to design the array mount and the pinhole camera to be adjustable since the 2D array might be installed elsewhere or with different objectives. The distance between the pinhole and the array will be adjustable with a bigger chamber (longer) and a moveable (retractable) mount. An interchangeable pinhole will be beneficial to increase/decrease signal level by using a bigger/smaller pinhole, but the spatial resolution will be lower/higher. The toroidal angle and the radial angle of the pinhole camera will be adjusted by attaching angled flanges or bellows at a port of a fusion machine where the 2D array will be installed.

Calibrating the 2D array will not require as extensive experiments as the benchtop testing. Calibrating one subarray at a time in the single-channel vacuum chamber might be more feasible due to vacuum window and alignment considerations. In addition, one high-vacuum pressure (<10^-6 Torr) will only be required for the calibration parameters since the operating pressure will be <10^-6 Torr. After all subarrays are calibrated, the 2D imaging FOB array will be assembled. Cleaning will be critical due to the vacuum pressure concerns. The inside of the pinhole camera and the gold plate of the FOBs will need to be darkened to reduce stray light and absorb visible-wavelength plasma radiation from near a divertor.

DIII-D Installation and Data Acquisition/Interpretation

The 2D imaging FOB will be installed at DIII-D after the final review. The author suspects the installation will be done mostly by DIII-D engineers. A position calibration after the installation will be required to check the pinhole location relative to the machine coordinates [64]. Distances (the method for measuring this distance has yet to be identified, but several options are available at DIII-D) from a fiducial marker of the DIII-D machine to the pinhole will provide the position in machine coordinates. The accurate

position of the pinhole and the FOBs calculated from the pinhole will be essential for an accurate tomographic reconstruction.

6 by 6 array will result in 9 I-MON spectrometers, and 8 by 8 array will result in 16 I-MON spectrometers. A separate computer will be required to acquire data from all I-MON spectrometers. I-MON DAQ program will need to be developed to accommodate multiple I-MONs. In addition, a better data-saving method will be required due to a file size problem. The file size of the single-channel FOB was ~120 MB per shot. It will be 288 GB per day due to 80 channels for 6 by 6 and 30 shots per day, which is huge. A program will be required to automatically upload the data into DIII-D server (MDSplus server). The raw measurements need to be processed to power/power density measurements. The current python code requires 15 to 20 minutes for two channels per shot for processing using DIII-D server (IRIS), which is already too slow for between shot analysis (~10 minutes between shots) and will be a serious problem for 80 channels. The new Fourier transform processing method will be essential for between-shot analysis. Finally, the developed regularized iterative will produce emissivity profiles using the processed data. The final emissivity profiles will be used for physics analyses.

Complex Benchtop Testing for 2D Imaging FOB Arrays

The project could be delayed for many reasons like COVID mutations, DIII-D reviews, etc. In the case of significant delays to the installation on DIII-D, the project will be diverted to assuring the performance of the 2D imaging FOB array. Although calibrations and simulations could predict good spatial or temporal resolutions, they are not a direct validation. A direct validation will be possible with more complex benchtop testing.

A laser can be used to mimic the plasma radiation structures. A defocused laser could have an acceptably uniform power density at a certain distance. If a semi-transparent material with adjustable transparency is placed in front of the laser, the power density of the laser at a certain distance will be adjustable. The semi-transparent material could be a Plexiglas or acrylic plate. The transparency can be adjusted by color shades such that darker/lighter shade would result in lower/higher transparency. Also, it can be

adjusted by changing the thickness of a dark-shaded plate such that thinner/thicker would result in higher/lower transparency. Tests will be required to see how the power density changes at the distance of the array with changing transparency. Plasma radiation structures (synthetic or real examples) imprinted on the array will be simulated by CHERAB. With the transparency calibration result and the CHERAB result, a shade or thickness structure for the image (that will be on the array) will be obtained. The transparency structure on a plate will mimic the plasma radiation structures on the array. The benchtop testing would look something like Figure 146. Many different plates with different transparency structure (corresponding to different plasma radiation structures) will be used to test the spatial resolution of the array. Either the plates need to be changed at a desired speed or the laser needs to be pulsed with a desired width for testing the time-resolution.

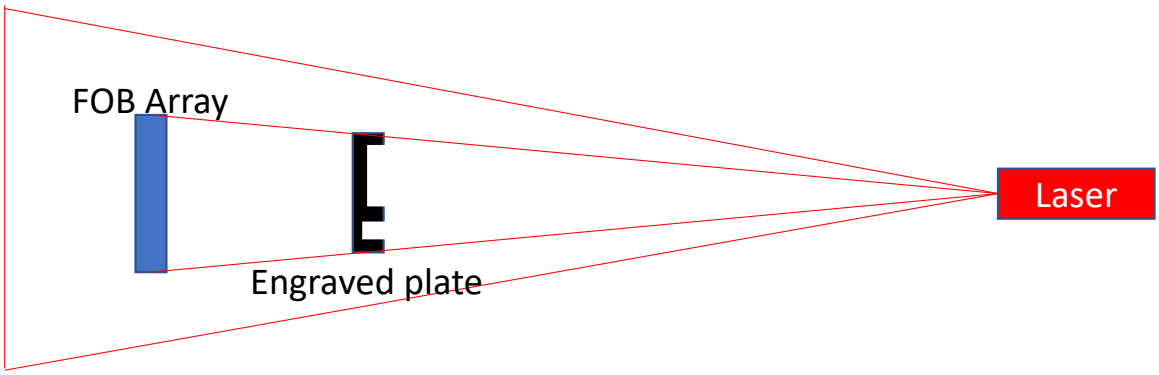

Figure 146 Complex benchtop testing schematic for the thickness control method.

List of References

1 Ongena, J., et al. “Magnetic-Confinement Fusion.” Nature Physics, vol. 12, no. 5, 2016, pp. 398–410, doi:10.1038/nphys3745.

2 Yamada, H. “Magnetic Confinement Experiments: Plasma-Material Interactions, Divertors, Limiters, Scrape-Off Layer (EX/D), Stability (EX/S), Wave-Plasma Interactions, Current Drive, Heating, Energetic Particles (EX/W).” Nuclear Fusion, vol. 53, no. 10, IOP Publishing and International Atomic Energy Agency, 2013, p. 104025–, doi:10.1088/0029-5515/53/10/104025.

3 McCracken, G. M., and P. E. Stott. Fusion : the Energy of the Universe. 2nd ed. / Garry M. McCracken and Peter Stott., Academic Press, 2013.

4 Meister, H., et al. “Bolometer Developments in Diagnostics for Magnetic Confinement Fusion.” Journal of Instrumentation, vol. 14, no. 10, 2019, pp. C10004–C10004, doi:10.1088/1748-0221/14/10/C10004

5 Wischmeier, M. “High Density Operation for Reactor-Relevant Power Exhaust.” Journal of Nuclear Materials, vol. 463, Elsevier B.V, 2015, pp. 22–29, doi:10.1016/j.jnucmat.2014.12.078.

6 Raffray, A., et al. “Critical Heat Flux Analysis and R&D for the Design of the ITER Divertor.” Fusion Engineering and Design, vol. 45, no. 4, Elsevier B.V, 1999, pp. 377–407, doi:10.1016/S0920-3796(99)00053-8.

7 Bernert, M., et al. “Power Exhaust by SOL and Pedestal Radiation at ASDEX Upgrade and JET.” Nuclear Materials and Energy, vol. 12, Elsevier Ltd, 2017, pp. 111–18, doi:10.1016/j.nme.2016.12.029.

8 Leonard, A. W. “Plasma Detachment in Divertor Tokamaks.” Plasma Physics and Controlled Fusion, vol. 60, no. 4, IOP Publishing, 2018, p. 44001–, doi:10.1088/1361-6587/aaa7a9.

9 Massoud, Mahmoud. Engineering Thermofluids Thermodynamics, Fluid Mechanics, and Heat Transfer . Springer-Verlag Berlin Heidelberg, 2005, p. 568

10 Loarte, A., et al. “Chapter 4: Power and Particle Control.” Nuclear Fusion, vol. 47, no. 6, IOP Publishing, 2007, pp. S203–S263, doi:10.1088/0029-5515/47/6/S04.

11 Reiter, D., et al. “The EIRENE and B2-EIRENE Codes.” Fusion Science and Technology, vol. 47, no. 2, Taylor & Francis, 2005, pp. 172–86, doi:10.13182/FST47-172.

12 Canik, J. M., et al. “Testing the Role of Molecular Physics in Dissipative Divertor Operations through Helium Plasmas at DIII-D.” Physics of Plasmas, vol. 24, no. 5, American Institute of Physics (AIP), 2017, p. 56116–, doi:10.1063/1.4982057.

13 Jaervinen, A., et al. “Progress in DIII-D Towards Validating Divertor Power Exhaust Predictions.” Nuclear Fusion, vol. 60, no. 5, IOP Publishing, 2020, p. 56021–, doi:10.1088/1741-4326/ab7f5c.

14 Ohno, N., et al. “Investigation of Recombination Front Region in Detached Plasmas in a Linear Divertor Plasma Simulator.” Nuclear Materials and Energy, vol. 19, Elsevier Ltd, 2019, pp. 458–62, doi: 10.1016/j.nme.2019.03.010.

15 Wiesen, S., et al. “Relevance of Collisionality in the Transport Model Assumptions for Divertor Detachment Multi-Fluid Modelling on JET.” Journal of Nuclear Materials, vol. 415, no. 1, Elsevier B.V, 2011, pp. S535–S539, doi: 10.1016/j.jnucmat.2010.12.010.

16 Rognlien, T., et al. “Simulation of Plasma Fluxes to Material Surfaces with Self-Consistent Edge Turbulence and Transport for Tokamaks.” Journal of Nuclear Materials, vol. 337-339, Elsevier B.V, 2005, pp. 327–31, doi: 10.1016/j.jnucmat.2004.10.023.

17 Kadomtsev, B. B. Plasma Turbulence. Academic Press, 1965.

18 Itoh, K. (Kimitaka), et al. Transport and Structural Formation in Plasmas. Institute of Physics Pub., 1999.

19 Itoh, Kimitaka, et al. “Anatomy of Plasma Turbulence.” Nature Physics, vol. 4, no. 9, 2008, pp. 721–25, doi:10.1038/nphys1029.

20 Boedo, J. A., et al. “Transport by Intermittent Convection in the Boundary of the DIII-D Tokamak.” Physics of Plasmas, vol. 8, no. 11, 2001, pp. 4826–33, doi:10.1063/1.1406940.

21 Carralero, D., et al. “On the Role of Filaments in Perpendicular Heat Transport at the Scrape-Off Layer.” Nuclear Fusion, vol. 58, no. 9, IOP Publishing, 2018, p. 96015–, doi:10.1088/1741-4326/aacb04.

22 Soukhanovskii, V. .., et al. “Developing Physics Basis for the Snowflake Divertor in the DIII-D Tokamak.” Nuclear Fusion, vol. 58, no. 3, IOP Publishing, 2018, p. 36018–, doi:10.1088/1741-4326/aaa6de.

23 Ryutov, D. D. “Geometrical Properties of a ‘snowflake’ Divertor.” Physics of Plasmas, vol. 14, no. 6, American Institute of Physics, 2007, pp. 064502–064502–4, doi:10.1063/1.2738399.
24 Leonard, A. .., et al. “Evolution of 2D Deuterium and Impurity Radiation Profiles During Transitions from Attached to Detached Divertor Operation in DIII-D.” Journal of Nuclear Materials, vol. 266, Elsevier B.V, 1999, pp. 348–53, doi:10.1016/S0022-3115(98)00581-9.
25 Leonard, A. W. “Edge-Localized-Modes in Tokamaks.” Physics of Plasmas, vol. 21, no. 9, American Institute of Physics (AIP), 2014, p. 90501–, doi:10.1063/1.4894742.
26 Lipschultz, B., et al. “Marfe: An Edge Plasma Phenomenon.” Nuclear Fusion, vol. 24, no. 8, IOP Publishing, 1984, pp. 977–88, doi:10.1088/0029-5515/24/8/002.
27 Bernert, M., et al. “X-Point Radiation, Its Control and an ELM Suppressed Radiating Regime at the ASDEX Upgrade Tokamak.” Nuclear Fusion, vol. 61, no. 2, IOP Publishing, 2020, doi:10.1088/1741-4326/abc936.
28 Canik, J. .., et al. “Modeling of Detachment Experiments at DIII-D.” Journal of Nuclear Materials, vol. 463, Elsevier B.V, 2015, pp. 569–72, doi:10.1016/j.jnucmat.2014.11.077.
29 Richards, P. L. “Bolometers for Infrared and Millimeter Waves.” Journal of Applied Physics, vol. 76, no. 1, American Institute of Physics, Inc, 1994, pp. 1–24, doi:10.1063/1.357128.
30 Korde, R., et al. "Silicon Photodiodes With Stable, Near-Theoretical Quantum Efficiency In The Soft X-Ray Region", Proc. SPIE 1140, X-Ray Instrumentation in Medicine and Biology, Plasma Physics, Astrophysics, and Synchrotron Radiation, 1989; doi:10.1117/12.961812.
31 Ingesson, L. C., et al. “Chapter 7: Tomography Diagnostics: Bolometry and Soft-X-Ray Detection.” Fusion Science and Technology, vol. 53, no. 2, Taylor & Francis, 2008, pp. 528–76, doi:10.13182/FST53-528.
32 Lee, Seungsup, et al. “Correction for Neutral Pressure-Driven Signal in Radiated Power Measurements on Proto-MPEX.” IEEE Transactions on Plasma Science, vol. 48, no. 6, IEEE, 2020, pp. 1649–54, doi:10.1109/TPS.2020.2984233.
33 Mast, K. F., et al. “A Low Noise Highly Integrated Bolometer Array for Absolute Measurement of VUV and Soft x Radiation.” Review of Scientific Instruments, vol. 62, no. 3, American Institute of Physics, 1991, pp. 744–50, doi:10.1063/1.1142078.
34 Liu, Guigen, et al. “High-Resolution and Fast-Response Fiber-Optic Temperature Sensor Using Silicon Fabry-Pérot Cavity.” Optics Express, vol. 23, no. 6, 2015, pp. 7237–47, doi:10.1364/OE.23.007237.
35 Reinke, M. .., et al. “Development of Plasma Bolometers Using Fiber-Optic Temperature Sensors.” Review of Scientific Instruments, vol. 87, no. 11, 2016, pp. 1–4, doi:10.1063/1.4960421.
36 Sheng, Qiwen, et al. “A Fiber-Optic Bolometer Based on a High-Finesse Silicon Fabry-Pérot Interferometer.” Review of Scientific Instruments, vol. 89, no. 6, American Institute of Physics, 2018, pp. 065002–065002, doi:10.1063/1.5027076.
37 Uddin, Nezm et al. “Multichannel fiber-optic silicon Fabry-Perot interferometric bolometers for plasma radiation measurements.” Photonics, under review, 2021.
38 Mlynar, Jan, et al. “Current Research into Applications of Tomography for Fusion Diagnostics.” Journal of Fusion Energy, vol. 38, no. 3, Springer US, 2019, pp. 458–66, doi:10.1007/s10894-018-0178-x.
39 Willoughby, Ralph A. “Solutions of Ill-Posed Problems.” SIAM Review, vol. 21, no. 2, The Society for Industrial and Applied Mathematics, 1979, pp. 266–67, doi:10.1137/1021044.
40 Mlynar, J., et al. “Investigation of the Consistency of Magnetic and Soft x-Ray Plasma Position Measurements on TCV by Means of a Rapid Tomographic Inversion Algorithm.” Plasma Physics and Controlled Fusion, vol. 45, no. 2, IOP Publishing, 2003, pp. 169–80, doi:10.1088/0741-3335/45/2/308.
41 Bühlmann, Peter., and Sara. van de Geer. Statistics for High-Dimensional Data Methods, Theory and Applications . Springer-Verlag Berlin Heidelberg, 2011.
42 Luxon, J. L. “A Brief Introduction to the DIII-D Tokamak.” Fusion Science and Technology, vol. 48, no. 2, Taylor & Francis, 2005, pp. 828–33, doi:10.13182/FST05-A1042.
43 Luxon, J. L., et al. “Overview of the DIII-D Fusion Science Program.” Fusion Science and Technology, vol. 48, no. 2, Taylor & Francis, 2005, pp. 807–27, doi:10.13182/FST05-A1041.
44 Mahdavi, M. A., et al. “Divertor Physics and Concept Development on DIII-D and Doublet-III Tokamaks.” Fusion Science and Technology, vol. 48, no. 2, Taylor & Francis, 2005, pp. 1072–82, doi:10.13182/FST05-A1061.

45 Minea, T. “Beam-plasma interaction in the ITER NBI.” (INIS-XA--08N0893). International Atomic Energy Agency (IAEA), 2008
46 HOSHINO, Katsumichi “Electron Cyclotron Heating (ECH) ofTokamak Plasmas,” Journal of Nuclear Science and Technology, 27:5, 391-405, 1990 DOI:10.1080/18811248.1990.9731201
47 Cengher, Mirela, et al. “Performance and Upgrades for the Electron Cyclotron Heating System on DIII-D.” IEEE Transactions on Plasma Science, vol. 42, no. 7, IEEE, 2014, pp. 1964–70, doi:10.1109/TPS.2013.2292299.
48 Leonard, A. W., et al. “2D Tomography with Bolometry in DIII-Da.” Review of Scientific Instruments, vol. 66, no. 2, 1995, pp. 1201–04, doi:10.1063/1.1146006.
49 Mitchell, Tom M. (Tom Michael). Machine Learning. McGraw-Hill, 1997.
50 Koza, John R., et al. “Automated Design of Both the Topology and Sizing of Analog Electrical Circuits Using Genetic Programming.” Artificial Intelligence in Design ’96, Springer Netherlands, pp. 151–70, https://doi.org/10.1007/978-94-009-0279-4_9.
51 What is Machine Learning?". www.ibm.com. Retrieved 2021-08-15.
52 Mockus, Jonas. Bayesian Approach to Global Optimization Theory and Applications. Springer Netherlands, 1989, https://doi.org/10.1007/978-94-009-0909-0.
53 Nogueira, Fernando, “Bayesian Optimization: Open source constrained global optimization tool for Python.” 2014, https://github.com/fmfn/BayesianOptimization.
54 Hardesty, Larry (14 April 2017). "Explained: Neural networks". MIT News Office. Retrieved 2 June 2022.
55 Chollet, Francois and others, “Keras.” GitHub, 2015, https://github.com/fchollet/keras
56 http://www.bmva.org/visionoverview Archived 2017-02-16 at the Wayback Machine The British Machine Vision Association and Society for Pattern Recognition Retrieved February 20, 2017
57 Bradski, G., “The OpenCV Library.”, Dr. Dobb's Journal of Software Tools, 2236121, 2000.
58 Hijazi, H., et al. “Tungsten Oxide Thin Film Exposed to Low Energy He Plasma: Evidence for a Thermal Enhancement of the Erosion Yield.” Journal of Nuclear Materials, vol. 484, Elsevier, 2017, pp. 91–97, doi:10.1016/j.jnucmat.2016.11.030.
59 Ciesielski, Arkadiusz, et al. “Evidence of Germanium Segregation in Gold Thin Films.” Surface Science, vol. 674, Elsevier B.V, 2018, pp. 73–78, doi:10.1016/j.susc.2018.03.020.
60 MÜLLER, E. R., and F. MAST. “A New Metal Resistor Bolometer for Measuring Vacuum Ultraviolet and Soft x Radiation.” Journal of Applied Physics, vol. 55, no. 7, American Institute of Physics, 1984, pp. 2635–41, doi:10.1063/1.333272.
61 Incropera, Frank P., and David P. DeWitt. Fundamentals of Heat and Mass Transfer . 5th ed., J. Wiley, 2002.
62 Meister, H., et al. “Broad-Band Efficiency Calibration of ITER Bolometer Prototypes Using Pt Absorbers on SiN Membranes.” Review of Scientific Instruments, vol. 84, no. 12, 2013, pp. 123501–123501, doi:10.1063/1.4834755.
63 Reinke, M. L., and I. H. Hutchinson. “Two Dimensional Radiated Power Diagnostics on Alcator C-Mod.” Review of Scientific Instruments, vol. 79, no. 10, 2008, p. 10F306. doi: 10.1063/1.2965018
64 Reinke, M. L., “Experimental Tests of Parallel Impurity Transport Theory in Tokamak Plasmas.” Massachusetts Institute of Technology, 2021, C.1.1.
65 Carr, M., et al. “Towards integrated data analysis of divertor diagnostics with ray-tracing.” 44th EPS Conference on Plasma Physics (2017), Belfast, Northern Ireland UK.
66 Rognlien, T.D., and Rensink, M.E., “Users Manual for the UEDGE Edge-Plasma Transport Code.” Lawrence Livermore National Laboratory, Livermore, CA 94551, 2015
67 Andersen, A. .., and A. .. Kak. “Simultaneous Algebraic Reconstruction Technique (SART): A Superior Implementation of the ART Algorithm.” Ultrasonic Imaging, vol. 6, no. 1, Elsevier Inc, 1984, pp. 81–94, doi:10.1016/0161-7346(84)90008-7.
68 Bro, Rasmus, and Sijmen De Jong. “A Fast Non-Negativity-Constrained Least Squares Algorithm.” Journal of Chemometrics, vol. 11, no. 5, John Wiley & Sons, Ltd, 1997, pp. 393–401, doi:10.1002/(SICI)1099-128X(199709/10)11:53.0.CO;2-L.
69 Myung, In Jae. “Tutorial on Maximum Likelihood Estimation.” Journal of Mathematical Psychology, vol. 47, no. 1, Elsevier Inc, 2003, pp. 90–100, doi:10.1016/S0022-2496(02)00028-7.

70 Craciunescu, Teddy, et al. “Maximum Likelihood Bolometric Tomography for the Determination of the Uncertainties in the Radiation Emission on JET TOKAMAK.” Review of Scientific Instruments, vol. 89, no. 5, 2018, pp. 053504–053504, doi:10.1063/1.5027880.
71 Reinke, M., “Development and Demonstration of 2D Fiber-Optic Bolometers.” ORNL project proposal, 0000246650.
72 Lao, L. .., et al. “Reconstruction of Current Profile Parameters and Plasma Shapes in Tokamaks.” Nuclear Fusion, vol. 25, no. 11, IOP Publishing, 1985, pp. 1611–22, doi:10.1088/0029-5515/25/11/007.
73 Rapp, J, et al. “The Development of the Material Plasma Exposure Experiment.” IEEE Transactions on Plasma Science, vol. 44, no. Dec. 2016, pp. 3456–3464. doi: 10.1109/TPS.2016.2628326.
74 Summers, H. P. (2004) The ADAS User Manual, version 2.6 http://www.adas.ac.uk
75 Muñoz Burgos, J.., et al. “Evaluation of an Improved Atomic Data Basis for Carbon in UEDGE Emission Modeling for L-Mode Plasmas in DIII-D.” Journal of Nuclear Materials, vol. 438, Elsevier B.V, 2013, pp. S406–S409, doi:10.1016/j.jnucmat.2013.01.081.
76 S. Girard, et al. “Radiation Effects on Silica-Based Optical Fibers: Recent Advances and Future Challenges.” IEEE Transactions on Nuclear Science, vol. 60, no. 3, IEEE, 2013, pp. 2015–36, doi: 10.1109/TNS.2012.2235464.
77 Matos, Francisco A., et al. “Deep Learning for Plasma Tomography Using the Bolometer System at JET.” Fusion Engineering and Design, vol. 114, 2017, pp. 18–25, https://doi.org/10.1016/j.fusengdes.2016.11.006.
78 M. Tobin, "Machine Learning-Based Tomography of Plasma Emissivity on C-2W," HTPD2022, PA-21
79 Srivastava, Nitish, et al. "Dropout: a simple way to prevent neural networks from overfitting." The journal of machine learning research 15.1 (2014): 1929-1958.
80 Fenstermacher, M. E., et al. “The Two-Dimensional Structure of Radiative Divertor Plasmas in the DIII-D Tokamak.” Physics of Plasmas, vol. 4, no. 5, 1997, pp. 1761–73, https://doi.org/10.1063/1.872278.
81 Petrie, T., et al. “Comparison of Radiating Divertor Behaviour in Single-Null and Double-Null Plasmas in DIII-D.” Nuclear Fusion, vol. 48, no. 4, IOP Publishing, 2008, p. 045010–, https://doi.org/10.1088/0029-5515/48/4/045010.
82 Wilks, T., et al. “Development of an Integrated Core–edge Scenario Using the Super H-Mode.” Nuclear Fusion, vol. 61, no. 12, IOP Publishing, 2021, p. 126064–, https://doi.org/10.1088/1741-4326/ac34d6.
83 Lee, Seungsup, et al. "Demonstration of Neutral Pressure Sensitivity in an Interferometric Fiber Optic Temperature Sensor." IEEE Transactions on Plasma Science (2022).
84 U. Wenzel, et al. “An Ionization Pressure Gauge with LaB6 Emitter for Long-Term Operation in Strong Magnetic Fields.” Review of Scientific Instruments, vol. 89, no. 3, 2018, pp. 33503–033503, doi: 10.1063/1.5019765.
85 B. LaBombard, “The Design and Construction of Miniature, High-Pressure, Penning Ionization Gauges for Alcator C-Mod.” MIT Plasma Science and Fusion Center, Cambridge, MA, USA, PSFC/RR-15-12, Dec. 2015
86 A. Kallenbach, et al. “Neutral Pressure and Separatrix Density Related Models for Seed Impurity Divertor Radiation in ASDEX Upgrade.” Nuclear Materials and Energy, vol. 18, Elsevier Ltd, 2019, pp. 166–74, doi: 10.1016/j.nme.2018.12.021.
87 A. P. Niemczewski, “NEUTRAL PARTICLE DYNAMICS IN THE ALCATOR C-MOD TOKAMAK,” Ph.D. dissertation, Dept. Nuclear Eng., Massachusetts Institute of Technology, Cambridge, MA, USA, 1995.
88 Laidler, Keith J., and Meiser, John H. Physical Chemistry. 1st ed., Benjamin/Cummings, 1982, pp.18.
89 Hoffmann, Heiko, et al. “Local Dimensionality Reduction for Non-Parametric Regression.” Neural Processing Letters, vol. 29, no. 2, 2009, pp. 109–131. doi: 10.1007/s11063-009-9098-0
90 Van Eden, et al. “Plasma Radiation Studies in Magnum-PSI Using Resistive Bolometry.” Nuclear Fusion, vol. 58, no. 10, 2018, p. 11.

91 Bernert, M, et al. “Application of AXUV Diode Detectors at ASDEX Upgrade.” Review of Scientific Instruments, vol. 85, no. 3, 2014, p. 033503. doi: 10.1063/1.4867662
92 Caneses, J. F., et al. “Differential Pumping Requirements for the Light-Ion Helicon Source and Heating Systems of Proto-MPEX.” Physics of Plasmas, vol. 25, no. Aug. 2018, p. 083518. doi: 10.1063/1.5001519.
93 U. Perera, “Bolometers for Fusion Plasma Diagnostics,” in Bolometers, IntechOpen, 2012, pp. 158-160.
94 Showers, Melissa. A Power Accounting Analysis of the Proto-MPEX Linear Device and Target Heat Flux Extrapolations to MPEX-based on Proto-MPEX discharges. 2019. The University of Tennessee, Knoxville. PhD dissertation.
95 Lawson, Charles L., and Richard J. Hanson. Solving Least Squares Problems. Society for Industrial and Applied Mathematics SIAM, 3600 Market Street, Floor 6, Philadelphia, PA 19104, 1995.
96 "Technology readiness levels (TRL); Extract from Part 19 - Commission Decision C(2014)4995.” ec.europa.eu. 2014. Retrieved 11 November 2019.
97 Meister, H., et al. “Broad-Band Efficiency Calibration of ITER Bolometer Prototypes Using Pt Absorbers on SiN Membranes.” Review of Scientific Instruments, vol. 84, no. 12, 2013, pp. 123501–123501, doi: 10.1063/1.4834755.
98 Peterson, Byron J., et al. “Development of Imaging Bolometers for Magnetic Fusion Reactors (invited)a.” Review of Scientific Instruments, vol. 79, no. 10, 2008, pp. 10E301–10E301–6, doi: 10.1063/1.2988822.
99 Peterson, B. J., et al. “Bolometer Diagnostics for One- and Two-Dimensional Measurements of Radiated Power on the Large Helical Device.” Plasma Physics and Controlled Fusion, vol. 45, no. 7, 2003, pp. 1167–82, doi: 10.1088/0741-3335/45/7/309.

Appendix

NNLS Algorithm in pseudocode [95]

- Inputs:
  - a real-valued matrix A of dimension $m \times n$,
  - a real-valued vector $\mathbf{y}$ of dimension m,
  - a real value ε, the tolerance for the stopping criterion.
- Initialize:
  - Set $P = \emptyset$.
  - Set $R = \{1, ..., n\}$.
  - Set $\mathbf{x}$ to an all-zero vector of dimension n.
  - Set $\mathbf{w} = A^{\mathrm{T}}(\mathbf{y} - A\mathbf{x})$.
  - Let w^R denote the sub-vector with indexes from R
- Main loop: while $R \neq \emptyset$ and $\max(\mathbf{w^R}) > \varepsilon$:
  - Let j in R be the index of $\max(\mathbf{w^R})$ in $\mathbf{w}$.
  - Add j to P.
  - Remove j from R.
  - Let A^P be A restricted to the variables included in P.
  - Let s be vector of same length as $\mathbf{x}$. Let s^P denote the sub-vector with indexes from P, and let s^R denote the sub-vector with indexes from R.
  - Set $s^P = ((A^P)^{\mathrm{T}} A^P)^{-1} (A^P)^{\mathrm{T}}\mathbf{y}$
  - Set s^R to zero
  - While $\min(s^P) \leq 0$:
    - Let $\alpha = \min x_i/x_i - s_i$ for i in P where $s_i \leq 0$.
    - Set $\mathbf{x}$ to $\mathbf{x} + \alpha(s - x)$.
    - Move to R all indices j in P such that $x_j \leq 0$.
    - Set $s^P = ((A^P)^{\mathrm{T}} A^P)^{-1} (A^P)^{\mathrm{T}}\mathbf{y}$
    - Set s^R to zero.
  - Set $\mathbf{x}$ to s.
  - Set $\mathbf{w}$ to $A^{\mathrm{T}}(\mathbf{y} - A\mathbf{x})$.
- Output: $\mathbf{x}$

Vita

Seungsup Lee was born in Seoul, South Korea. He graduated from Sungkyunkwan University in 2013. He served in Republic of Korean army as a Korean Augmentation To the US Army (KATUSA). He started his graduate studies in 2016 at the nuclear engineering department, University of Tennessee – Knoxville. He was a teaching assistant until he started the FOB project. He received Outstanding Graduate Teaching Award from the department of nuclear engineering. He worked on graphite digestion for the collector probe project. He worked on AXUV photodiode and the resistive bolometer for proto-MPEX. The worked on the FOB project for his dissertation. He published two papers, and he has one paper under review and one paper in preparation, during his graduate studies. He is ready to graduate.